UNIVERSITÉ DU QUÉBEC
INSTITUT NATIONAL DE LA RECHERCHE SCIENTIFIQUE
CENTRE – ÉNERGIE, MATÉRIAUX ET TÉLÉCOMMUNICATIONS

ANTENNES ROBUSTES ET EFFICACES POUR L'AMÉLIORATION DE LA PERFORMANCE DES LIENS À ONDES MILLIMÉTRIQUES

Par
Mohammadmahdi Farahani

Thèse présentée pour l'obtention du grade de Doctorat en Télécommunications,
Ph.D. en Télécommunications

Jury d'évaluation

Examinateur externe	Jean-Jacques Laurin, Ph.D. École Polytechnique de Montréal Canada
Examinateur externe	Mostafa Hefnawi, Ph.D. Royal Military College of Canada, Kingston, Canada
Examinateur interne	Serioja Ovidiu Tatu, Ph.D. Institut national de la recherche scientifique (INRS-EMT)
Codirecteur de recherche	Mourad Nedil, Ph.D. Université du Québec en Abitibi-Témiscamingue
Directeur de recherche	Tayeb A. Denidni, Ph.D. Institut national de la recherche scientifique (INRS-EMT)

Résumé

Récemment, les bandes mmWave ont gagné beaucoup d'attention parmi les chercheurs. Ils ont le potentiel de répondre aux demandes des nouveaux systèmes et applications de communication. De plus, les systèmes haute vitesse, large bande passante et haute capacité font des communications mmWave un choix approprié pour les communications sans fil à courte portée. Motivée par l'augmentation de la charge de trafic sur les systèmes cellulaires et l'augmentation associée du trafic via le réseau, la communication de périphérique à périphérique avec mmWave est une solution possible pour gérer cette tâche future. Cependant, les bandes mmWave ont de sérieux obstacles au développement de réseaux de communication. Dans la communication sans fil, le débit de la liaison de communication est l'un des indicateurs les plus importants pour estimer les performances. Le débit, cependant, dépend fortement des caractéristiques du canal de propagation, comme la perte de chemin, la distance entre les appareils, le bruit, etc. Grâce à la formule du modèle de perte de chemin en espace libre de Friis, la perte de chemin pour la bande des 60-GHz a une perte de près de 28 dB de plus par rapport à la bande des 5 GHz.

Pour surmonter le blocage, plusieurs approches de la couche physique à la couche réseau ont été proposées. Cependant, chaque approche a ses avantages et ses inconvénients, et ces approches doivent être combinées de manière intelligente pour obtenir des réseaux robustes et efficaces.

Le couplage mutuel a un impact sur les performances du système MIMO en modifiant l'impédance d'entrée des éléments rayonnants, en augmentant le niveau des lobes latéraux et en dégradant la forme du diagramme de rayonnement. Le couplage mutuel est principalement dû à trois composantes, les ondes de surface, le couplage entre les lignes d'alimentation et le couplage dû aux champs spatiaux. À cet égard, deux approches distinctes ont été proposées pour réduire le couplage mutuel dû aux champs spatiaux. Dans la première approche, une technique intéressante pour réduire le couplage mutuel entre les antennes à résonateur diélectrique (DRA) mmWave en utilisant une nouvelle paroi de polarisation-rotateur métamatériaux (MPR) est étudiée et réalisée. Le couplage mutuel est diminué en installant des murs MPR parmi les DRA, qui sont situés dans le plan H. En utilisant ces murs MPR, les modes TE des antennes deviennent orthogonaux, ce qui diminue le couplage mutuel entre les antennes. Dans la deuxième approche, une nouvelle méthode est proposée pour réduire le couplage dû à l'interaction électromagnétique spatiale entre deux éléments rayonnants à polarisation circulaire en utilisant une couche superstrate FSS.

De plus, différentes techniques sont étudiées pour augmenter le gain de l'antenne. Il y a un grand défi concernant le développement d'un système dans la bande de 60-GHz, en raison de la grande quantité de pertes de propagation dans cette bande de fréquences qui a nécessité la conception des récepteurs à haute sensibilité pour surmonter cet inconvénient. Concernant les antennes, il est nécessaire de développer des

antennes directives à gain élevé. Dans cet effort, la conception d'une ligne de transmission à faible perte et à haut rendement joue un rôle important pour atteindre cet objectif. Deux approches ont été étudiées sur la couche superstrate FSS et la métasurface à gradient de phase (PGM), respectivement. L'avantage des techniques proposées est qu'elles n'utilisent pas de réseaux d'alimentation qui ajoutent une grande quantité de pertes au réseau à mmWave.

Pour répondre aux exigences des structures de guidage à faible perte de mmWave, nous avons proposé une nouvelle structure de guide d'ondes, appelée Hedgehog waveguide, qui présente plusieurs avantages par rapport aux lignes de transmission conventionnelles rapportées dans la littérature. Le principal avantage du guide d'ondes Hedgehog est qu'il peut supporter la propagation avec des pertes plus faibles. De plus, du fait que les champs électromagnétiques sont captés dans l'espace à l'intérieur du guide d'onde, les pertes de rayonnement sont maintenues très faibles, résultant en une bonne immunité aux perturbations électromagnétiques externes par rapport à la technologie microruban. Un autre avantage principal du guide d'ondes Hedgehog est la compatibilité avec les guides d'ondes creux, ce qui donne un degré de liberté supplémentaire pour utiliser le guide d'ondes proposé pour plusieurs conceptions d'ondes mmWve. De plus, le guide d'ondes à arête creuse et la méthode de transition à microruban sont expliqués et comparés avec le guide d'ondes Hedgehog, et un coupleur hybride à 3 ouvertures et à faible perte avec technologie d'écart de crête est conçu et fabriqué.

En tant que formateur de faisceaux robuste et efficace, un réseau de formation de faisceaux LH/RH CP à double polarisation exceptionnelle est introduit et étudié dans la bande de 60-GHz. Le guide d'onde Hedgehog est utilisé comme une structure de guidage à faible perte notamment pour mettre en œuvre les déphaseurs cruciaux. La constante d'atténuation du guide d'ondes Hedgehog est significativement plus petite que les structures de guidage traditionnelles similaires, par exemple, les guides d'ondes SIW, ridge-gap, hollow et gap-waveguide dans la bande de 60-GHz. Le formateur de faisceau proposé produit des ondes de sortie à phase progressive uniformes pour alimenter un réseau d'antennes avec les huit diagrammes de rayonnement distincts associés à chacun des huit ports d'entrée. Pour augmenter le gain et réduire les lobes secondaires, un réseau d'alimentation 8×8 est utilisé. En utilisant le réseau d'alimentation introduit, les lobes latéraux sont réduits à -19 dB. En augmentant le nombre d'éléments rayonnants à 8, la directivité du formateur de faisceau recommandé augmente d'environ 3 dB. De plus, l'antenne à fente progressive est utilisée pour obtenir une largeur de bande à rapport axial à large bande. La largeur de bande de 10.75% et l'efficacité de rayonnement de 90% pour chaque port sont obtenues en utilisant le réseau de formation de faisceau prévu.

ABSTRACT

Recently mmWave bands have gained much focus among the researchers. They have the potential to meet the demands of emerging communication systems and applications. Besides, the high-speed, large bandwidth, high-capacity systems make the mmWave communications a suitable choice for short-range wireless communications. Motivated by the increase of traffic load on cellular systems and the associated increase of traffic through the network, device-to-device (D2D) communication with mmWave is a possible solution to manage this future task. However, the mmWave bands have severe obstacles in developing communication networks. In wireless communication, the throughput of the communication link is one of the most important indicators to estimate the performance. The throughput, however, highly depends on the characteristic of the propagation channel, like path loss, the distance between devices, noise, etc. Through the formula of Friis free-space path loss model, the path loss for the 60-GHz band has a nearly 28 dB loss more versus the 5-GHz band.

To overcome blockage, multiple approaches from the physical layer to the network layer have been proposed. However, every approach has its advantages and shortcomings, and these approaches should be combined in an intelligent way to achieve robust and efficient networks.

The mutual coupling has an impact on (multiple input, multiple output) MIMO system performance through changing the input impedance of the radiating elements, increasing the sidelobe level, and degrading radiation pattern shape. The mutual coupling is mainly due to three components, the surface waves, the coupling between the feeding lines, and coupling due to spatial fields. In this regard, two distinguished approaches have been proposed to reduce the mutual coupling due to the spatial fields. In the first approach, a valuable technique for reducing the mutual coupling among mmWave dielectric resonator antennas (DRAs) using a new metamaterial polarization-rotator (MPR) wall is studied and performed. The mutual coupling is decreased by installing MPR walls among DRAs, which are located in the H-plane. Utilizing this MPR walls, the TE modes of the antennas become orthogonal, which decreases the mutual coupling among the antennas. In the second approach, a novel method is proposed to reduce the coupling due to spatial electromagnetic interaction among two circularly-polarised radiating elements utilizing an FSS superstrate layer.

Furthermore, different techniques are investigated for increasing the gain of the antenna. There is a big challenge regarding the development of a system at 60-GHz band, due to the high amount of propagation losses at this frequency-band which required designing the high-sensitivity receivers to overcome that drawback. In antenna regards, it is needed to develop directive high-gain antennas. In this effort, designing a high-efficiency low-loss transmission line plays an important rule to achieve that goal. Two approaches

based on the FSS superstrate layer and phase gradient metasurface (PGM) have been studied, respectively. The advantage of the proposed techniques is that they do not employ feeding networks which add a high amount of losses to the network at mmWave.

To answer the demands of low-loss guiding structures at mmWave, we proposed a novel waveguide structure, named Hedgehog waveguide, which has several advantages compared to the conventional transmission lines reported in literature. The main advantage of the Hedgehog waveguide is that it can support propagation with lower losses. Moreover, the fact that the electromagnetic fields are captured to space within the waveguide, radiation losses are kept very low, resulting in good immunity from external electromagnetic disturbance compared to the microstrip technology. Another main advantage of the Hedgehog waveguide is the compatibility with the hollow waveguides, which gives an extra degree of freedom to use the proposed waveguide for several mmWave designs. Also, the ridge gap waveguide and transition method to microstrip are explained and compared with Hedgehog waveguide, and a low-loss multi-aperture 3-dB hybrid coupler with ridge gap technology is designed and fabricated.

As a robust and efficient beamformer, an exceptional high-efficiency dual left/right-hand circularly-polarized (LH/RH CP) beamforming network is introduced and studied at 60-GHz mmWave band. The Hedgehog waveguide is employed as a notably low-loss guiding structure to implement the crucial phase shifters. The attenuation constant of the Hedgehog waveguide is significantly smaller than similar traditional guiding structures, e.g., SIW, ridge gap, hollow, and gap waveguides at the 60-GHz mmWave band. The offered beamformer produces uniform progressive-phase output waves to supply an array of antennas with the eight separate radiation patterns associated with each of the eight input ports. For enhancing the gain and reducing the sidelobes, an 8×8 feeding network is employed. Utilizing the introduced feeding network, the sidelobes are reduced to -19 dB. By expanding the number of radiating elements to 8, the directivity of the recommended beamformer raises about 3 dB. Furthermore, the progressive slot antenna is utilized to obtain a broadband axial-ratio bandwidth. The bandwidth of 10.75% and the radiating efficiency of 90% for each port is obtained utilizing the intended beamforming network.

Acknowledgements

The successful achievement of research production similar the one presented in this dissertation is the consequence of many determinants. Of course, self-confidence, energy, determination, and hard works are required to obtain any goals. But it couldn't be feasible out of the external emotional support, supervision and encouragement of essential personalities around us. In my case, I have been excessively fortunate to have the best people close to me giving their assistance, direction and encouragements. This thesis wouldn't be achieved without their names in it.

First of all, I want to send my appreciation to my supervisor, Prof. Tayeb A. Denidni. I genuinely appreciate his supervision, counsel, and enthusiasm to take time to explain and review my analysis results. He has taught me relevant teachings to become a better professional researcher.

I would like to sincerely thank Prof. Abdel Razik Sebak at Concordia University for his support in all parts of my Ph.D. research, maintenance, responsibility, and motivations. No significance of words is enough to show my appreciation for his patience.

I also thank my co-supervisor Prof. Mourad Nedil, for his support throughout my Ph.D. research. His valuable advice for my thesis will always accompany me.

Moreover, I would like to thank my dear friend Dr. Mohammad Akbari. We have contributed together to several projects during these years. Friends like him, who can be depended upon to show up in a pinch, are hard to find. I admire his energy, thoughtfulness and your ability to keep everyone on track.

I shall not forget my dear group members in INRS-EMT antenna Lab. I want to thank Dr. Abdolmahdi Dadgarpour, Mansour Dashti, Behnam Zarghooni, Saman Zarbakhsh, Arun Kesavan, Jamal Zaid, Javad Pourahmadazar, Jin xin, and Amin Ebrahimzadeh for their emotional supports, stimulating discussions and their friendship. To all of them, thank you for your kindness in giving me not only your scientific information but also your countries cultures and your skills. Thank you for making me feel I was part of a new, big family.

I thank especially Prof. Ahmed Kishk at Concordia University for their ideas and valuable advice on the Antenna course projects regards to use his excellent antenna engineering science.

Finally, I thank the Institut National de la Recherche Scientifique - Energie, Matériaux et Télécommunications (INRS-EMT), Université du Québec for providing the full funding which supported me to undertake this Ph.D. research.

Contribution of Authors

This thesis is a collection of several publications (seven journal articles and four conference papers), which were published/submitted in high-quality IEEE journals and conference proceedings. The key contributions of authors in this dissertation, that realize the objectives mentioned in chapter 1, are explained in detail in the following. Moreover, my supervisor, Prof. Tayeb A. denidni, attested to the accuracy of this statement.

Chapter 2: Efficient mmWave MIMO Antennas

These works, have been done in this chapter, have been published in the following journals and conferences and the contributions are summarized in the following:

- M. Farahani, J. Pourahmadazar, M. Akbari, M. Nedil, A. R. Sebak and T. A. Denidni, "Mutual Coupling Reduction in Millimeter-Wave MIMO Antenna Array Using a Metamaterial Polarization-Rotator Wall," IEEE Antennas and Wireless Propagation Letters, vol. 16, pp. 2324-2327, 2017.

I was the main contributor to this work. More specifically, my key contributions were as follows: a) I have introduced the distinguished technique to make two antennas orthogonal in term of receiving signal from each other in order to cancel the special coupling between two antennas at 60-GHz mmWave, b) I have investigated, studied this technique, and moreover, I have designed the polarization rotator wall employed in this work, c) I have simulated and realized the proposed MIMO Antenna prototypes, d) I have finalized the files for fabrication and sent them for fabrication e) I, Mr. Pourahmadazar, and Mr. Akbari have equally contributed in measurement process. f) I, Mr. Pourahmadazar, and Mr. Akbari have equally contributed to write the paper and answer the reviewers in the publication process equally. g) Other authors have contributed to improve and investigate the concept and review the first draft of the manuscript. As the research supervisor and co-supervisor, Prof. Denidni and Prof. Nedil provided guidance and direction on all aspects of the considered topic. Prof. Sebak gave comments on the practical settings of the techniques considered in this work, enabling the authors to have application-oriented assumptions and simulations. He also reviewed the paper and provided insightful comments.

- M. Farahani, J. Zaid, T. A. Denidni, M. Akbari, A. R. Sebak and M. Nedil, "Mutual coupling reduction in millimeter-wave MIMO dielectric resonator antenna using metamaterial polarization rotator wall," IEEE International Symposium on Antennas and Propagation & USNC/URSI National Radio Science Meeting, San Diego, CA, 2017, pp. 1261-1262.

I was the main contributor to this work. More specifically, my key contributions were as follows: a) I have introduced the distinguished technique to make two antennas orthogonal in term of receiving signal from each other in order to cancel the special coupling between two antennas at 60-GHz mmWave, b) I have studied and simulated the intended antenna, c) I, Mr. Zaid, and Mr. Akbari have equally contributed to write the paper. d) Other authors have contributed to improve and investigate the concept and review the first draft of the manuscript.

- M. Farahani, M. Akbari, M. Nedil and T. A. Denidni, "Mutual coupling reduction in dielectric resonator MIMO antenna arrays using metasurface orthogonalize wall," European Conference on Antennas and Propagation (EUCAP), Paris, 2017, pp. 985-987.

I was the main contributor to this work. More specifically, my key contributions were as follows: a) I have introduced the distinguished technique to make two antennas orthogonal in term of receiving signal from each other in order to cancel the special coupling between two antennas at 60-GHz mmWave, b) I have studied and simulated the intended antenna, c) I, and Mr. Akbari have equally contributed to write the paper. d) Other authors have contributed to improve and investigate the concept and review the first draft of the manuscript.

- M. Farahani, J. Zaid, J. Pourahmadazar, T. A. Denidni and M. Nedil, "Millimeter-wave couraggated surface for mutual coupling reduction between dipole antennas," 17th International Symposium on Antenna Technology and Applied Electromagnetics (ANTEM), Montreal, QC, 2016, pp. 1-2.

I was the main contributor to this work. More specifically, my key contributions were as follows: a) I have introduced the soft surface and realize it with corrugated surface to reduce the special coupling between two antennas, b) I have studied and simulated the intended antenna, c) I, Mr. Zaid and Mr. Pourahmadazar have equally contributed to write the paper. d) Other authors have contributed to improve and investigate the concept and review the first draft of the manuscript.

- M. Akbari, H. Abo Ghalyon, M. Farahani, A. Sebak and T. A. Denidni, "Spatially Decoupling of CP Antennas Based on FSS for 30-GHz MIMO Systems," IEEE Access, vol. 5, pp. 6527-6537, 2017.

I have equally contributed to this work. More specifically, my key contributions were as follows: a) I and Mr. Akbari have introduved and investigated the idea of reducing special coupling among CP antennas in a MIMO array using a superstrate layer, b) I and Mr. Akbari have equally work to evaluate the reflection array factor concerning the reflected waves from the superstrate layer c) I and Mr. Akbari have equally contributed in measurement process. d) I, Mr. Akbari and Mr. Ghalyon have equally contributed to write the paper and answer the reviewers in the publication process. e) Mr. Akbari finalized the antenna simulation and sent it for fabrication. f) Other authors have contributed to improve and investigate the concept and review the first draft of the manuscript.

- M. Akbari, M. M. Ali, M. Farahani, A. R. Sebak and T. Denidni, “Spatially mutual coupling reduction between CP-MIMO antennas using FSS superstrate,” Electronics Letters, vol. 53, no. 8, pp. 516-518, 13 4 2017.

I have equally contributed to this work. More specifically, my key contributions were as follows: a) I and Mr. Akbari have studied, investigated and implemented the intended approach of supressing the special coupling between two CP radiating ellemnts in a MIMO array using a superstrate layer, b) I and Mr. Akbari have equally contributed in measurement process. c) I and Mr. Akbari have equally contributed to write the paper and answer the reviewers in the publication process. d) Mr. Akbari finalized the antenna simulation and sent it for fabrication. e) Other authors have contributed to improve and investigate the concept and review the first draft of the manuscript.

Chapter 3: mmWave High Gain Antennas

These works, have been done in this chapter, have been published in the following journal and conference and the contributions are summarized in the following:

- M. Akbari, S. Gupta, M. Farahani, A. R. Sebak and T. A. Denidni, “Gain Enhancement of Circularly Polarized Dielectric Resonator Antenna Based on FSS Superstrate for MMW Applications,” IEEE Transactions on Antennas and Propagation, vol. 64, no. 12, pp. 5542-5546, Dec. 2016.

I have equally contributed to this work. More specifically, my key contributions were as follows: a) I and Mr. Akbari have introduced and investigated the idea of enhancing gain of an antenna using the superstrate layer, b) I and Mr. Akbari have equally work on proposing a model for the proposed antenna c) I and Mr. Akbari have equally contributed in measurement process. d) I and Mr. Akbari have equally contributed to write the paper and answer the reviewers in the publication process. e) Mr. Akbari finalized the antenna simulation and sent it for fabrication. f) Other authors have contributed to improve and investigate the concept and review the first draft of the manuscript.

- M. Farahani, J. Pourahmadazar, T. Denidni and M. Nedil, “Millimeter-Wave High-Gain Ridge Gap Beam Steerable Antenna for 5G wireless Networks,” International Symposium on Antenna Technology and Applied Electromagnetics (ANTEM), Waterloo, ON, 2018, pp. 1-2.

I was the main contributor to this work. More specifically, my key contributions were as follows: a) I have studied and developed the phase gradient metasurface for beam steering at 60-GHz, b) I have studied and simulated the intended antenna, c) I and Mr. Pourahmadazar have equally contributed to write the paper. d) Other authors have contributed to improve and investigate the concept and review the first draft of the manuscript.

Chapter 4: Low-loss Wave Guiding Structures at mmWave

These works, have been done in this chapter, have been published in the following journals and the contributions are summarized in the following:

- M. Farahani, M. Nedil and T. A. Denidni, "A Novel Hedgehog Waveguide and its Application in Designing a Phase Shifter Compatible With Hollow Waveguide Technology," IEEE Transactions on Microwave Theory and Techniques, vol. 67, no. 10, pp. 4107-4117, Oct. 2019.

I was the main contributor to this work. More specifically, my key contributions were as follows: a) I have introduced Hedgehog Waveguide in antenna society in this work, b) I have investigated, studied and formularized Hedgehog Waveguide along with the transition technique to the hollow waveguide. c) Other authors have contributed to improve and investigate the concept and review the first draft of the manuscript. As the research supervisor and co-supervisor, Prof. Denidni and Prof. Nedil provided guidance and direction on all aspects of the considered topic. Moreover Prof. Denidni gave comments on the practical settings of the technique considered in this work, enabling the author to have application-oriented assumptions and simulations. He also reviewed the paper and provided insightful comments.

- M. Farahani, M. Akbari, M. Nedil, T. A. Denidni and A. R. Sebak, "A Novel Low-Loss Millimeter-Wave 3-dB 90° Ridge-Gap Coupler Using Large Aperture Progressive Phase Compensation," IEEE Access, vol. 5, pp. 9610-9618, 2017.

I was the main contributor to this work. More specifically, my key contributions were as follows: a) I have introduced the idea of using large coupling aperture to compensate for the progressive phase of a coupler in order to realize a very low output phase error, b) I have formularized the large coupling aperture to be able to utilize in our design,c) I have simulated and realized the intended approach in ridge gap waveguide technology, d) I have finalized the files for fabrication and sent them for fabrication e) I and Mr. Akbari have contributed in measurement process equally. f) I and Mr. Akbari have contributed to write the paper and answer the reviewers in the publication process equally. g) Other authors have contributed to improve and investigate the concept, and review the first draft of the manuscript.

Chapter 5: State-of-the-art mmWave Beamformer Networks

This works, have been done in this chapter, have been submitted to the following journals and the contributions are summarized in the following:

- M. Farahani, M. Akbari, M. Nedil, A. R. Sebak and T. A. Denidni, "Millimeter-Wave Dual Left/Right-Hand Circularly-Polarized Beamforming Network," submitted to the IEEE Transactions on Antennas and Propagation.

I was the main contributor to this work. More precisely, my key contributions were as follows: a) I have proposed and developed the idea of Dual LH/RH CP antenna and employed SLL reduction technique, b) I have simulated and realized the intended approach in hollow waveguide technology, c) I have finalized the files for fabrication and sent them for fabrication d) I and Mr. Akbari have contributed in measurement process equally. e) I and Mr. Akbari have contributed to write the paper and answer the reviewers in the publication process equally. f) Other authors have contributed to improve and investigate the concept, and review the manuscript.

- M. Akbari, M. Farahani, S. Zarbakhsh, M. Dashti Ardakani, A. R. Sebak, T. A. Denidni and Omar M. Ramahi, "Highly Efficient 30-GHz 2×2 Beamformer Based on Rectangular Air-Filled Coaxial Line," submitted to the IEEE Transactions on Antennas and Propagation, 2019.

I have equally contributed to this work. More specifically, my key contributions were as follows: a) I, Mr. Akbari, Mr. Zarbakhsh, and Mr. Dashti have introduced and investigated the idea of enhancing gain of an antenna, b) I have equally work on simulations c) I have equally contributed in measurement process. d) I have equally contributed to write the paper and answer the reviewers in the publication process. e) Mr. Akbari finalized the antenna simulation and sent it for fabrication. f) Dr. Sebak, Dr. Denidni, and Dr. Ramahi have contributed to improve and investigate the concept and review the first draft and revised version of the manuscript, .

Contents

List of Figures

List of Tables

Abbreviations

AOA	Angle-Of-Arrival
MIMO	Multi Input Multi Output
ECC	Envelope correlation coefficient
EBG	Electromagnetic band-gap
SIW	Substrate integrated waveguide
SIR	Signal to interference ratio
AOD	Angles-of-departure
ECC	Envelope correlation coefficient
FSS	Frequency selective surface
DRAs	Dielectric resonator antennas
MPR	Metamaterial polarization-rotator
SRRs	Split-ring resonators
LHCP	Left-hand circularly-polarized
RHCP	Right-hand circularly-polarized
SNR	Signal-to-noise ratio
CP	Circularly-polarised
AR	Axial ratio
ACMA	Aperture coupled microstrip antenna
FPC	Fabry Perot Cavity
PRS	Partially reflective surface
PGM	Phase Gradient Metasurface
WiGig	Wireless Gigabit
LOS	Line-of-sight
NLOS	Non-line-of-sight
FCC	Federal Communications Commission
RF	Radio Frequency
SIWs	Substrate-Integrated Waveguides
EM	Electromagnetic
AC	Alternating current
DC	Direct current
QoE	Quality of experience
SLL	Sidelobe level
PSO	Particle Swarm Optimization
LP	Linearly-polarized
BOL	Beam overlap level

Chapter 1 Introduction

1.1 Background, Motivation and Research Problem Objectives

In [1], Sanjib Sur et al. have conducted a study on 802.11ad-based 60-GHz indoor WLAN (Figure 1.1), concerning the influence of the radiation patterns on the link performance, for several environments under blockage/versatility. The mmWave links do not work in a pseudo-optical behavior [1]; it has been observed that extremely directional radiation patterns experience less penetration loss across common barriers (excluding the human body) in an indoor setting, and coverage can be realized exceeding a single room (Figure 1.2). Unlike the common perception that the MIMO gain is correlated with inter-element spacing as assumed in communications theoretic models (Figure 1.3), it is correlated with the distance among the transmitter and receiver at 60-GHz mmWave [1].

Regarding the antenna movement scenarios, it has been observed that the 802.11ad's pattern searching algorithm takes a longer time than the Gbps data transfer time, and therefore deteriorates throughput even for a radiation pattern with 22.5^0 beamwidth with a nearly small scanning field [1]. 802.11ad suggests a quasi-Omni style attempting to expedite the AP-client discovery method by broadening radiation patterns, but it has been seen this hardly benefits due to that the mmWave link itself presents a densely concentrated Angle-Of-Arrival (AOA) pattern [1]. It has been also discovered that 802.11ad links themselves tend to be asymmetric due to the complex interaction between radiation patterns and environment dynamics. Further, even thoroughly slim beams (e.g. 3.4^o) can leak signals causing interference and deteriorate spatial reuse because of the reflection and strong antenna side lobes [1].

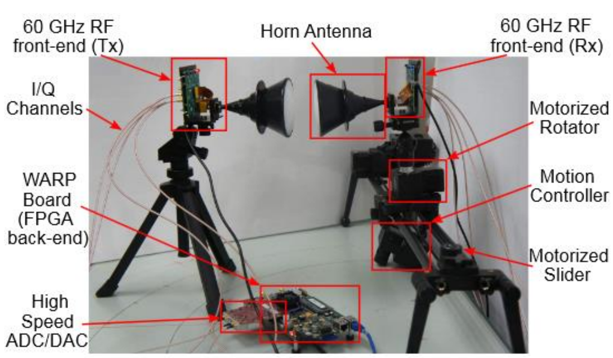

Figure 1.1: 60-GHz band software-radio platform (S. Sur et al. [1], @2015 ACM).

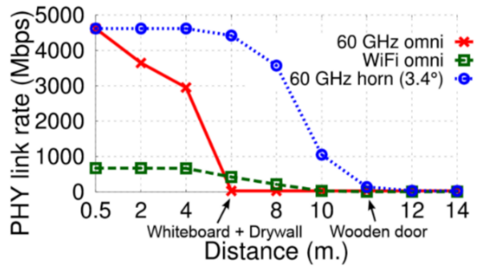

Figure 1.2: Throughput and coverage in indoor environment. Transmit power of 60-GHz links are calibrated to match minimum RSS required for highest data rate at 50cm. WiFi is calibrated to have 28 dB higher gain than 60-GHz (S. Sur et al. [1], @2015 ACM).

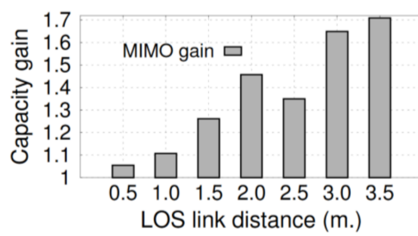

Figure 1.3: 2×2 MIMO capacity gain for different link distances (S. Sur et al. [1], @2015 ACM).

Researchers have proposed several techniques for the enhancement of antenna's characteristics in mmWave frequency-bands. The mmWave communication systems allow high data-rate due to huge bandwidth but experience weak link budget. This is due to the blockage of the mmWave propagating waves by the barriers of a volume comparable to that of the wavelength of the signal. Multiple approaches are stated to recover the signal strength. For instance, using highly directive antennas ensures signal delivery if a line of sight communication is among the transmitter and receiver.

Another alternative approach is Multi-Input Multi-Output (MIMO) technique that utilizes the channel characteristics to direct the radiation patterns in a way that enhances the multiplexing gain and beamforming gain. Concerning the coupling among radiating elements in MIMO networks, which in most circumstances, appears in degeneration of the scheduled radiation pattern characteristics and influences both the radiating element pattern and the radiating element input impedances, has been studied and investigated by several researchers [2]-[7]. The coupling influences MIMO system performance by modifying the input impedances of radiating elements, raising sidelobes, and corrupting radiation pattern shape [2]. In [2], it is announced that to enhance the channel capacity of MIMO networks and promoting the signal-to-noise ratio (SNR), the spacing among the radiating elements must be minimized. Nevertheless, the spacing among the radiating elements commonly considered as a half-wavelength because of implementation limitations. Such a spacing yields strong coupling among radiating elements. The high degree of isolation and low envelope correlation coefficient (ECC) are essential in MIMO networks [3]. The ECC is relevant to the coupling, and it is proportional to the mutual coupling among channels [3]. The mutual coupling is primarily because of three sources, the surface-waves, coupling among feeding lines, and coupling due to spatial fields. To reduce the mutual coupling due to surface waves, a band-gap can be achieved employing electromagnetic band-gap (EBG) structures to prevent the surface-waves propagation toward the neighboring antenna [2]. To decrease the coupling among the feed lines, there are fascinating methods in literature such as utilizing a differential feeding network [8]. There are likewise other methods to decrease coupling, including confocal elliptical metasurface cloaks [4], parasitic element slots [5], and cavity-backed resonator [6]. Because of fabrication space limitation at mmWave, these techniques are not practical. The spacing among the radiating elements is less than a few millimeters in mmWave MIMO arrays. In [7], a frequency selective surface wall has been utilized for decreasing mutual coupling. Another method for mutual coupling reduction utilizing a coplanar strip wall between two antennas is described in [9]. A metasurface shield wall in [10] and a frequency selective surface in [11] have been intended in our research group for mutual coupling reduction. But, these methods deteriorate the antennas' radiation characteristics. This is since the frequency selective surface wall or the coplanar strip wall is not matched. As a consequence, the beam is tilted due to the reflected waves from the installed wall between antennas. Next-generation of wireless data networks or 5G mobile communications assumed to operate on systems working in mmWave frequency range from 57 to 64 GHz for dense urban next generation of wireless data networks (5G) and WiFi [12]. A massive MIMO system is a great competitor that grants exceptional gains in terms of capacity and link performance for 5G. Such a massive MIMO network is performed utilizing extremely large numbers of antennas at the base station and typically a small MIMO antenna system in mobile devices [13]. In such a MIMO arrangement (massive base station MIMO antenna system and small handheld devices MIMO antenna system), the channel correlation will considerably degenerate the performance of the overall MIMO system, for instance, its capacity. As a result, the handheld devices' antennas must be designed in a way to have the lowest correlation and this cannot be obtained only by low mutual coupling MIMO antenna array. Besides having low mutual couplings, the radiation pattern must not be deteriorated, in order to obtain the lowest spatial correlation.

An alternative approach to enhance signal strength is beamforming techniques. Switched-beam intelligent antenna arrangements may be more affordable than an equivalent phased array antenna, particularly when few beams are required. Lately, switched-beam intelligent antenna arrangements such as Butler matrix are employed and investigated to promote the performance of mmWave systems. The reputation of the Butler matrix as a beamformer in switched-beam intelligent antenna arrangements is due to several advantages. Primary, it can be performed simply utilizing hybrids and phase shifters. Secondary, the formed patterns are orthogonal of the Woodward-Lawson type and have narrow beamwidth and high directivity. Third, it has the least signal path length and number of elements associated with different uniform excitation beamforming systems. Nevertheless, because of a miniature dimension and a high value of propagation loss at mmWave, implementing them has been a challenging assignment for designers. In the past decade, there were several efforts to invent low-loss high-efficiency waveguides and transmission lines for high-frequency microwave and mmWave frequency ranges. For instance, the substrate integrated waveguide (SIW) technology was developed in the past decade as a low-loss waveguide [14]-[16]. Nevertheless, implementing the microwave components, such as couplers with SIW technology, degenerates the low-loss characteristics of the SIW waveguide though disturbing the host SIW waveguide characteristic[17]-[19]. To overcome these drawbacks an alternative guiding structure, termed ridge gap waveguide, has been introduced [20]. Ridge gap waveguide is a remarkably low-loss guiding structure at mmWave [20]-[22]. In this technology, the electric and magnetic waves are arrested between two metal walls and two open sidewalls. Consequently, the electric and magnetic waves are moving in the air gap. In the ridge gap waveguide, losses are less than SIW waveguide due to that the electric and magnetic waves are moving in the air and host dielectric, respectively. Furthermore, performing bend, slot or any disturbance in the SIW waveguide decays its low-loss characteristic because of disturbing the host SIW waveguide environment. Moreover, the ridge gap waveguide is less sensitive to disturbance such as bend or slot. For example, in both SIW and ridge gap waveguides, the loading effect of a bend in the transmission line will be compensated, but the difference comes from the fact that SIW is filled with a dielectric, which has electric and magnetic losses. In both SIW and ridge-gap, the loading effect of the bend is compensated by truncating the corner, but the wave will reflect several times at the corner. These reflected waves in SIW and ridge gap are moving in the air and host dielectric, respectively, which make the SIW more lossy to the disturbance in the transmission line.

1.2 Contributions of the Thesis

This thesis is a collection of several publications (seven journal articles and four conference papers), which were published in high-quality IEEE journals and conference proceedings. The key contributions of this dissertation that realize the objectives mentioned in Section 1.1 are explained in detail in the following.

1.2.1 Chapter 2: Efficient mmWave MIMO Antennas

These works, have been done in this chapter, have been published in the following journals and conferences and the contributions are summarized in the following:

- M. Farahani, J. Pourahmadazar, M. Akbari, M. Nedil, A. R. Sebak and T. A. Denidni, “Mutual Coupling Reduction in Millimeter-Wave MIMO Antenna Array Using a Metamaterial Polarization-Rotator Wall,” IEEE Antennas and Wireless Propagation Letters, vol. 16, pp. 2324-2327, 2017.
- M. Farahani, J. Zaid, T. A. Denidni, M. Akbari, A. R. Sebak and M. Nedil, “Mutual coupling reduction in millimeter-wave MIMO dielectric resonator antenna using metamaterial polarization rotator wall,” IEEE International Symposium on Antennas and Propagation & USNC/URSI National Radio Science Meeting, San Diego, CA, 2017, pp. 1261-1262.
- M. Farahani, M. Akbari, M. Nedil and T. A. Denidni, “Mutual coupling reduction in dielectric resonator MIMO antenna arrays using metasurface orthogonalize wall,” European Conference on Antennas and Propagation (EUCAP), Paris, 2017, pp. 985-987.
- M. Farahani, J. Zaid, J. Pourahmadazar, T. A. Denidni and M. Nedil, “Millimeter-wave couraggated surface for mutual coupling reduction between dipole antennas,” 17th International Symposium on Antenna Technology and Applied Electromagnetics (ANTEM), Montreal, QC, 2016, pp. 1-2.
- M. Akbari, H. Abo Ghalyon, M. Farahani, A. Sebak and T. A. Denidni, “Spatially Decoupling of CP Antennas Based on FSS for 30-GHz MIMO Systems,” IEEE Access, vol. 5, pp. 6527-6537, 2017.
- M. Akbari, M. M. Ali, M. Farahani, A. R. Sebak and T. Denidni, “Spatially mutual coupling reduction between CP-MIMO antennas using FSS superstrate,” Electronics Letters, vol. 53, no. 8, pp. 516-518, 13 4 2017.

The mutual coupling has an impact on MIMO system performance through changing the input impedance of the radiating elements, increasing the sidelobe level, and degrading radiation pattern shape. The mutual coupling is mainly due to three components, the surface waves, the coupling between the feeding lines, and coupling due to spatial fields. In this chapter, two distinguished approaches have been proposed to reduce the mutual coupling due to the spatial fields.

In the first approach, a valuable technique for reducing the mutual coupling among mmWave dielectric resonator (DR) antennas (DRAs) using a new metamaterial polarization-rotator (MPR) wall is studied and performed in this chapter. The mutual coupling is decreased by installing MPR walls among DRAs, that are located in the H-plane. Utilizing this MPR walls, the TE modes of the antennas become orthogonal, which decreases the mutual coupling among the antennas.

In the second approach, a novel method to reduce the coupling due to spatial electromagnetic interaction among two circularly-polarised radiating elements utilizing an FSS superstrate layer is proposed.

1.2.2 Chapter 3: mmWave High Gain Antennas

These works, have been done in this chapter, have been published in the following journal and conference and the contributions are summarized in the following:

- M. Akbari, S. Gupta, M. Farahani, A. R. Sebak and T. A. Denidni, "Gain Enhancement of Circularly Polarized Dielectric Resonator Antenna Based on FSS Superstrate for MMW Applications," IEEE Transactions on Antennas and Propagation, vol. 64, no. 12, pp. 5542-5546, Dec. 2016.
- M. Farahani, J. Pourahmadazar, T. Denidni and M. Nedil, "Millimeter-Wave High-Gain Ridge Gap Beam Steerable Antenna for 5G wireless Networks," International Symposium on Antenna Technology and Applied Electromagnetics (ANTEM), Waterloo, ON, 2018, pp. 1-2.

In this chapter, different techniques are investigated for increasing the gain of the antenna. There are a big challenge regarding the development of a system at mmWave bands, due to the high amount of propagation losses which required designing the high-sensitivity receivers to overcome that drawback. In antenna regards, it is needed to develop directive high-gain antennas. In this effort, designing a high-efficiency low-loss transmission line plays an important rule to achieve that goal.

1.2.3 Chapter 4: Low-loss Wave Guiding Structures at mmWave

These works, have been done in this chapter, have been published in the following journals and the contributions are summarized in the following:

- M. Farahani, M. Nedil and T. A. Denidni, "A Novel Hedgehog Waveguide and its Application in Designing a Phase Shifter Compatible With Hollow Waveguide Technology," IEEE Transactions on Microwave Theory and Techniques, vol. 67, no. 10, pp. 4107-4117, Oct. 2019.
- M. Farahani, M. Akbari, M. Nedil, T. A. Denidni and A. R. Sebak, "A Novel Low-Loss Millimeter-Wave 3-dB 90° Ridge-Gap Coupler Using Large Aperture Progressive Phase Compensation," IEEE Access, vol. 5, pp. 9610-9618, 2017.

In this chapter, the ridge gap waveguide and transition method to microstrip are explained, and a low-loss multi-aperture 3 dB 90^o hybrid coupler with ridge gap technology is designed and fabricated.

Moreover, we proposed a novel waveguide structure, named Hedgehog waveguide, which has several advantages compared to the conventional waveguides and transmission lines reported in literature. The main advantage of the Hedgehog waveguide is that it can support propagation with lower loss. Moreover, the fact that the electromagnetic fields are captured to space within the waveguide, radiation losses are kept very low, resulting in good immunity from external electromagnetic disturbance compared to the microstrip technology. Another main advantage of the Hedgehog waveguide is the compatibility with the hollow waveguides, which gives an extra degree of freedom to use the proposed waveguide for several mmWave designs.

1.2.4 Chapter 5: State-of-the-art mmWave Beamformer Networks

These works, have been done in this chapter, have been submitted to the following journals and the contributions are summarized in the following:

- M. Farahani, M. Akbari, M. Nedil, A. R. Sebak and T. A. Denidni, “Millimeter-Wave Dual Left/Right-Hand Circularly-Polarized Beamforming Network,” submitted to the IEEE Transactions on Antennas and Propagation.
- M. Akbari, M. Farahani, S. Zarbakhsh, M. Dashti Ardakani, A. R. Sebak, T. A. Denidni and Omar M. Ramahi, “Highly Efficient 30-GHz 2×2 Beamformer Based on Rectangular Air-Filled Coaxial Line,” submitted to the IEEE Transactions on Antennas and Propagation, 2019.

In this chapter, an exceptional high-efficiency dual LH/RH CP beamforming network is introduced and studied at 60-GHz mmWave band. The Hedgehog waveguide is employed as a notably low-loss guiding structure to implement the crucial phase shifters. The attenuation constant of the Hedgehog waveguide is significantly smaller than similar traditional guiding structures, e.g., SIW, ridge gap, hollow, and gap waveguides at the 60-GHz band [23]. The offered beamformer produces uniform progressive-phase output waves to supply an array of antennas with the eight separate radiation patterns associated with each of the eight input ports. For enhancing the gain and reducing the sidelobes, an 4×8 feeding network is employed. Utilizing the introduced feeding network, the sidelobes are reduced to -19 dB. By expanding the number of radiating elements to 8, the directivity of the recommended beamformer raises about 3 dB. Furthermore, the progressive slot antenna is utilized to obtain a broadband axial-ratio bandwidth. The bandwidth of 10.75% and the radiating efficiency of 90% for each port is obtained utilizing the intended beamforming network.

Furthermore, an extremely qualified two-dimensional (2D) 2×2 beamformer at the 30-GHz band has been investigated and designed. Respecting the nature of the input ports, guiding structure, and antenna design, this arrangement is well-referred to as a waveguide-coaxial-waveguide beamformer network. The beamformer network can produce four switched beams. The measurement results determined that the network has a broadband performance (25.8%) with the radiation efficiency of more than 90% over the working frequency-band at 30-GHz. Furthermore, a flat gain (16.5±0.5 dB) and a sidelobe level (SLL) (lower than 20 dB) were obtained. These advantages candidate the intended beamformer a charming competitor for future 5G demands.

1.3 List of Publications

Publications included in this dissertation:

This dissertation includes material extracted from the following publications:

Journals:

- M. Farahani, M. Akbari, M. Nedil, A. R. Sebak and T. A. Denidni, “Millimeter-Wave Dual Left/Right-Hand Circularly-Polarized Beamforming Network,” submitted to the IEEE Transactions on Antennas and Propagation.
- M. Farahani, M. Nedil and T. A. Denidni, “A Novel Hedgehog Waveguide and its Application in Designing a Phase Shifter Compatible With Hollow Waveguide Technology,” IEEE Transactions on Microwave Theory and Techniques, vol. 67, no. 10, pp. 4107-4117, Oct. 2019.
- M. Akbari, M. Farahani, S. Zarbakhsh, M. Dashti, A. R. Sebak, T. A. Denidni and O. M. Ramahi, “Highly Efficient 30-GHz 2×2 Beamformer Based on Rectangular Air-Filled Coaxial Line,” submitted to the IEEE Transactions on Antennas and Propagation.
- M. Farahani, J. Pourahmadazar, M. Akbari, M. Nedil, A. R. Sebak and T. A. Denidni, “Mutual Coupling Reduction in Millimeter-Wave MIMO Antenna Array Using a Metamaterial Polarization-Rotator Wall,” IEEE Antennas and Wireless Propagation Letters, vol. 16, pp. 2324-2327, 2017.
- M. Farahani, M. Akbari, M. Nedil, T. A. Denidni and A. R. Sebak, “A Novel Low-Loss Millimeter-Wave 3-dB 90° Ridge-Gap Coupler Using Large Aperture Progressive Phase Compensation,” IEEE Access, vol. 5, pp. 9610-9618, 2017.
- M. Akbari, S. Gupta, M. Farahani, A. R. Sebak and T. A. Denidni, “Gain Enhancement of Circularly Polarized Dielectric Resonator Antenna Based on FSS Superstrate for MMW Applications,” IEEE Transactions on Antennas and Propagation, vol. 64, no. 12, pp. 5542-5546, Dec. 2016.
- M. Akbari, H. Abo Ghalyon, M. Farahani, A. Sebak and T. A. Denidni, “Spatially Decoupling of CP Antennas Based on FSS for 30-GHz MIMO Systems,” IEEE Access, vol. 5, pp. 6527-6537, 2017.
- M. Akbari, M. M. Ali, M. Farahani, A. R. Sebak and T. Denidni, “Spatially mutual coupling reduction between CP-MIMO antennas using FSS superstrate,” Electronics Letters, vol. 53, no. 8, pp. 516-518, 13 4 2017.

Conference Proceedings:

- M. Farahani, J. Pourahmadazar, T. Denidni and M. Nedil, “Millimeter-Wave High-Gain Ridge Gap Beam Steerable Antenna for 5G wireless Networks,” International Symposium on Antenna Technology and Applied Electromagnetics (ANTEM), Waterloo, ON, 2018, pp. 1-2.

- M. Farahani, J. Zaid, T. A. Denidni, M. Akbari, A. R. Sebak and M. Nedil, "Mutual coupling reduction in millimeter-wave MIMO dielectric resonator antenna using metamaterial polarization rotator wall," IEEE International Symposium on Antennas and Propagation & USNC/URSI National Radio Science Meeting, San Diego, CA, 2017, pp. 1261-1262.
- M. Farahani, M. Akbari, M. Nedil and T. A. Denidni, "Mutual coupling reduction in dielectric resonator MIMO antenna arrays using metasurface orthogonalize wall," European Conference on Antennas and Propagation (EUCAP), Paris, 2017, pp. 985-987.
- M. Farahani, J. Zaid, J. Pourahmadazar, T. A. Denidni and M. Nedil, "Millimeter-wave couraggated surface for mutual coupling reduction between dipole antennas," 17th International Symposium on Antenna Technology and Applied Electromagnetics (ANTEM), Montreal, QC, 2016, pp. 1-2.

Publications not included in this dissertation:

The following papers have also been published or submitted during the Ph.D. studies. However, their content is not included in this dissertation for compactness.

Journals:

- M. Akbari, M. Farahani, A. Ghayekhloo, S. Zarbakhsh, A. Sebak and T. Denidni, "Phase Gradient Surface Approaches for 60 GHz Beam Tilting Antenna," in IEEE Transactions on Antennas and Propagation. Early Access, doi: 10.1109/TAP.2020.2972375
- S. Zarbakhsh, M. Akbari, M. Farahani, A. Ghayekhloo, T. A. Denidni and A. Sebak, "Optically Transparent Subarray Antenna Based on Solar Panel for CubeSat Application," in IEEE Transactions on Antennas and Propagation, vol. 68, no. 1, pp. 319-328, Jan. 2020.
- M. Farahani, M. Akbari, M. Nedil, A. R. Sebak and T. A. Denidni, "Miniaturised circularly-polarised antenna with high-constitutive parameter substrate," Electronics Letters, vol. 53, no. 20, pp. 1343-1344, 28 9 2017.
- J. Zaid, M. Farahani and T. A. Denidni, "Magneto-dielectric substrate-based microstrip antenna for RFID applications," IET Microwaves, Antennas & Propagation, vol. 11, no. 10, pp. 1389-1392, 16 8 2017.
- M. Akbari, M. Farahani, A. Sebak and T. A. Denidni, "Ka-Band Linear to Circular Polarization Converter Based on Multilayer Slab With Broadband Performance," in IEEE Access, vol. 5, pp. 17927-17937, 2017.
- Jamal Zaid, M. Farahani, Tayeb A. Denidni, "A compact circularly-polarized GPS antenna using LTCC technology," Microwave and Optical Technology Letters, Vol. 58, No. 12, December 2016.
- M. Akbari, S. Gupta, M. Farahani, A. R. Sebak, T.A. Denidni "Analytic study on CP enhancement of millimeter wave DR and patch subarray antennas" International Journal of RF and Microwave Computer-Aided Engineering, Volume 27, Issue1, Sep, 2016.

Conference Proceedings:

- M. Farahani, T. A. Denidni and M. Nedil, “Ridge Gap Array Antenna with Inter-Element Spacing of a Wavelength,” 2019 IEEE International Symposium on Antennas and Propagation and USNC-URSI Radio Science Meeting, Atlanta, GA, USA, 2019, pp. 667-668.
- M. Farahani, T. A. Denidni and M. Nedil, “Design of a Low Output-Phase Error Ridge-Gap Coupler for Antenna Arrays Applications,” IEEE International Symposium on Antennas and Propagation & USNC/URSI National Radio Science Meeting, Boston, MA, 2018, pp. 1099-1100.
- J. Pourahmadazar, M. Farahani and T. A. Denidni, “Printed Gap Waveguide Rotman Lens for Millimetre-wave Applications,” International Symposium on Antenna Technology and Applied Electromagnetics (ANTEM), Waterloo, ON, 2018, pp. 1-2.
- M. Akbari, A. Farahbakhsh, M. Farahani, A. R. Sebak and T. A. Denidni, “A sequential-phase feed antenna subarray based on ridge gap waveguide,” IEEE International Symposium on Antennas and Propagation & USNC/URSI National Radio Science Meeting, San Diego, CA, 2017, pp. 2125-2126.
- J. Zaid, M. Farahani, A. Kesavan and T. A. Denidni, “Miniaturized microstrip patch antenna using Electromagnetic Band Gap (EBG) structures for multiport passive UHF RFID-tag applications,” IEEE International Symposium on Antennas and Propagation & USNC/URSI National Radio Science Meeting, San Diego, CA, 2017, pp. 2459-2460.
- M. Akbari, M. Farahani, A. R. Sebak and T. A. Denidni, “A 30 GHz high-gain circularly-polarized pattemsteerable antenna based on parasitic patches,” European Conference on Antennas and Propagation (EUCAP), Paris, 2017, pp. 3044-3046.
- M. Farahani, J. Zaid, T. A. Denidni and M. Nedil, “Miniaturized two dimensional circular polarized magnetodielectric substrate antenna,” IEEE International Symposium on Antennas and Propagation (APSURSI), Fajardo, 2016, pp. 1103-1104.
- J. Zaid, M. Farahani and T. A. Denidni, “A CP-GPS antenna using low temperature cofired ceramic technology,” IEEE International Symposium on Antennas and Propagation (APSURSI), Fajardo, 2016, pp. 121-122.
- J. Zaid, M. Farahani and T. A. Denidni, “Miniatunrized microstrip patch antenna using electromagnetic bandgap (EBG) for GPS applications,” 17th International Symposium on Antenna Technology and Applied Electromagnetics (ANTEM), Montreal, QC, 2016, pp. 1-2.
- J. Pourahmadazar, R. Karimian, M. Farahani and T. Denidni, “Planar microwave lens based beam-forming phased antenna array system using non-coplanar SIW fed bowtie antenna,” International Symposium on Antenna Technology and Applied Electromagnetics (ANTEM), Montreal, QC, 2016, pp. 1-4.

1.4 Dissertation Outline

The objectives of this proposal are to conduct a thorough investigation on the mmWave antenna systems to improve the characteristics of the communication link. Different techniques have being studied for improving the communication link at the mmWave bands. These techniques can be categorized as follow:

- MIMO Systems: It has been discovered that 60-GHz MIMO gain becomes correlated with link distance, instead of inter-element spacing as assumed in communications-theoretic models [1].
- High Gain Antennas: Unlike conventional perception that 60-GHz beams behave in a pseudo-optical manner, highly directional beams suffer less penetration loss across typical obstacles (except human body) in an office environment, and coverage can be achieved beyond a single room [1].
- Beam-steering: Device mobility breaks the beam adjustment and requires constant retraining, significantly increasing the beamforming overhead. This holds especially for device rotation. From experiments with a 7 degree beam width system it is found that a mere misalignment of 18 degree reduces the link budget by around 17 dB. According to IEEE 802.11ad coding sensitivities [24], this drop can reduce the maximum throughput by up to 6 Gbps or break the link entirely.

Based on the above categorization, the contents of the dissertation are divided into 6 chapters with the abstract, publication list, and the reference.

Chapter 2: Different MIMO antennas are presented and investigated in this chapter to improve the characteristics of the communication link at mmWave bands, where the link budget suffer from poor radiation patterns of the conventional MIMO antenna systems.

Chapter 3: In this chapter, different techniques are investigated for increasing the gain of the antenna. There are a big challenge regarding the development of a system at mmWave bands, due to the high amount of propagation losses at these frequency-bands which required designing the high-sensitivity receivers to overcome that drawback. In antenna regards, it is needed to develop directive high-gain antennas. In this effort, designing a high-efficiency low-loss transmission line plays an important rule to achieve that goal.

Chapter 4: Having the ability to transmit signals through guided structures is considered as the first baby step toward developing communication systems. From DC to terahertz frequency-bands, researchers and engineers have developed different kinds of transmission lines and waveguides, which have their own pros and cons [25]-[43]. Any electromagnetic guiding structure that at least consists of two electrically separated conductors, can only propagate the fundamental TEM mode, which transmits signals at arbitrarily low frequencies and is called a transmission line. The waveguides are electromagnetic guiding structures that do not propagate the TEM mode and consist of only one conductor. Moreover, there is another guiding structure that does not consist of a conductor at all, which is called dielectric slab [44]. The capability of supporting higher-order modes in waveguides gives them the ability to operate in modes with lower loss performance compared to transmission lines by changing the host waveguide topology. This concept comes from the fact that waveguide operating mode affects the propagation loss characteristics. In addition, waveguides are used in high frequencies due to the fact that they have a lower loss, lower leakage, and capability of handling higher power compared to the transmission lines [41]. In this chapter, ridge gap transmission line and the transition method to microstrip are explained, and a low-loss multi-aperture 3 dB 90^o hybrid coupler with ridge gap technology is designed and fabricated. Moreover, we propose a novel waveguide structure, named Hedgehog waveguide, which has several advantages compared to the conventional waveguides and transmission lines reported in literature. The main advantage of the Hedgehog waveguide is that it can support propagation with lower loss. Moreover, the fact that the electromagnetic fields are captured to space within the waveguide, radiation losses are kept very low, resulting in good immunity from external electromagnetic disturbance compared to the microstrip technology. Another main advantage of the Hedgehog waveguide is the compatibility with the hollow waveguides, which gives an extra degree of freedom to use the proposed waveguide for several mmWave designs.

Chapter 5: Beamforming antenna arrays play an important role in 5G implementations since even handsets can accommodate a larger number of antenna elements at mmWave frequencies. These antenna arrays are essential for beamforming operations that play a significant role in next-generation networks. Aside from a higher directive gain, these antenna types offer complex beamforming capabilities. This allows enhancing the capacity of cellular networks by increasing the signal to interference ratio (SIR) through direct targeting of user groups. The narrow transmit beams simultaneously lower the amount of interference in the radio environment and make it possible to maintain sufficient signal power at the receiver terminal at larger distances in rural areas.

Chapter 6: This chapter concludes the dissertation. The future work in the proposed research area is included in this chapter.

Chapter 2 Efficient mmWave MIMO Antennas

This chapter contains material extracted from the following publications:

[45] M. Farahani, M. Akbari, M. Nedil and T. A. Denidni, "Mutual coupling reduction in dielectric resonator MIMO antenna arrays using metasurface orthogonalize wall," *2017 11th European Conference on Antennas and Propagation (EUCAP)*, Paris, 2017, pp. 985-987.

[46] M. Farahani, J. Zaid, T. A. Denidni, M. Akbari, A. R. Sebak and M. Nedil, "Mutual coupling reduction in millimeter-wave MIMO dielectric resonator antenna using metamaterial polarization rotator wall," *2017 IEEE International Symposium on Antennas and Propagation & USNC/URSI National Radio Science Meeting*, San Diego, CA, 2017, pp. 1261-1262.

[47] M. Farahani, J. Pourahmadazar, M. Akbari, M. Nedil, A. R. Sebak and T. A. Denidni, "Mutual Coupling Reduction in Millimeter-Wave MIMO Antenna Array Using a Metamaterial Polarization-Rotator Wall," in *IEEE Antennas and Wireless Propagation Letters*, vol. 16, pp. 2324-2327, 2017.

[48] M. Farahani, J. Zaid, J. Pourahmadazar, T. A. Denidni and M. Nedil, "Millimeter-wave couraggated surface for mutual coupling reduction between dipole antennas," *2016 17th International Symposium on Antenna Technology and Applied Electromagnetics (ANTEM)*, Montreal, QC, 2016, pp. 1-2.

[49] M. Akbari, M. M. Ali, M. Farahani, A. R. Sebak and T. Denidni, "Spatially mutual coupling reduction between CP-MIMO antennas using FSS superstrate," in *Electronics Letters*, vol. 53, no. 8, pp. 516-518, 13 4 2017.

[50] M. Akbari, H. Abo Ghalyon, M. Farahani, A. Sebak and T. A. Denidni, "Spatially Decoupling of CP Antennas Based on FSS for 30-GHz MIMO Systems," in *IEEE Access*, vol. 5, pp. 6527-6537, 2017.

2.1 Introduction

The performance of a MIMO system is mainly dependent on having independent multiple channels. In MIMO systems, dependent multiple channels will degrade the performance of a MIMO system, for instance, its capacity. Channel correlation is a parameter to measure the similarity or likeliness between the channels in MIMO systems. In the worst case, if the channels are completely correlated, then the MIMO system will act as a single-antenna communication system. In general, the channel capacity is reversely proportional to the channel correlation. In MIMO systems, the channel correlation is usually due to the spatial-correlation and antenna mutual coupling [51]-[52]. The spatial correlation defined by the multipath signal direction. Multipath-signals will be transmitted from the transmitter in spatial angular directions, that is being named angles-of-departure (AOD), rather than a specific direction. For the receiver, there is the same definition for the received multipath-signals which is called angles-of-arrival (AOA). The spatial correlation is reversely proportional to the AOD and AOA. So the ideal scenario is that the AOA at the receiver is being 360^o on the plane (H-plane) perpendicular to the dipole antennas and the radiation pattern of the dipole antennas are being Omni-directional (see Figure 2.1). However, this is impossible in real circumstances. For instance, designers are intended to use a half-space radiating antennas for practical reasons such as having more gain or limiting radiation toward the body in handheld devices. Moreover, the two dipole antenna affect each other and they do not have an Omni-directional radiation pattern. So the best practical scenario is having two half-space radiating antennas with the minimum inter-element distance, and the same radiation characteristic as much as possible. In this work, it was our priority to design a MIMO antenna with a low correlation coefficient. To reach this purpose, the two radiating elements in the proposed MIMO antenna should have the same radiating characteristic, otherwise, even though they have a low amount of mutual coupling, the correlation is high. The correlation between channels in a MIMO system is related to the mutual coupling, and it is proportional to the mutual coupling between two channels if the spatial correlation is being lowed [3].

2.2 Metamaterial Polarization-Rotator Wall and MIMO Antenna

Decreasing the mutual coupling among the antennas in a MIMO antenna array, which, in most cases, results in deterioration of the expected radiation characteristics and influences both the embedded element radiation characteristics and the antennas' input impedances, has been studied by many researchers [2]-[3], [7]-[11], [49]-[50]. A high level of isolation and low envelope correlation coefficient (ECC) are critical parameters in MIMO networks [3]. The ECC is relevant to the mutual coupling, and it is proportionate to the mutual coupling among channels [3]. The mutual coupling is primarily due to three sources: coupling between the feeding lines, the surface waves, and coupling caused by spatial fields. To lessen the mutual coupling caused by surface waves, a band-gap may be achieved utilizing electromagnetic band-gap (EBG) structures to prevent the surface-wave propagation toward the neighboring antenna [2]. For lessening the mutual coupling caused by feed lines, there are some methods in the literature such as utilizing a symmetric feeding structure [8]. In [7], a frequency selective surface (FSS) wall has been utilized for decreasing the mutual coupling caused by spatial fields. A different approach for mutual coupling reduction utilizing a coplanar strip wall among antennas has been described in [9]. A metasurface shield wall in [10] and FSSs in [11] have been proposed for mutual coupling reduction. However, these methods deteriorate the antennas' radiation characteristics. This is because an FSS wall or a coplanar strip wall is not matched. As a consequence, the radiation pattern is shifted due to the reflected waves from the installed wall among the antennas.

A valuable technique for reducing the mutual coupling among mmWave dielectric resonator antennas (DRAs) using a metamaterial polarization-rotator (MPR) wall is studied and performed in this section. The mutual coupling is decreased by installing MPR walls among DRAs, that are located in the H-plane. Utilizing these MPR walls, the TE modes of the antennas become orthogonal, which decreases the mutual coupling among them. The mutual coupling is decreased by more than 15 dB on average while the MPR walls are located among the antennas. The presented MPR walls nearly do not affect the antenna properties in terms of input impedance and radiation characteristics. Three types of the metamaterial polarization-rotator walls have been studied and explained which are named Case 1 to Case 3.

2.2.1 Case 1 MPR Wall

The first structure includes a periodical arrangement of metamaterial unit cells, presented in Figure 2.2, that consists of split-ring resonators (SRRs) on one side, and a coupling strip on the other side. The ring forms the inductance, and the gap in the ring produces capacitance, and the coupling strip is employed to twist the E-field and arrange the polarization of the two antennas orthogonal. The suggested metasurface is implemented on the host substrate of the RT5880 with relative permittivity of 2.2. To estimate the transmission coefficients, the full-wave EM simulation has been carried out using Ansys HFSS. The famous Floquet port settings under specified boundary conditions described in Figure 2.2(d) fires two plane waves with orthogonal electric fields in the metasurface wall's plane, although higher-order modes may also be defined in the port properties details. Co-polar and cross-polar coupling between the modes, both reflection and transmission coefficients, are given in terms of scattering parameters (Figure 2.3). The co-polarized reflection of mode 1 at port 1 would thus, for example, be identified $S_{11}^{(\text{port2Mode1,port1Mode1})}$, and the co-polarised transmission for mode 1 at both the ports 1 and 2 would be called $S_{21}^{(\text{port2Mode1,port1Mode1})}$. Moreover, the cross-polarized reflection of mode 1 at port 1, while port 2 is in mode 2 would be entitled $S_{11}^{(\text{port2Mode2,port1Mode1})}$, and the cross-polarized transmission between modes 2 and 1 would be called $S_{21}^{(\text{port2Mode2,port1Mode1})}$. As displayed in Figure 2.3, the offered metasurface behaves as a transmission layer, with low insertion loss, close to -3dB on wide range of the frequency band, for both $S_{21}^{(\text{port2Mode1,port1Mode1})}$ and $S_{21}^{(\text{port2Mode2,port1Mode1})}$, as it can be observed from the S-parameters of the metasurface unit cell (Figure 2.3).

2.2.2 Case 2 MPR Wall

The second structure is inspired by the technique in [53], that an N-section polarization-rotator wall, composed of periodic arrangements of wires, has been presented. It is quite well known that a periodic arrangement of parallel wires or strips has the ability to rotate the plane of polarization of a linearly-polarized wave by a desired angle over a wide frequency band. To achieve high precision with this method in a wide frequency band, and improve the transmission coefficient at the same time, it is important to employ a large number of screens [54]. That consequently means a significant increase in both the polarizer thickness and weight of the polarization-rotator wall. Our realizations will be made from multilayer thin screens that are two-dimensional periodic arrangements with a period considerably smaller than the wavelength. We have employed a periodic arrangement of metamaterial unit cells, presented in Figure 2.4. The presented MPR wall is embedded in the host substrate of the RT5880 with relative permittivity of 2.2. To determine the transmission coefficients, the full-wave EM simulation is carried out using Ansys HFSS. The famous Floquet port settings, under specified boundary conditions described in Figure 2.4(c), fire two plane waves with orthogonal electric fields such as TE and TM modes. Co-polar and cross-polar coupling between the modes, both reflection and transmission coefficients, are shown in terms of S-parameters in Figure 2.5.

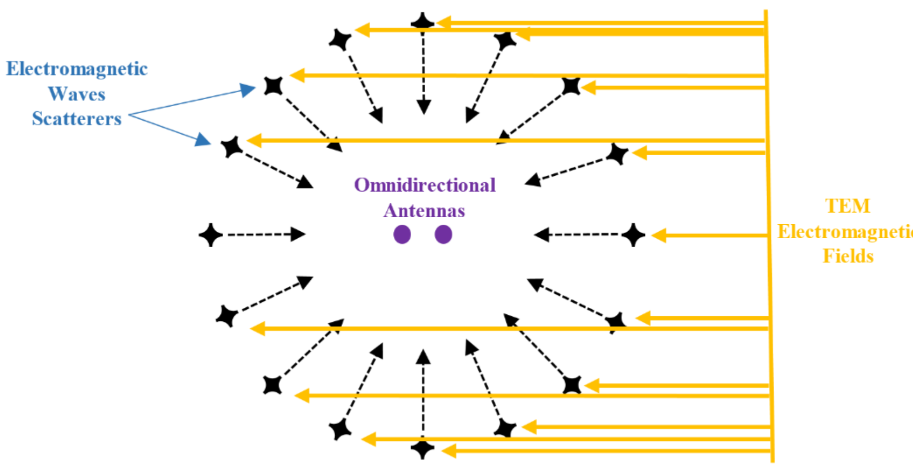

Figure 2.1: The ideal scenario in terms of the lowest correlation between the two channels in a MIMO system. The AOA at the receiver is being 360^o on the plane (H-plane) perpendicular to a dipole antennas and the radiation patterns of the dipole antennas are being omni-directional.

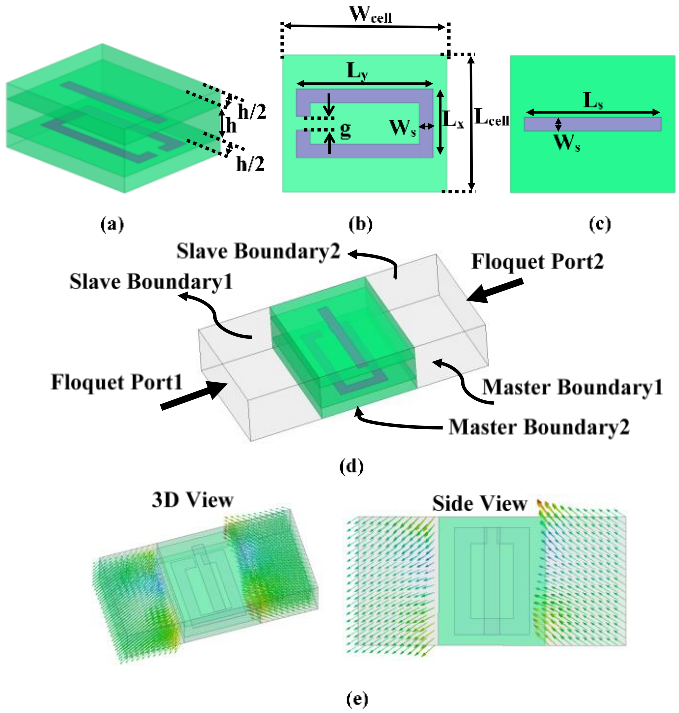

Figure 2.2: (a) Perspective view of the unit cell, (b) Metallic SRR-like on the top bottom, (c) Metallic strip on the top surface, (d) Specific boundary conditions and defined Floquet port excitation to extract scattering parameters. The dimensions are $L_{cell} = 1$, $W_{cell} = 1.2$, $L_y = 1$, $L_x = 0.7$, $L_s = 1$, $g = 0.1$, $W_s = 0.15$, $h = 0.254$, and all in millimeter (M. Farahani et al. [45], @2017 IEEE).

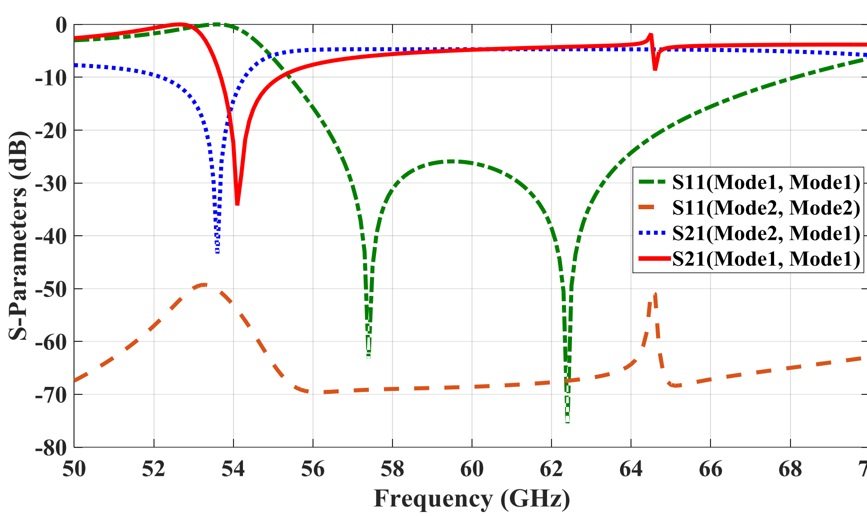

Figure 2.3: Simulated S-parameters of the proposed metasurface unit cell, under specific boundary conditions presented in Figure 2.2(d) (M. Farahani et al. [45], @2017 IEEE).

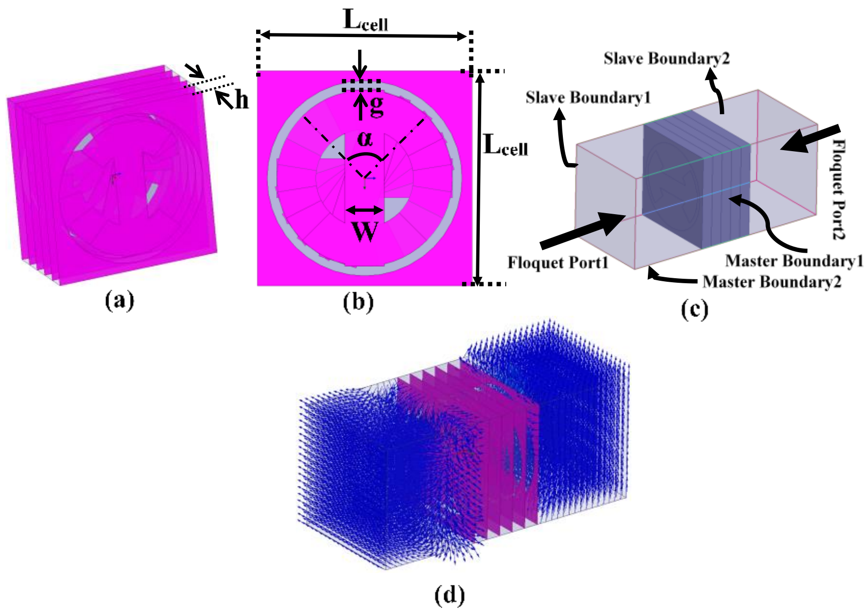

Figure 2.4: (a) Perspective view of the MPR unit cell, (b) Front view of the unit cell, (c) Specific boundary conditions and defined Floquet port excitation, (d) E-fields distribution at 60-GHz. The dimensions are $L_{cell} = 1.1$, $W = 0.2$, $g = 0.1$, $\alpha = 45^o$, $h = 0.13$, and all in millimeter (M. Farahani et al. [46], @2017 IEEE).

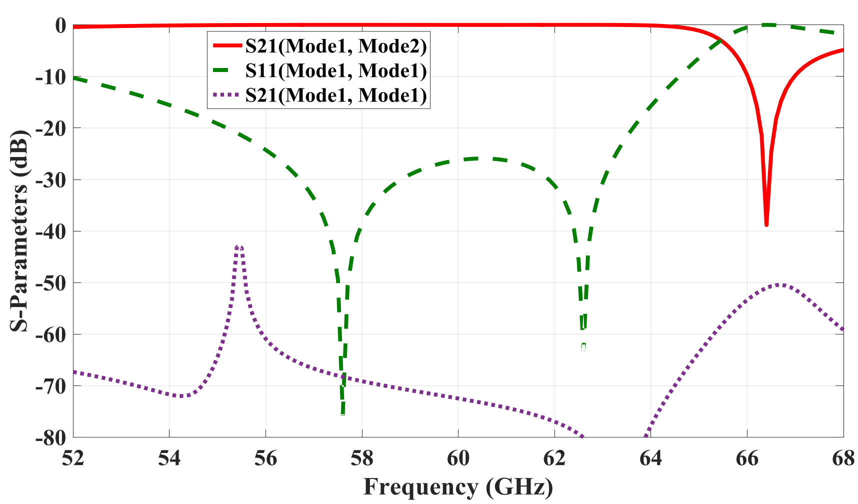

Figure 2.5: Transmission/reflection coefficients of the proposed MPR unit cell in Figure 2.4 (M. Farahani et al. [46], @2017 IEEE).

2.2.3 Case 3 MPR Wall

The third structure is inspired by the presented technique in [55] which comprises a periodic arrangement of metamaterial unit cells, as displayed in Figure 2.6. It is made of an SRR on one side, a coupling strip in the middle, and another SRR on the other side. The SRR is a well-known structure to achieve negative effective permeability and is utilized for designing metamaterials. The ring forms inductance, and the gap between the rings produces capacitance. The coupling strip is employed to alternate the E-field and to adjust the polarization of the two antennas orthogonal. A linearly-polarized wave can be viewed as a summation of two circularly-polarized waves, one left-hand circularly-polarized (LHCP) and one right-hand circularly-polarized (RHCP), with the equal amplitude and 90^o out of phase. The metamaterial polarization-rotator (MPR) has a distinct transmission phase for LHCP and RHCP incident waves. Therefore, the polarization direction of a linearly-polarized wave will be rotated by the MPR wall if the transmission amplitude is the same for both LHCP and RHCP incident waves. The presented MPR wall is integrated on the host substrate Rogers RT5880 with relative permittivity of 2.2. To estimate the transmission coefficients, a full-wave EM simulation is carried out using Ansys HFSS. As is represented in Figure 2.6(e), the bottom xy-plane is the first master boundary, and the top xy-plane is the correspondent slave boundary. Likewise, the xz-planes are the second correspondent master/slave boundaries. The two ports are placed in yz-planes, and the interval between them is 2.5 mm, corresponding to a half-wavelength in free space at 60-GHz. The Floquet port settings, under the specified boundary conditions (described in Figure 2.6(e)), fire two plane waves with orthogonal electric fields along y- and z- directions toward the MPR wall plane. Moreover, higher-order modes may additionally be defined in the port properties. The simulated co-polar and cross-polar coupling between the modes, both reflection and transmission coefficients, are expressed in terms of scattering parameters in Figure 2.7. For instance, the co-polarized reflection of mode 1 at port 1 is called $S_{11}^{(\mathrm{Mode1,Mode1})}$, and the co-polarized transmission for mode 1 is called $S_{21}^{(\mathrm{Mode1,Mode1})}$. Furthermore, the cross-polarized transmission between modes 2 and 1 would be called $S_{21}^{(\mathrm{Mode1,Mode2})}$. As displayed in Figure 2.7, the MPR wall acts as an electromagnetic transparent layer with low insertion-loss close to 0 dB on a broad frequency range. Meanwhile, the E-field rotates 90^o through the MPR wall (Figure 2.6(f)) and makes the two DRA antennas orthogonal in terms of the received signal from each other DRA. The resonance frequency is shifting by adjusting the dimensions of the unit cell. The radii of the SRRs (L_{r1} and L_{r2}) are the most significant parameters, that influence the unit cell resonance frequency. The resonance frequency reduces by increasing the radii of the split-ring resonators (L_{r1} and L_{r2}). The metallic strip in the middle is utilized to rotate the E-field and does not have a significant impact on the resonance frequency. As it can be observed from Figure 2.7, the -10 dB bandwidth of the investigated MPR unit cell is about 12-GHz from 55 to 67 GHz.

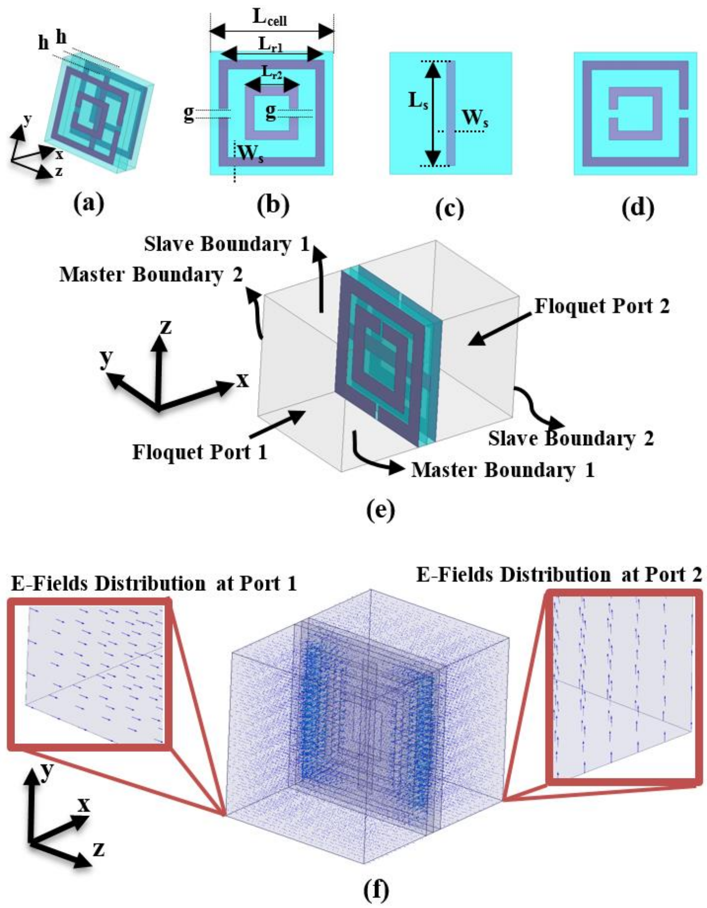

Figure 2.6: (a) Perspective view of the unit cell, (b) Metallic SRR-like on the top surface, (c) Metallic strip on the middle surface, (d) Metallic SRR-like on the bottom surface, (e) Specific boundary conditions and defined Floquet port excitation to extract scattering parameters, (f) E-fields distribution at 60-GHz. The dimensions are $L_{cell} = 2$, $L_{r1} = 1.6$, $L_{r2} = 1$, $g = 0.05$, $W_s = 0.2$, $h = 0.127$, and all in millimeter (M. Farahani et al. [47], @2017 IEEE).

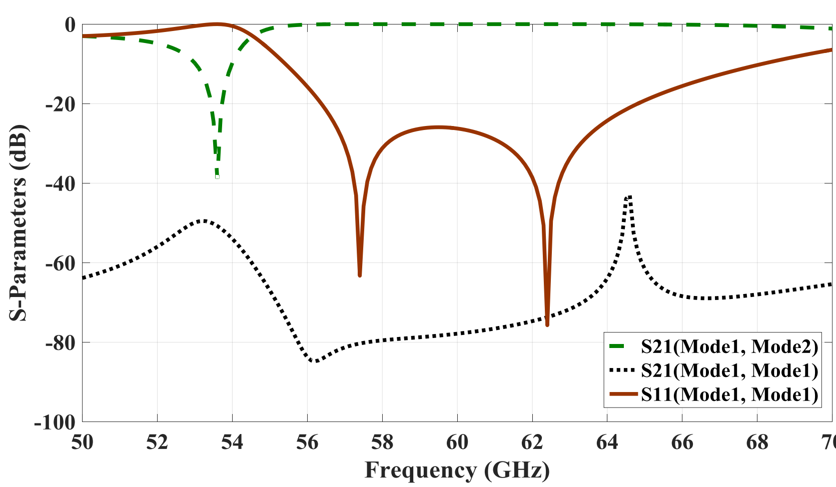

Figure 2.7: Transmission/reflection coefficients of the proposed MPR unit cell in Figure 2.6 (M. Farahani et al. [47], @2017 IEEE).

2.2.4 Integrating MPR Walls and Dielectric Resonator Antenna Arrays

The DRA arrays are designed based on reference [2]. The DRA antenna is made of a cylindrical dielectric resonator with a relative permittivity of 10.2 (RT6010). The fundamental mode $HEM_{11\delta}$ is stimulated by exciting the cylindrical dielectric resonator with a slot at the center of it. The arrangement of 1×2 DRA arrays are arrayed in the H-plane with an inter-ellement-spacing of 2.5 mm corresponding to $\lambda_o/2$ at 60-GHz. To decrease the mutual coupling among the DRA radiating elements, the MPR walls are placed between the antennas, as depicted in Figure 2.8, Figure 2.11 and Figure 2.14, concerning Case 1 to Case 3, respectively. The MPR walls are comprised of 4×5, 2×7, 1×7 unit cells along the E-plane, concerning Case 1 to Case 3, respectively. The number of MPR unit cells is chosen through a parametric study. For example, concerning Case 3 results, shown in Figure 2.15, the mutual coupling would not be reduced further for a number of unit cells more than 7, because the spatial field contribution in mutual coupling is insignificant for a number of unit cells more than 7 unit cells. The MPR walls have to be matched over the working frequency range, to reduce any potential impact on the input impedance of the DRAs. As can be concluded from Figure 2.3, Figure 2.5 and Figure 2.7, the MPR walls are matched over the working frequency range from 57 to 64 GHz in all three cases. The mutual coupling reduction transpires from the fact that the E-fields rotate 90^o and makes the coupling among the antennas orthogonal. The rotation of the E-field is displayed in Figure 2.2(e), Figure 2.4(d), and Figure 2.6(f). As a conclusion, the two radiating elements are orthogonal, which leads to lower coupling among the antennas in the arrays. Meanwhile, they have identical polarization in the far-field radiation point of view. The introduced MIMO antenna arrays with and without MPR walls are simulated using Ansys HFSS. Figure 2.9, Figure 2.12 and Figure 2.16 display the S-parameters of the antennas with and without MPR walls. As can be observed from Figure 2.16, the mutual coupling is decreased by more than 15 dB on average (8 dB at 57-GHz, 22 dB at 60-GHz, 14 dB at 62-GHz). Besides, utilizing the MPR wall does not have any impact on the radiation pattern, opposed to other techniques such as using EBG structures for blocking the surface waves [2]. The radiation pattern is substantially maintained due to having the well-matched MPR walls (Figure 2.10, Figure 2.13, and Figure 2.18).

The Case 3 MIMO array integrated the MPR wall is constructed and measured. The photo of the constructed prototype is displayed in Figure 2.19. A 1.85 mm end-lunch connector (1892-03A-5 from Southwest-Microwave Inc.) is employed to examine the fabricated MIMO antenna. The reflection coefficient and mutual coupling measurement results of the introduced MIMO antenna are presented in Figure 2.17. As can be observed from Figure 2.17, the reflection coefficient of the antenna is below -10 dB over the working frequency range from 57 to 64 GHz. Nevertheless, the coupling between the two DRAs is decreased effectively in frequencies below 63.5 GHz. As can be noticed from Figure 2.16, the coupling between the two DRAs is reduced by more than 16 dB on average covering the working mmWave frequency-band from 57 to 64 GHz. Figure 2.18 presents the normalized simulated and measured H- and E-plane radiation patterns at 60-GHz of a DRA in the array, while the other DRA is terminated with a 50 Ohm load. It can be observed that the radiation characteristics are almost preserved compared to the MIMO array without the MPR wall. The radiation efficiency is a beneficial parameter for assessing the performance of an antenna with the Omni-directional pattern due to that it does not take into account radiation direction. To put it differently, antenna 3D gain is a better parameter for assessing the performance of an antenna if it is designed as a directive antenna (in this project, the designed antenna has a half-space radiation pattern). Nevertheless, the radiation efficiencies of the fabricated DRA antennas using the D/G method [56] without and with the MPR wall are 92% and 88% at 60-GHz, respectively, which is decreased 4% compared to the DRA array without MPR wall. In [56], it is determined by examination that in the antennas where the cross-polar radiation contribution in near field is significant, in this project due to the MPR wall, Wheeler cap approach is more reliable [56], rather than that obtained in the D/G approach, where the undesired cross-polar radiation contribution is not regularly taken into account. The radiation efficiencies of the fabricated DRA MIMO arrays in the Wheeler cap approach without and with the MPR wall are 93% and 92% at 60-GHz, respectively, which presents an improvement 3% compared to the D/G approach.

The ability of a MIMO system is principally reliant on possessing independent extra channels. In MIMO systems, dependent multiple channels would deteriorate the performance of the system, for example, its capacity. Channel correlation is a parameter to measure the similarity or likeliness between the channels in MIMO systems. In the most unfortunate scenario, if the channels are quite correlated, then the MIMO system would operate as a single-antenna communication system. Predominantly, the channel capacity is reversely proportional to the channel correlation. The channel correlation is regularly due to the spatial-correlation and antenna mutual coupling in MIMO systems [51]. In this project, it was our preference to design a MIMO system with a low correlation coefficient. To attain this objective, the two radiating elements in the presented MIMO antenna should possess identical radiating characteristic, otherwise, even though they possess a low amount of coupling, the correlation is large. The correlation among channels in a MIMO system is linked to the mutual coupling, and it is proportional to the mutual coupling among channels if the spatial correlation is holding lowed [3]. The correlation coefficient measurement result of the designed antenna is described in Figure 2.19. Table 2.1 compares the various methods for mutual coupling reduction in literature.

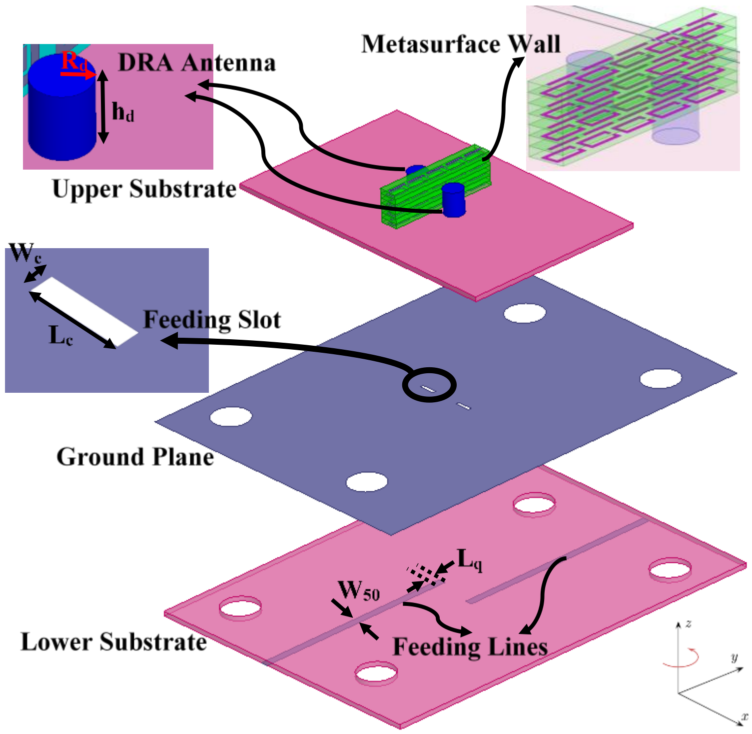

Figure 2.8: The Case 1 schematic of the DRA MIMO antenna arrays with the proposed metasurface wall. The dimensions are $R_d = 0.53$, $h_d = 1.27$, $W_c = 0.18$, $L_c = 0.87$, $W_{50} = 0.4$, $L_q = 0.3$, and all in millimeter (M. Farahani et al. [45], @2017 IEEE).

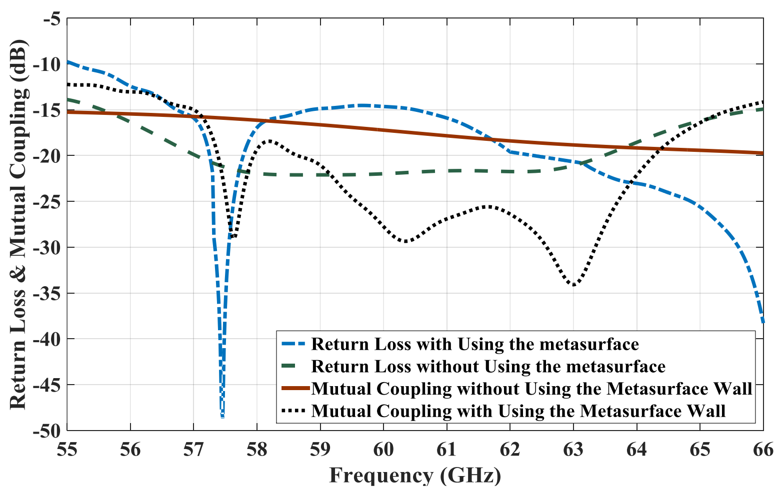

Figure 2.9: The Case 1 simulated S-parameter results of the DRA MIMO arrays with and without metasurface wall between the two radiating elements (M. Farahani et al. [45], @2017 IEEE).

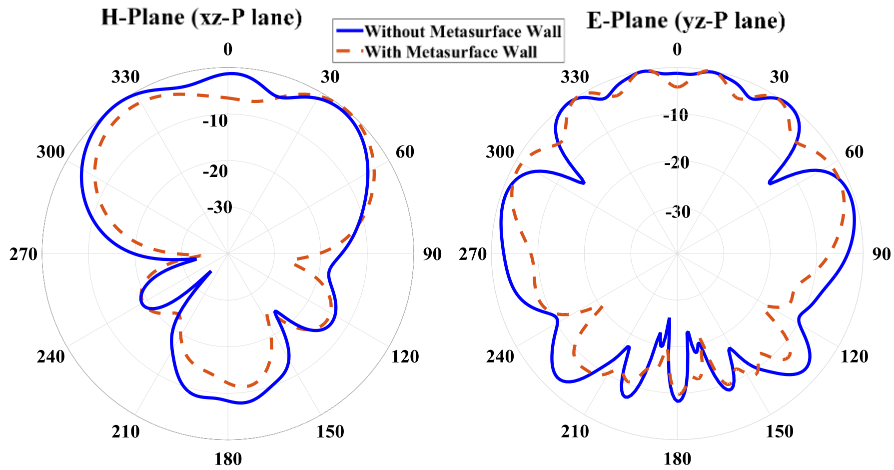

Figure 2.10: The Case 1 radiation patterns of the DRA MIMO arrays with and without metasurface wall between the two radiating elements (M. Farahani et al. [45], @2017 IEEE).

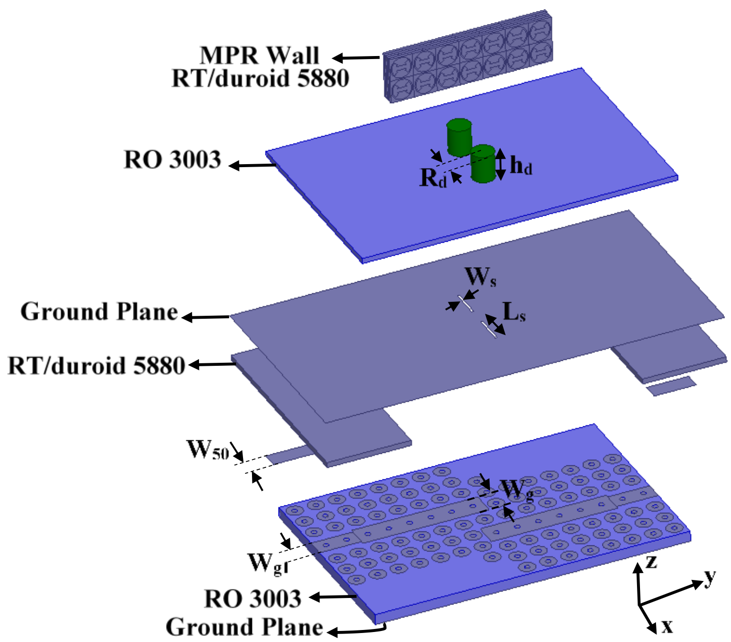

Figure 2.11: The Case 2 schematic of the DRA MIMO arrays with the proposed MPR wall. The dimensions are $R_d = 0.53$, $h_d = 1.27$, $W_s = 0.1$, $L_s = 1.5$, $W_{50} = 0.8$, $W_{g1} = 0.9$, $W_g = 1.2$, and all in millimeter (M. Farahani et al. [46], @2017 IEEE).

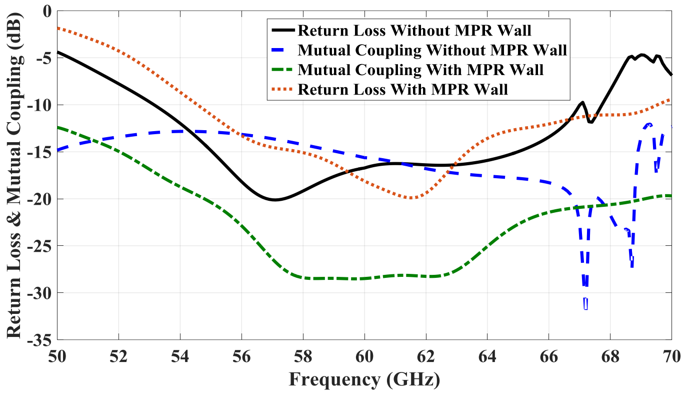

Figure 2.12: The Case 2 simulation results of the DRA MIMO arrays with and without the MPR wall between the two radiating elements (M. Farahani et al. [46], @2017 IEEE).

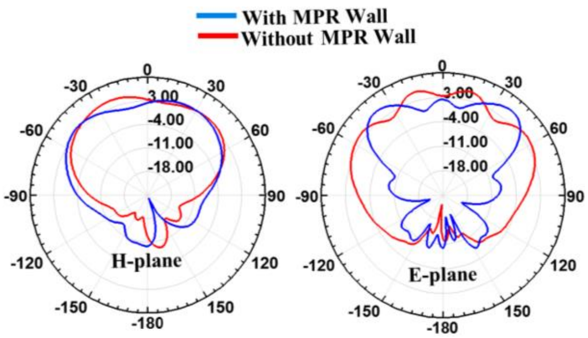

Figure 2.13: The Case 2 radiation patterns of the DRA MIMO arrays with and without MPR wall between the two radiating elements (M. Farahani et al. [46], @2017 IEEE).

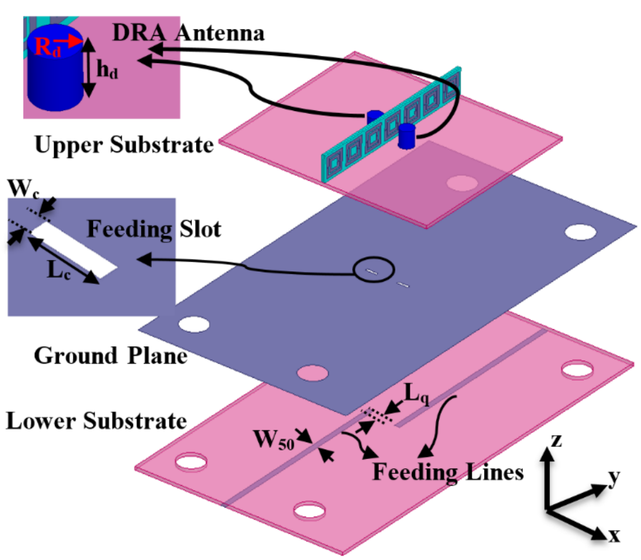

Figure 2.14: Layout of Case 3 of the 1×2 DRA MIMO array with the MPR wall. The dimensions are $R_d = 0.53$, $h_d = 1.27$, $W_c = 0.18$, $L_c = 0.87$, $W_{50} = 0.41$, $L_q = 0.3$, and all in millimeter (M. Farahani et al. [47], @2017 IEEE).

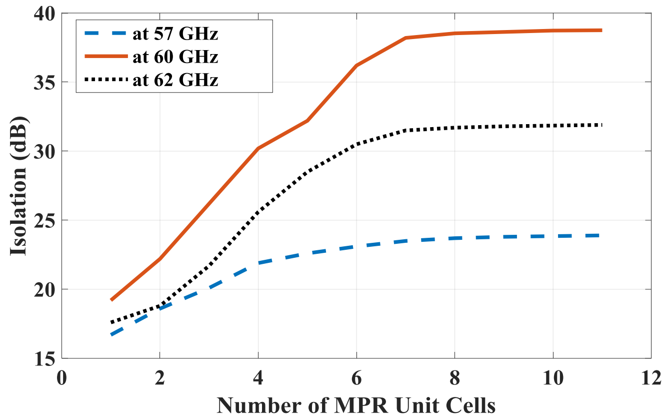

Figure 2.15: Case 3 isolation versus the number of MPR unit cells at the frequencies of 57 GHz, 60 GHz, and 62 GHz (M. Farahani et al. [47], @2017 IEEE).

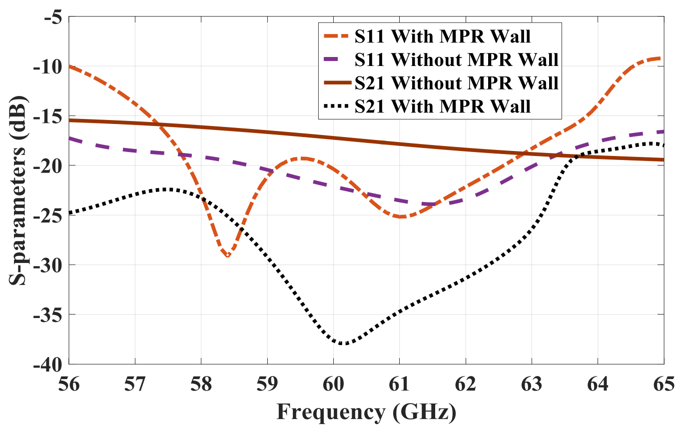

Figure 2.16: Case 3 S-parameters simulation results of 1×2 DRA MIMO array with and without MPR wall between the two radiating elements (M. Farahani et al. [47], @2017 IEEE).

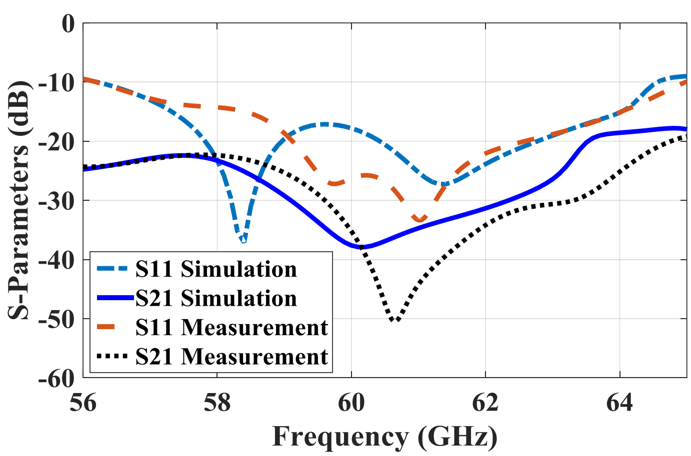

Figure 2.17: Case 3 simulated and measured results of 1×2 DRA MIMO array with MPR wall between two radiating elements (M. Farahani et al. [47], @2017 IEEE).

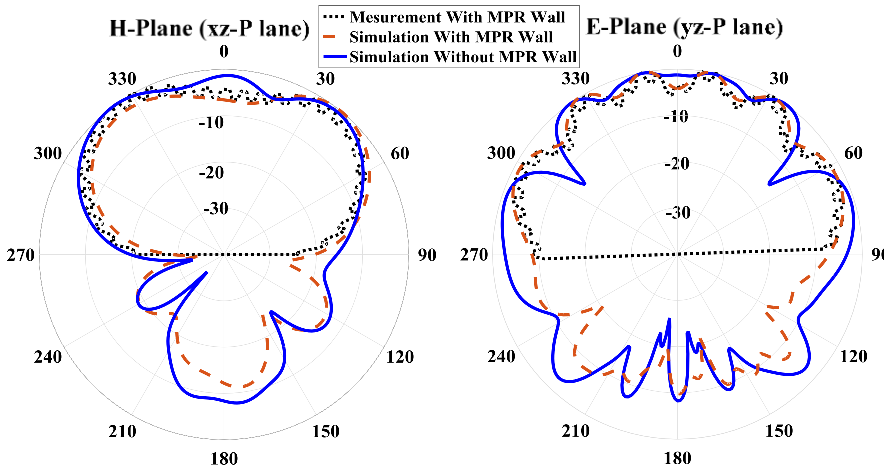

Figure 2.18: Case 3 simulated and measured radiation pattern of 1×2 DRA MIMO array with and without MPR wall between two radiating elements (M. Farahani et al. [47], @2017 IEEE).

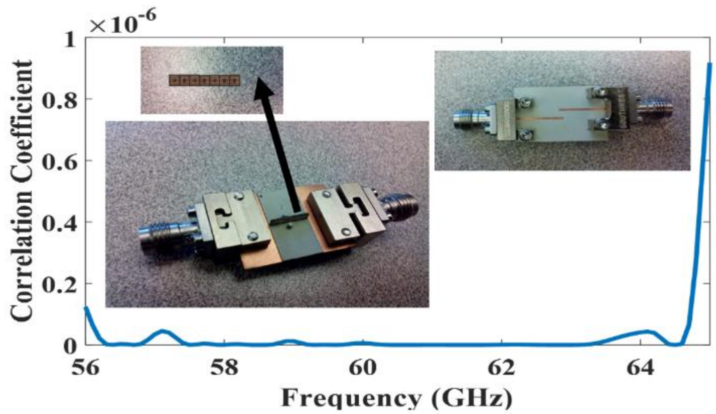

Figure 2.19: Case 3 measured result for correlation coefficient between the two DRA MIMO array with MPR wall between the two radiating elements, and the photo of the proposed fabricated prototype (M. Farahani et al. [47], @2017 IEEE).

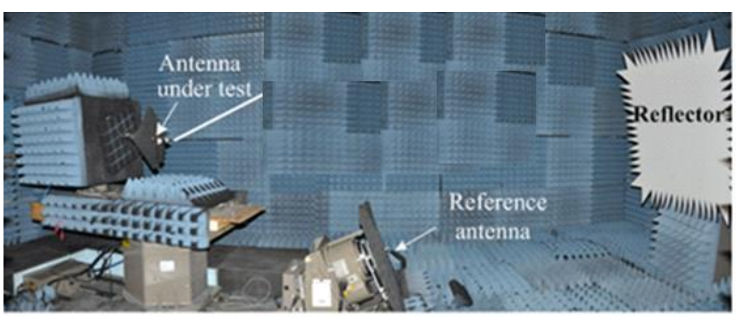

Figure 2.20: Case 3 radiation pattern measurement setup with receiving mode of the antenna under test (M. Farahani et al. [47], @2017 IEEE).

Table 2.1: Comparison Case 3 to the other decoupling structures (M. Farahani et al. [47], @2017 IEEE).

Case	Frequency-Band	Average Mutual Coupling Reduction	ABSOLUTE MUTUAL COUPLING			Tilted beam (degree)
			57 GHz	60 GHz	64 GHz	
Ref. [2]	57-64 GHz	13dB	-3dB	-10dB	0dB	30º
Ref. [7]	4.06-4.095 GHz	10dB	-	-	-	36º
Ref. [9]	5-7 GHz	14dB	-	-	-	27º
Ref. [10]	57-64 GHz	14dB	-18dB	-15dB	0dB	33º
Ref. [11]	57-64 GHz	15dB	-10dB	-13dB	-7dB	34º
This work	57-64 GHz	16dB	-8dB	-22dB	0dB	Almost unchanged

2.3 Millimeter-Wave Corrugated Surface for Mutual Coupling Reduction

The mutual coupling has a destructive impact on array antennas performance by loading the input impedance of the radiating elements, raising the sidelobe level and deteriorating the radiation pattern [2]. In phased array antennas an optimum spacing among the radiating elements is about half a wavelength to prevent the grating Lobes to contribute in the array factor. But, this situation yields strong coupling among radiating elements. There are different methods to decrease mutual coupling, including confocal elliptical metasurface cloaks [4], parasitic element slots [5], cavity-backed resonator [6], and electromagnetic band-gap (EBG) structures [2]. Because of the fabrication constraint at the mmWave frequency range, these techniques are not effective. The spacing among the radiating elements is less than a few millimeters in mmWave array antennas.

In this section, a corrugated surface is introduced for diminishing the coupling among radiating elements in mmWave array antennas. The corrugated surface makes a bandgap along the propagation direction toward the neighboring antenna. The recommended structure does not deteriorate the radiation characteristics at 60-GHz band, although it has a notable impact on the radiation characteristics at lower frequencies.

2.3.1 1×2 Dipole Antenna Array

The layout of the employed 1×2 dipole array antenna is presented in Figure 2.21. Each antenna is excited through a microstrip transmission line. The ground plane terminated at the center of L_2-line to work as a balun and stimulates the dipole gates by 180^o out of phase. The dipole antenna is not grounded and radiates in all three directions. The spacing among the radiating dipoles is half a free-space wavelength. Rogers RT6002 with relative permittivity of $\varepsilon_r = 2.94$ is utilized as the host substrate, and the antenna dimensions are given in Figure 2.21.

2.3.2 Corrugated Surface and Mutual Coupling Reduction

The traditional corrugated surface and the recommended corrugated surface are presented in Figure 2.22. The traditional corrugated surface works similar to a soft surface along the x-direction [57], and the surface impedance can be estimated as

$$Z_X = \frac{E_X}{H_Y} = j\left(\frac{W}{P}\right)\eta \tan k_g d \qquad (2-1)$$

The surface impedance is infinite when $d = \lambda_g/4$, which operates similar to a surface produced of the periodical parallel thin strips of PEC and PMC oriented in y-direction (Figure 2.22c). The available bandwidth remains in the range of $0 < k_g d < \pi$, although surface waves may be significant when $d \neq \lambda_g/4$. Generally, available relative bandwidth is up to 3%, although the most suitable E-Plane performance is when $k_g d = \pi/2$.

The surface impedance of the recommended corrugated surface (Figure 2.22b) can be given as following

$$Z_X = \frac{E_X}{H_Y} = j\left(\frac{W}{P}\right)\eta \cot k_g d \qquad (2-2)$$

As has been stated, this corrugated surface has a pretty narrow band performance, in general, the accessible relative bandwidth is up to 3%. To increase the bandwidth of the suggested corrugated surface, a dual-band ridged surface (Figure 2.22d) is suggested to embrace the frequency range from 57 to 64 GHz (11.5% relative bandwidth).

The offered corrugated surface is located between the two radiating dipoles and is displayed in Figure 2.23. This technique can be employed efficiently at 60-GHz band due to the fact that $d = \lambda_g/2$ is huge at microwave bands up to 20-GHz, and therefore inserting this structure within the antennas has notable impact on radiation characteristics and will affect the input impedance of the array elements by charging the antenna radiation. At 60-GHz band, $d = \lambda_g/2$ is comparable with the host dielectric thickness and does not have a significant effect on the radiation pattern and input impedance of the array elements.

The array antennas with and without the corrugated surface are simulated using Ansys HFSS. The S-parameters of the antennas are presented in Figure 2.24. The mutual coupling is decreased between 4 to 20 dB while the corrugated surface is located between the dipoles. The simulated radiation patterns of the 1×2 MIMO array are given in Figure 2.25.

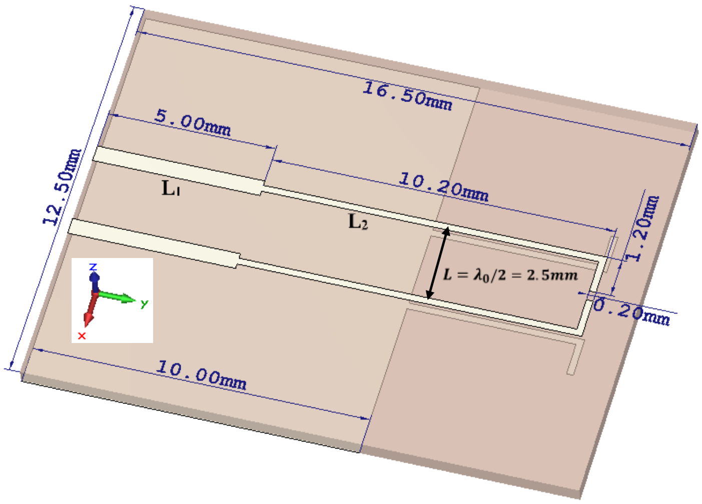

Figure 2.21: Schematic diagram of 1×2 dipole antenna array (M. Farahani et al. [48], @2016 IEEE).

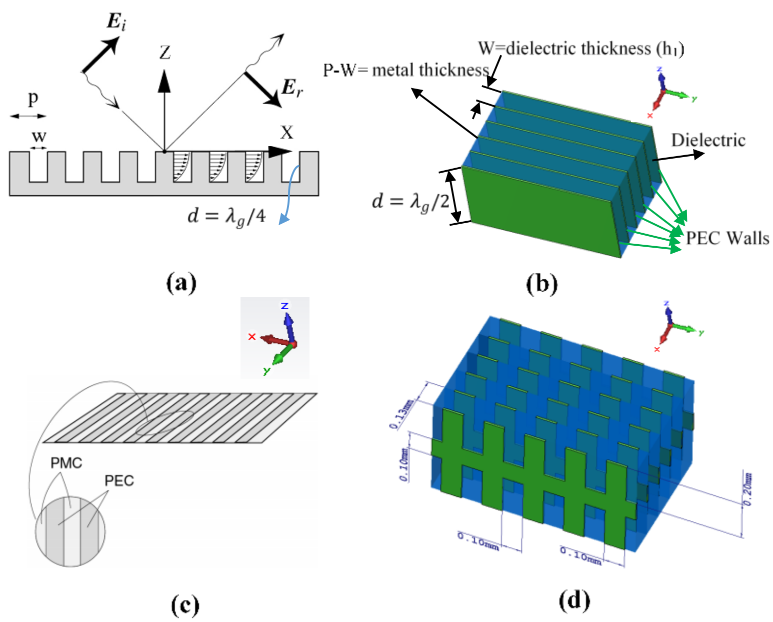

Figure 2.22: Corrugated surfaces. (a) Conventional corrugated surface. (b) Proposed corrugated surface. (c) Equivalent model of corrugated surface. (d) Proposed dual-band corrugated surface (M. Farahani et al. [48], @2016 IEEE).

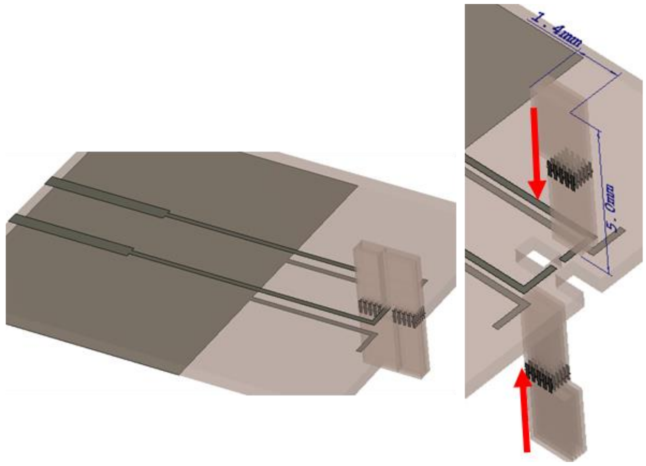

Figure 2.23: Proposed 1×2 dipole antenna array with corrugated surface (M. Farahani et al. [48], @2016 IEEE).

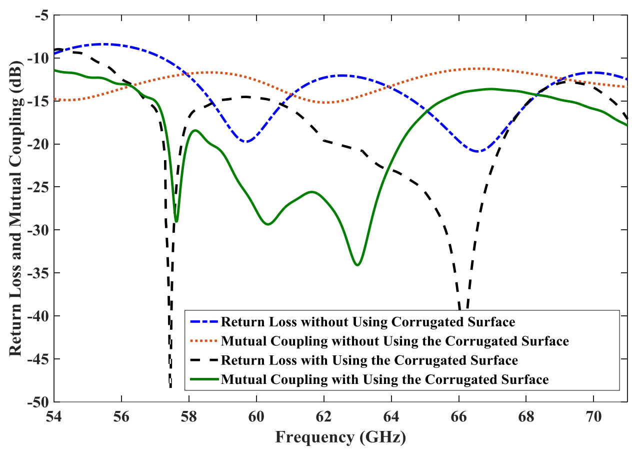

Figure 2.24: Return loss and mutual coupling of the 1×2 antenna array, with and without the corrugated surface (M. Farahani et al. [48], @2016 IEEE).

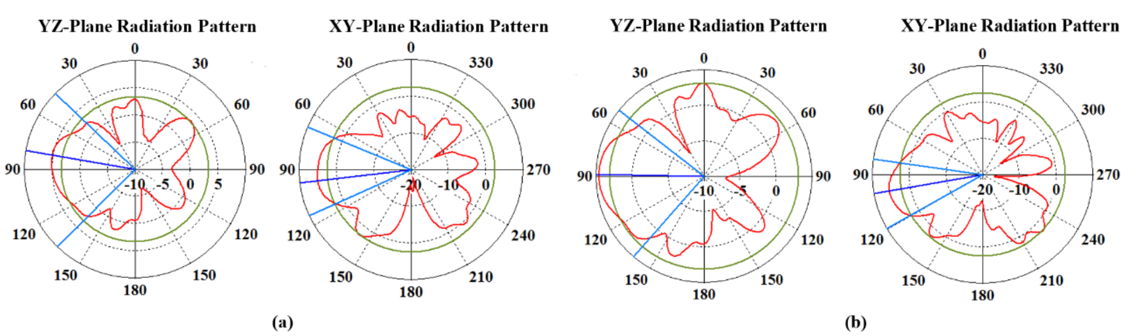

Figure 2.25: Simulated radiation patterns of 1×2 MIMO antenna system. (a) Without corrugated surface between two dipole antennas. (b) With corrugated surface between two dipole antennas (M. Farahani et al. [48], @2016 IEEE).

2.4 mmWave MIMO Antenna and FSS Superstrate

2.4.1 Spatially Mutual Coupling Reduction Between CP-MIMO Antennas Using FSS Superstrate

A novel method to reduce the coupling due to spatial electromagnetic interaction among two circularly-polarised (CP) radiating elements utilizing an FSS superstrate layer is proposed at 30-GHz. The FSS layer, with the CP performance, is located above a 1×2 MIMO arrangement. The investigation reveals that the FSS superstrate layer may reduce the coupling between two neighboring CP MIMO array by more than 10 dB. The recommended method does not deteriorate the radiation characteristics of the CP antenna compared to the antenna without the FSS superstrate layer.

The structure of the presented MIMO array with the FSS superstrate layer is depicted in Figure 2.26. It is made by three separate substrate layers, the lower layer is Rogers 3006 with $\varepsilon_r = 6.15$, and the two upper layers are Rogers 5880 with $\varepsilon_r = 2.2$. The two circular metal patches are placed on the top of the middle layer with the inter-elements spacing of 'd' equals to $\lambda_o/2$ (5 mm). They are excited through the two slots in the ground on the bottom side of the middle layer. The FSS superstrate layer is located at '$h = 3.6$ mm' above the MIMO array.

The structure of the FSS unit cell along with the physical dimensions are shown in Figure 2.27(a). The idea of the presented unit cell begins by a metal strip and rectangle split-ring resonator (SRR) embedded on the lower and upper sides of Rogers 5880 substrate with a thickness of 0.381 mm. The dimension of the unit cell is 5×5 mm^2. One should note that the rotation angle (w) of the metal strip on the unit cell is 45^o. Nevertheless, it is adjusted to 22.5^o in the finalized design to lessen the reflection impacts. A full-wave simulation has been carried out by Ansys HFSS to extract the scattering parameters. As shown in Figure 2.27(b), the FSS superstrate layer works as an electromagnetic transparent layer for incident CP waves, where the magnitude and phase variations for two orthogonal field components (TE and TM) are almost identical. As a result, the superstrate layer has excellent electromagnetic transparency for the CP wave. Moreover, the presented superstrate layer covers the frequency range from 26 to 34.5 GHz (28%).

The presented MIMO array with the FSS superstrate layer is manufactured and examined. The coupling parameter is determined by normalizing the experimental coupling results with total radiated power and eliminating reliance on impedance matching. Therefore, the coupling parameter is estimated as [58].

$$C(dB) = 10log\left(\frac{|S_{21}|^2}{(1-|S_{11}|^2)(1-|S_{22}|^2)}\right) \qquad (2-3)$$

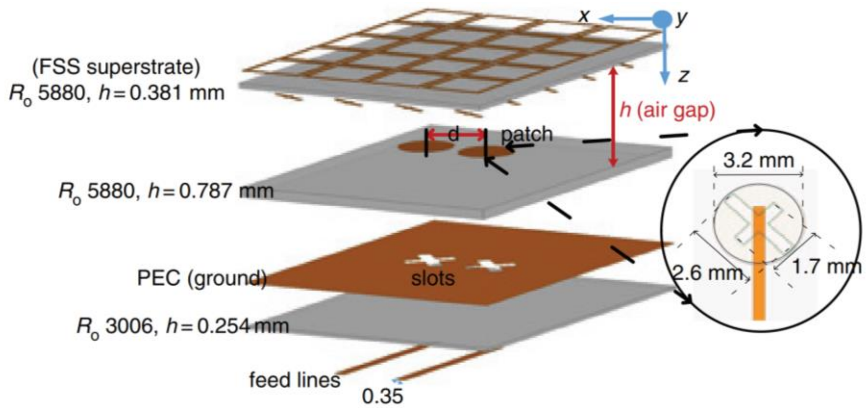

Figure 2.26: Schematic of the CP-MIMO antennas with FSS superstrate (d = 0.5λ, h = 0.36λ at 30 GHz) (M. Akbari et al. [49], @2017 IET).

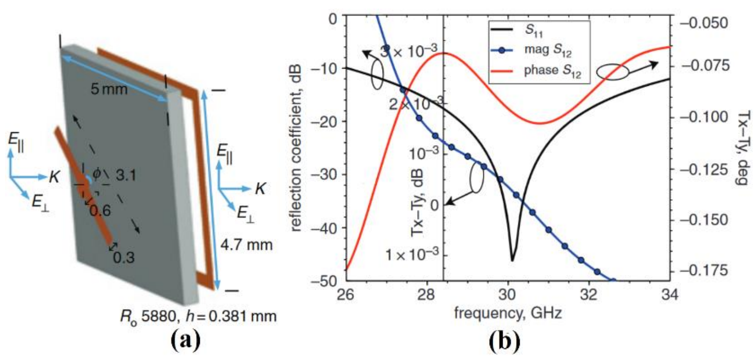

Figure 2.27: Structure and S-parameter results of FSS unit cell model. (a) 3D view of the proposed FSS unit cell. (b) Curves of reflection coefficient along with magnitude and phase differences between two the orthogonal field components. Tx and Ty are two the orthogonal field components along the x- and y-axes, respectivelly (M. Akbari et al. [49], @2017 IET).

The measurement and simulation results of the coupling, axial ratio (AR), scattering parameters, accompanying E-field distributions at 30-GHz are displayed in Figure 2.27 for the proposed MIMO array with and without the FSS superstrate layer. It can be observed that impedance bandwidth ($|S11|) < -10\ dB$) covers the frequency range from 27 to 33.5 GHz (Figure 2.27(a)). The AR of the MIMO array, given in Figure 2.28(b), calculated utilizing [59]-[60]:

$$AR(dB) = 10log\left(\left|\frac{\left|\overrightarrow{E_\theta} + j\overrightarrow{E_\varphi}\right| + \left|\overrightarrow{E_\theta} - j\overrightarrow{E_\varphi}\right|}{\left|\overrightarrow{E_\theta} + j\overrightarrow{E_\varphi}\right| - \left|\overrightarrow{E_\theta} - j\overrightarrow{E_\varphi}\right|}\right|\right) \quad (2-4)$$

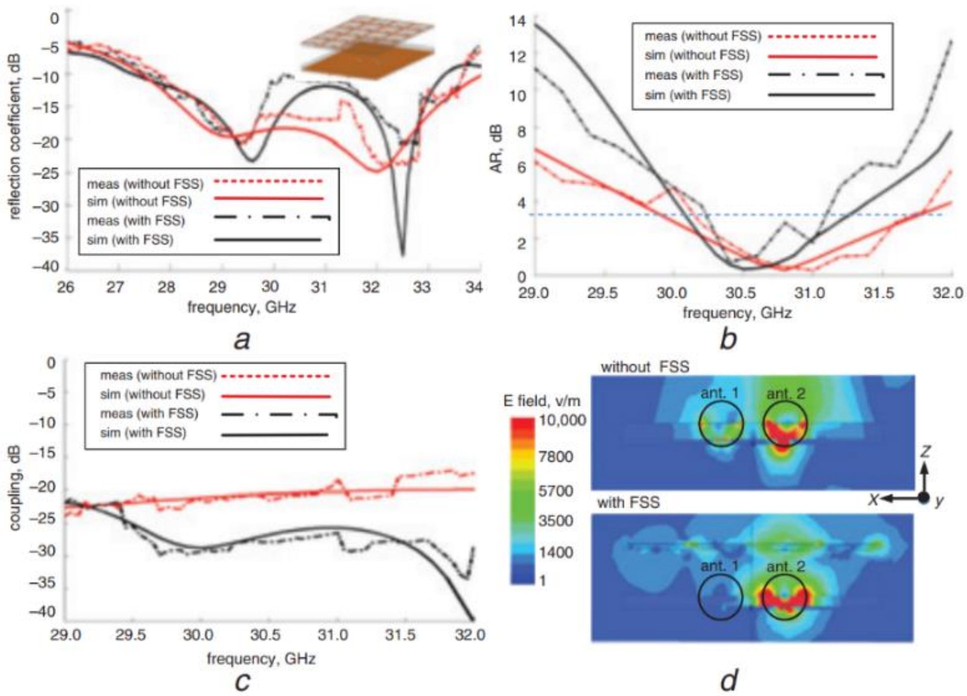

Figure 2.28: Measured and simulated results. (a) Reflection coefficient. (b) Axial ratio. (c) Coupling. (d) E-field distributions at 30.5 GHz (M. Akbari et al. [49], @2017 IET).

2.4.2 Spatially Decoupling of CP Antennas Based on FSS for 30-GHz MIMO Systems

A powerful method for decreasing the coupling among a four-port CP MIMO array at 30-GHz is investigated and developed. This is achieved by employing two electromagnetic transparent FSS superstrate layers consist of two crossed metal strips. The mutual couplings, while the radiating elements are radiating in free space, are compared with the same topology in the presence of the FSS superstrate layers. The simulations, in the presence of the FSS superstrate layers, exhibit an average of 9 dB enhancement in the isolation among four neighboring radiating elements in the MIMO array. Besides, a detailed investigation is carried out to redirect those unimportant reflected waves caused by the FSS superstrate layers and also block any interference. The suggested 2×2 MIMO array with the FSS superstrate layer is realized and examined to verify the simulated results. Experimental results of S-parameters, coupling, and axial ratio determine a good agreement with the simulated results.

The electromagnetic transparent FSS superstrate layer is given in Figure 2.29, consisting of two stacked dielectric substrates of Rogers 5880 with $\varepsilon_r = 2.2$ and thickness of 0.787 mm. The same cross dipole metal strips are on each layer as depicted in Figure 2.29. The designed FSS superstrate layer can pass most of the CP incident waves within the working frequency range without a notable impact on the signal's phase and magnitude, as revealed in Figure 2.29.

Figure 2.30 presents the circuit model of the FSS superstrate layer using capacitive and inductive elements and transmission-lines model. The cross dipole strips could be divided into horizontal and vertical metal strips, and are represented as capacitive and inductive elements, respectively. For an arrangement of slim, endless, very long and ideally conductive narrow strips, the parallel impedance could be capacitive or inductive, replying on incident waves, whether it is polarized perpendicular or parallel to the edge of the strips [61]. The vertical strips, co-ordinate to the electric-field orientation for TE-wave, are considered as parallel inductors in the circuit model. It should be pointed out that cross strips are identical in horizontal and vertical viewpoints. Meanwhile, a CP wave can be analyzed as two orthogonal LP waves with 90 degrees out of phase. In addition, the equivalent circuit inductive reactance $F(P, W, \lambda)$ is given by [61]:

$$\frac{X_l}{Z_o} = \frac{d}{p} F(P, W, \lambda) \qquad (2-5)$$

$$B_g = 4\frac{w}{p} F(P, W, \lambda) \qquad (2-6)$$

$$B_d = 4\frac{d}{p} F(P, P-W, \lambda) \qquad (2-7)$$

where several model parameters in (2-5)-(2-7) for the unit cell of crossed strips are given in Figure 2.31.

It is remarked that the identical crossed strips are embeded on the bottom, middle, and top of the two substrates of Rogers 5880 with $\varepsilon_r = 2.2$ and thickness of 0.787 mm. When P is considerably shorter than a wavelength, by the LC circuit model in both directions of vertical and horizontal, not just the several resonances can simply be created, but additionally the ability of phase control is allowed on the operating frequency range, offering a broader bandwidth. To perceive the performance of the crossed strips with tremendous components, the Ansys HFSS unit cell model, that is a finite element method solved by a full-wave simulator, is utilized. In this regards, two Floquet ports are utilized under specified master/slave boundaries conditions. As presented in Figure 2.32, the working bandwidth of the intended unit cell for $S_{11} \leq -10\ dB$ is from 28.5 to 34.5 GHz (19%).

The electromagnetic transparent performance of the unit cells can be concluded by the phase and magnitude of the S-parameters. It is perceived in Figure 2.32 that on the S11 bandwidth from 28.5 to 34.5 GHz, phase and amplitude variation of two orthogonal transmitted waves for the exciting CP wave is negligible. As an outcome, the FSS superstrate layers almost have a perfect transmission characteristic for the exciting CP wave.

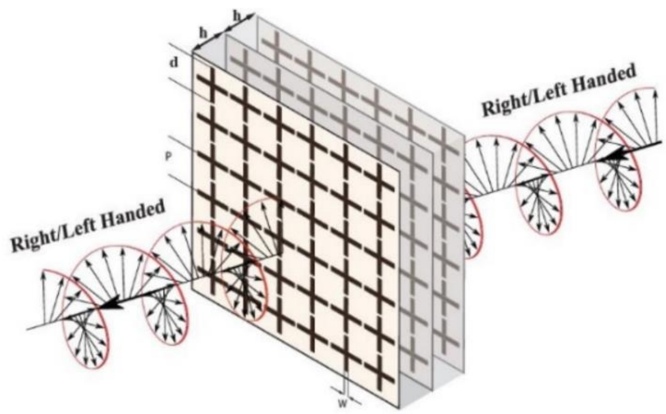

Figure 2.29: Schematic model of the transmission-type FSS superstrate illuminating by CP wave (The dimensions are $h = 0.787$, $d = 2.7$, $P = 3$, and $W = 0.3$, all in millimeters) (M. Akbari et al. [50], @2017 IEEE).

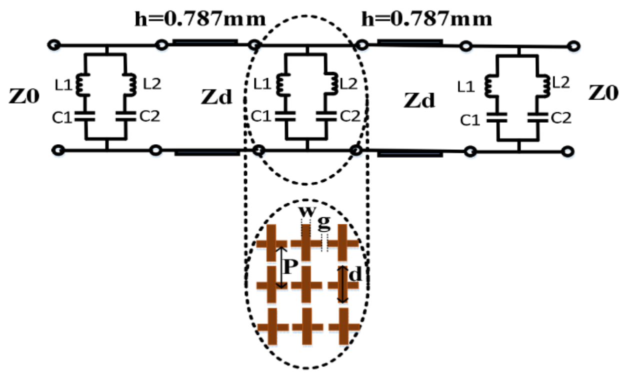

Figure 2.30: Equivalent circuit of FSS layer including inductive and capacitive elements [61], where ($z_d = \frac{Z_o}{\sqrt{\varepsilon_r}}$) (M. Akbari et al. [50], @2017 IEEE).

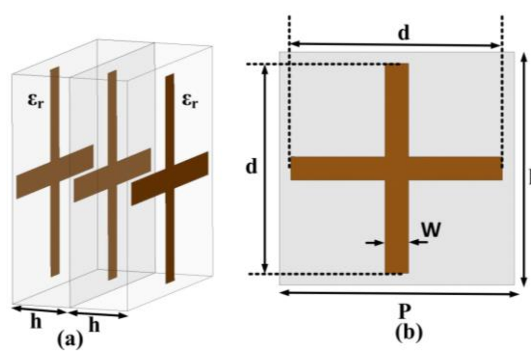

Figure 2.31: The unit cell model of crossed dipole FSS (a) side view and (b) top view (The dimensions are $d = 2.7$, $P = 3$, $W = 0.3$, $\varepsilon_r = 2.2$, and $h = 0.787$, all in millimeters) (M. Akbari et al. [50], @2017 IEEE).

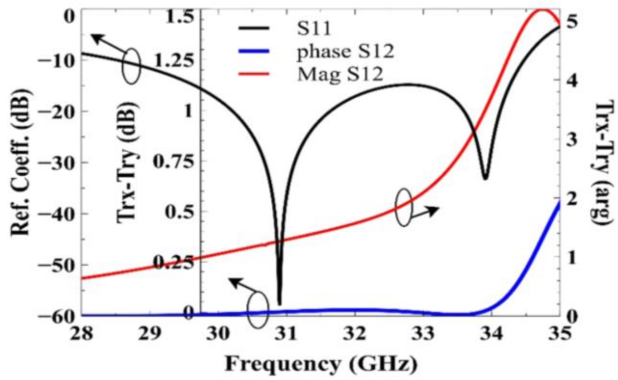

Figure 2.32: Simulated results of S-parameter for the unit cell model of FSS (M. Akbari et al. [50], @2017 IEEE).

To provide a wide operating frequency range and having broadside radiation characteristics, an aperture coupled microstrip antenna (ACMA) is designed. As described in Figure 2.33, the ACMA, with the ability of CP operation, constructed of two separate substrates of Rogers 3006 ($\varepsilon_r = 2.2$, $H_2 = 0.787$ mm) in the bottom and Rogers 5880 ($\varepsilon_r = 2.2$, $H_2 = 0.787$ mm) in the top. The exciting slot etched off on the middle layer ground plane, is employed to excite the patch. Additionally, a 50 Ohm microstrip feeding line and a circle patch are embedded in the lower and upper sides of the bottom and top substrates, respectively. The antenna is intended to work at the 30-GHz center frequency. The simulation results in terms of axial ratio and reflection coefficient are presented in Figure 2.34, which shows the ACMA antenna works in terms of input impedance and CP bandwidths from 28 to 34 GHz (19.3%) and 29.2 GHz to 31 GHz (6%), respectively.

A MIMO system is respected as a method for increasing the capacity of a communication system employing additional transmitter and receiver links to overwork multipath channels [62]. Adopting this idea, the introduced method in this project intends to define the impact of the coupling among radiating elements of the MIMO array. To realize this purpose, the four radiating elements of the MIMO array are arranged in 2×2 array to excite the FSS superstrate layers. The arrangement of the proposed MIMO array is shown in Figure 2.35, where the coupling among the radiating elements are determined by parameters ‘‘C_d’’, ‘‘C_v’’, ‘‘C_h’’ and ‘‘di’’.

The main drawback of this technique is encountering partially reflected waves from the FSS superstrate layers. These partially reflected waves happen since the radiating elements stimulate the FSS superstrate layers with various incidence angles. In other words, while the FSS unit cells are arranged as a planar array, these reflections may deteriorate radiation characteristics of the illuminating radiating elements, and also increase the mutual coupling among the radiating elements. Hence, to get out of the way this obstacle, the array factor (AF(Near-Field)) concerning reflections in the near-field area is investigated and extracted.

Considering that this extracted AF(Near-Field) is always dominated by the FSS unit cell reflection coefficients, which are complex values determining how the incident waves reflected from the various unit cells. In Figure 2.36, the configuration of the proposed MIMO array with FSS superstrate layers along with indicated transmission and reflection gains associated with the scattering parameters, AF(Near-Field) and AF(Far-Field) is remarked. It is worth to mention that the transmission gain is larger than reflection gain confirming that the FSS superstrate layers are transparent in terms of incident electromagnetic waves. Thus, it would transfer a large part of the exciting waves and reflects a small proportion as exhibited in Figure 2.36. To discuss the reflection problem, some factors of the intended topology have to be selected in a way that the AF(Near-Field) radiation nulls be redirected toward radiating element sources. This limits any possible interference and deterioration in the radiation characteristics of radiating element sources which would lead to a reduction of mutual coupling in the proposed MIMO array.

To discuss the above concern, the AF(Near-Field) is studied. Figure 2.37 displays the configuration of a 9×9 unit cells on the FSS superstrate layer along with the 2×2 ACMA MIMO array. The FSS array of 9×9 unit cells is uniform spaced and planar in the xy-plane, as displayed in Figure 2.37. The FSS superstrate layer located 2.5 mm ($\lambda_o/4$ at 30-GHz) above the ACMA MIMO array. Hence, the produced current amplitude variation on each FSS unit cell is considered insignificant.

Accordingly, to express the AF(Near-Field), the reflection phases of FSS unit cells while illuminated by incident waves from the 2×2 MIMO array have to be considered. Figure 2.38 presents the arrangement of the uniform FSS unit cells, including 81 FSS unit cells above 2×2 MIMO array, to calculate the AF(Near-Field) in the near-field range. The physical size of FSS unit cells is 3×3 mm^2 on the xy-plane. As shown in Figure 2.38, $R_s(n)$ indicates the position of each ACMA radiating ellements, where n=1, 2, 3, 4, and the location of the FSS unit cell is provided by $R_{cell}(m)$, where m=1, 2, 3, ..., 81. Accordingly, the electric field vector at the middle of the m^{th}FSS unit cell while excited by the n^{th} ACMA radiating ellement can be determined as

$$\vec{E}_t(n,m) = E_o\left(e^{-\alpha R_t(n,m)} \times e^{-j\beta R_t(n,m)}\right)\widehat{a_r} \qquad (2-8)$$

where

$$R_t(n,m) = R_{cell}(m) - R_s(n) \qquad (2-9)$$

where α is the attenuation constant in the free space, and it is insignificant and nearly zero, and β is the propagation constant in the free space. Besides, E_o is considered as a reference for the magnitude of the electric field at each ACMA radiating element which is considered to be a fixed value. Therefore, it may be simplified following

$$\vec{E}_t(n,m) = E_o e^{-j\beta R_t(n,m)} \tag{2-10}$$

Meanwhile, R_p and $R_r(m)$ can be expressed as

$$R_p = x\widehat{a_x} + y\widehat{a_y} \tag{2-11}$$

$$R_r(m) = R_p + R_{cell}(m) \tag{2-12}$$

When the n^{th} ACMA radiating element is exciting the FSS superstrate layer, the reflected waves at location of $(\mathrm{x}, \mathrm{y}, \mathrm{z} = 0)$ can be determined as

$$\vec{E}_r(x,y,z=0,n) = E_o \sum_{m=1}^{81} \Gamma(n,m) \times e^{-j\beta R_t(n,m)} \times e^{-j\beta R_r(m)}\ \widehat{a_r} \tag{2-13}$$

where $\Gamma(n,m)$ is the reflection coefficient at the middle of the m^{th} unit cell, while the wave is emitted from the n^{th} ACMA radiating element. It is worth to mention that, $\Gamma(n,m)$ is estimated utilizing the FSS unit cell simulation results carried out by Ansys HFSS, as presented in Figure 2.32. The ACMA radiating element has a CP operation. Meanwhile, Since CP wave can be viewed as a superposition of two orthogonal LP waves with 90^o out of phase, hence, the normalized reflected electric field amplitude at location of $(\mathrm{x}, \mathrm{y}, \mathrm{z} = 0)$ when the n^{th} ACMA radiating element is radiating can be determined as

$$\left|\vec{E}_r(x,y,z=0,n)\right| = \sum_{m=1}^{81} \Gamma(n,m) \times e^{-j\beta R_t(n,m)} \times e^{-j\beta R_r(m)} \tag{2-14}$$

Figure 2.39 exhibits the simulation results regarding 2D normalized reflected electric field amplitude at $z = 0$, while specific ACMA radiating elements are radiating. It can be seen that the distance between FSS superstrate layer and the ACMA radiating elements plane is a key design factor. For the intended configuration, the distance with value 2.5 mm (λ /4 at 30-GHz) is the right selection to redirect the reflected waves away from the location of ACMA radiating elements to limit interference and deterioration of the antenna radiation characteristics.

The simulation results regarding the scattering parameters and axial ratio of the designed MIMO arrays with and without using FSS couplings technique, while the radiating elements separation varies from 0.5λ to 0.7λ, are shown in Figure 2.40. It can be noted that the $S_{11} \leq -10\ dB$ bandwidth for all circumstances is almost alike, covering a frequency range from 28 to 33 GHz (16.4%). Accordingly, it is seen that the radiating elements separation and FSS superstrate layer do not have a significant impact on the input impedance characteristics. Contrarily, the axial ratio is given, when the radiating elements separation is varied, for the MIMO array with and without using FSS couplings technique. It is perceived that in the case of MIMO array without using FSS couplings technique, by changing radiating elements separation from

0.5λ to 0.7λ, the axial ratio has an insignificant variation without any frequency shift. But, the axial ratio is deteriorated, in terms of magnitude and frequency shift, when FSS superstrate layer is applied. It is concluded that the distance between FSS superstrate layer and MIMO array varies the phase of two electric field segments.

Thus, to meet the demand of 3 dB axial ratio bandwidth in the case of MIMO array with using FSS couplings technique, the radiating elements separation 0.5λ yields a satisfactory response as compared with 0.6λ and 0.7λ radiating elements separation as given in Figure 2.40. It is worthy to consider that mutual coupling is better when the radiating elements separation is supposed to be 0.7λ in contrary to the other values of 0.5λ and 0.6λ. Nevertheless, our priority is to meet the demand of 3 dB axial ratio bandwidth and then reducing the mutual coupling.

The simulation results, regarding the electric field distribution for both cases MIMO arrays with and without using FSS couplings technique at 31.2 GHz carried out using Ansys HFSS, is presented in Figure 2.41. Considering that the aim of selecting 31.2 GHz is that the most desirable condition of the axial ratio is achieved. It can be observed that in the case of MIMO array with using FSS couplings technique, the spacial field propagation toward the neighboring radiating elements in the xz- and yz-planes is more limited compared to the one without using FSS couplings technique.

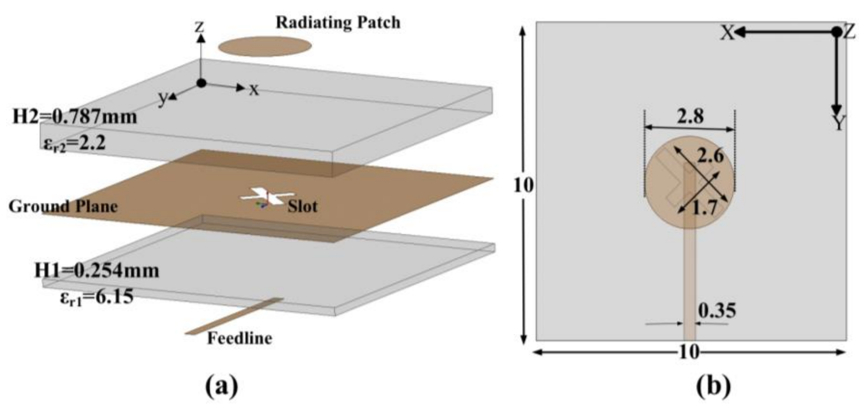

Figure 2.33: Geometry of single CP-ACMA (a) side view and (b) top view (M. Akbari et al. [50], @2017 IEEE).

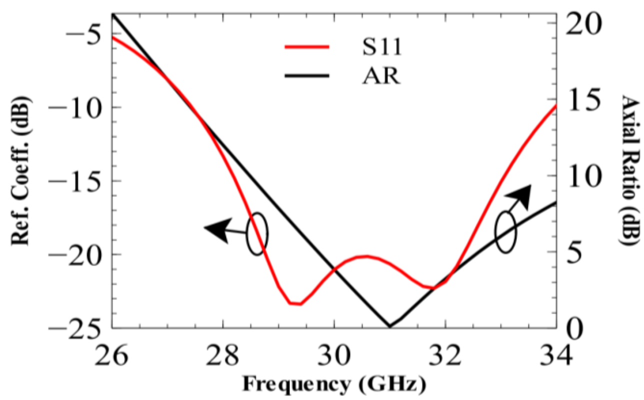

Figure 2.34: Reflection coefficient and axial ratio of a single element CP patch (M. Akbari et al. [50], @2017 IEEE).

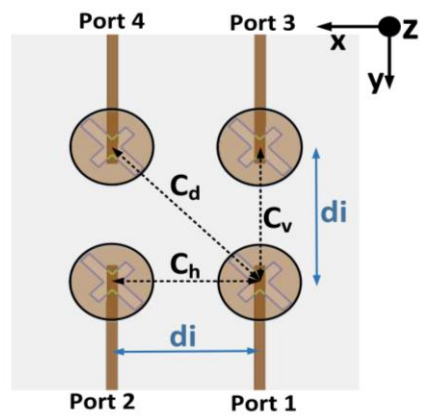

Figure 2.35: Schematic diagram of the MIMO-ACMAs with coupling coefficients (C_d, C_h, and C_v) and the inter-ACMA element spacing (di) (M. Akbari et al. [50], @2017 IEEE).

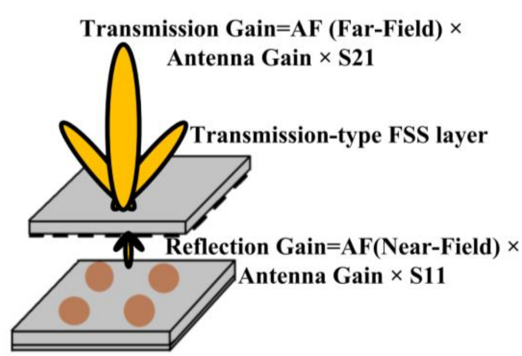

Figure 2.36: Schematic of the transmission-type FSS layer with transmission and reflection gains (M. Akbari et al. [50], @2017 IEEE).

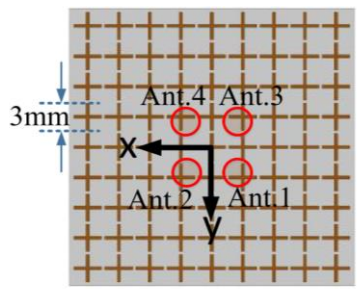

Figure 2.37: The formation schematic of FSS superstrate including 9×9 FSS elements, and the precise position of a 2×2 MIMO-ACMA below the superstrate in the x-y plane (M. Akbari et al. [50], @2017 IEEE).

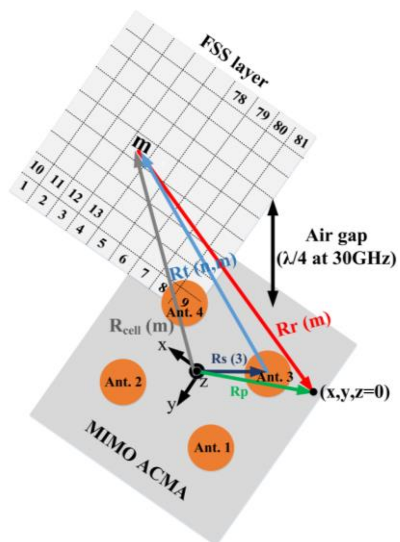

Figure 2.38: The sketch of a uniform rectangular array of 81 FSS elements along the x and y-axis above 2×2 MIMO-ACMA (M. Akbari et al. [50], @2017 IEEE).

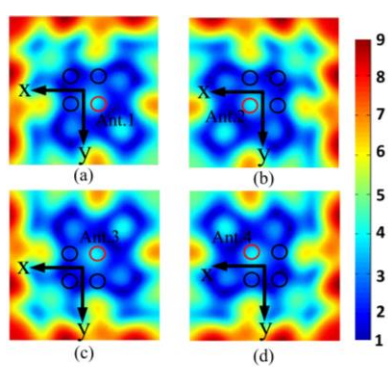

Figure 2.39: The 2-D reflected power density from the FSS elements on the antenna plane associated with diferent antennas' excitations. (a) Ant. 1, (b) Ant. 2, (c) Ant. 3, and (d) Ant. 4 (M. Akbari et al. [50], @2017 IEEE).

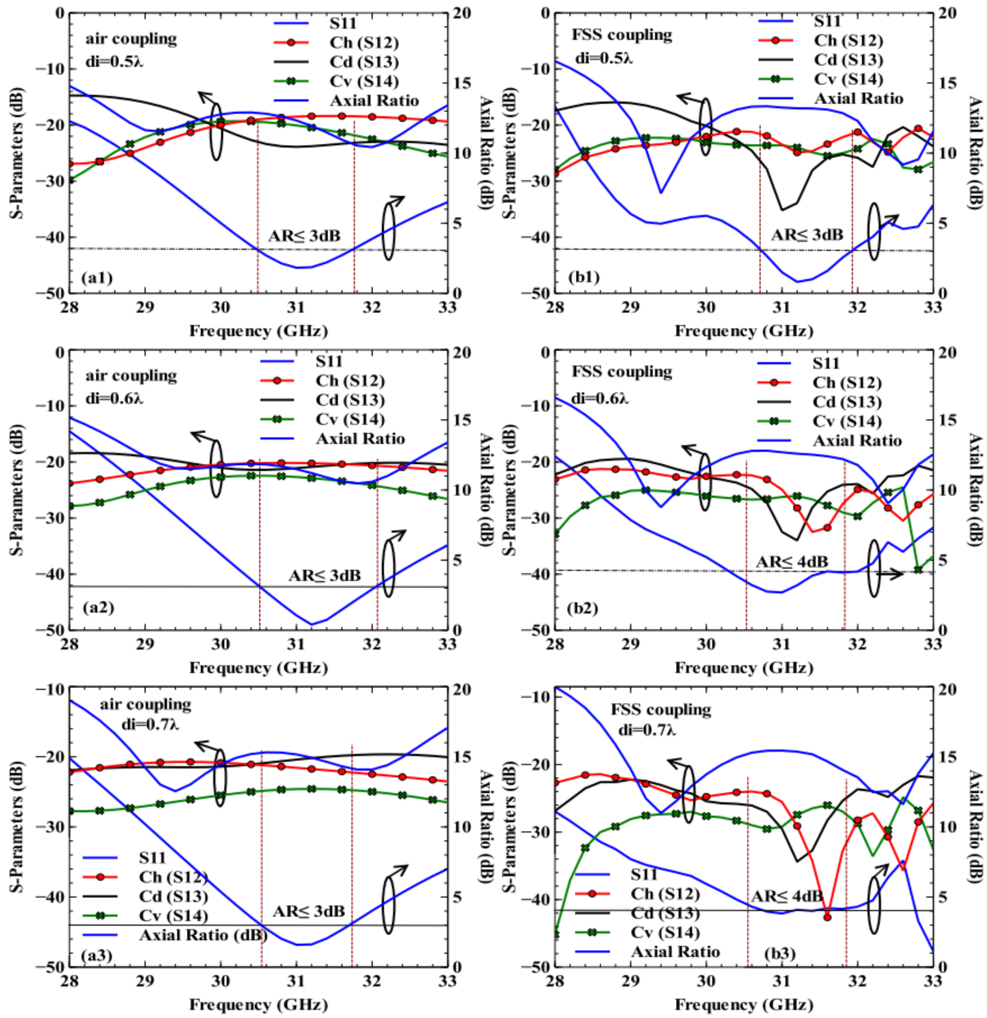

Figure 2.40: Simulated results of axial ratio and S-parameters for different cases of (a) Air coupling and (b) FSS coupling; including (a1) and (b1) ($di = 0.5\lambda$), (a2) and (b2) ($di = 0.6\lambda$), and (c1) and (c2) ($di = 0.7\lambda$) (M. Akbari et al. [50], @2017 IEEE).

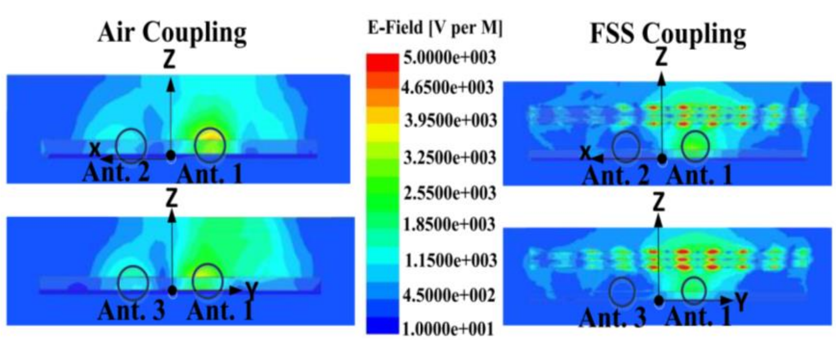

Figure 2.41: Simulated E-Field distribution on the 2×2 MIMO-ACMA for both cases of the air and FSS couplings in the xz- and yz- planes at 31.2 GHz (M. Akbari et al. [50], @2017 IEEE).

Ultimately, the intended 2×2 ACMA MIMO array with the radiating element separation of $\lambda/2$ for both cases of MIMO arrays with and without using FSS couplings technique are fabricated and measured. The images of the fabricated prototypes are displayed in Figure 2.42. Moreover, the S-parameters with and without using FSS couplings technique are measured. The mutual coupling among the radiating element of the 2×2 MIMO array is measured with a two-port Agilent N5227A PNA Network Analyzer (10 MHz-67 GHz). For all setups, the mutual coupling values are calculated by normalizing the experimental results with the total radiated power [63]. Utilizing this method equation and the measured s-parameters, the mutual couplings "C_v", "C_h", and "C_d" can be calculated.

The photo of the fabricated prototype plus the test setup is shown in Figure 2.43. It has to be considered that the simulation results regarding the mutual couplings S_{21}, S_{31}, and S_{41}, are extracted directly using Ansys HFSS. Figure 2.44 presents the simulation and experiment results for scattering parameters and axial ratio concerning the designed MIMO array. The measurements confirm a satisfactory agreement with simulations.

The left-hand CP gain in the xz- and yz-planes are carried out using Ansys HFSS. Moreover, the radiation patterns are measured in both cases of the MIMO arrays with and without using FSS couplings technique at frequency 31-GHz. As displayed in Figure 2.45(a) and (b), when the ACMA array without using FSS couplings technique is radiating at 31-GHz, the radiation pattern is tilted due to the spatially mutual coupling.

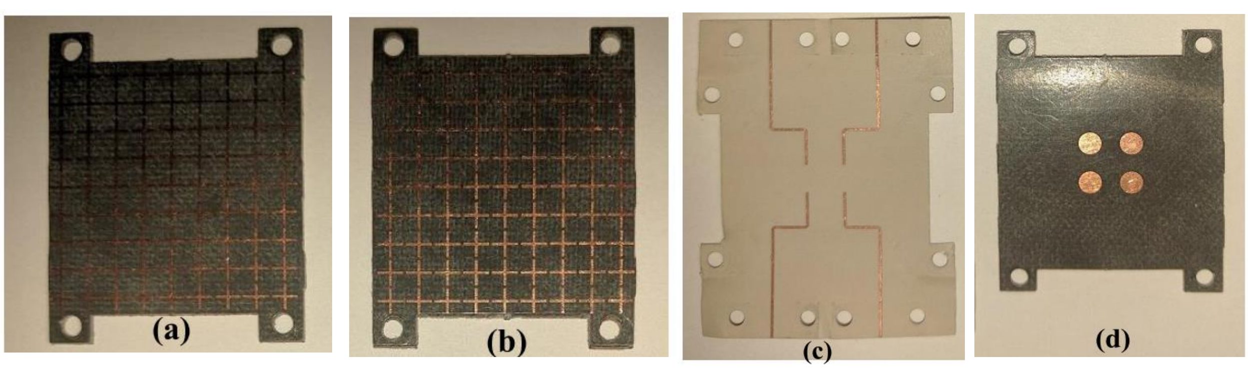

Figure 2.42: Photos of the fabricated 2×2 MIMO-ACMA: (a) and (b) FSS layers, (c) feed lines, and (d) patches (M. Akbari et al. [50], @2017 IEEE).

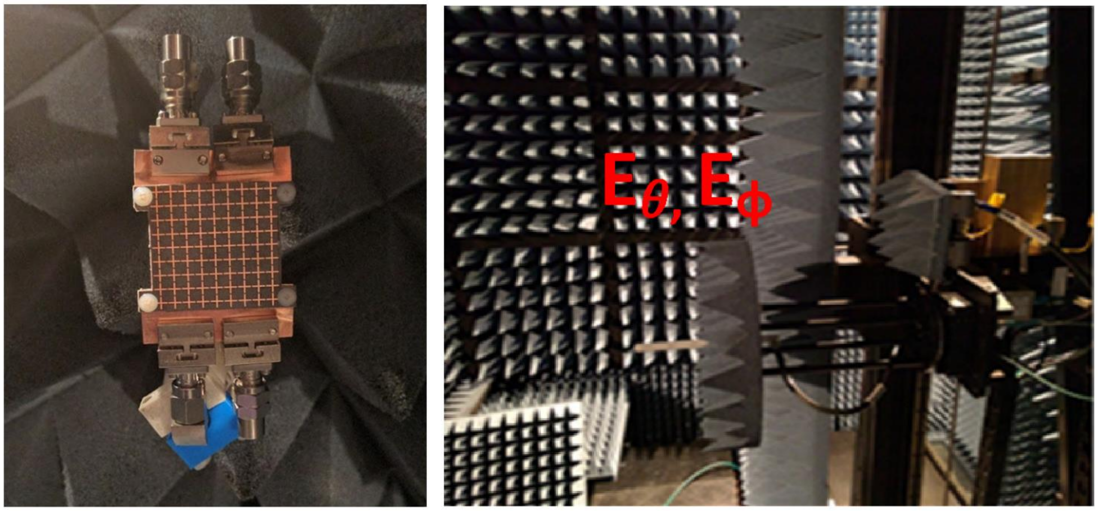

Figure 2.43: The photo of the fabricated 2×2 CP-MIMO antennas under test as transmitter and the open ended waveguide (NSI RF WR28) as receiver in the far-field anechoic chamber (M. Akbari et al. [50], @2017 IEEE).

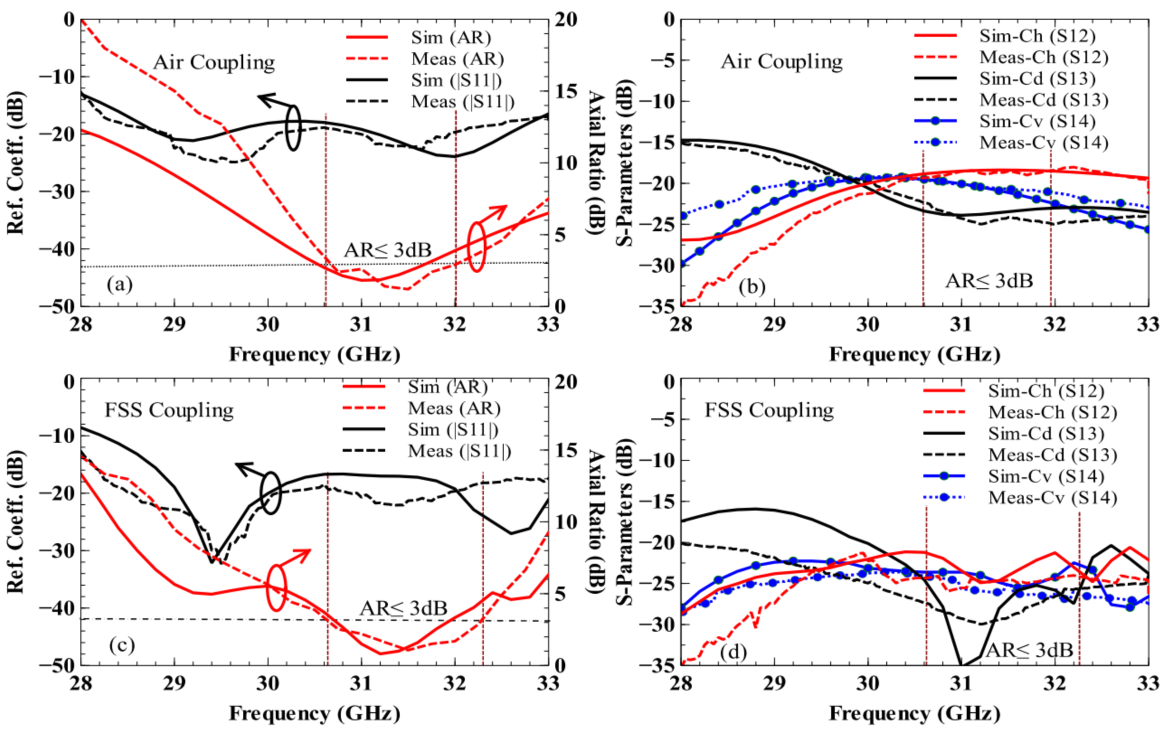

Figure 2.44: Measured and simulated results of axial ratio, reflection coefficient for different cases of (a) air and (c) FSS couplings, along with measured and simulated results of coupling for different cases of (b) air and (d) FSS couplings (M. Akbari et al. [50], @2017 IEEE).

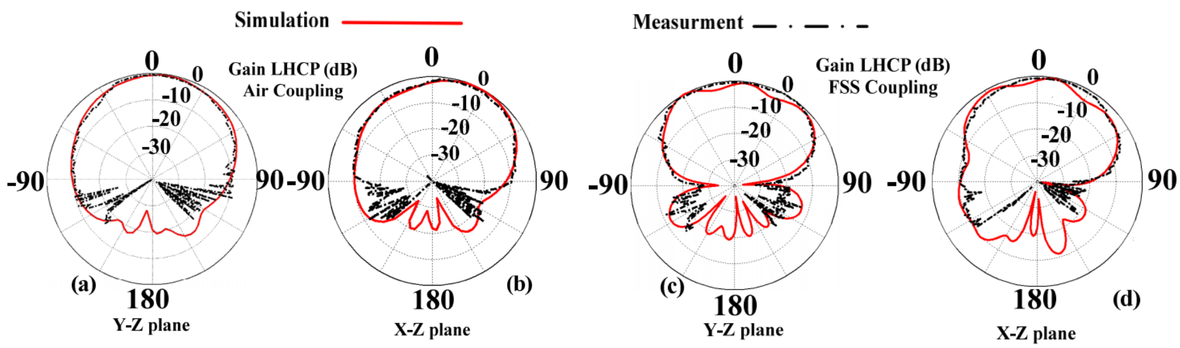

Figure 2.45: Measured and simulated LHCP gain for both cases of (a), (b) air coupling and (c), (d) FSS coupling in the yz- and xz- planes at frequency 31 GHz (M. Akbari et al. [50], @2017 IEEE).

2.5 Conclusion

The performance of a MIMO system is mainly dependent on owning independent multiple channels. Dependent multiple channels will degrade the performance of a MIMO system, for instance, its capacity. The channel correlation is usually due to the spatial-correlation and antenna mutual coupling. As it is been discussed, the best practical scenario in mmWave is possessing two half-space radiating antennas with the minimum inter-element distance, and the same radiation characteristic as much as possible. In this chapter, it was our priority to design a MIMO antenna with a low correlation coefficient. To reach this objective, the two radiating elements in the intended MIMO antenna should have the same radiating characteristic, otherwise, even though they have a low amount of mutual coupling, the correlation is high. In this chapter, two distinguished approaches have been introduced to reduce mutual coupling due to the spatial fields.

In the first approach, an innovative technique for decreasing the mutual coupling among mmWave dielectric resonator antennas (DRAs) using a new metamaterial polarization-rotator (MPR) wall is studied and performed. The mutual coupling is decreased by installing MPR walls among DRAs that are located in the H-plane. Utilizing this MPR walls, the TE modes of the antennas become orthogonal, which decreases the mutual coupling between the antennas. The radiation pattern is almost unchanged compared to the antenna without an MPR wall. Measured results have shown that the mutual coupling between antenna elements has been decreased on average by more than 16 dB in mmWave frequency range from 57 to 64 GHz.

In the second approach, a novel method to reduce the coupling due to spatial electromagnetic interaction among two circularly-polarised radiating elements utilizing an FSS superstrate layer is proposed. The experimental results indicate when the FSS superstrate layers are employed, an average coupling suppression of 6 to 7 dB has been achieved at the working frequency band at 31 GHz while the radiation pattern is almost unchanged compared to the antenna without the FSS superstrate layers.

Chapter 3 mmWave High Gain Antennas

This chapter contains material extracted from the following publications:

[64] M. Farahani, J. Pourahmadazar, T. Denidni and M. Nedil, "Millimeter-Wave High-Gain Ridge Gap Beam Steerable Antenna for 5G wireless Networks," *18th International Symposium on Antenna Technology and Applied Electromagnetics (ANTEM)*, Waterloo, ON, 2018, pp. 1-2.

[59] M. Akbari, S. Gupta, M. Farahani, A. R. Sebak and T. A. Denidni, "Gain Enhancement of Circularly Polarized Dielectric Resonator Antenna Based on FSS Superstrate for MMW Applications," *IEEE Trans. on Antennas and Propag.*, vol. 64, no. 12, pp. 5542-5546, Dec. 2016.

3.1 Introduction

There are severe obstacles in developing the mmWave wireless networks. In wireless communication, the throughput of the communication link is one of the most important indicators to estimate the performance. The throughput, however, highly depends on the characteristic of the propagation channel, like path loss, distance between devices, the noise, etc. Through the formula of Friis free space path loss model, the path loss for 60-GHz has a nearly 28 dB loss more versus the 5 GHz band. Meanwhile, additional loss (7-15.5 dB/km power loss) needs to be considered in the received signal at 60-GHz carrier frequencies because of atmospheric absorption [65]. Besides these, the rainfall rate also affects the performance of the system. Around 8-18 dB/km additional atmospheric attenuation while the rainfall rate is 50 mm per hour [65]. In addition to the high attenuation, 60-GHz mmWave radio also experiences the weak capability of penetration [66]. Furthermore, although the physical size of antennas is so small, design of the antenna feeding networks become complex and a challenging matter for designers due to the high amount of losses at mmWave bands.

To overcome blockage, multiple approaches from the physical layer to the network layer have been proposed. However, every approach has its advantages and shortcomings, and these approaches should be combined in an intelligent way to achieve robust and efficient network performance.

Unlike conventional perception that mmWave bands beams behave in a pseudo-optical manner, highly directional beams suffer less penetration loss across typical obstacles (except human body) in an office environment, and coverage can be achieved beyond a single room [1].

In this chapter, different techniques are investigated for increasing the gain of the antennas. There are a big challenge regarding the development of systems at mmWave bands, due to the high amount of propagation loss at these bands which required designing high-sensitivity receivers to overcome that drawback. In antenna regards, it is needed to develop directive high-gain antennas.

3.2 Gain Enhancement Using FSS Superstrate

The next generation of mobile network (5G) demands high-gain and broadband antennas working in the mmWave frequency-band. An effective technique to increase the gain of antennas is employing a Fabry Perot Cavity (FPC) method, that employs an FSS superstrate layer or partially reflective surface (PRS) above an antenna with a complete ground plane at the distance of nearly a half wavelength. By exciting the FPC by a source radiating element, a significant increase in the antenna gain can be obtained [67]-[70]. This technique has been proposed and investigated utilizing different kinds of PRS superstrate layers formed by the periodical array of patches or slots [71]-[73], in one layer [74] or multiple layers [75]-[76]. An important drawback of these techniques is their gain flatness behavior that will be improved in our designed structure based on image theory and effective medium method. Moreover, the minimum size of the PRS superstrate layer is acheived by presenting a model of the diffraction and transmission rays.

3.2.1 Dielectric Resonator Antennas

The topology of the proposed DRA source antenna along with the FSS superstrate layer is represented in Figure 3.1. The source DRA antenna is constructed of two stacked substrates. The first substrate is Rogers 3006 with a thickness of 0.254 mm and $\varepsilon_r = 6.15$. The 50-ohm feeding line is implemented on the bottom of this substrate. The second substrate is Rogers 5880 with a thickness of 0.787 and $\varepsilon_r = 2.2$. An x-shaped aperture is formed on the ground plane on the upper side of the lower substrate. The high-efficiency low-loss square DRA is excited by the x-shaped aperture. The physical size of the DRA antenna and x-shaped aperture are presented in Figure 3.1(b). The picture of the fabricated prototype is displayed in Figure 3.2.

The dielectric waveguide model is utilized to estimate the resonant frequency of the DRA antenna. The resonant frequency for square DRA can be estimated as following [77]-[78]:

$$f_r = \frac{c}{2\pi\sqrt{\varepsilon_r}}\sqrt{(\frac{m\pi}{a})^2 + k_y^2 + (\frac{nl\pi}{2d})^2} \qquad (3-1)$$

$$k_y \tan(\frac{k_y b}{2}) = \sqrt{(\varepsilon_r - 1)k_o^2 + k_y^2} \quad (n = 1) \qquad (3-2)$$

$$(\frac{m\pi}{a})^2 + k_y^2 + (\frac{nl\pi}{2d})^2 = \varepsilon_r k_o^2 \qquad (3-3)$$

where c is the velocity of light in free space, k_o and k_y are the propagation constants in free space and inside the dielectric resonator in the y-direction, respectively. Parameters a, b and d are the dimentions of the DRA antenna. Using the dielectric waveguide model the resonant frequency of 30-GHz is achieved for the dimentions of $a = 3.7\,mm$, $b = 3.7\,mm$, and $d = 0.64\,mm$ by selecting Rogers 6010 substrate with dielectric constant 10.2.

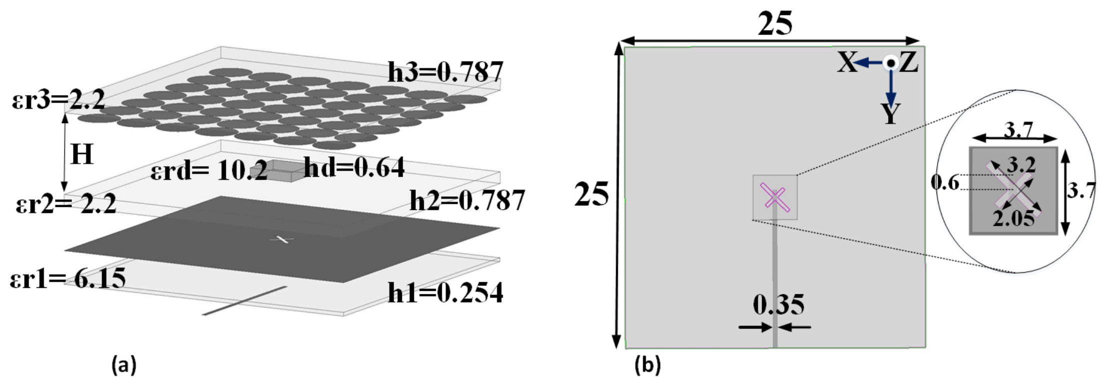

Figure 3.1: The geometry of the FPC antenna with radiating DR and an FSS superstrate layer (a) 3D view and (b) top view (measurements are in millimetre) (M. Akbari et al. [59], @2016 IEEE).

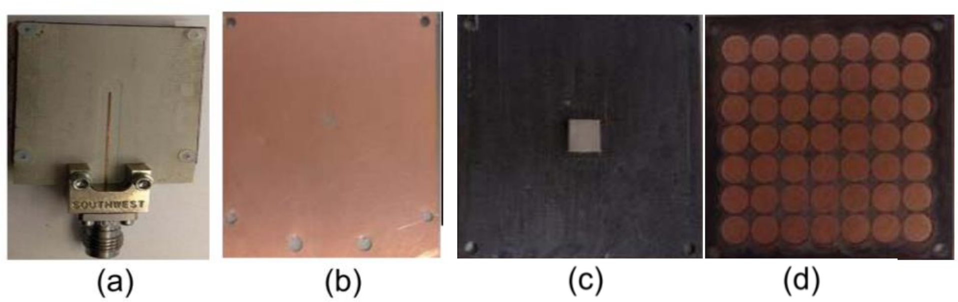

Figure 3.2: Photos of the fabricated antenna (a) the bottom surface of first layer (feed line), (b) top surface of the first layer (ground plane), (c) top surface of the second layer (DR), and (d) the bottom surface of the third layer (FSS elements) (M. Akbari et al. [59], @2016 IEEE).

3.2.2 Design of the Superstrate Layer

The proposed FSS superstrate layer consists of a periodical arrangement of 7×7 cells on the lower side of the superstrate. The superstrate is located at the distance of H above the DR antenna. Principally, the different resonance frequencies for wideband applications parameters are defined by the key parameters such as the DR antenna characteristics (dielectric constant, shape, and dimension), shape and dimensions of the coupling aperture, the separation distance of the superstrate from the DRA antenna, and the FSS unit cells phase and amplitude response.

In this work, the simulations are carried out utilizing Ansys HFSS. The simulated scattering parameters, maximum gain vs frequency, the axial ratio at broadside vs frequency and radiation efficiency of the antenna without the FSS superstrate layer are represented in Figure 3.3. The impedance bandwidth ($S_{11} < -10\ dB$) of the proposed design is from 25 to 31.4 GHz (22.7%); however, the CP-bandwidth ($AR < 3\ dB$ at broadside direction) is from 26.9 to 34.8 GHz (25.6%) with a maximum gain of 6.4 dB at 30-GHz. As can be observed in Figure 3.3, the radiation efficiency of the DRA antenna without the FSS superstrate layer is more than 90% in the operating frequency-band; however, the maximum gain is not suitable to respond to the demands in mmWave applications at 30-GHz.

The directivity is increased using the FSS superstrate layer located above a source DRA antenna. Meanwhile, it is worth to mention that employing more FSS superstrate layers, multiple resonant frequencies can be obtained; however, the number of FSS superstrate layers is restricted by the antenna size limitation. The FSS unit cell dimensions are depicted in Figure 3.4(a). The multiple reflected rays within the cavity and the transmitted rays through the FSS superstrate layer is illustrated in Figure 3.4(b). By controlling the FSS unit cell behaivior and selecting the proper separation distance between FSS superstrate layer and source DRA antenna, the transmitted rays, first, second, and third-order reflected waves can be tuned in a way that they become precisely in phase in order to increase the gain accordingly.

Figure 3.5 represents a circuit model for the proposed DRA antenna employing FSS superstrate layer. It includes two series transmission lines with lengths of H and h2, and characteristic impedances of Z_o and Z_d, respectivelly, and signal generator and load impedances of Z_g and Z_L, respectively. The input impedance can be calculated as follows [79]:

$$Z_{in} = Z_o \frac{Z_L + jZ_o tan\beta h_2}{Z_o + jZ_L tan\beta h_2} \qquad (3-4)$$

Z_{in} is the observed input impedance from input of the transmission line with the length $h_2$connected to Z_L . Considering that a ground plate is used as a short load (Figure 3.5), the (3-4) can be simplified as follows

$$Z_{L1} = Z_{in1} = jZ_d tan\beta h_2 \qquad (3-5)$$

where $Z_d = (Z_0/\sqrt{\varepsilon_r})$ and $\beta = \left(\frac{2\pi\sqrt{\varepsilon_r}}{\lambda_0}\right)$. As presented in Figure 3.5, the reflection coefficient at the input of the transmission line with the length H can be expressed as

$$\Gamma = \frac{jZ_d tan\beta h_2 - Z_o}{jZ_d tan\beta h_2 + Z_o} \qquad (3-6)$$

From (3-6) the phase of reflection coefficient can be estimated as below

$$\varphi_\Gamma(ground, sub) = \pi - 2\tan^{-1}\left(\frac{Z_d}{Z_o}\tan(\beta h_2)\right) \qquad (3-7)$$

Hence

$$\varphi_\Gamma(ground, sub) + \varphi_{FSS} - \frac{4\pi H}{\lambda} = 2N\pi \qquad (3-8)$$

where, “H” is the seperation distance between the DRA antenna and FSS superstrate layer, and “N” is an integer number. Utilizing (3-8), it is inferred that the overal bandwidth can be increased if the FSS reflection phase reduces accordinglly. The directivity enhancement compared to the source antenna can be expressed by the amplitude of the reflection coefficient on the broadside direction as [80]:

$$D_r = \frac{1 + |\Gamma_{FSS}|}{1 - |\Gamma_{FSS}|} \qquad (3-9)$$

It can be concluded from (3-9) that the overal directivity of system enhanced by increasing the amplitude of the reflection coefficient. Therefore, to design the optimum FSS superstrate layer, FSS unit cells need to satisfy conditions of proper reflection phase response and high reflection amplitude over the operating frequency-band [81]. The unit cell is simulated using Ansys HFSS. The Floquet ports under specific boundary conditions are employed to simulate the infinite number of unit cells. The FSS superstrate layer is implimented on Rogers 5880 with $\varepsilon_r = 2.2$ and thickness of 0.787 mm. The unit cell displayed in Figure 3.4(a) is a circular patch with a radius of 1.7 mm and periodicity of 3.5×3.5 mm^2. The phase response of the reflection and transmission coefficients, as well as the reflection amplitude of the unit cell, are represented in Figure 3.6. The amplitude of the reflection coeficient is more than 0.9 in the frequency ranges from 20 to 40 GHz, and the phase of the reflection coeficient is reducing linearly with frequency, resulting in high directivity in a broad frequency-band.

One of the difficulties in this technique is to define the dimensions of the superstrate layer, or in other words, the number of used FSS units. To answer this difficulty, we use and develop a technique to estimate optimum dimensions of the superstrate layer [82], as displayed in Figure 3.7.

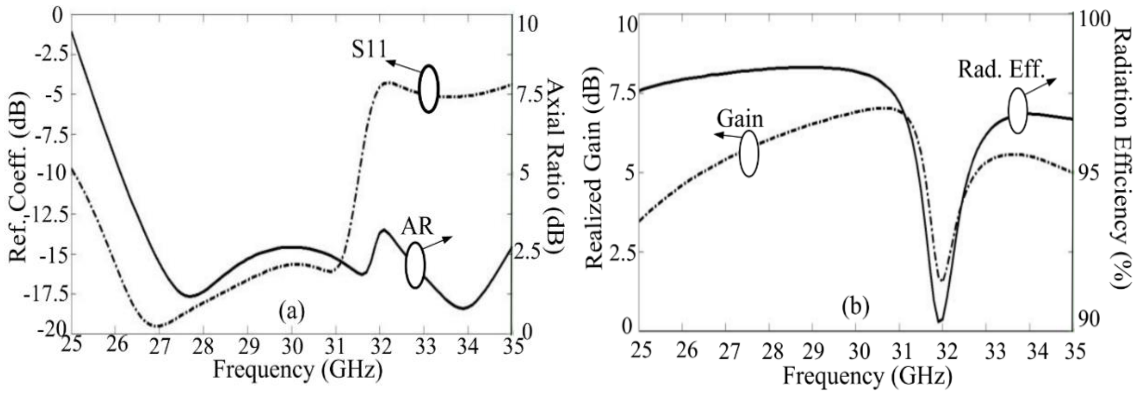

Figure 3.3: The simulated results of (a) reflection coefficient and axial ratio, and (b) total gain and radiation efficiency of the DRA without the FSS layer (M. Akbari et al. [59], @2016 IEEE).

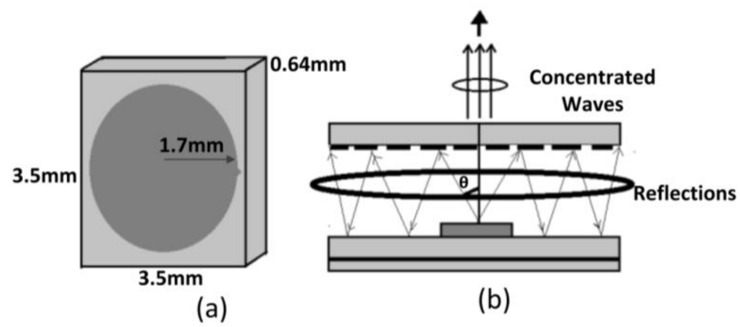

Figure 3.4: (a) The dimensions of the FSS unit cell and (b) illustration of multiple reflections and leaky waves (M. Akbari et al. [59], @2016 IEEE).

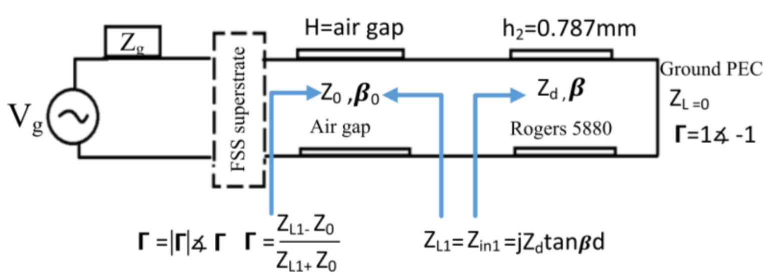

Figure 3.5: Transmission line circuit model for mismatched load and generator (M. Akbari et al. [59], @2016 IEEE).

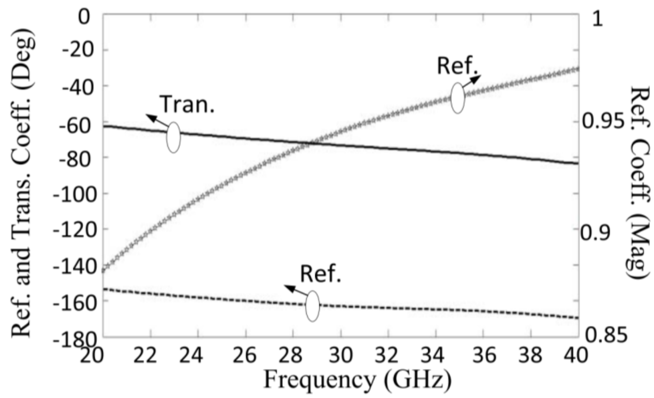

Figure 3.6: The phase and magnitude of reflection and transmission coefficients of the FSS unit cell (M. Akbari et al. [59], @2016 IEEE).

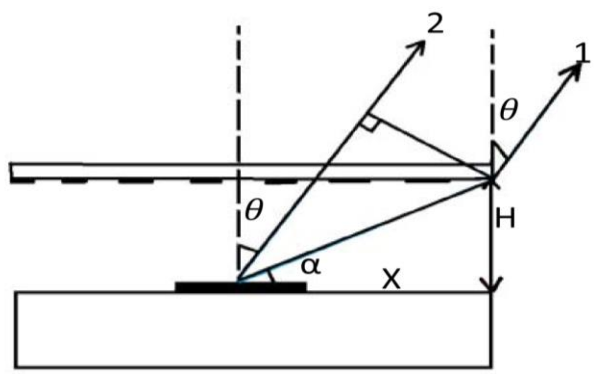

Figure 3.7: Model of the diffraction and transmission rays [82] (M. Akbari et al. [59], @2016 IEEE).

The technique shows diffraction and transmitted rays from the FSS superstrate layer that lead to the same phase of the transmitted and diffracted rays ending in an additional directivity enrichment. In Figure 3.7, rays 1 and 2 are the edge diffracted and transmitted rays and their corresponding phases are expressed as following [82]

$$(phase)_1 = e^{-j(\frac{2\pi H}{\lambda sin\alpha})} \qquad (3-10)$$

$$(phase)_2 = e^{-j(\left(\frac{2\pi H cos\left(\frac{\pi}{2}-\alpha-\theta\right)}{\lambda sin\alpha}\right)+\varphi_{tr})} \qquad (3-11)$$

where α and θ are the propagation direction angles of the ray 1 and rays 2, respectively. Moreover, φ_{tr} is the transmission coefficient phase of the unit cell. Considering (3-10) and (3-11), the phase of diffracted and transmitted rays are similar if the following equation satisfied

$$\frac{2nH}{\lambda sin\alpha} = \frac{2\pi H cos(\frac{\pi}{2} - \alpha - \theta)}{\lambda sin\alpha} + \varphi_{tr} \qquad (3-12)$$

where "θ" is considered to be extremely small due to that the antenna radiate at broadside, therefore, (3-12) can be simplified as

$$\frac{H}{\lambda}\left(\frac{1}{sin\alpha} - 1\right) - \frac{\varphi_{tr}}{2\pi} = N \qquad (3-13)$$

To achieve the optimum dimensions of the FSS superstrate layer, or in other words, the number of unit cells, (3-4) to (3-8) are utilized and result in $\varphi(ground, sub)$ is 128^o and seperation distance of ($H = 4.5$ mm). Parametric studies carried out using Ansys HFSS, as represented in Figure 3.8, are applied to reach the maximum gain while additionally improving the CP bandwidth over the operating frequency range. Different parameters in (3-4) through (3-13) are reviewed in Table 3.1.

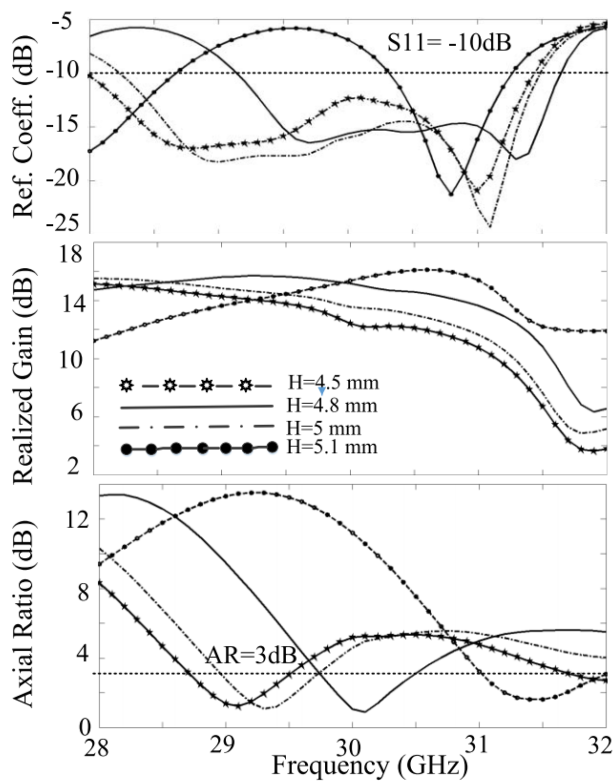

Figure 3.8: The simulated results of the reflection coefficient, total gain, and axial ratio for different values of the air gap heigh *H* (M. Akbari et al. [59], @2016 IEEE).

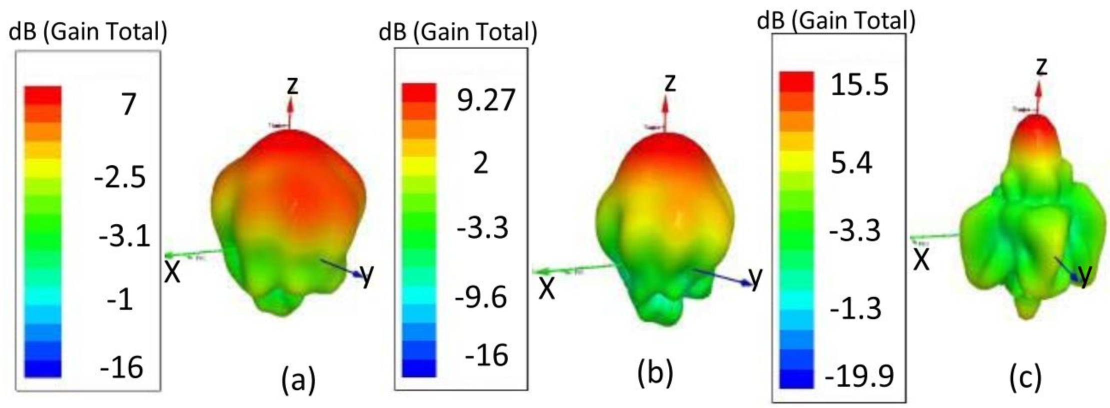

Figure 3.9: 3D radiation patterns of the aperture coupled DRA at 30 GHz for three cases: (a) the basic DRA, (b) the DRA with the only superstrate, and (c) DRA with the FSS superstrate (M. Akbari et al. [59], @2016 IEEE).

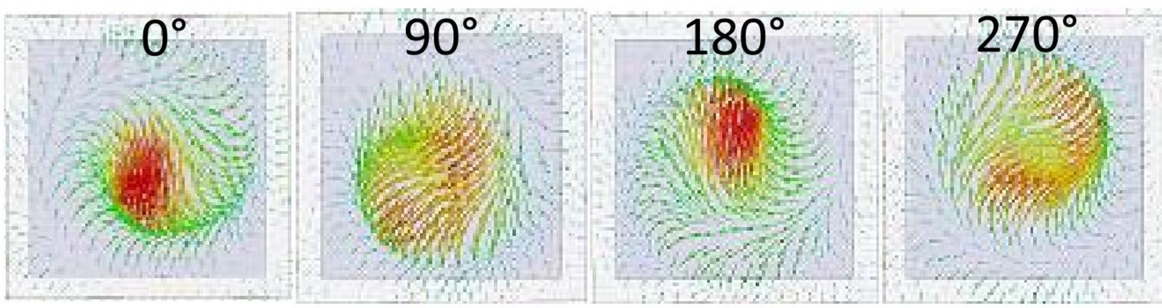

Figure 3.10: RHCP E-field variations at different phases (a) 0^o, (b) 90^o, (c) 180^o, and (d) 270^o at the centre frequency 30 GHz (M. Akbari et al. [59], @2016 IEEE).

Table 3.1: Parameter values of equations of (3-4) to (3-13).

Parameter	**values**	**Parameter**	**values**	**Parameter**	***values***
$f_f\ (GHz)$	30	β	0.9	$\varphi_{(FSS)}$ (deg)	-163
$Z_{0\ (ohm)}$	377	$d_{(mm)}$	0.787	φ_{tr} (deg)	-73
ε_r	2.2	$Z_{d\ (ohm)}$	254.7	$\alpha_{(deg)}$	22
N	1	$\varphi_\Gamma(ground, sub)$	128	$X_{(mm)}$	12

The separation distance of "H" is 4.8 mm which is slightly bigger than the expected distance of 4.5 mm calculated from the theoretical analysis. From the theory, the predicted dimensions of the FSS superstrate layer are 24 mm×24 mm. Because the dimensions of the unit cell are 3.5 mm×3.5 mm, the dimensions of the array of 7×7 unit cells are 25 mm×25 mm. Figure 3.9 displays the radiation patterns of the proposed DR antenna with and without the FSS superstrate layer at 30 GHz. It can be remarked that the simulated gain of DR antenna without the FSS superstrate layer, DR antenna with the conventional dielectric superstrate without unit cells, and the DR antenna with the FSS superstrate layer are 7 dB, 9.27 dB, and 15.5 dB, respectively. The E-field at the distance of a wavelength above the antenna for different phases are displayed in Figure 3.10.

3.2.3 Experimental Results

As it is shown in Figure 3.10, the E-field rotates in a clockwise direction, meaning it is a right-hand circularly-polarized wave. The intended DR antenna with the FSS superstrate layer is fabricated and measured. The experimental results of the S-parameter (S11) for the antennas is obtained using an Agilent N5227A PNA Network Analyzer (10 MHz-67 GHz). A linearly-polarized probe is utilized to measure the radiated field in two orthogonal directions to estimate the measured radiation pattern. The left and right-hand pattern and the axial ratio of the proposed antenna are then extracted from the measured electric fields [83]:

$$\overrightarrow{E_\theta} = |E_\theta| \measuredangle E_\theta, \quad \overrightarrow{E_\varphi} = |E_\varphi| \measuredangle E_\varphi \tag{3-14}$$

$$\overrightarrow{E_{RH}} = \frac{1}{\sqrt{2}}\left(\overrightarrow{E_\theta} + j\overrightarrow{E_\varphi}\right), \quad \overrightarrow{E_{LH}} = \frac{1}{\sqrt{2}}\left(\overrightarrow{E_\theta} - j\overrightarrow{E_\varphi}\right) \tag{3-15}$$

$$AR(dB) = 10\log\left(\left|\frac{|\overrightarrow{E_{RH}}| + |\overrightarrow{E_{LH}}|}{|\overrightarrow{E_{RH}}| - |\overrightarrow{E_{LH}}|}\right|\right) \tag{3-16}$$

The measurement and simulation results including the gain, axial ratio, and scattering parameter are given in Figure 3.11. The simulation and measurement results are in good agreement. The proposed antenna has the impedance frequency range from 29 to 31.5 GHz (8.26%) with an 3-dB axial ratio frequency range from 29.7 to 30.6 GHz (2.97%), and a maximum gain of 15.5 dB at 30-GHz. Figure 3.12 shows the radiation pattern of the DR antenna with the FSS superstrate layer at 30-GHz on the xz- and yz-planes. The side lobes are lower than -13 dB.

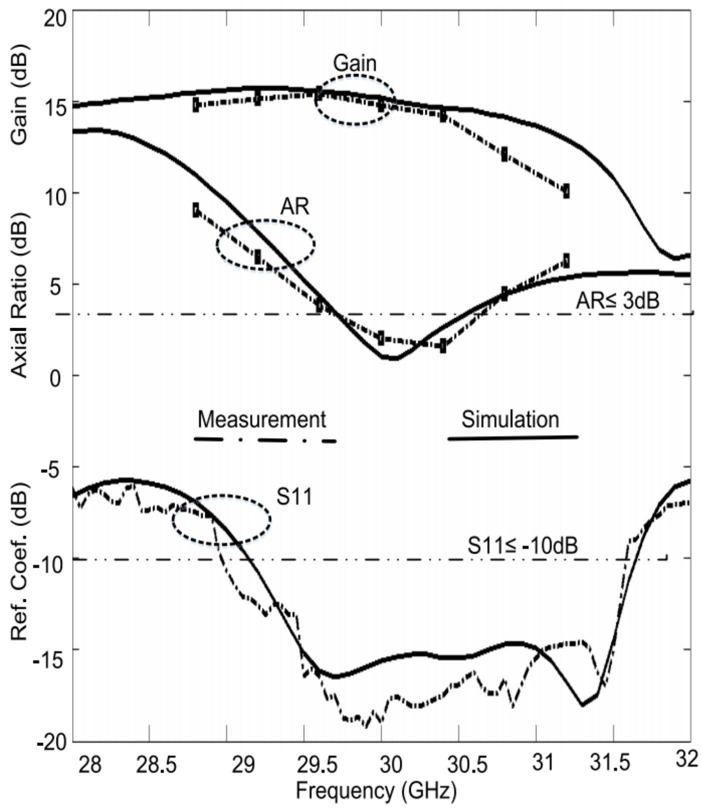

Figure 3.11: Measured and simulated curves of the total gain, axial ratio, and reflection coefficient of the proposed antenna (M. Akbari et al. [59], @2016 IEEE).

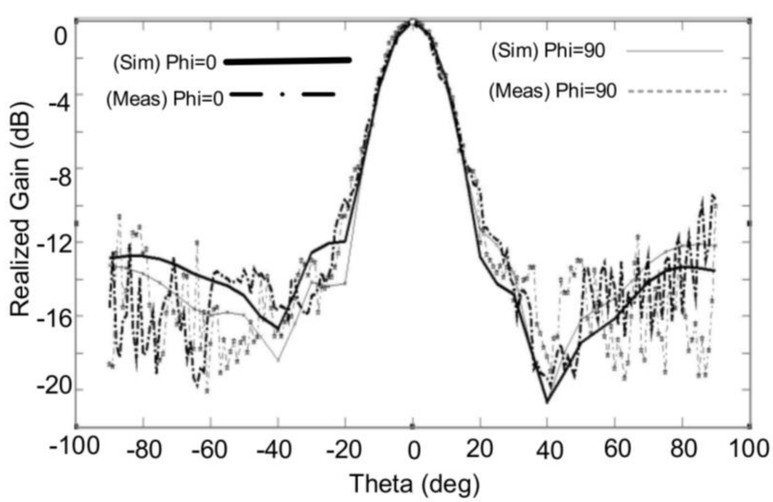

Figure 3.12: The normalized gain of the proposed antenna at 30 GHz on both planes phi=0 and phi=90 (M. Akbari et al. [59], @2016 IEEE).

3.3 Gain Enhancement Using Phase Gradient Metasurface (PGM)

The WiFi technology at mmWave alternatively known as Wireless Gigabit (WiGig) essentially employs the frequency range from 57 to 64 GHz to improve communication links with multiple users with greater data rate but allows a smaller coverage area due to a large value of propagation losses [34, 84, 47]. Furthermore, the 60-GHz electromagnetic waves experience severe penetration rates through walls and objects. In [84], it has been attested that pass-loss would increase 30 dB in line-of-sight (LOS) links by expanding the distance between the transmitter and receiver from 1 to 50 meter, but, in non-line-of-sight (NLOS) links, the signal-to-noise ratio (SNR) deteriorates up to 65 dB by expanding the distance from 1 to 50 meter. To resolve the problem of the high amount of propagation losses and reduce the NLOS SNR degeneration at the 60-GHz band, a system with the steerable pattern can be a suitable candidate to adjust communication links where the transmitter and receiver antennas are not in LOS.

In [85]-[88], the offered beam-steering methods obtain only two or four fixed beams associated with the excitation of different ports of the antennas. In fact, they are beam-tilted antennas that have a usage to employ in the base station to tilt the beam toward the neighboring base station antenna; but, they are not able to considerably improve the link performance in the communication links with mobile devices.

In this section, a high-gain beam steerable antenna using the PGM surface is presented. The PGM surface is placed on the top of a broadside nulled pattern patch antenna fed with microstrip ridge gap waveguide. By mechanically rotating the PGM surface around its center, the radiation pattern can be rotated accordingly.

3.3.1 PGM Surface and Microstrip Ridge Gap Patch Antenna

To direct the main beam of the source ridge gap patch antenna, the intended PGM surface is installed on top of the source ridge gap patch antenna as displayed in Figure 3.13.

The PGM surface is implemented on the host medium of the RO3003 with relative permittivity of 3 and thickness of 0.13 mm, shaped semicircle with a radius of 7.3 mm. Figure 3.13 shows the geometry of the PGM surface. The PGM surface includes a periodical arrangement of rectangular patch unit cells located on a PEC ground plane. The surface waves propagate along the radial axis with an $e^{(-\alpha_{PGM}-j\beta_{PGM})r}$ propagation factor. To investigate the surface wave propagation along the radial axis, the boundary condition between the PGM surface and air should be considered, then solve Maxwell's equations. As a result, the PGM surface reinforces the surface waves and forms extra phase center for the antenna with specific phase and magnitude, different from the source patch antenna. This phenomenon can deviate the antenna main beam from the broadside axis (z-axis). Meanwhile, by rotating the PGM surface mechanically around its axis, the radiation pattern will continuously sweep the space. Furthermore, since employing this method the radiating aperture of the antenna is extended, the gain of the antenna enhanced to about 15.2 dBi compared to the antenna without PGM surface that is about 7 dBi.

The proposed patch antenna is implemented on the RO3003 substrate with a thickness of 0.5 mm that is fed by a microstrip ridge gap waveguide. The rectangular slot in the middle of the patch will trigger the fundamental mode. In the microstrip ridge gap waveguide, electric and magnetic fields are caught between two metal walls on the upper and lower sides and two open sides. A band-gap along x- and y-directions is realized by implanting an arrangement like a bed of mushroom ridge along both open sides, and only the Q-TEM mode will propagate at this band-gap.

The intended beam steerable antenna is simulated using Ansys HFSS with and without the PGM surface. Simulation results confirm that the gain is enhanced by approximately 8 dBi compared to the antenna without the PGM surface. A maximum gain of 15.2 dBi with a half-power beamwidth of 20^o is obtained for the proposed antenna with the PGM surface. The antenna works in the frequency range from 57 to 64 GHz. The reflection coefficient and radiation pattern of the proposed beam steerable antenna for three different rotating angles of the PGM surface are displayed in Figure 3.14 and Figure 3.15, respectively.

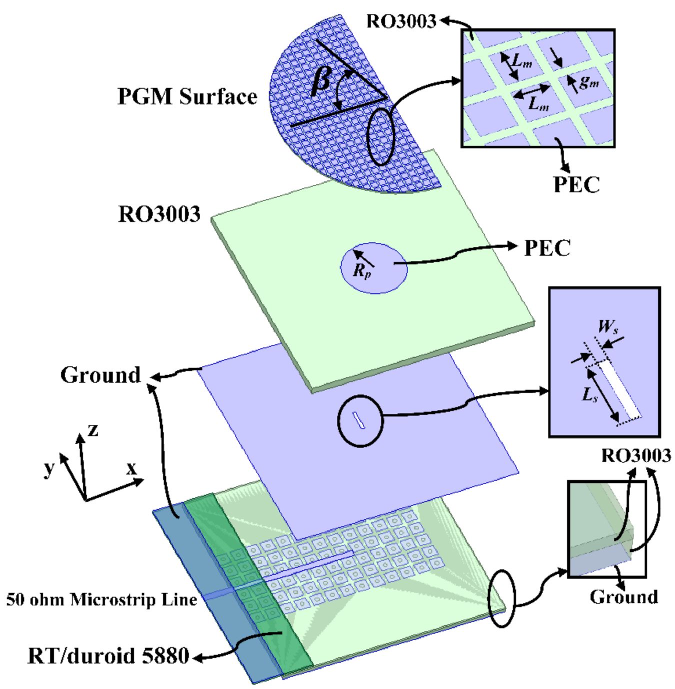

Figure 3.13: Assembly schematic of the proposed beam steerable antenna. The dimensions are $R_p = 2$, $L_s = 1.35$, $W_s = 0.2$, $L_m = 0.4$, $g_m = 0.1$, and all in millimeter (M. Farahani et al. [64], @2018 IEEE).

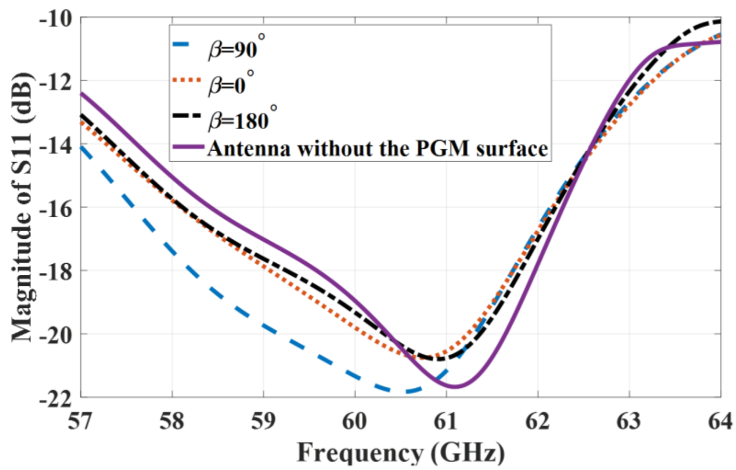

Figure 3.14: Scattering parameters of the beam steerable antenna for three different rotating angles of the PGM surface (M. Farahani et al. [64], @2018 IEEE).

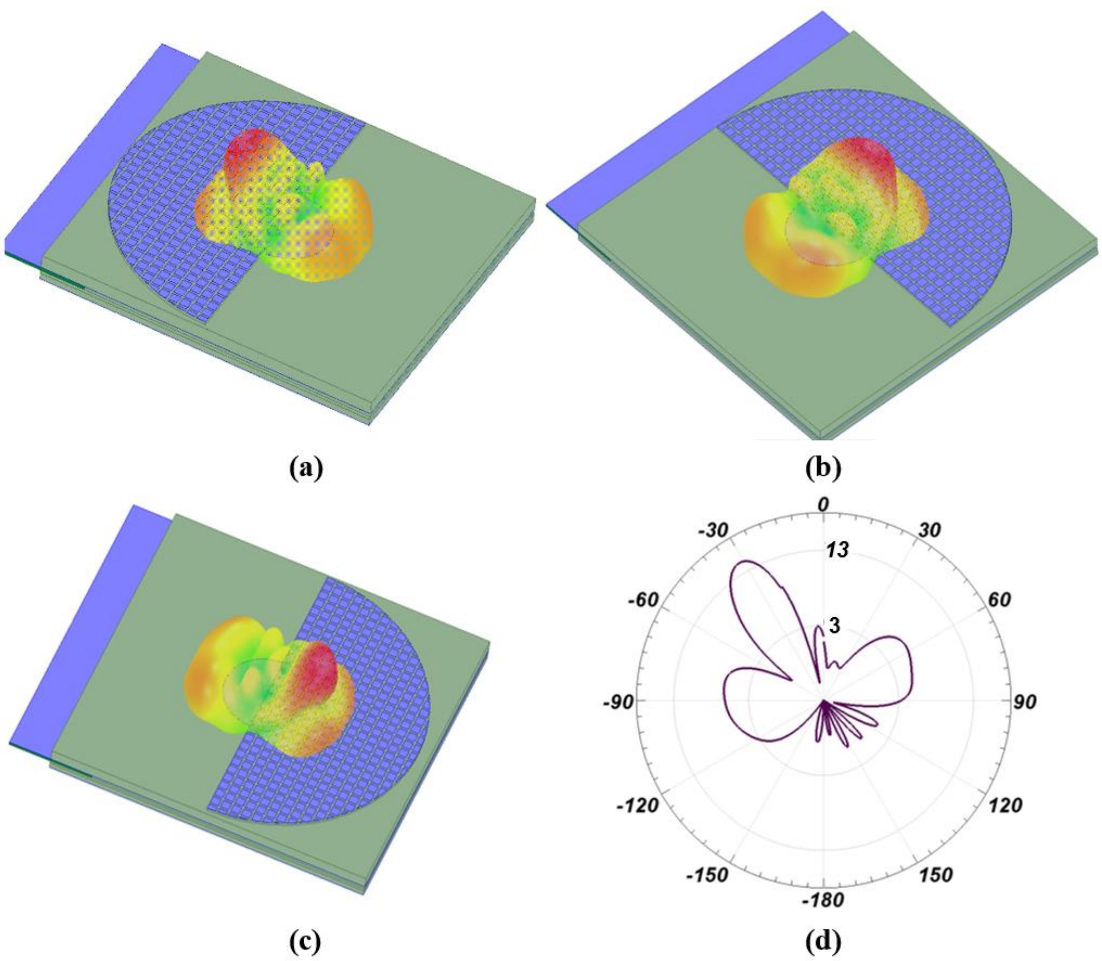

Figure 3.15: Radiation pattern of the beam steerable antenna for three different rotating angles of the PGM surface. (a) $\beta = 0^o$. (b) $\beta = 90^o$ (c) $\beta = 180^o$. (d) xz-plane radiation pattern at $\beta = 0^o$ (M. Farahani et al. [64], @2018 IEEE).

3.4 Conclusion

In this chapter, two different approaches have been introduced to increase the directivity of the antenna at mmWave bands to overcome the high amount of propagation losses at these bands.

In mmWave bands, the polarization mismatch loss can deteriorate the link performance of the system due to the propagation channel characteristics. The circularly-polarized antennas represent a good solution for resolving the polarization mismatch loss problem, reducing the fading issue, and providing flexibility in the direction between antennas at transmitter and receiver. As the first design in this chapter, a high-gain circularly-polarized antenna has been proposed for mmWave applications. The gain of the proposed antenna has been increased to about 15.5 dB using a superstrate layer. The experiment results have been shown that the intended antenna has the impedance and axial-ratio bandwidths of 8.26% and 2.97%, respectively. Using this approach the antenna gain is increased by about 8.5 dBi compared to the antenna without the superstrate layer. It is good to know that we need to make an 4×4 array from the base antenna to reach to this gain using conventional arrays, which needs a huge feeding network that would reduce the total efficiency of the antenna. However, the presented technique using the FSS superstrate layer does not need a feeding network, and as a result, this approach has convenient radiation efficiency compared to conventional array antennas. The proposed technique using FSS superstrate layer is more complicated and larger compared to the conventional array antennas which are planar circuits. Moreover, the separation space between the base antenna and the superstrate layer would significantly affect the antenna characteristics, which make the installation more complex.

As the second design approach in this chapter, a method has been introduced to increase the directivity along with the capability to sweep the beam continuously. The PGM surface has been used to rotate the beam of a broadside patch antenna. Simulation results have shown that the gain is increased by about 8 dBi compared to the antenna without the PGM surface. A maximum gain of 15.2 dBi with a HPBW of 20^o has achieved for the antenna with the PGM surface. The intended antenna covered the frequency range from 57 to 64 GHz. However, we need to rotate the PMG surface mechanically to sweep the beam, which would make the fabrication more complex.

Chapter 4 Low-loss Wave Guiding Structures at mmWave

This chapter contains material extracted from the following publications:

[23] M. Farahani, M. Nedil and T. A. Denidni, "A Novel Hedgehog Waveguide and its Application in Designing a Phase Shifter Compatible With Hollow Waveguide Technology," *IEEE Transactions on Microwave Theory and Techniques*, vol. 67, no. 10, pp. 4107-4117, Oct. 2019.

[34] M. Farahani, M. Akbari, M. Nedil, T. A. Denidni and A. R. Sebak, "A Novel Low-Loss Millimeter-Wave 3-dB 90° Ridge-Gap Coupler Using Large Aperture Progressive Phase Compensation," *IEEE Access*, vol. 5, pp. 9610-9618, 2017.

[89] M. Farahani, T. A. Denidni and M. Nedi, "Design of a Low Output-Phase Error Ridge-Gap Coupler for Antenna Arrays Applications," 2018 IEEE International Symposium on Antennas and Propagation & USNC/URSI National Radio Science Meeting, Boston, MA, 2018, pp. 1099-1100.

4.1 Introduction

The capability of propagating electromagnetic waves through guided structures is recognized as the beginning step toward designing telecommunication systems. In different frequency ranges from DC to terahertz, researchers and designers have designed and investigated several types of waveguides and transmission lines, that have their own advantages and shortcomings[25]-[43]. Each electromagnetic guiding structure that constructed of more than one electrically separated metal, can only propagate the fundamental TEM mode, which can transmit electromagnetic waves from the arbitrarily low frequencies, and is named a transmission line. The waveguides are electromagnetic guiding structures that can not propagate the TEM mode, and constructed of just one metal. Furthermore, there is a different guiding structure that does not consist of a conductor at all, which is named dielectric slab [44]. The ability to support higher-order modes in waveguides provides them the capability to work in modes with lower propagation loss characteristics, as opposed to transmission lines, by modifying the topology of the host waveguide. This idea arises from the reality that waveguide operation mode influences the propagation loss performance. Consider a simple parallel plate waveguide in order to make it clear to understand this concept. The propagating TEM mode has a uniform distributed electric field; but, when it is stimulated with TE mode, the electric field is zero on the conductor walls. In [90], it is determined that propagation losses will increase by decreasing the metal plates' distance and increasing frequency for TEM mode, whereas the losses are decreased by increasing the metal plates' distance and increasing frequency for TE mode. Besides, waveguides are utilized in higher frequencies since they have lower propagation loss, lower leakage, and capability of handling more high-priced power as opposed to the transmission lines [41].

The Federal Communications Commission (FCC) has designated a supreme 7 GHz of the unlicensed frequency spectrum range from 57 to 64 GHz [91]. This frequency range obtains the capacity to achieve multi-gigabit Radio Frequency (RF) links as opposed to the less than 0.5 GHz available spectrum from 2 to 6 GHz for WiFi or other license-free applications. Nevertheless, there is a significant difficulty concerning the design of wireless systems at 60-GHz frequency-band, due to a large value of propagation loss in free space, which needs building high-sensitivity transceivers to defeat this shortcoming. In this respect, building high-efficiency low-loss guiding structures plays an essential part to reach this aim.

Substrate-Integrated Waveguides (SIWs) are low-loss waveguides that have been introduced and investigated for millimeter-wave and microwave frequencies during the past 20 years [40], [92]-[93]. In 2009, Per-Simon Kildal et al. have introduced the concept of a new electromagnetic guiding structure that can support quasi-TEM mode along the desired path within the air gap between two separated conductor surfaces [94]-[95]. Besides, a microstrip transmission line implemented in MHMIC, unlike the implementation in a conventional substrate, may also be utilized at 60-GHz frequency-band [37]. The distinctive characteristics of these guiding structures are highlighted in Table I. SIW waveguides are planar structures and own a low fabrication cost. Nevertheless, the electromagnetic fields are moving inside the host dielectric substrate, which increases the propagation losses due to the dielectric loss tangent of the host substrate, particularly at 60-GHz frequency-band. Furthermore, the conductive vias' diameters and the periodicity among them become smaller to reduce the leakage [96], which would lead to enhancing the complexity and fabrication cost. Besides, the power-handling capacity is small as opposed to hollow waveguides since their electromagnetic fields travell in a dielectric, which has a lower breakdown voltage than air in a hollow waveguide. Opposite to the SIW waveguides, the propagation losses are small due to the fact that the electromagnetic fields are moving within the air in the ridge gap waveguide [97]. In addition to greater loss characteristics opposed to SIW, the imperfect metallic contact problem is resolved compared to the hollow waveguides since there is an air gap between the two lower and upper plates in the ridge gap waveguide topology, which leads to the easier fabrication [98]. Although the microstrip ridge gap waveguide is a suitable competitor as a low-loss waveguide at mmWave frequency-bands, the implementation of a very long and slim metallic pin rises the complexity and manufacturing cost of the intended circuits. Lately, some efforts have been made to decrease the cost and complexity of this fabrication process. In [99], half-height pins are introduced to overcome the complexity and cost of the microstrip ridge gap waveguides. In [42], a new cost-effective approach has been introduced to implement the pin surface easier. The fabrication ease is significantly enhanced utilizing this technique since utilized EBG structure includes only holes rather than the pins. Moreover, the periodicity of the EBG unit cell is increased by 2.5 times of periodicity of the pins in the microstrip ridge gap waveguides.

In Section 4.2 of this chapter, the microstrip ridge-gap waveguide and the transition approach to the microstrip transmission line are described, and a low-loss multi-aperture 3-dB 90^o hybrid coupler implemented in the ridge-gap technology is designed and fabricated. The coupler has a very low amount of output-phase error. This is achieved by because Bethe's small coupling aperture theory [100], cannot show an exact formulation for large square aperture in a multi-aperture coupler. In the case of large square aperture, the coupling and isolation coefficients are frequency-dependent and the phase varies over the large coupling aperture, which can be utilized to compensate for the progressive-phase nature of the coupler.

In Section 4.3 of this chapter, we introduce a novel waveguide structure that has several advantages compared to the conventional transmission lines and waveguides reported in literature. The primary advantage of the Hedgehog waveguide is that it can support propagation with lower loss. Furthermore, the fact that the electromagnetic fields are captivated to space within the waveguide, radiation losses are kept very low, resulting in good immunity from external electromagnetic disturbance as opposed to the microstrip technology. Another key advantage of the Hedgehog waveguide is the compatibility with the hollow waveguides, which provides an extra degree of freedom to utilize the intended waveguide for several mmWave applications.

4.2 Microstrip Ridge Gap Waveguide and Designed Hybrid Coupler

Considering a miniature size and huge value of free-space propagation losses at mmWave frequency ranges, realizing passive components at mmWave bands has been a demanding matter for engineers. Several efforts have been made to introduce an innovative implementable and low-loss guiding structures for use in mmWave bands over the past decade. As an example, the substrate integrated waveguide (SIW) was investigated and studied during the past decade as a low-loss planar waveguide [14]-[16]. Nevertheless, realizing mmWave components, for instance, couplers using SIW, degrades the low-loss features of SIW waveguide, by perturbing the host SIW structure [17]-[19].

Table 4.1: Comparing different guiding structures with the Hedgehog waveguide (M. Farahani et al. [23], @2019 IEEE).

Characteristic	Ref.	Preferred Mode	Other Modes	Dispersion	BW	Loss	Component Integration	Fabrication Ease	Photo
Microstrip	[37]	Quasi -TEM	TM, TE	Low	High	High	Easy	Real Easy	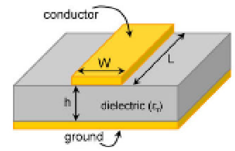
Substrate-Integrated Waveguide (SIW)	[40]	TE_{10}	TM, TE	Medium	Low	Medium	Hard	Easy	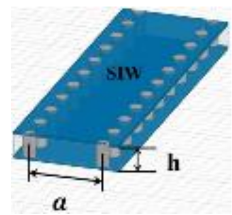
Hollow Waveguide	[41]	TE_{10}	TM, TE	Medium	Low	Low	Hard	Medium	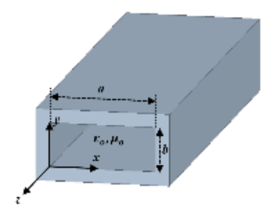
Microstrip Ridge gap Waveguide	[34]	Quasi -TEM	NO	Medium	Low	Low	Hard	Easy	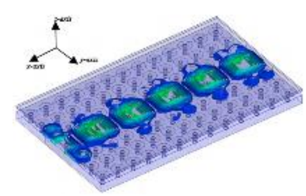
Gap Waveguide	[42]	TE_{10}	TM, TE	Medium	Low	Low	Hard	Real Easy	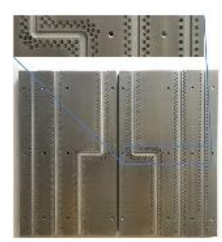
Proposed Hedgehog Waveguide	[23]	TE_{10}	NO	Medium	Low	Low	Hard	Medium	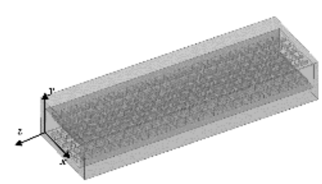

An alternative technique named microstrip ridge gap waveguide technology has been recommended [20] to conquer those drawbacks. The microstrip ridge gap waveguide is a remarkably low-loss waveguide at mmWave bands [20]-[21], [33]. In these structures, the electromagnetic waves are contained within two conductive walls and two open sides. A band-gap can be achieved in x- and y-direction by implementing a combination, for instance, an array of pins adjacent to the two open sides, as illustrated in Figure 4.1. Accordingly, the electromagnetic waves would travel in the created air gap under specified boundaries (Figure 4.1(b)). The losses of the microstrip ridge gap waveguide are less than SIW because the electromagnetic waves are propagating in air and host substrate in the microstrip ridge gap and SIW waveguides, respectively. Besides, performing any perturbation, for instance, bends and slots in the host SIW waveguides, degrades their low-loss performance, since perturb their characteristics. Unlike SIW waveguides, the microstrip ridge gap waveguides are less sensitive to the perturbations, for instance, bends and slots.

Different topologies have been proposed to design a low-loss 90^o 3-dB coupler among the researchers, such as SIW branch line couplers [18] and [101], and a two-layer SIW coupler [102]. These approaches have a huge amount of losses at mmWave bands. The second drawback of these approaches is a large value of output phase-error that arises from the progressive phase characteristics of them.

In this Section, the host microstrip ridge gap waveguide and transition topology to the microstrip transmission line are studied and developed. Additionally, the principles of the suggested phase compensated hybrid coupler are investigated and explained. Ultimately, the intended coupler is implemented in microstrip ridge gap waveguide technology, and mesurement results are obtained and compared to the simulated ones.

4.2.1 Physical Theory of the Proposed Microstrip Ridge Gap Waveguide

The introduced microstrip ridge gap waveguide is illustrated in Figure 4.1. The electromagnetic waves are confined among the two conductive walls and two open sides. A band-gap can be achieved in x- and y-direction by implementing a combination, for instance, an array of pins adjacent to the two open sides. The dispersion diagram of the band-gap structure and microstrip ridge gap waveguide are carried out using CST Studio Suite and are presented in Figure 4.2 and Figure 4.3, respectively. As can be observed from Figure 4.3, a band-gap exists within the frequency range from 45 to 68 GHz. The proposed waveguide has the unique feature of simultaneous supporting of several independent local quasi-TEM (Q-TEM) modes based on the concept of PEC-over-PMC plates to eliminate global TEM modes in a parallel-plate waveguide (PEC-over-PEC). In the longitudinal orientation, it operates as PMC walls in the direction transverse to the waveguide line. So that, PEC-over-hard surface walls can be considered as PEC-over-PMC walls in the transverse orientation and as PEC-over-PEC walls in the longitudinal orientation. Consequently, different modes are prevented except for the Q-TEM mode along the ridge gap line. Accordingly, the electromagnetic waves are traveling in the air gap as shown in Figure 4.1(b).

The introduced method in [33], is utilized as the transition from the microstrip transmission line to the microstrip ridge gap waveguide, presented in Figure 4.4. The designed microstrip ridge gap waveguide characteristic impedance is 50 ohm. The S-parameters of the transition is carried out using Ansys HFSS, exhibited in Figure 4.5.

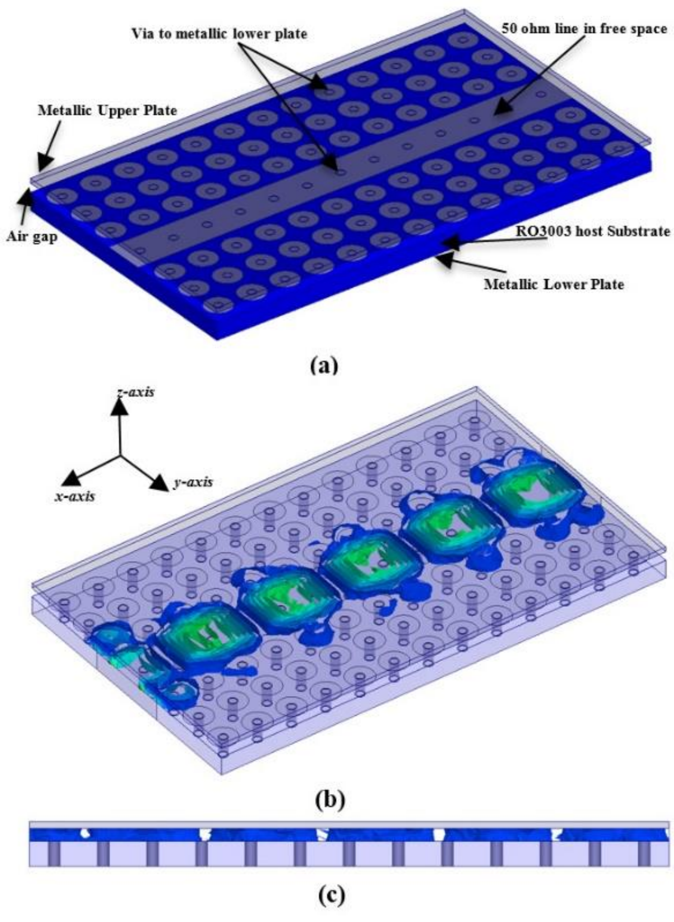

Figure 4.1: (a) Proposed ridge-gap waveguide. (b) Travelling electric fields in the air gap. (c) Side view of travelling electric fields in the air gap (M. Farahani et al. [34], @2017 IEEE).

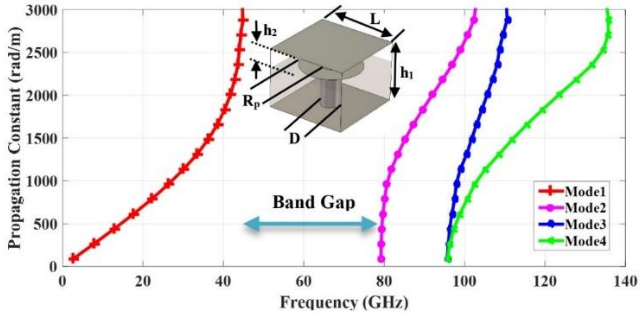

Figure 4.2: Dispersion diagram of the periodic unit cell of mushroom-like ridge. The unit cell dimensions are $D = 0.25mm$, $R_p = 0.38mm$, $L = 1mm$, $h_1 = 0.5mm$, $h_2 = 0.25mm$ (M. Farahani et al. [34], @2017 IEEE).

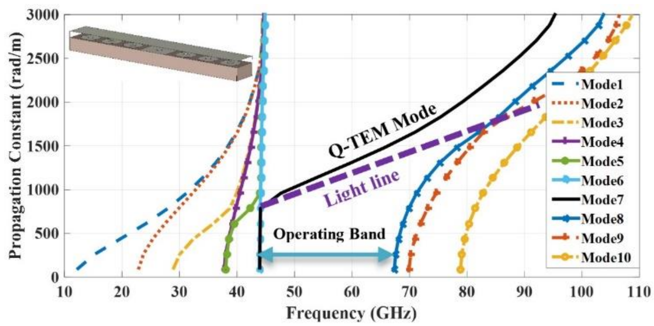

Figure 4.3: Dispersion diagram of the proposed ridge-gap waveguide in Figure 4.1 (M. Farahani et al. [34], @2017 IEEE).

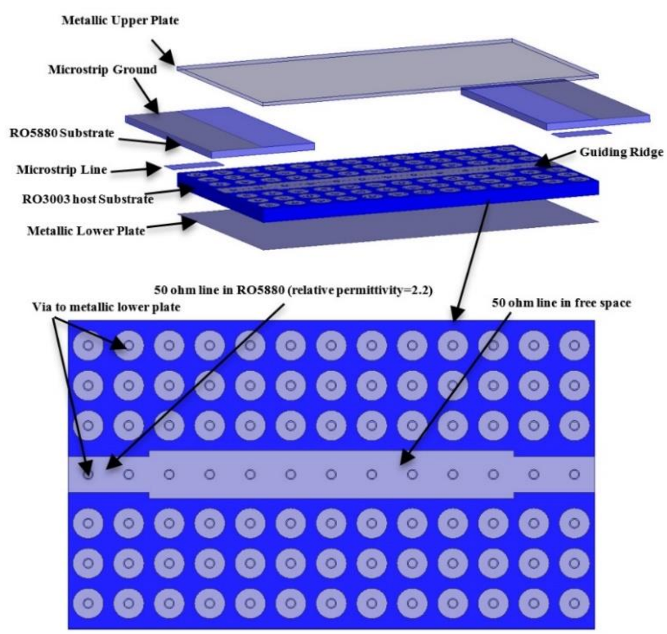

Figure 4.4: The ridge-gap waveguide transition to microstrip waveguide (M. Farahani et al. [34], @2017 IEEE).

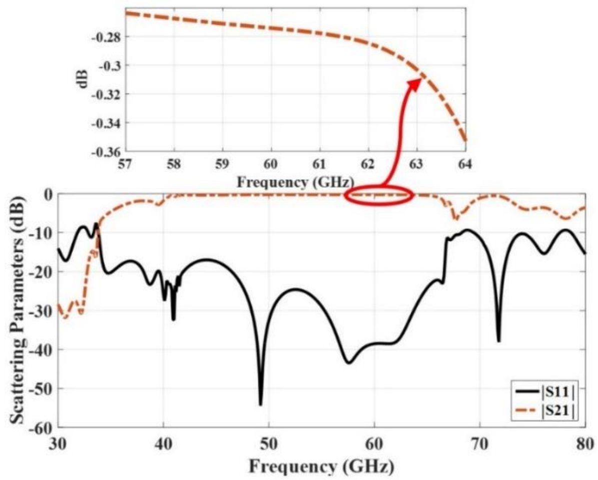

Figure 4.5: Simulated scattering parameters of the proposed transition from microstrip to ridge-gap waveguide in Figure 4.4 (M. Farahani et al. [34], @2017 IEEE).

4.2.2 Theory of the Phase Compensated Six Stage Hybrid Coupler

The cascaded coupling-slot approach is utilized for designing the intended coupler, as presented in Figure 4.6. There are different approaches to enhance the working bandwidth of couplers, for instance, utilizing multiple series coupling slots [103]. The classical approach for designing multi-hole directional couplers in the literature [103] considers that the signal power in the feeding waveguide is almost constant over all of the holes because of its limited power coupling at the holes. But, this theory is not valid in the situation of extremely tight coupling over -10 dB, because of a significant portion of input power leaks to the coupled waveguide due to a considerable coupling constant at the holes. Studying the six-slot coupling aperture arrangement in Figure 4.6, the forward and backward coupled signal components in the upper waveguide can be determined, as displayed in Figure 4.6. The forward and backward coupled power can be estimated as

$$P_2 = A_7 \tag{4-1}$$

$$P_3 = \sum_{n=1}^{n=6} A_n C_n e^{-j\beta(6-n)S} \tag{4-2}$$

$$P_4 = \sum_{n=1}^{n=6} A_n b_n e^{-j\beta(n-1)S} \tag{4-3}$$

where A_n is expressed as

$$A_n = \begin{cases} P_1 & ,n = 1 \\ P_1 e^{-j(n-1)\beta S} \times \prod_{i=1}^{n-1}(1 - b_i - C_i) & ,n = 2,3,4,5,6,7 \end{cases} \quad (4-4)$$

For tiny apertures, the isolation and coupling coefficients (b_n and C_n) are frequency-independent quantities [100]. Rectangular large apertures are high-coupling and narrowband structures opposed to small apertures. The Bethe's tiny coupling-hole theory [100] is not able to represent an accurate expression for a big rectangular aperture. Regarding a big rectangular aperture, the isolation and coupling coefficients (b_n and C_n) are defined by [100]:

$$C_n = b_n = 0.508 \times {W_s}^3 \times \frac{\tan\left(\frac{\pi f}{2 f_{co}}\right)}{\frac{\pi f}{2 f_{co}}} e^{\left(-\frac{2\pi h_m f_{co} Q}{C_0}\sqrt{1-\left(\frac{f}{f_{co}}\right)^2}\right)} \quad (4-5)$$

The first term is determined by Cohn [104], which takes into account the impact of aperture resonant frequency (f_{co}). The exponential term is the factor to compensate for the impact of the thickness of the coupling wall (h_m), and Q is an empirical parameter that represents the impact of the apparent extra electrical thickness of the coupling wall. For circular apertures, Q is provided by [104] as

$$Q = \frac{\alpha D}{h_m} + 1 \quad (4-6)$$

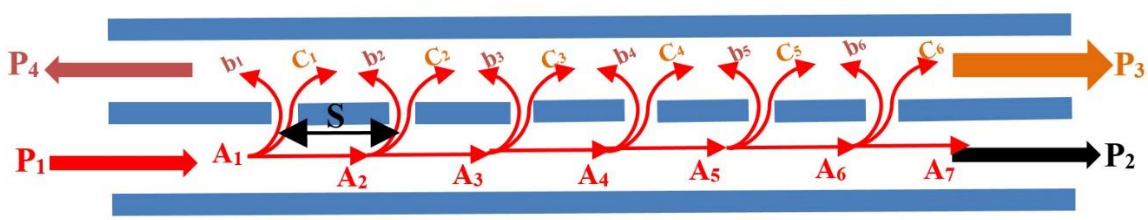

Figure 4.6: Geometry of the proposed six stage coupler (M. Farahani et al. [34], @2017 IEEE).

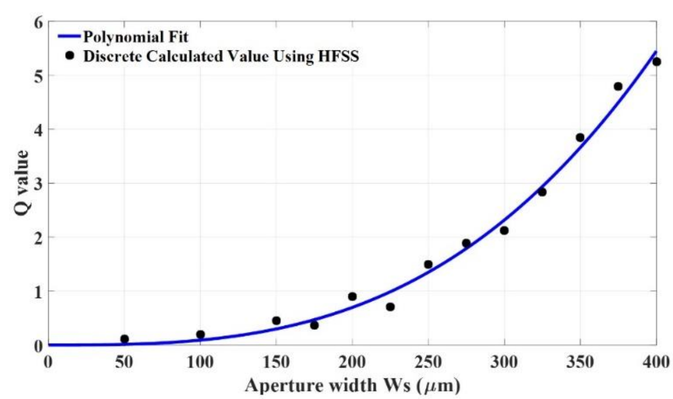

Figure 4.7: The calculated discrete corrected Q factor and polynomial fit (M. Farahani et al. [34], @2017 IEEE).

where D is the hole diameter, and α is a fixed value (0.065). This expression is not valid for a big rectangular aperture. To correct Q, several aperture widths are considered and simulated using Ansys HFSS and the following expression for Q is fitted to a polynomial functional form concerning the different aperture size as

$$Q = 0.02768{W_s}^3 - 0.27583{W_s}^2 + 0.85232W_s + 0.97261 \qquad (4-7)$$

where W_s is the aperture width in μm, and the thickness of the coupling wall (h_m) is considered a fixed value of 0.127 mm. The extracted discrete corrected Q factor and estimated polynomial fit are presented in Figure 4.7. The coupling factor of the aperture is determined in Appendix A and can be represented as

$$Coupling = 10\log\left|\frac{1-\left(1-1.016\times {W_s}^3\times\frac{\tan\left(\frac{\pi f}{2f_{co}}\right)}{\frac{\pi f}{2f_{co}}}e^{\left(-\frac{2\pi h_m f_{co} Q}{C_0}\sqrt{1-\left(\frac{f}{f_{co}}\right)^2}\right)}\right)^6}{2}\right| \qquad (4-8)$$

The phase difference between the two output ports (θ) can be given as

$$\theta = \angle(P_3/P_2) \qquad (4-9)$$

In the proposed coupler, the output-phase difference can be re-expressed as

$$\theta = \theta_1 + \theta_2 \qquad (4-10)$$

which can be separated into two terms, the linear output-phase difference (θ_1) and the big coupling aperture output-phase error (θ_2). These two terms are determined in Appendix B and are presented in (4-11) and (4-12).

$$\theta_1 = \beta S \qquad (4-11)$$

$$\theta_2 = \angle\left(\frac{1-\left(1-2\times 0.508\times {W_s}^3\times\frac{\tan\left(\frac{\pi f}{2f_{co}}\right)}{\frac{\pi f}{2f_{co}}}e^{\left(-\frac{2\pi h_m f_{co} Q}{C_0}\sqrt{1-\left(\frac{f}{f_{co}}\right)^2}\right)}\right)^6}{2\left(1-2\times 0.508\times {W_s}^3\times\frac{\tan\left(\frac{\pi f}{2f_{co}}\right)}{\frac{\pi f}{2f_{co}}}e^{\left(-\frac{2\pi h_m f_{co} Q}{C_0}\sqrt{1-\left(\frac{f}{f_{co}}\right)^2}\right)}\right)^6}\right) \qquad (4-12)$$

The estimated θ_1 and θ_2 utilizing (4-11) and (4-12) are plotted utilizing Matlab versus frequency in Figure 4.8. The big coupling aperture output-phase error (θ_2) is zero for the frequencies smaller than f_{co}. For the frequencies more than f_{co}, it possesses a negative slope that can utilize in order to compensate for the positive slope of θ_1. Accordingly, a very flat output-phase difference will be obtained for frequencies more than f_{co} if θ_1 and θ_2 possess identical magnitude slope with a reverse sign, as illustrated regarding the ideal scenario displayed in Figure 4.8. Nevertheless, the real θ_2 is not a straight line as the ideal θ_2 in (4-12), which is displayed in Figure 4.8 for frequencies more than f_{co}. The real θ_2 is carreid out utilizing Ansys HFSS for a typical aperture to determine the real performance it (Figure 4.9). f_{co} represents the point where a tiny aperture area and a big aperture area are separated. In a tiny aperture area, there is not any signal phase variation across the aperture. To explain this clear regarding the small apertures, the isolation and coupling coefficients (b_n and C_n) are frequency-independent quantities [100]. f_{co} is influenced by the aperture length (L_s) and aperture width (W_s). Meanwhile, it is worth to mention that by considering that the aperture length (L_s) five times bigger than the aperture width (W_s), f_{co} is essentially defined by the aperture length (L_s). The design steps for the proposed coupler is demonstrated later in this section. The coupler is simulated utilizing Ansys HFSS. Figure 4.9 presents the simulated phase difference for various values of W_s, L_s, θ_1 and θ_2. The distance among apertures (S) is considered to be 1.875 mm, and the thickness of the coupling wall (h_m) is a fixed value of 0.127 mm. As can be observed from Figure 4.9, the aperture resonant frequency (f_{co}) is principally influenced by the aperture length (L_s). Altering the aperture length (L_s) would also influence the slope of the θ_2. Moreover, it can be noticed that the slope of θ_2 is proportional to the aperture width (W_s), although it does not have a notable impact on the aperture resonant frequency (f_{co}). The slope of θ_2 enhanced by increasing W_s. This behavior was expected scince by reducing W_s, the coupling strength of the aperture would be decreased and it will act similar to a small coupling aperture with frequency-independence behavior.

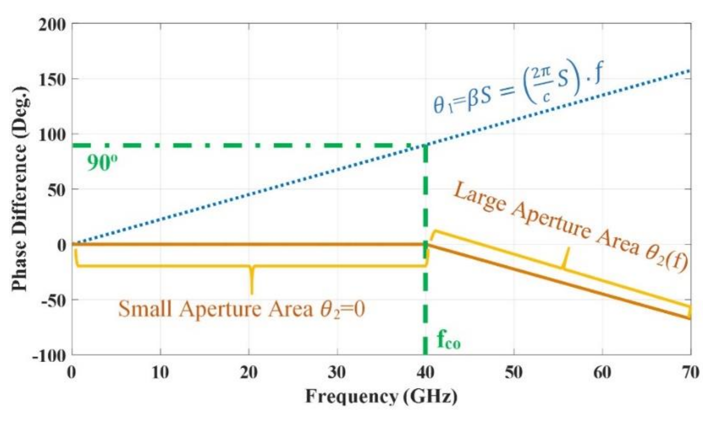

Figure 4.8: The large coupling aperture output phase difference.(M. Farahani et al. [34], @2017 IEEE).

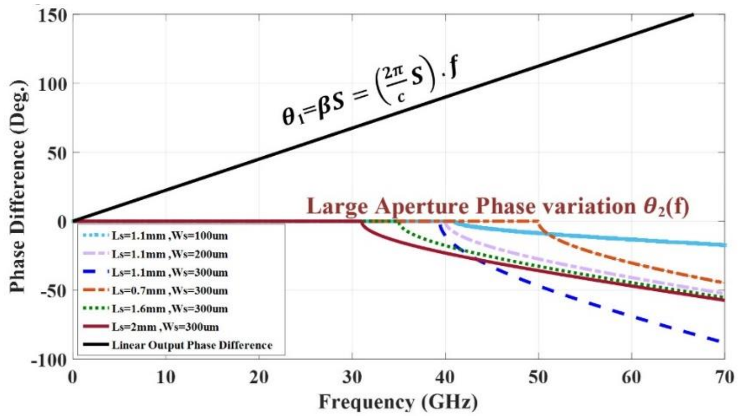

Figure 4.9: Simulated phase difference using HFSS for different values of W_s and L_s.We considered that the distance between apertures (S) is 1.875 mm, and the coupling wall thickness (h_m) is 0.127 mm (M. Farahani et al. [34], @2017 IEEE).

4.2.3 Design of the Proposed Hybrid Coupler

The above-mentioned approach is applied to determine the initial values for the coupling aperture dimensions of the intended six-stages coupler. The realized schematic of the coupler implemented in the ridge gap technology is displayed in Figure 4.10. The coupling aperture size is given in Figure 4.10. The thickness of the coupling wall is a fixed value of 0.127 mm, and then Q factor is calculated by (4-7). In the last subsection, it is determined that in the big coupling apertures at the frequencies more than f_{co}, θ_2 has a negative slope, which can compensate for the positive slope of θ_1. As it is shown before, the aperture resonant frequency (f_{co}) is principally influenced by the aperture length (L_s), and it is also explained that the slope of θ_2 is proportional to the aperture width (W_s), but it does not have a meaningful influence on the aperture resonant frequency (f_{co}) (Figure 4.9). Furthermore, the absolute coupling can be determined by (4-8), which is a function of the aperture width (W_s) and the aperture resonant frequency (f_{co}) directly, and it is thoroughly a function of the coupling wall thickness (h_m), which is considered to be 0.127 mm. The coupling is not immediately a function of the aperture length (L_s); nevertheless, the aperture resonant frequency (f_{co}) is dramatically influenced by the aperture length (L_s). Furthermore, the coupling is a function of Q factor, and the Q factor is a function of the coupling wall thickness (h_m) and the aperture width (W_s). But, in this work, the Q factor is extracted for a fixed value of h_m that is equal to 0.127 mm.

The initial start for implementing the intended coupler is choosing the precise amounts for the coupling aperture width (W_s) and the aperture length (L_s) in a way which θ_2 and θ_1 possess similar slope magnitude with opposite signs, in order to neutralize the progressive phase of θ_1 and obtain a pretty flat output phase response. Subsequently, W_s and L_s will alter the value of the coupling coefficients. Meanwhile, the impact of L_s on the coupling coefficients is through the aperture resonant frequency (f_{co}) that is insignificant as opposed to the aperture width (W_s). Therefore, the initial dimension is selected for W_s to grant us the 3 dB coupling factor. Then, the proper amounts for L_s and S can be determined by optimizing L_s and S (aperture separation distance) to neutralize the progressive phase of θ_1 by θ_2 and while satisfying the condition of $\theta_1(f_{co}) = 90^o$. Following this method, the aperture dimensions are obtained as $W_s = 0.35$, $L_s = 1.2$ and $\mathrm{S} = 1.875$, all in millimeters.

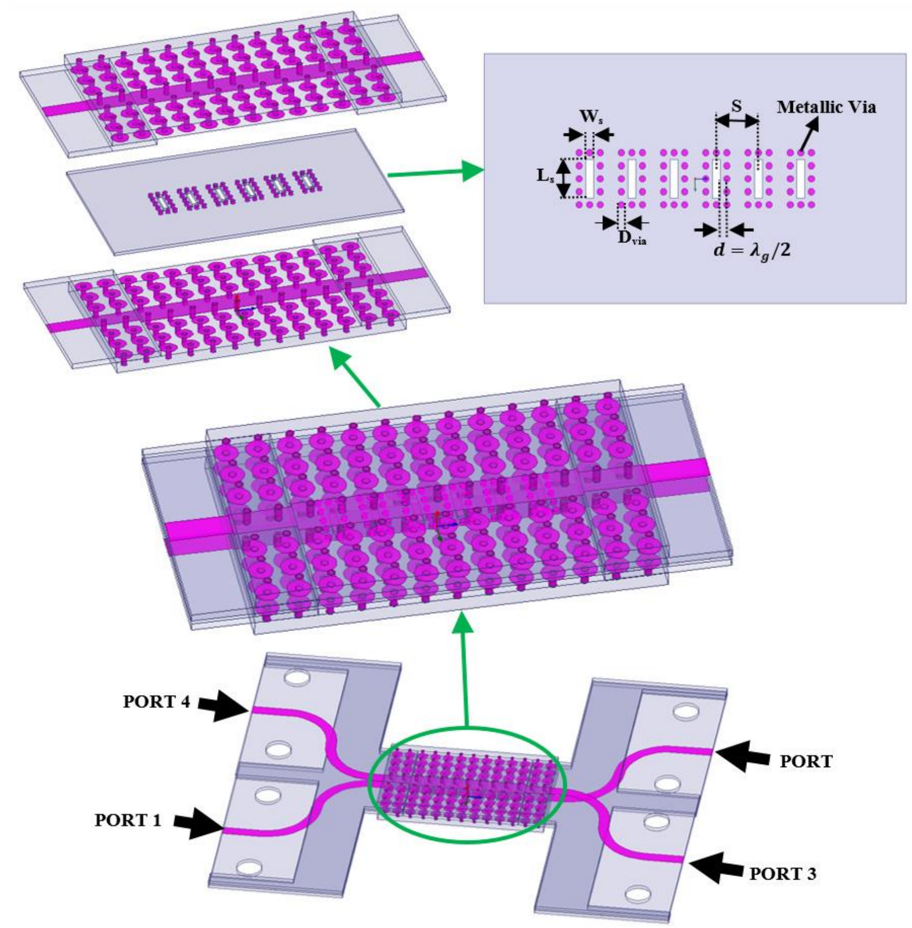

Figure 4.10: Geometry of the proposed two layer 3 dB hybrid coupler.($W_s = 0.35\ mm$, $L_s = 1.2\ mm$, $D_{via} = 0.3\ mm$, $D = 0.52\ mm$) (M. Farahani et al. [34], @2017 IEEE).

In (4-5), the isolation and coupling coefficients (b_n and C_n) are provided for a fully PEC coupling surface [100], but in this project, Rogers RO3003 substrate is employed as the coupling wall. The lower and upper sides of this wall are PEC, nevertheless, four sides on the aperture, separating the upper and lower sides, are not PEC (Figure 4.11(a)). The coupling wall can be recognized as a parallel PEC-plate waveguide, filled by RO3003 substrate. Thus the following expression can be expressed for a shorted waveguide (Figure 4.11(b))

$$Z_z = \frac{E_z}{H_Y} = j\left(\frac{W}{P}\right)\eta \tan k_g d \qquad (4-13)$$

where λ_g is the wavelength in the parallel plate waveguide filled with RO3003 substrate. The surface impedance on the edge will be zero if $d = \lambda_g/2$, that equivalent to a PEC surface as shown in Figure 4.11(c).

Figure 4.12 displays the electrical waves inside the designed coupler. The S-parameters of the intended ridge gap coupler are carried out utilizing Ansys HFSS and is shown in Figure 4.13. As can be observed from Figure 4.13, the insertion losses are lower than 3.5 dB within the working frequency range from 57 to 64 GHz, which reveals the truly low-loss characteristics of the intended ridge gap coupler.

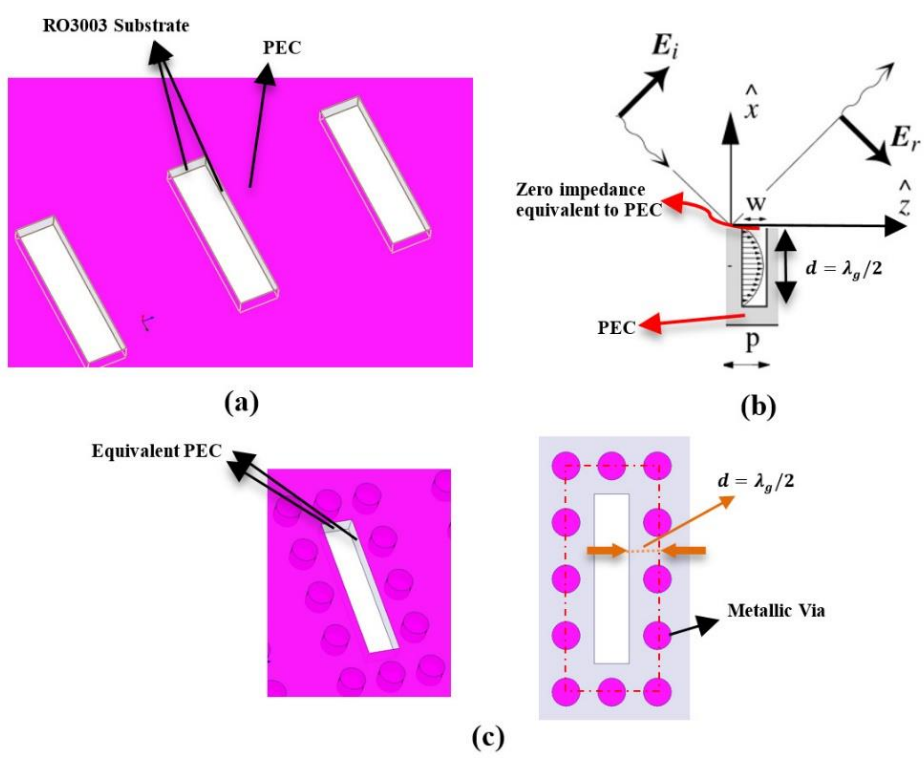

Figure 4.11: The PEC coupling aperture composes of $\lambda_g/2$ shorted parallel plate waveguide filled with RO3003 substrate (M. Farahani et al. [34], @2017 IEEE).

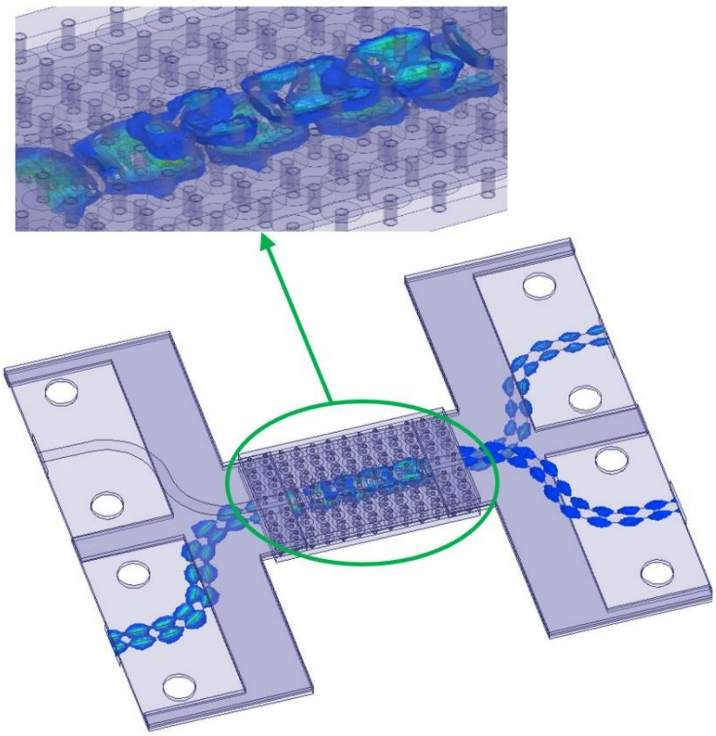

Figure 4.12: Magnitude of the travelling electric fields (M. Farahani et al. [34], @2017 IEEE).

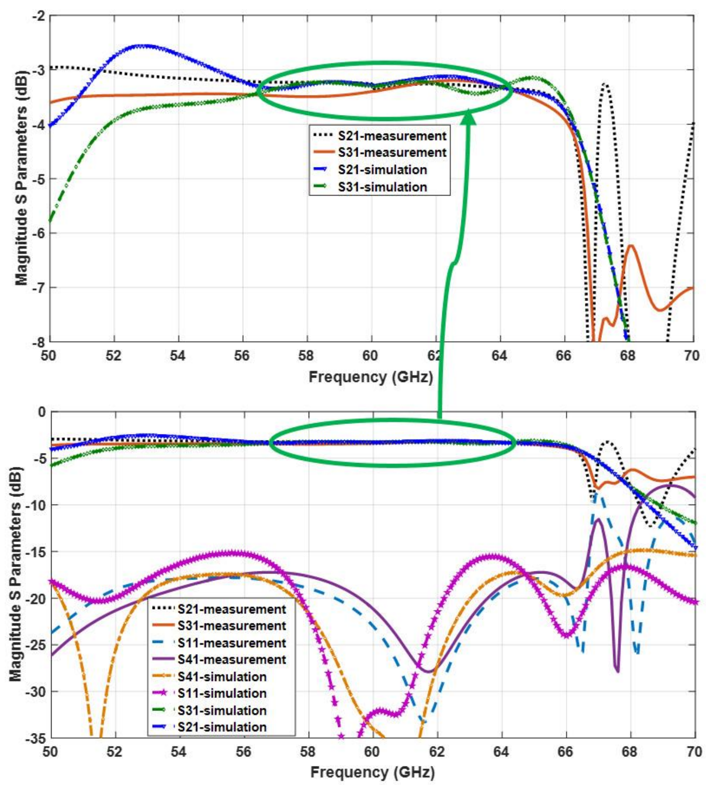

Figure 4.13: Measured and simulated results of the proposed ride-gap 3 dB hybrid coupler (M. Farahani et al. [34], @2017 IEEE).

4.2.4 Experimental Results

An image of the fabricated prototype is displayed in Figure 4.14. To measure the fabricated prototype, the connector characteristics and losses of the feeding microstrip transmission lines have to be considered in the calibration process. Figure 4.15 illustrates the scattering parameters of the connectors along with feeding microstrip lines. A 1.85 mm end-lunch connector with the part number of 1892-03A-5 from Southwest-Microwave Inc. is utilized to measure the intended fabricated coupler. The proposed connector operates up to a frequency of 67-GHz. The connector performance is not provided beyond this frequency by the manufacturer. Therefore, the test platform in Figure 4.15(a) is utilized to extract the connector response at frequencies more than 67-GHz and besides calibrating the measurement devices. As can be observed from Figure 4.15(b), there is 2 to 5 dB loss in the frequencies below 66-GHz, which represent losses caused by the feeding microstrip line. Some resonances exist in the frequencies around 67-GHz caused by the connector. This pattern shows himself in the measured results in Figure 4.13, where the losses caused the microstrip feeding lines and connectors are considered in the calibration procedure of measuring devices. The output phase performance of the intended coupler is presented in Figure 4.16. In Table 4.2, some specs of the proposed coupler are compared with the equivalent reported couplers in the literature. As can be understood from this table, the greatest blessing of this design is its low-loss characteristics of the microstrip ridge gap waveguide. For example, the insertion loss is smaller than 3.5 dB in the entire working frequency range from 57 to 64 GHz. The secondary interest of this technique is the exceptionally low amount of output-phase error, which is smaller than 1 degree in the entire working frequency range.

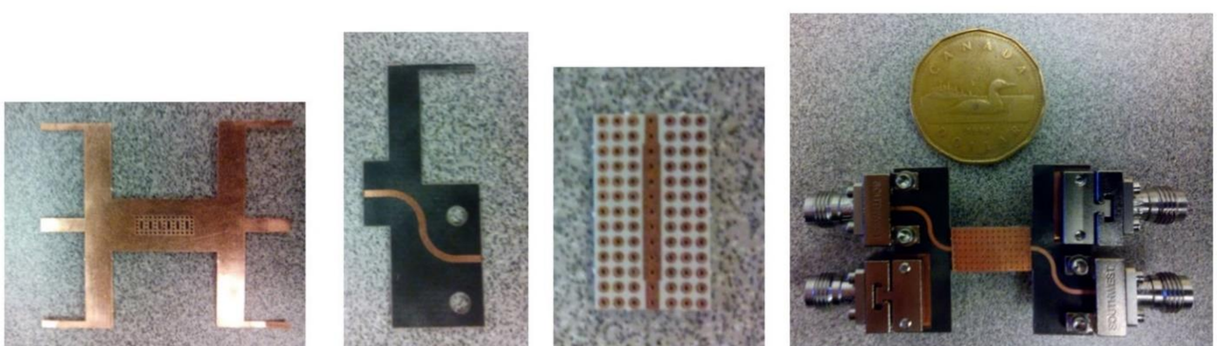
(a) (b) (c) (d)

Figure 4.14: Photo of the fabricated proposed ridge-gap coupler.(a) Coupling wall. (b) Feeding microstrip line. (c) Host ridge-gap. (d) Proposed ridge-gap coupler (M. Farahani et al. [34], @2017 IEEE).

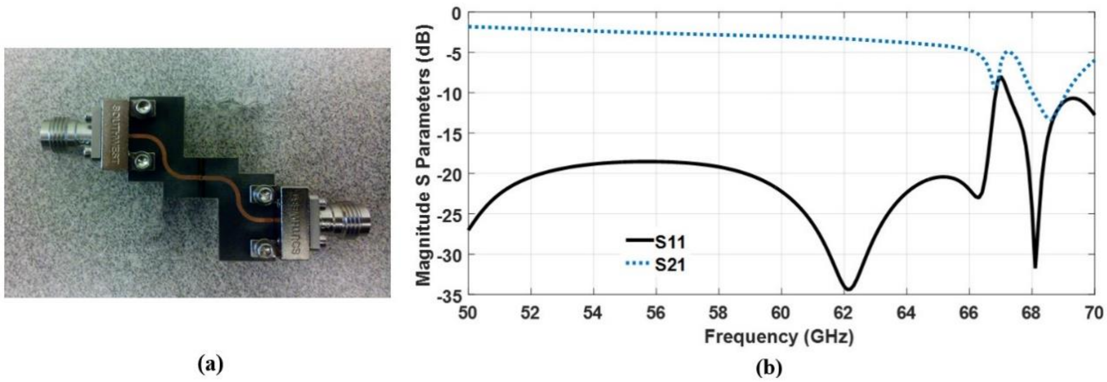

Figure 4.15: Test setup for measuring the connector and feeding microstrip line responses.(a) Test circuit. (b) Measurement results (M. Farahani et al. [34], @2017 IEEE).

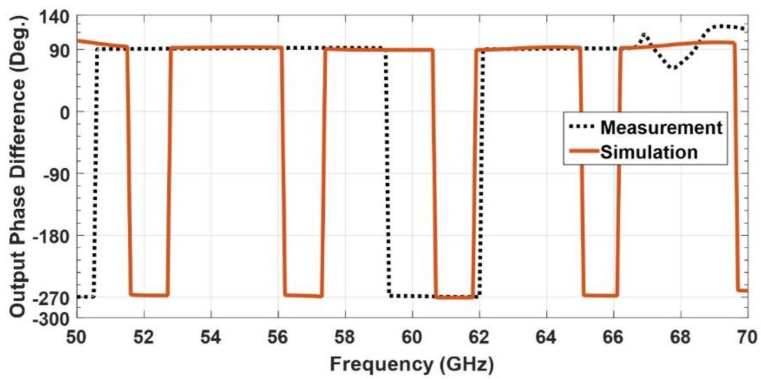

Figure 4.16: Output phase response of the proposed ride gap hybrid coupler (M. Farahani et al. [34], @2017 IEEE).

Table 4.2: Proposed microstrip ridge gap coupler compared with other equivalent presented coupler in literature (M. Farahani et al. [34], @2017 IEEE).

	Operating Frequency Band	**Maximum Insertion loss**	**Maximum output phase error (degree)**
Proposed ridge gap coupler	57-64 GHz	3.5dB	1
Ref [16]	93-95 GHz	5.2dB	3
Ref [18]	9-11 GHz	3.9dB	2.6
Ref [19]	11-14 GHz	3.95dB	2.15

4.3 Hedgehog Waveguide and Its Application in Designing a Phase Shifter

A novel waveguide, designed by an array of pins installed in a host rectangular hollow waveguide, is introduced and studied as an extremely low-loss waveguide for mmWave frequency ranges. The intended Hedgehog waveguide is named based on its electromagnetic behavior. As hedgehogs root through hedges and other undergrowth in search of their preferred meals, the recommended waveguide root through its installed array of pins. While we select a waveguide to implement our designs, it is worth spending some time scaling the advantages and shortcomings of the different kinds of waveguides on offer. The offered Hedgehog waveguide is notably low-loss and is compatible by the hollow waveguide technology, which grants the capacity to design various components such as extremely low-loss and notably low phase-error phase shifters. The offered Hedgehog waveguide is analytically studied, and a transition to the hollow waveguide is proposed. Furthermore, the low-loss characteristics of the Hedgehog waveguide are compared with the hollow waveguide. Ultimately, the suggested waveguide is implimented, simulated and measured. The simulation and measurement results indicate a good agreement, which verifies the design concept.

Through the next sections, we introduce, analyze and investigate Hedgehog waveguide, in particular, associated with their principle of operation, applications, and possible problem areas.

4.3.1 Physical Theory of the Proposed Hedgehog Waveguide

The offered Hedgehog waveguide constructed of a rectangular hollow waveguide arranged by an array of pins in both upper and lower surfaces, as demonstrated in Figure 4.17(a). The propagation loss of the intended waveguide is extremely low associated with equivalent hollow waveguides and other traditional waveguides or transmission lines at the frequency of interest, which is studied and reviewed in Section 4.3.4. The propagation loss of the Hedgehog waveguide principally causes by ohmic losses on metallic surfaces. To decrease the metallic losses in waveguides, the power density near the interior metallic surfaces of the waveguide must be lessened [105]. For example, the waveguide operating mode influences the propagation loss characteristics. For better understanding, imaging an uncomplicated parallel plate waveguide. The transverse TEM mode has a uniform distributed E-field; meanwhile, while it is triggered with TE mode, the E-field is zero on the conductive surfaces. In [90], it is determined that losses will raise by decreasing the plate separation and increasing frequency for TEM mode, whereas they are decreased by expanding the plate separation and increasing frequency for TE mode. Besides the low-loss performance of the intended waveguide, it is harmonious with the hollow waveguide topology; and much more importantly, it possesses fascinating phase behavior, which makes it perfect for designing wideband low-loss phase shifters at mmWave frequency ranges. In Section 4.3.5, a 45^{o} phase shifter is designed utilizing this technology.

4.3.2 Dispersion Diagram of the Proposed Hedgehog Waveguide

The offered Hedgehog waveguide is illustrated in Figure 4.17(a). The proposed waveguide is viewed as periodical cascaded sequences of the traditional hollow waveguide and longitudinally corrugated waveguide, as shown in Figure 4.17(b). Meanwhile, in order to obtain the required tools for extracting the dispersion diagram of Hedgehog waveguide considering a periodical cascaded sequence of two waveguides with arbitrary propagation constants and wave impedances (Figure 4.18). The consecutive sections are assigned with the index of m, and the borders between two consecutive sections are assigned with the index of n in Figure 4.18. If an infinite number of cascaded waveguides with propagation constants of β_1 and β_2 both having matching impedances facing each other is considered, then the input power to the section number m is equal to the power entered into the network number $m+1$ [106]. Thus, the following expression is satisfied for the Poynting vector

$$P_{n(m-1)} = P_{(n+1)m} \qquad (4-22)$$

where $P_{n(m-1)}$ is the directional energy flux at the border number n toward section number m. Therfore we have the following expression

$$\frac{1}{2}\mathrm{Re}\{E_{n(m-1)} \times H^*_{n(m-1)}\} = \frac{1}{2}\mathrm{Re}\{E_{(n+1)m} \times H^*_{(n+1)m}\} = \frac{1}{2}\mathrm{Re}\{E_{(n+2)(m+1)} \times H^*_{(n+2)(m+1)}\} \qquad (4-23)$$

The transverse impedance regarding a TE mode for section m is determined as

$$Z_{om} = \frac{-E_y}{H_x} \qquad (4-24)$$

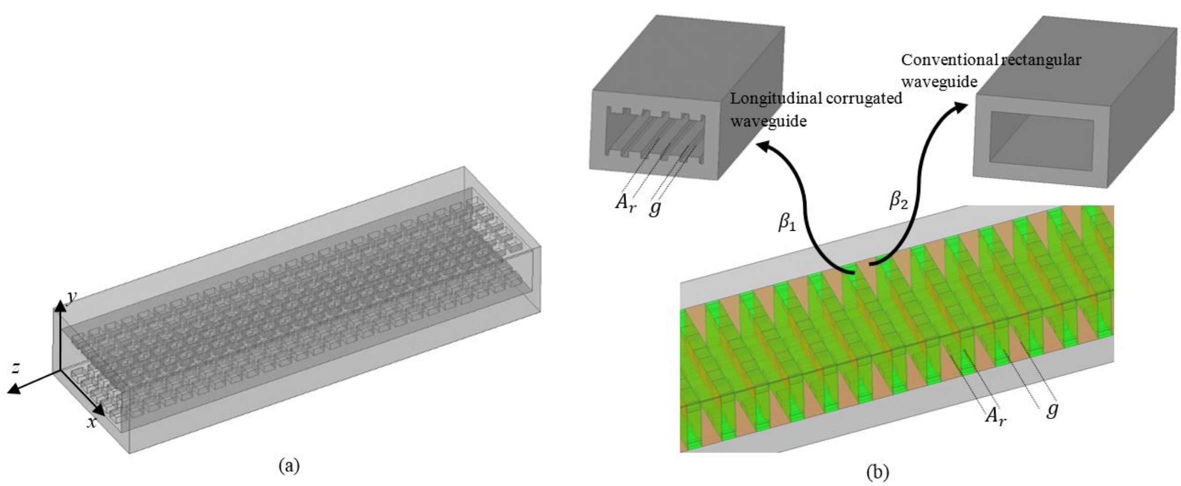

Figure 4.17: The proposed Hedgehog waveguide.(a) Hedgehog waveguide consists of a hollow waveguide loaded with a bed of pins in the both upper and lower walls. (b) Considering the Hedgehog waveguide as periodic combinations of the cascaded longitudinal corrugated waveguide and conventional hollow waveguide (M. Farahani et al. [23], @2019 IEEE).

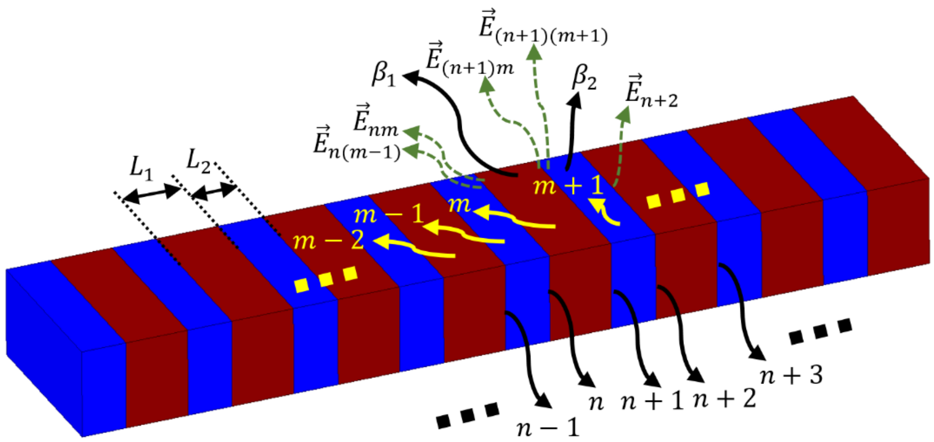

Figure 4.18: Considering Hedgehog waveguide as a periodic combination of two waveguides with propagating constants of β_1 and β_2 (M. Farahani et al. [23], @2019 IEEE).

Therefore, the Poynting vector may be rewritten as

$$\frac{1}{2}\frac{\left|\mathrm{E}_{yn(m-1)}\right|^2}{Z_{o(m-1)}} = \frac{1}{2}\frac{\left|\mathrm{E}_{y(n+1)m}\right|^2}{Z_{om}} = \frac{1}{2}\frac{\left|\mathrm{E}_{y(n+2)(m+1)}\right|^2}{Z_{o(m+1)}} \qquad (4-25)$$

The following expression can be concluded to the following equations.

$$\frac{\mathrm{E}_{yn(m-1)}}{\mathrm{E}_{y(n+1)m}} = \sqrt{\frac{Z_{o(m-1)}}{Z_{om}}}\; e^{j\beta_1 L_1} \qquad (4-26)$$

$$\frac{\mathrm{E}_{y(n+1)m}}{\mathrm{E}_{y(n+2)(m+1)}} = \sqrt{\frac{Z_{om}}{Z_{o(m+1)}}}\; e^{j\beta_2 L_2} \qquad (4-27)$$

In here, β_1 and β_2 are propagation constants within the cascaded waveguides, and the terms $\sqrt{Z_{on}/Z_{om}}$ are impedance scaling terms [106]. The overall electric vector ratio is provided by

$$\frac{\mathrm{E}_{yn(m-1)}}{\mathrm{E}_{y(n+2)(m+1)}} = \frac{\mathrm{E}_{yn(m-1)}}{\mathrm{E}_{y(n+1)m}} \times \frac{\mathrm{E}_{y(n+1)m}}{\mathrm{E}_{y(n+2)(m+1)}} = \sqrt{\frac{Z_{o(m-1)}}{Z_{o(m+1)}}}\; e^{j(\beta_1 L_1 + \beta_2 L_2)} \qquad (4-28)$$

Therefore, for a periodical cascaded sequence all owning matching impedances facing each other, the overall propagation constant can be determined by

$$\frac{\beta_1 L_1 + \beta_2 L_2}{L_1 + L_2} \qquad (4-29)$$

where β_1 and β_2 are the propagation constants of the hollow waveguide and longitudinally corrugated waveguide indicated in Figure 4.17(b), respectively.

In [107], a method called Overlapping T-Blocks (TB) has been proposed to obtain the dispersion diagram of a T-waveguide (Figure 4.19). The electromagnetic (EM) fields of a T-Block can be determined utilizing Green's function and mode-matching technique. The mode-matching technique [108]-[109] is among several exact and effective methods to analyze waveguide structures. It is a popular technique for analyzing waveguide transitions, high-efficiency filters, multiplexers, or polarization duplexer. The basic concept behind this method is based on dividing the structure under study into various building blocks. A weighted superposition of the waveguide modes describes the EM-fields at each of those building blocks. By employing the boundary conditions at the source and load of the whole structure and the adjacent building blocks, the magnitude of all modes will be expressed. Therefore, the mode-matching approach, unlike other numerical methods, decreases the 3D electromagnetic problems to a linear system based on the magnitude of each EM-mode.

Consider the TE-mode inside a T-waveguide (Figure 4.19(a)). In region (I) ($-\frac{A_r}{2} < x < 0$), H_z can be expressed as [107]:

$$H_z^I(x,y) = \sum_{m=0}^{\infty} q_m \cos(a_m(y + \frac{b}{2} - h)) \cos(\xi_m(x + \frac{A_r}{2} - h)) \times \left[u\left(y + \frac{b}{2} - h\right) - u\left(y - \frac{b}{2} + h\right)\right] \quad (4-30)$$

where $a_m = m\pi/(b - 2h)$, $\xi_m = k_o^2 - \beta^2 - a_m^2$, $k_o = 2\pi/\lambda_o$, and $u(\cdot)$ is a step function.

To express the H_z in region (II) ($0 < x < \frac{g}{2}$), the region (II) is divided into two sub-regions such as indicated in Figure 4.19(b) and (c). Employing the superposition theory [107], the H_z in region (II) is defined as

$$H_z^{II}(x,y) = \sum_{m=0}^{\infty} S_m[H_m(x,y) + R_m^H(x,y)] \quad (4-31)$$

where $H_m(x,y)$ and $R_m^H(x,y)$ are the field components inside sub-regions of Figure 4.19(b) and (c), respectively. Similar to $H_z^I(x,y)$, $H_m(x,y)$ is defined as

$$H_m(x,y) = \frac{1}{\xi_m \sin(\frac{\xi_m g}{2})} \cos(a_m(y + \frac{b}{2} - h)) \cos(\xi_m(x - \frac{g}{2})) \times \left[u\left(y + \frac{b}{2} - h\right) - u\left(y - \frac{b}{2} + h\right)\right] \quad (4-32)$$

S_m is calculated in [107] by considering the field continuity at $x = 0$ and integrating over $-b/2 + h < y < b/2 - h$ as follow

$$S_m = -q_m \xi_m \sin\left(\frac{\xi_m A_r}{2}\right) \quad (4-33)$$

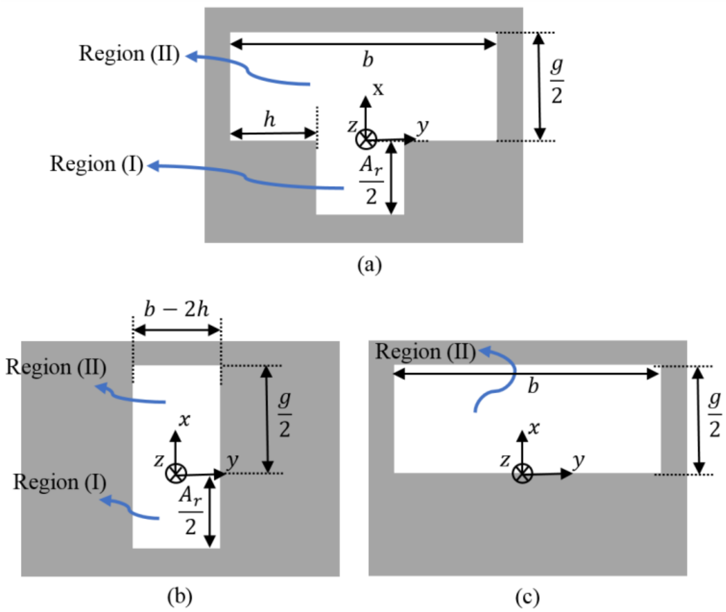

Figure 4.19: Geometry of a T-waveguide.(a) T-waveguide. (b) Sub-region for $H_m(x;\ y)$. (c) Sub-region for $R_m^H\ (x;\ y)$ (M. Farahani et al. [23], @2019 IEEE).

Using the method in [107], the term $R_m^H(x,y)$ can be obtained utilizing Green's function relation [110] as

$$R_m^H(x,y) = -\int H_m(r')\frac{\partial}{\partial n}[G_H(r,r')]dr' = -\frac{2}{g}\sum_{v=0}^{\infty}\frac{\cos(\eta_v x)}{\alpha_v(\zeta_v^2 - a_m^2)} \times \left[f_H\left(y,-\frac{b-2h}{2}+h;\zeta_v\right) - (-1)^m f_H\left(y,\frac{b-2h}{2};\zeta_v\right)\right] \quad (4-34)$$

where n is the outward normal direction to r', and

$$G_H(r,r') = \frac{4}{g}\sum_{v=0}^{\infty}\frac{\cos(\eta_v x)\cos(\eta_v x')}{\alpha_v} g(y,y';\zeta_v) \quad (4-35)$$

$$g(y,y';\zeta_v) = \frac{\sin(\zeta_v(y_< + \frac{b}{2}))\sin(\zeta_v(\frac{b}{2} - y_>))}{\zeta_v \sin(\zeta_v b)} \quad (4-36)$$

$$f_H(y,y';\zeta_v) = \frac{\mathrm{sgn}(y-y')[e^{j\zeta_v|y-y'|} - (-1)^m e^{j\zeta_v(b-|y-y'|)}]}{1-(-1)^m e^{j\zeta_v b}} \quad (4-37)$$

where $sgn(y) = 2u(y) - 1$. Thus, the total longitudinal magnetic field is given as

$$T_H(x,y) = H_z^I(x,y) + H_z^{II}(x,y) \quad (4-38)$$

The dispersion diagram of the TB can be defined by applying boundary continuity of $T_H(x,y)$ for $-b/2 + h < y < b/2 - h$ and $x = 0$. The dispersion diagram of a waveguide structure can be determined by dividing the waveguide into a number of TB building blocks using (4-38). The strength of the TB approach comes from that (4-38) can be repeatedly employed for each TB. In the following, the dispersion diagram for a longitudinally corrugated waveguide will be obtained from (4-38).

An H-waveguide dispersion diagram can be obtained utilizing the TB approach by dividing the H-waveguide in Figure 4.20 into two T-waveguides, as illustrated in Figure 4.20(b). The H_z-field in the H-waveguide is expressed as

$$D_H(x,y) = T_H^{(1)}(x,y) + T_H^{(2)}(-x-A_r,-y) \tag{4-39}$$

The longitudinally corrugated waveguide is split into five transformed H-waveguides as presented in Figure 4.21(c). The H_z can be yielded by considering the superposition of five transformed H-waveguides, as following

$$H_z(x,y) = D_H^{(1)}(x+2A_r+2g,y) + D_H^{(2)}(x+A_r+g,y) + D_H^{(3)}(x,y) + D_H^{(4)}(x-A_r-g,y) + D_H^{(5)}(x-2A_r-2g,y) \tag{4-40}$$

The TE dispersion diagram of a longitudinally corrugated waveguide can be extracted by applying the boundary continuities of the $H_z(x,-(b-2h)/2)$ and $H_z(x,(b-2h)/2)$ for $2A_r+2g<x<2A_r+3g$, $A_r+g<x<A_r+2g$, $0<x<g$, $-A_r-g<x<-A_r$, $-2A_r-2g<x<-2A_r-g$. The matching procedures of H_z are the same as [107].

Figure 4.22 depicts the dispersion diagrams of the TE_{10} mode in the intended Hedgehog waveguide.

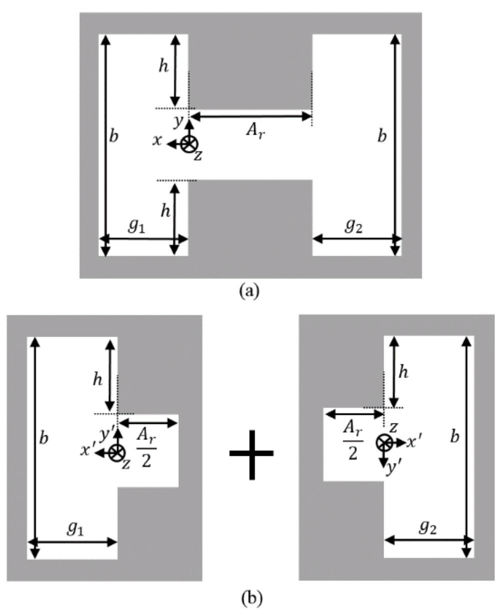

Figure 4.20: Geometry of a H-waveguide.(a) H-waveguide. (b) Superposition of two T-waveguide (M. Farahani et al. [23], @2019 IEEE).

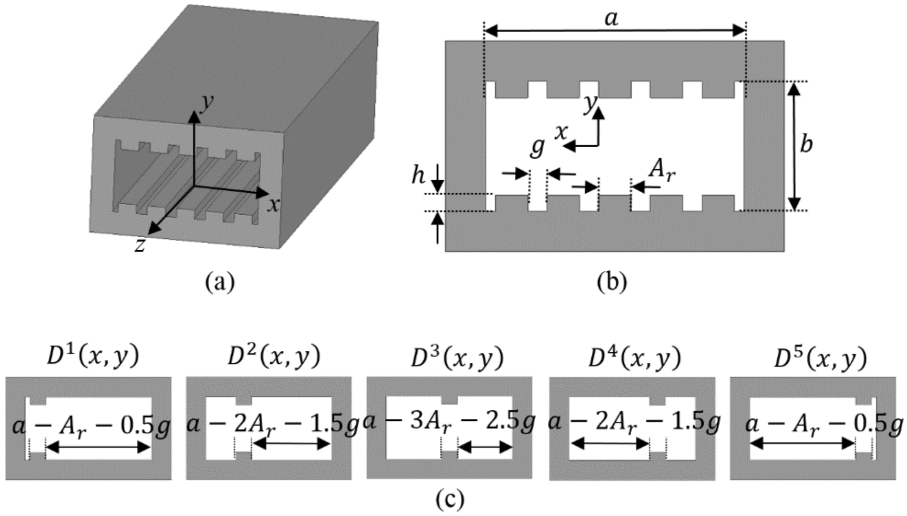

Figure 4.21: Geometry of a longitudinal corrugated waveguide.(a) 3D view. (b) Side view. (c) Superposition of five asymmetric H-waveguide (M. Farahani et al. [23], @2019 IEEE).

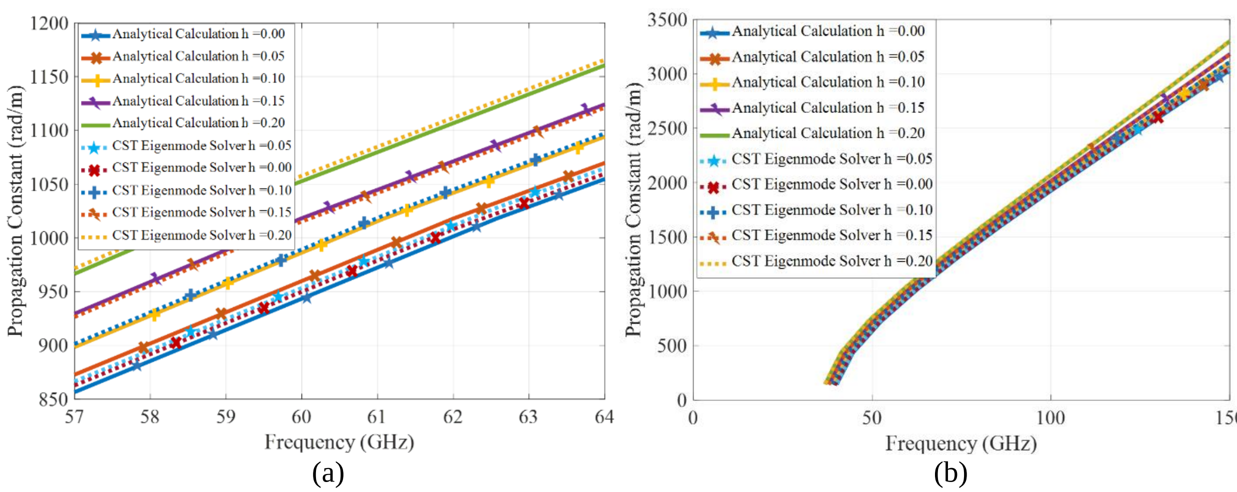

Figure 4.22: Dispersion diagram of the Hedgehog waveguide calculated with analytical calculation compared with the results carried out using CST Microwave Studio eigenmode solver. (a) From 57 to 64 GHz. (b) From 0 to 150 GHz. The dimensions are $A_r = 0.4$, $g = 0.2$, $a = 3.8$, $b = 1.6$, all in millimeters (M. Farahani et al. [23], @2019 IEEE).

4.3.3 Analysis of Propagation Losses in the Proposed Hedgehog Waveguide

A. Principal Concept

The impedance boundary condition method [111] is utilized to determine electromagnetic fields outside of conductive surfaces with finite conductivity value. The tangential elements of electromagnetic fields at the conductive surfaces can be determined using the Leontovich condition as follow

$$E_t = Z_s(\hat{n} \times H_t) \qquad (4-41)$$

where E_t and H_t are the tangential elements of electric and magnetic fields at the conductive surfaces, respectively; and $\hat{n}$ and Z_s are outward normal unit vector to the surface and surface impedance tensor, respectively. Z_s is presented as follow [112]

$$Z_s = \frac{1+j}{\sigma\delta} \qquad (4-42)$$

$$\delta = \sqrt{\frac{2}{\mu_c \omega \sigma}} \qquad (4-43)$$

where δ, σ and μ_c are the skin depth, metallic conductivity and magnetic permeability of the metal, respectively.

The attenuation constant can be presented as [110]

$$\alpha = -\frac{1}{2P}\frac{dP}{dz} = \frac{1}{2}\frac{P_{Diss}}{P_{Tran}} \qquad (4-44)$$

$$\frac{dP}{dz} = -\frac{1}{2}Re\{\hat{n} \cdot E_t \times H_t^*\} \qquad (4-45)$$

where P_{Diss} and P_{Tran} are the total propagating power, dissipated power in ohmic loss per unit length of the waveguide, and power transmitted, respectively. The dissipated power and transmitted can be estimated as

$$P_{Diss} = \frac{1}{2}Re\{Z_s \oint_l |H_t|^2 \, dl\} \qquad (4-46)$$

$$P_{Tran} = \frac{1}{2}Re\{\oint_S E \times H^* \cdot ds\} \qquad (4-47)$$

As a result of the aforementioned analyzes, notwithstanding the ideal conductive surface where the tangential electric field components are zero at the surface, the presence of tangential electric field components generates an ohmic loss on the surface of a conductive surface with finite conductivity values

[113]. To decrease the ohmic losses in the waveguides, the energy density close to the interior conductive walls should be lessened.

The ability to support higher-order modes in waveguides grants them the capability to work under modes with lower loss performance by modifying the host guiding structure, opposed to the transmission lines that can only support the fundamental TEM mode. The aforementioned concept comes from the point that the waveguide working mode influences the propagation loss performance. For a better explanation, suppose an uncomplicated parallel plate waveguide. The transverse TEM mode has a uniform distributed E-field, but, while it is triggered with TE mode, the E-field is zero on the conductive surfaces. In [90], it is determined that losses will increase by decreasing the plate separation and increasing the operating frequency for TEM mode, whereas they are decreased by increasing the plate separation and increasing operating frequency for TE mode.

Concerning the intended Hedgehog waveguide, the $R_m^H(x,y)$ in (4-31) expresses the H-field component in the space among the pins, and it is reduced in the space among the pins from $y = h$ to $y = 0$, and $y = b - h$ to $y = b$ on the lower and upper walls, respectively (Figure 4.23(c)). Figure 4.23(c) displays the H-field inside the Hedgehog waveguide at $z = 0$ plane. As it is explicit from this figure, the H-field is zero on the side walls and has a uniform distribution along the y-axis in the space where $h < y < b - h$, but, its amplitude is reduced in the space among the pins (Figure 4.23(c)). Moreover, it is being represented in (4-46) that the losses will reduce by decreasing the tangential element of the H-field (H_t) on the walls. As a consequence, the dissipated power can be estimated by integrating H_t around the designated curve at $z = 0$ plane in Figure 4.23(b). Meanwhile, in a conventional hollow waveguide, the tangential element of H-field is zero on the side walls and has a uniform distribution along the y-axis in the space between the lower and upper walls, as depicted in Figure 4.23(c). It is obvious from this figure that H_t has a large amplitude on the entire lower and upper walls opposed to the intended Hedgehog waveguide that has H_t almost zero on the space among the pins on the lower and upper walls. The attenuation constants are estimated by numerical analysis for the intended Hedgehog waveguide and compared with the hollow waveguide in Figure 4.24.

B. Experimental Results

It is a bit complicated to extract the experimental results, and the subsequent test setup should be pursued to be capable of evaluating the propagation losses of the intended Hedgehog waveguide and eliminate the losses caused by the transition parts. As specified in [21], subtracting S_{21}^{Case2} from S_{21}^{Case1}, regarding the waveguides with various lengths shown in Figure 4.25, would eliminate the losses caused by both hollow-to-Hedgehog waveguides and vertical-to-horizontal hollow waveguide transition parts. To determine the experimental propagation loss per meter of the Hedgehog waveguide, equation (4-48) can be utilized [21].

The experimental propagation losses in dB per meter are represented in Figure 4.26 for comparison between both waveguides.

$$Hedgehog\ Waveguide\ Loss = \frac{S_{21}^{\mathrm{Case2}} - S_{21}^{\mathrm{Case1}}}{L_{g2} - L_{g1}} \qquad (4-48)$$

$$Hollow\ Waveguide\ Loss = \frac{S_{21}^{\mathrm{Case4}} - S_{21}^{\mathrm{Case3}}}{L_{g2} - L_{g1}} \qquad (4-49)$$

C. Power Handling Capacity

The power handling potential of a guiding structure is subjected to both temperature (average power) and voltage breakdown level (peak power) restrictions. Concerning voltage breakdown restrictions, it would be estimated by using the Boltzmann equation while an electromagnetic field is applied. Meanwhile, the voltage breakdown level in the atmosphere depends on the applied EM-field frequency and the environmental variables, such as humidity and atmospheric pressure [114]. An effective electric field is represented as [114]

$$E_{eff} = \frac{E_{rms}}{(1 + \frac{\omega^2}{v_c^2})^{\frac{1}{2}}} \qquad (4-50)$$

In here, E_{rms} is the root mean square electric field, ω is the angular frequency ($2\pi f$) and v_c is the frequency of collision of electrons. For air, the frequency of collision of electrons is [114]

$$v_c = 5 \times 10^9 p \qquad (S^{-1}) \qquad (4-51)$$

p is the atmospheric pressure in $Torr$. The effective field term is quite useful since it decreases the voltage breakdown restrictions in the alternating current (AC) to the corona phenomena in the direct current (DC) [115]. It can be supposed that the effective field provides the equal field intensity as in a DC field, so experimental data can be analyzed in DC rather than AC [115]. For an applied electrostatic field, we have

$$E = \frac{V}{d} \qquad (4-52)$$

In here, d is the length along the electric field orientation, and V is the breakdown voltage level which is approximately 3 kV/mm for the air. The numerical integration is conducted on the electrical field regarding waveguides to extract E_{rms}, and the values of 3120 kW and 3585 kW are evaluated for the Hedgehog and hollow waveguides utilizing the numerical computation, respectively.

Concerning the temperature (average power), the power handling parameter is determined by imposing a specified temperature rise in the conductive surfaces of a waveguide [116]. The dissipated energy is then associated with the rate of heat transfer from the waveguide surfaces to reach the power rating of the waveguide through the thermal convection rate equation [116].

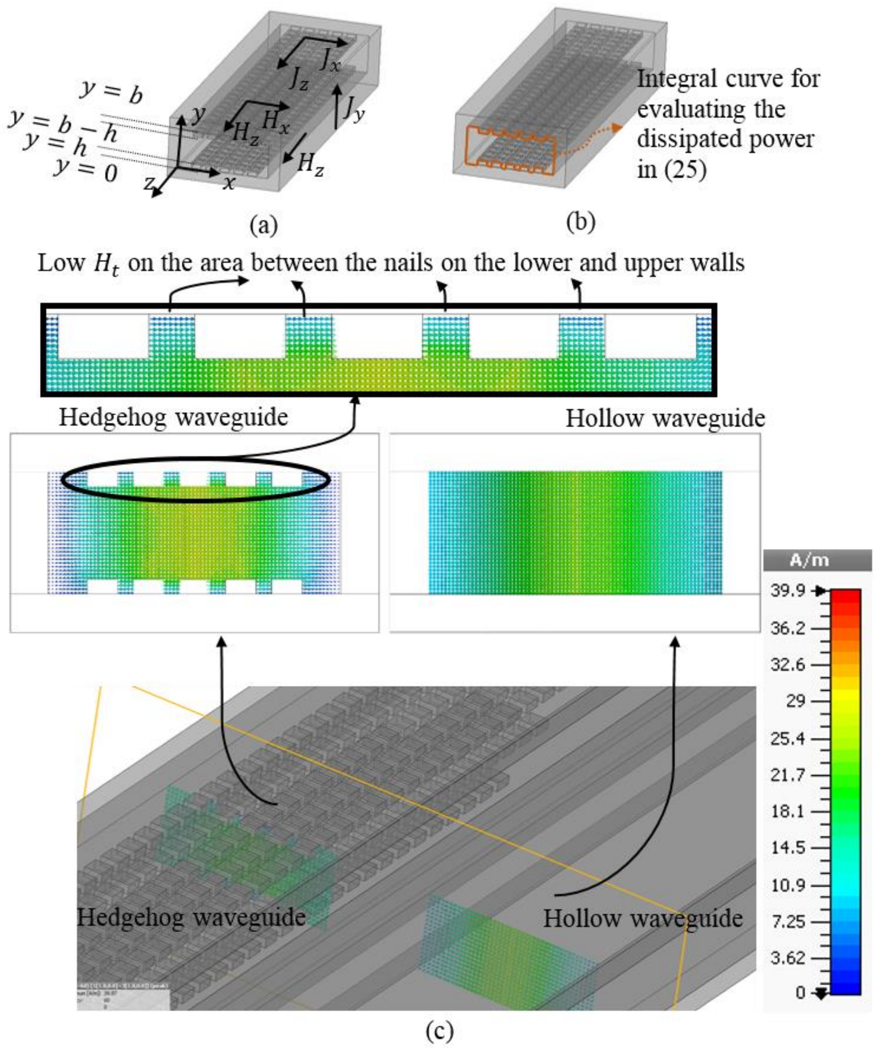

Figure 4.23: Indicating that the energy density near the inner metallic walls of the waveguide is reduced.(a) Existing fields inside the waveguide and currents on inner waveguide walls. (b) The dissipated power can be evaluated by integrating H_t around the indicated curve at $z = 0$ plane. (c) Magnetic field vectors at $z = 0$ plane. The $|H_t|$ density on the metal is reduced in the area between the pins in the proposed Hedgehog waveguide (M. Farahani et al. [23], @2019 IEEE).

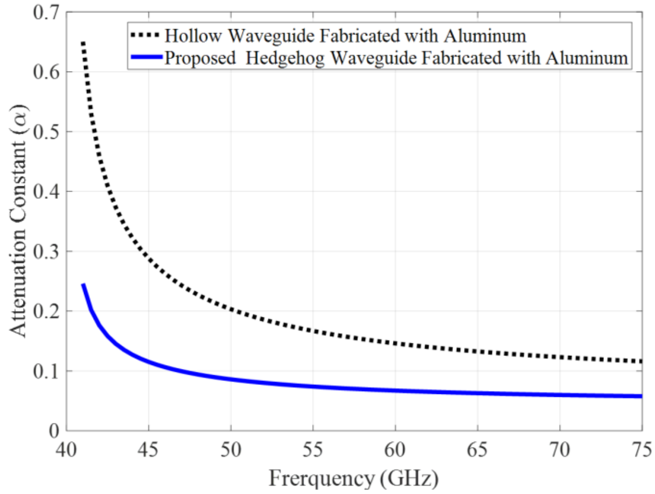

Figure 4.24: Comparison of attenuation constants of the Hedgehog waveguide and hollow waveguide fabricated with aluminum. The dimensions are $h = 0.13$, $A_r = 0.4$, $g = 0.2$, $a = 3.8$, $b = 1.6$, all in millimeters (M. Farahani et al. [23], @2019 IEEE).

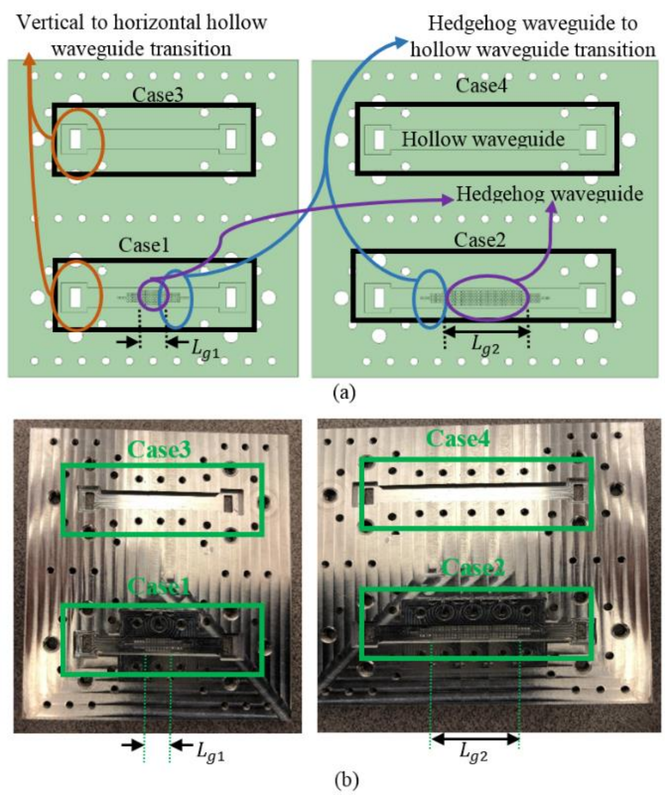

Figure 4.25: Two Hedgehog waveguides with different lengths for measuring propagation losses per meter using equation (4-48). The upper parts of waveguides are not shown for simplicity. (a) Top view of the lower body of waveguides. (b) Photo of fabricated prototypes (M. Farahani et al. [23], @2019 IEEE).

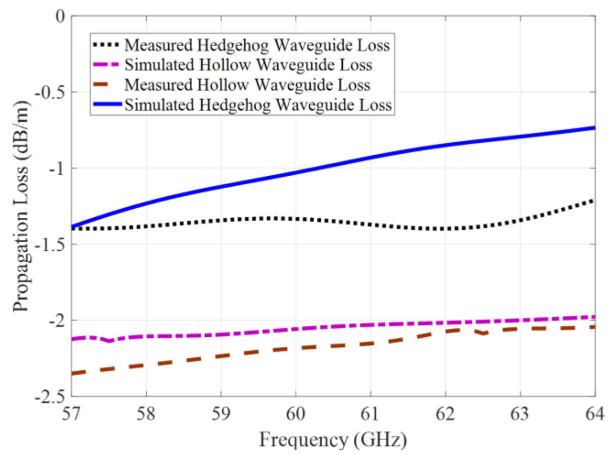

Figure 4.26: Results comparison of the Hedgehog and hollow waveguides experimental propagation losses in dB per meter (M. Farahani et al. [23], @2019 IEEE).

4.3.4 Hedgehog Waveguide Phase Shifter

A. Principal Concept

Phase shifters are fundamental elements for improving mmWave communication systems. Several methods have been introduced for developing phase shifters in the literature that can be classified into three groups. The first group is utilized delay lines, which are described as switched-line phase shifters [117]. The second group is those whose phase shift is caused by lumped elements associated with a distributed transmission line. The reflection-type phase shifter that is formed by a hybrid coupler connected to variable capacitors, is an example of this type [118]. The third group is those who presenting different phase shifts by modifying the properties of the host guiding structure [119]. In this project, we utilize the intended Hedgehog waveguide to modify the dispersion characteristics of the host hollow waveguide to realize a low phase-error wideband phase shifter. Figure 4.22 presents the dispersion diagram of the Hedgehog waveguide. It can be understood from this figure, that the propagation constant inside the waveguide is shifted up by increasing the height of the pins. In other words, the propagation constant difference between the hollow and Hedgehog waveguides is constant across the working frequency range from 57 to 64 GHz, that indicates the phase variation for the traveling wave inside the Hedgehog waveguide compared to the hollow waveguide is constant across the working frequency range and is estimated as following

$$\theta = \beta_{diff3} \times L \qquad (4-53)$$

In here, θ is the shifted phase associated with the conventional hollow waveguide, and L is the physical length of the Hedgehog waveguide. β_{diff3} is the propagation constant difference between the Hedgehog and hollow waveguides, as displayed in Figure 4.27(e).

B. Hedgehog Waveguide to Hollow Waveguide Transition

In the preceding section, it is determined that the propagation constant difference between the hollow and Hedgehog waveguides is constant across the entire working frequency range from 57 to 64 GHz, that indicates the phase variation for the traveling EM-waves inside the Hedgehog waveguide associated with the traditional hollow waveguide is frequency-independent and is estimated utilizing (4-52). Nevertheless, this frequency-independent performance can be degenerated by employing an unprofessional transition. Therefore, it is important to employ a transition from the Hedgehog to the hollow waveguides that setting up the impedance matching between the two waveguides and has no effect on the phase.

Through a parametric study carried out utilizing Ansys HFSS, the most reliable approach to transit from the Hedgehog to the hollow waveguides is decreasing the numbers of implemented pins smoothly to achieve the most desirable impedance matching condition. Figure 4.28 presents different possible combinations for such a transition, and the most desirable matching condition is achieved for the arrangement exhibited in Figure 4.28(a). Moreover, it is essential to make the impact of the intended transition zero on the phase response of the phase shifter. To perform such an approach, the dispersion diagram of the one-row and three-rows pins are obtained and represented in Figure 4.27. As it is explicit from this figure, the dispersion curves are parallel and just shifted up by installing the pins in the host hollow waveguide. The frequency-independent phase response of the phase shifter is determined using (4-52), and the extra phase caused by the transition can be estimated as following

$$\Phi = 2 \times (\beta_{diff1} \times L_1 + \beta_{diff2} \times L_2) \qquad (4-54)$$

In here, β_{diff1} and β_{diff2} and are the propagation constant differences among the hollow and one-row pins and three-rows pins waveguides, respectively, as displayed in Figure 4.27(e). L_1 and L_2 are the physical lengths of the one-row pins and three-rows pins in the transition part, respectively, as illustrated in Figure 4.29. β_{diff1} and β_{diff2} are constant values across the entire frequency range from 57 to 64 GHz. The extra phase caused by the transition is frequency-independent and can be set to zero ($2n\pi$ where n is integer number) or a fixed amount by choosing the appropriate amounts for the physical lengths L_1 and L_2.

Figure 4.29 presents the phase shifter and invented transition. The phase response and S-parameters of the introduced phase shifter utilizing the intended transition are presented in Figure 4.30 and Figure 4.31, respectively. The physical lengths of L, L_1, L_2 are chosen utilizing (4-53) and (4-54) to obtain 45^o phase shift. The dimensions are $L = 5.4$, $L_1 = 1.8$, $L_2 = 2.4$, $h = 0.13$, $A_r = 0.4$, $g = 0.2$, $a = 3.8$, $b = 1.6$, all in millimeters.

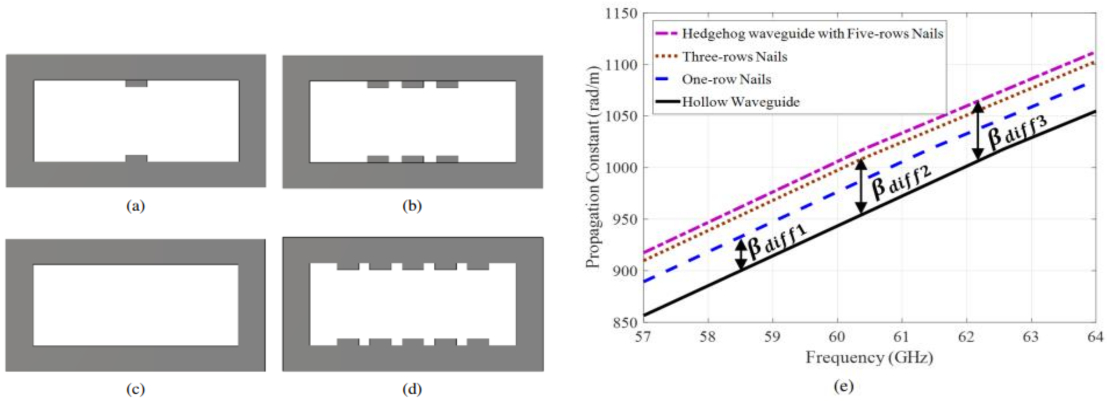

Figure 4.27: Extracted dispersion diagram of waveguides with (a) One-row of pins. (b) Three-rows of pins (c) Hollow waveguide (d) Proposed Hedgehog waveguide with five-raws of pins.Cross view of waveguides in (a) to (d) (M. Farahani et al. [23], @2019 IEEE).

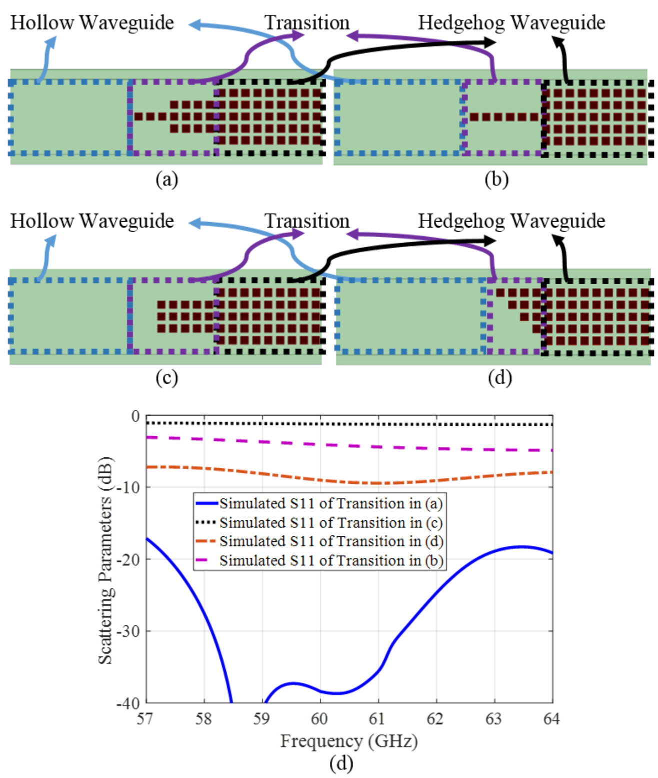

Figure 4.28: Parametric study of different topologies for the Hedgehog waveguide to hollow waveguide transition (a) First topology. (b) Second topology. (c) Third topology. (d) Fourth topology. Top view of waveguides in (a) to (d). (d) Scattering parameters regarding four different topologies for transitions given in (a) to (d) (M. Farahani et al. [23], @2019 IEEE).

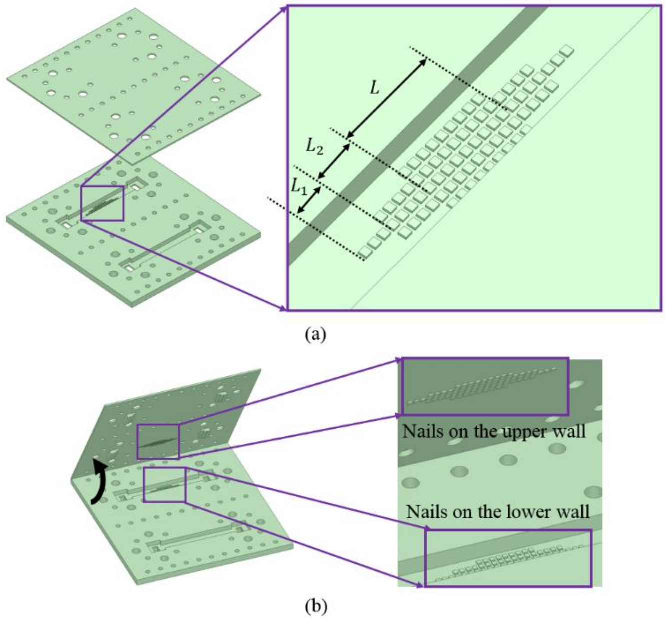

Figure 4.29: The proposed Hedgehog waveguide phase shifter and designed transition (M. Farahani et al. [23], @2019 IEEE).

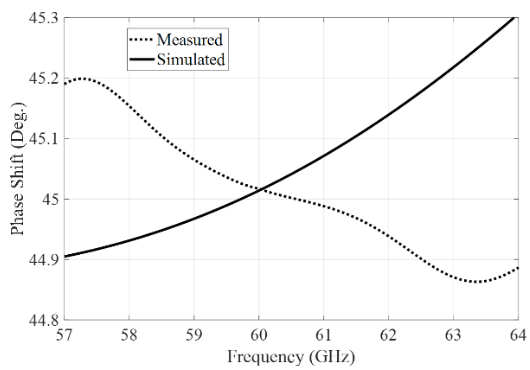

Figure 4.30: Phase response of the proposed phase shifter (M. Farahani et al. [23], @2019 IEEE).

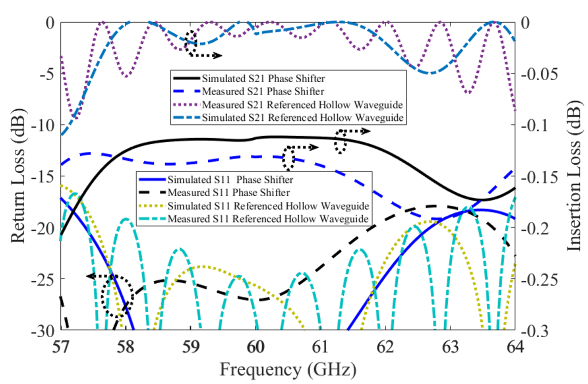

Figure 4.31: Measured and simulated S-parameters of the phase shifter (M. Farahani et al. [23], @2019 IEEE).

4.3.5 Experimental Results

The image of the fabricated phase shifter and the experiment settings are presented in Figure 4.32. PNA series network analyzer and N5260A millimeter head controller with regular WR-15 waveguide connections are utilized to extract the measurement results. A common hollow waveguide is implemented on the same platform next to the phase shifter to neutralize the impact of the vertical-to-horizontal transition and the hollow waveguide losses. Figure 4.31 presents the simulated and measured S-parameters of the intended phase shifter. The measured return loss is lower than -20 dB in the whole frequency range from 57 to 64 GHz. The numerical and experimental results accord considerably well with each other. The insertion loss is lower than 0.2 dB across the whole frequency range. The simulated and measured phase response, associated with the traditional hollow waveguide implemented next to the phase shifter, is presented in Figure 4.30. An accurate phase shift of 45^o with the phase-error lower than 0.4^o is obtained across the entire working frequency range. Table 4.3 distinguishes the intended phase shifter with the other published shifters [120]-[123]. As can be perceived from this table, the offered phase shifter has the best loss performance and phase-error at 60-GHz frequency-band.

Table 4.3: Comparison between the proposed phase shifter and some other phase shifters reported in literature (M. Farahani et al. [23], @2019 IEEE).

Reference	Maximum Insertion Loss	phase-error within 57-64 GHz	f (GHz)
Ref. [120]	10.7 dB	1.5^o	60
Ref. [121]	5.9 dB	17.5^o	60
Ref. [122]	3.0 dB	33^o	60
Ref. [123]	2.4 dB	11^o	60
This work	0.2 dB	0.4^o	60

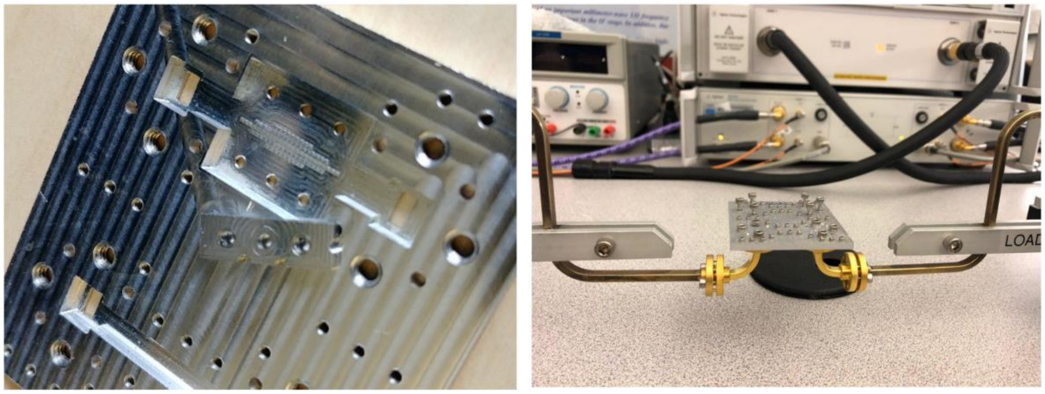

(a) **(b)**

Figure 4.32: The photo of the fabricated prototype and test setup.(a) Fabricated prototype. (b) Test setup (M. Farahani et al. [23], @2019 IEEE).

4.4 Conclusion

In this chapter, an innovative Hedgehog waveguide has been introduced fully studied. The dispersion characteristics and losses of the waveguide have been obtained, and a wideband transition from the intended Hedgehog to hollow waveguides has likewise been proposed. The low-loss characteristics of the Hedgehog waveguide present it as a great competitor for implementing mmWave components. For example, a 45^o phase shifter has been proposed and fabricated utilizing this technology. The features of the Hedgehog waveguide make it a good candidate for developing phase shifters at mmWave with insertion losses less than 0.2 dB and low phase-error smaller than 0.3^o in the whole working frequency range from 57 to 64 GHz. The flat phase behavior of the phase shifter makes it exceptional for developing mmWave beamformers where the phase shifters in these systems usually are implemented using a delay line, that has a larger phase-error in the working frequency ranges, or are implemented using active phase shifters which have a huge amount of insertion loss. Furthermore, the presented waveguide is compatible with the hollow waveguide, which makes developing the beamformers with these technologies easier.

Moreover, an mmWave 3-dB hybrid coupler implemented in microstrip ridge gap waveguide has been designed and fabricated in this chapter. The dispersion diagram of the intended microstrip ridge gap waveguide has been obtained, and a transition to the microstrip transmission line has been introduced. The multi-coupling aperture approach has been employed for designing the coupler. The formulas have been expressed to model the large coupling apertures where Bethe's small-aperture coupling theory does not lead to good anticipation. The phase response of the large coupling apertures has been utilized to neutralize the output progressive phase of the coupler. The designed coupler has a pretty low insertion loss at mmWave frequency range. It has been demonstrated that why the recommended ridge gap coupler has an extremely low insertion loss compared to the other mmWave couplers manufactured with other technologies such as SIW waveguide or microstrip transmission line.

Chapter 5 State-of-the-art mmWave Beamformer Networks

This chapter contains materials extracted from the following publications:

[J1] M. Farahani, M. Akbari, M. Nedil, A. R. Sebak and T. A. Denidni, “Millimeter-Wave Dual Left/Right-Hand Circularly-Polarized Beamforming Network,” submitted to the *IEEE Transactions on Antennas and Propagation,* 2019.

[J2] M. Akbari, M. Farahani, S. Zarbakhsh, M. Dashti Ardakani, A. R. Sebak, T. A. Denidni and Omar M. Ramahi, “Highly Efficient 30-GHz 2×2 Beamformer Based on Rectangular Air-Filled Coaxial Line,” submitted to the *IEEE Transactions on Antennas and Propagation,* 2019.

5.1 Introduction

The mmWave band has provided notable attention since it can obtain considerable available spectrum resources to answer the developing demands in the future 5G, the next generation of mobile communication, for a greater quality of experience (QoE) [24]. Nevertheless, the mmWave propagating waves confront considerable free-space propagation loss, penetrating reluctance, rain impact, and air absorption. One approach is employing a state-of-the-art method that employs a considerable number of antenna elements at the base stations to compensate for these drawbacks in the mmWave communication systems that can provide high directive beams to compensate for the significant propagation loss. Besides, user movement breaks the pattern alignment and requires continuous retraining, considerably increasing the beamforming duty [24]. This especially is valid for user rotation. In 60-GHz band, the experiments prove that a small misadjustment of 18^o degenerate the link budget about 17 dB in a communication system with an 7^o antenna beamwidth. Based on IEEE 802.11ad coding sensitivities [24], the greatest throughput would reduce by up to 6 Gbps upon this degeneration or break the connection fully.

To resolve this difficulty, Butler matrixes can be a qualified technique as a low-cost beamforming approach when we are searching for a potential alternative [124]. A combination of this passive beamforming system along with a linear array of antennas would be employed in future 5G technologies. The main beam of the system is oriented at specific points, by stimulating several input ports. The Butler matrix approach with SIW waveguide has been investigated in the literature [124]-[127]. The size reduction and bandwidth improvement have been studied in most of these methods. Another technology for realizing the Butler matrixes is the hollow waveguide [128]-[129]. It is a qualified choice as the host guiding structure in many mmWave systems. Tremendous feeding circuits can be realized in the hollow waveguide with nearly low insertion losses.

In Section 5.2 of this chapter, an exceptional high-efficiency dual left/right-hand circularly-polarized (LH/RH CP) beamforming network is introduced and studied at 60-GHz mmWave band. The Hedgehog waveguide is employed as a notably low-loss guiding structure to implement the crucial phase shifters. The offered beamformer produces uniform progressive-phase output waves to supply an array of antennas with the eight separate radiation patterns associated with each of the eight input ports. Furthermore, the progressive slot antenna is utilized to obtain a broadband axial-ratio bandwidth. The bandwidth of 10.75% and the radiating efficiency of 90% for each port is obtained utilizing the intended beamforming network.

In Section 5.3 of this chapter, we introduce a low loss 4×4 beamformer with a capability of two-dimensional scanning in elevation and azimuth directions at 30-GHz for future 5G applications. The suggested beamformer is based on the broadband and highly-efficient rectangular air-filled coaxial line.

5.2 Dual Left/Right-Hand Circularly-Polarized Beamformer Network

In 60-GHz mmWave band, the CP operation is interested because it can reduce likely polarization mismatch among the base stations and users, and it can lessen the multipath effects contrary to the linearly-polarized networks [130] and are furthermore more powerful to mitigating fading and undesired multipath [130]-[132]. Meanwhile, a regular 4×4 Butler matrix can provide approximately 9 dBi gain (6 dBi array factor plus 5 dBi single antenna minus 2 dB losses), which is not sufficient at 60-GHz mmWave band.

In this project, an exceptional high-efficiency dual LH/RH CP beamforming network is introduced and studied at 60-GHz mmWave band. The Hedgehog waveguide is employed as a notably low-loss guiding structure to implement the crucial phase shifters [23]. The attenuation constant of the Hedgehog waveguide is significantly smaller than similar traditional guiding structures, e.g., SIW, ridge gap, hollow, and gap waveguides at the 60-GHz mmWave band [23]. The offered beamformer produces uniform progressive-phase output waves to supply an array of antennas with the eight separate radiation patterns associated with each of the eight input ports. For enhancing the gain and reducing the sidelobes, an 8×8 feeding network is employed. Utilizing the introduced feeding network, the sidelobes are reduced to -19 dB. By expanding the number of radiating elements to 8, the directivity of the recommended beamformer raises about 3 dB. Furthermore, the progressive slot antenna is utilized to obtain a broadband axial-ratio bandwidth. The bandwidth of 10.75% and the radiating efficiency of 90% for each port is obtained utilizing the intended beamforming network.

5.2.1 Proposed Beamforming Network Architecture

As an example of a passive beamformer network, we can mention Butler matrix that can obtain uniform progressive-phase signals (i.e., $\pm 45^o$ and $\pm 135^o$) and equal-magnitude signals, to stimulate an array of antennas with the four separate radiation patterns, associated with each of the four input ports [133]. Moreover, a standard 4×4 Butler matrix, in the best scenario, can obtain radiation gain up to 9 dBi (i.e., 6 dBi array factor plus 5 dBi single antenna minus 2 dBi losses), which is not sufficient at 60-GHz mmWave band. For enhancing the gain of the standard Butler matrix, the number of the antenna elements is increased utilizing the proposed network exhibited in Figure 5.1. Referring to this figure, the beamforming chain includes two 4×4 Butler matrix and two pattern control networks. The pattern control network aims to provide the required excitations for both sub-arrays represented in Figure 5.1. As demonstrated in this figure, the number of antenna elements doubled which provides 3-dB extra gain. The radiation features of the extended array in Figure 5.1 depends on the magnitude and phase distribution of the excitations of antenna elements, pattern characteristics, geometrical placement, and inter-element spacing of the antenna elements [134]. A directive beam in a specific point while preserving the sidelobe level (SLL) small, is a growing demand in phased array antenna to avoid interference with other systems and to improve the radiation efficiency of the systems [127], [135]-[138]. In most cases, this would be achieved by controlling the magnitude and phase of the excitation signals. In a Butler matrix, exciting a small linear array, the SLL can be reduced by increasing the number of antenna elements and considering the "lattice condition" [139]-[140] without degenerating the overall array radiation performance. Utilizing this method, the number of radiating elements is doubled in a 4×4 Butler matrix by employing the pattern control networks (Figure 5.1) among the Butler matrices and antenna elements.

The SLL of a uniform progressive-phase signals and equal-magnitude excitation linear array is nearly -13.5 dB [134]. Nevertheless, the spacial coupling among radiating elements and the reflections coefficients of the antenna elements degenerate the SLL to smaller than 10 dB [134]. Furthermore, by extending the separation distance among the radiating elements larger than a wavelength, the grating lobes will emerge in the visible zone. To decrease the SLL and cancel the effect of grating lobes, the number of antenna elements is doubled [139]-[141]. Therefore, the beamforming network will be more complex compared to a regular 4×4 Butler matrix. For holding greater levels of freedom, the amplitude tapering technique [134] is employed for reducing sidelobes more. The four unbalanced power dividers have the task to supply the antenna elements unbalanced. As can be observed from Figure 5.1, the magnitude of the antenna elements excitations are symmetrical with respect to the center and tapered to the sides if various arguments of $90 - q$, $90 - g$, g, and q ($0 < q < g < 45^o$) from the top to the bottom be chosen as the coupling coefficients for the four unbalanced power dividers. The $q = 31.72^o$ and $g = 36.86^o$ are chosen by utilizing the Particle Swarm Optimization (PSO) [141]. As a result of above discussion, the SLL is decreased to 19 dB adopting this approach for all beams in E-plane. The simulated radiation patterns with and without employing the SLL reduction technique are illustrated in Figure 5.2.

The signal flow diagram of the suggested pattern control network is shown in Figure 5.1. As can be observed from this figure, the pattern control network includes three stages of the cross-over sections and phase shifters. The pattern control network provides the required excitations for both sub-arrays presented in Figure 5.1. For achieving a uniformly phased array, the second sub-array should be 180^o lagging the first sub-array as demonstrated in Figure 5.3. This condition is implemented in the signal flow diagram of the pattern control network by employing the 180^o phase shifters as presented in Figure 5.1. Figure 5.3 presents the phasor diagram of the signals in the beamforming network. By feeding $Port$ 1 and 2, the progressive phases of $\pm 45^o$ and $\pm 135^o$ will be produced respectively at the output ports of the Butler matrix, as shown in the left side Figure 5.3. The pattern control network distributes the output signals of the Butler matrix among the two sub-arrays. In this situation, the total array factor is a multiplication of the two separate array factors, the array factor concerning one of the sub-arrays and a 1×2 array with radiating element separation distance of P (Figure 5.1). The sub-arrays will radiate in four different directions, which determines that the 1×2 array with radiating element separation distance of P must be accompanied by at least two smart phase shifter, associated with the $Port$ 1 and 2 excitations. Actuality, there are two solutions to resolve this difficulty. The first solution is based on choosing the radiating element separation distance between the two sub-arrays eight times of the radiating element separation distance in sub-arrays, which lead to emerging grating lobes in the visible zone. The sub-arrays are radiating at φ_1 and φ_2 while exciting $Port$ 1 and 2 as follow:

$$Port\ 1\ excitation \xrightarrow{yields} kS\cos(\varphi_1) + 45^o = 0 \qquad (5-1)$$

$$\Rightarrow \quad \cos(\varphi_1) = -\frac{45^o}{kS} \qquad (5-2)$$

$$Port\ 2\ excitation \xrightarrow{yields} kS\cos(\varphi_2) + 135^o = 0 \qquad (5-3)$$

$$\Rightarrow \quad \cos(\varphi_1) = -\frac{135^o}{kS} \qquad (5-4)$$

In here, k is the propagation constant. To satisfy the condition that the 1×2 array with radiating element separation distance of P also radiates at φ_1 and φ_2, the two following conditions should be satisfied:

$$Port\ 1\ excitation \xrightarrow{yields} kP\cos(\varphi_1) = 0 \qquad (5-5)$$

$$Port\ 2\ excitation \xrightarrow{yields} kP\cos(\varphi_2) = 0 \qquad (5-6)$$

By substituting φ_1 and φ_2 from (5-1) and (5-3) into (5-5) and (5-6), the only solution is P equals to $8 \times S$, which indicates that the radiating element separation distance among the two sub-arrays must be eight times of the radiating element separation distance in sub-arrays. With this solution, there is no demand for extra phase shifters; nevertheless, this leads to emerging grating lobes in the visible zone. Additionally, the second solution is employing a 180^o phase shifter among the two sub-arrays as illustrated in Figure 5.3. By employing this approach, the grating lobes difficulty in the first solution would be resolved; but, eight more phase shifters are required.

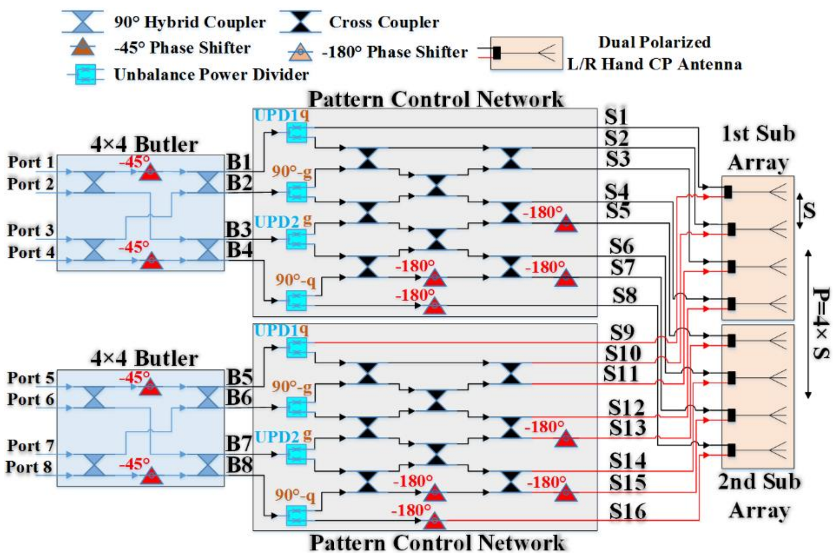

Figure 5.1: Proposed dual LH/RH CP beamforming network architecture (M. Farahani et al. [J1], @n.d. IEEE).

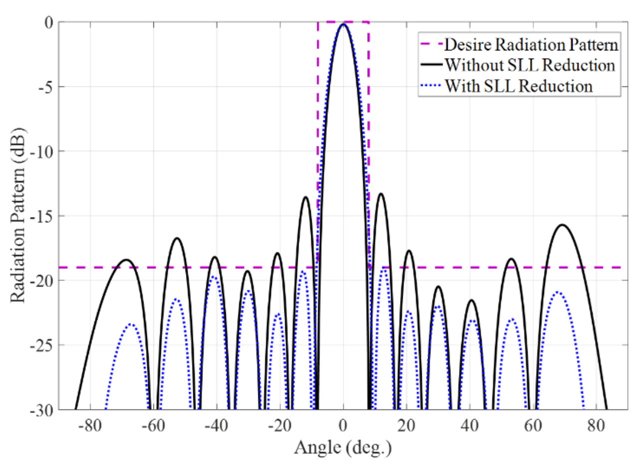

Figure 5.2: The simulated radiation pattern with and without SLL reduction (M. Farahani et al. [J1], @n.d. IEEE).

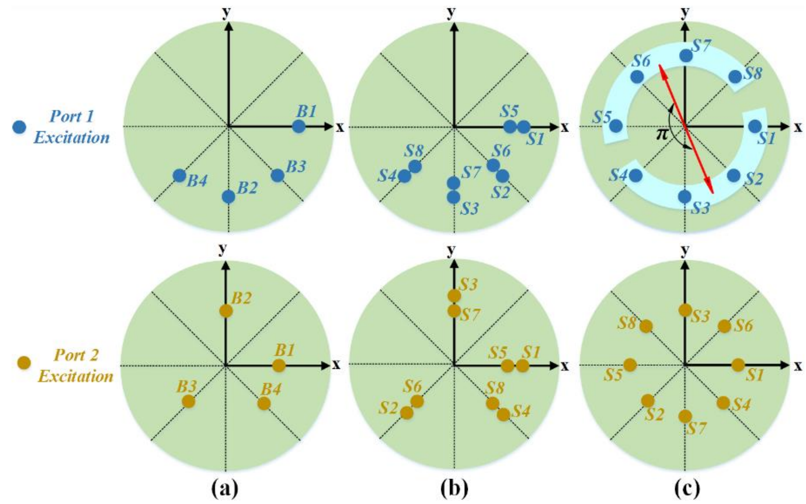

Figure 5.3: Phasor diagram of the proposed beamformer in Figure 5.1 (M. Farahani et al. [J1], @n.d. IEEE).

5.2.2 Travelling-Wave Progressive Slot Antenna

The polarization mismatch loss can deteriorate the link performance of the system because of propagation channel characteristics at the 60-GHz mmWave band. It has been explained that mysterious notches may exist in received power unlike systems at lower microwave bands since multipath signals are negligible at 60-GHz mmWave band [142]. Besides, signals which are reflected for the second time are typically 10 dB weaker than the line-of-sight (LOS) signals [143]. Therefore, the LOS and first time reflected signals are typically participating in the received signal at the receiver. As a result, the 60-GHz mmWave band works considerably different from those at microwave bands because of the wide bandwidth, polarization mismatch loss, and short-wavelength. The CP antennas suggest a desirable answer for resolving the polarization mismatch loss and lessening the fading difficulty and giving flexibility concerning the orientation among antennas at transmitter and receiver [144]-[145].

The Vivaldi Aerials are theoretically frequency-independent antennas [146]. These antennas have linear polarisation and can be designed to have a fixed gain over the working frequency range. There were many attempts in literature to determine the radiation pattern [147], cross-polarization [148] and introduced several methods to enhance the antenna performance, such as corrugated technique for enhancing the gain [149]-[150], gain improvement using artificial material [151], and various slot shape to enhance the impedance bandwidth [152]. Nevertheless, all of these approaches are linearly-polarized (LP). In [153]-[158], the circularly-polarized antipodal antennas have been introduced by Xiaodong Chen et al. for mmWave frequency-bands. These structures are wideband and can obtain a bandwidth of up to 40%.

In this project, we introduce an innovative dual LH/RH CP antenna implemented in hollow-waveguide. Figure 5.4 displays the 3D view of the recommended dual LH/RH CP antenna. The antenna constructed of two waveguides attached on each other and a triangle slot on the common wall to create the desire x-axis mode. Furthermore, there are two slots on the lower and upper walls as described in [154].

$$Curve\ 1: \qquad y_1(\mathrm{z}) = \pm\left(\frac{2(M_0 + M_1)}{1 + e^{-\xi_1 z}} - 2M_0 - M_1\right) \qquad (5-7)$$

$$Curve\ 2: \qquad y_2(\mathrm{z}) = \pm\left(\frac{2(M_2 - M_3)}{1 + e^{-\xi_2 z}} - 2M_2 + M_3\right) \qquad (5-8)$$

where z varies from 0 mm to L_a. The value of M_0, M_1 and ξ_1 define the starting point and opening aperture size of the Curve 1, respectively. The value of M_2, M_3 and ξ_2 have the same rule for Curve 2.

The presented method for studying the CP operation in the recommended two-layer hollow waveguide is based on odd/even-modes analyses. The feeding rectangular waveguides at $Input$ 1 and 2 are operating at TE_{10} mode. By exciting $Input$ 1, the feeding TE_{10} field will be converted to the other modes that can be analyzed by odd- and even-mode fields, as demonstrated in Figure 5.5. The electric fields have the alike direction in both lower and upper waveguides and have the reverse orientation in the lower and upper waveguides by considering the odd-mode fields (see Figure 5.5). These lead to the unchanged TE_{10} mode at $Input$ 1 without coupling between $Input$ 1 and 2. The other mode along the x-axis (TE_{01}) will be triggered gradually by moving along the triangle slot (BB'), as described in Figure 5.5. Meanwhile, it is well-known that the CP waves are formed by two LP modes with 90^o out of phase and equal amplitude [159]. The different guided wavelengths of two TE_{10} and TE_{01} modes obtain the required 90^o phase shift. Eventually, through the progressive slot in the upper and lower sides, the condition for equal amplitude is satisfied. The width of the slot gradually increases while moving toward the antenna aperture on the upper and lower sides, which excites increasing TE_{01} amplitude (see Figure 5.5). The amplitude and phase difference of the two orthogonal modes (TE_{10} and TE_{01}) in the antenna aperture at 60-GHz are presented in Figure 5.6. As a result, the condition for two LP modes with 90^o out of phase and equal amplitude is perfectly satisfied.

Moreover, by exciting $Input$ 2 alternatively, the theory for exciting the CP wave is alike, whereas the field vectors are only inverted in the odd mode. Besides, the fields vectors rotate in the opposite direction on the antenna aperture excited by $Input$ 2, opposed to that excited by $Input$ 1. Accordingly, a dual LH/RH CP operation can be achieved for the intended antenna by exciting each of the input ports.

The intended antenna is simulated utilizing Ansys HFSS. The simulated S-parameters and axial ratio of the antenna are displayed in Figure 5.7. As can be seen, the reflection coefficients are lower than -25 dB. Furthermore, the isolation among the ports is better than -20 dB in the working frequency range. The radiation patterns, concerning different exciting ports, at 60-GHz are presented in Figure 5.8.

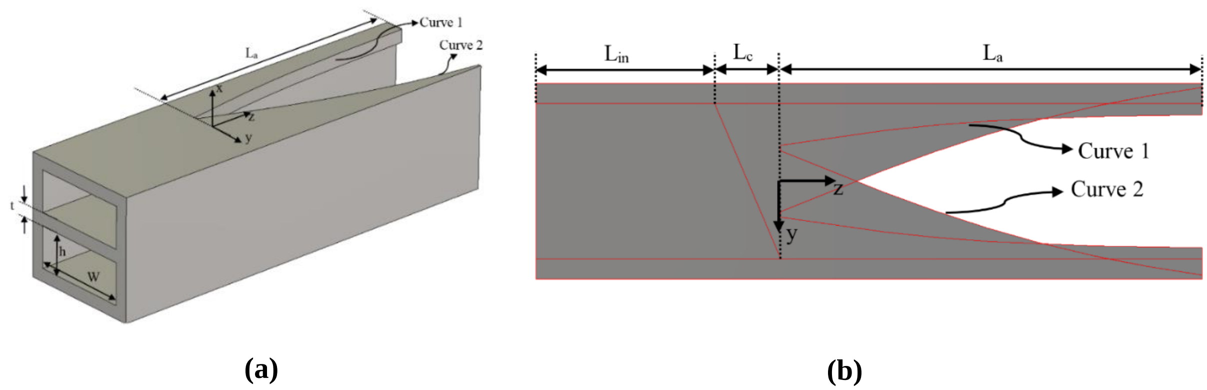

Figure 5.4: 3D view of the proposed dual-polarized LH/RH CP antenna.(a) Side view. (b) Top view. The dimensions are $L_a = 10.31$, $L_c = 1.62$, $L_{in} = 6$, $h = 1.6$, $W = 3.8$, $t = 1$, $M_0 = 0.74$, $M_1 = 3$, $M_2 = 0.87$, $M_3 = 1.65$, all in millimeters, and $\xi_1 = 0.22$ (mm^{-1}), $\xi_2 = 0.4$ (mm^{-1}) (M. Farahani et al. [J1], @n.d. IEEE).

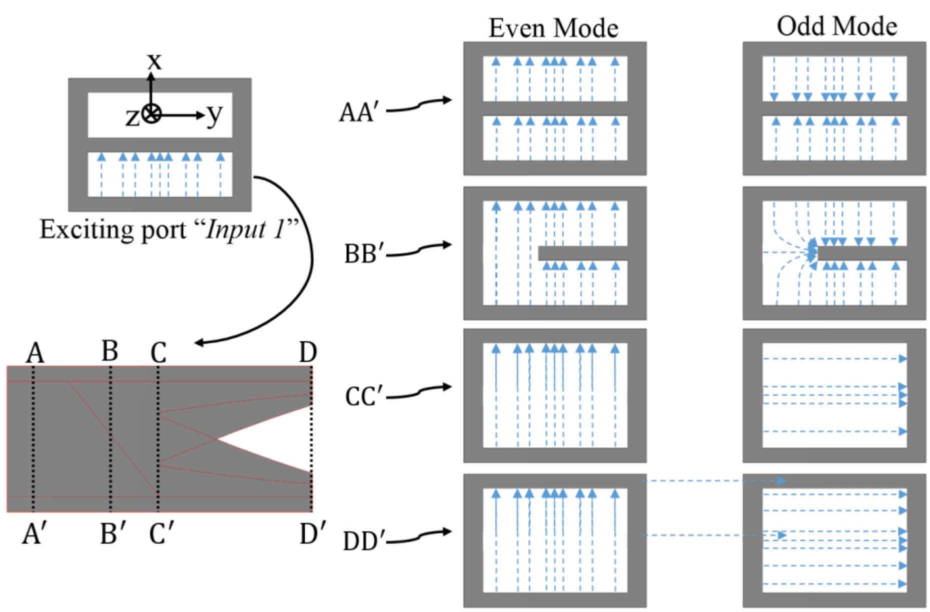

Figure 5.5: The principal theory for exciting the CP wave is investigable based on odd/even-mode analyses.The feeding rectangular waveguides at ports $Input$ 1 and 2 are working at TE_{10} mode. Electric fields at different planes are illustrated (M. Farahani et al. [J1], @n.d. IEEE).

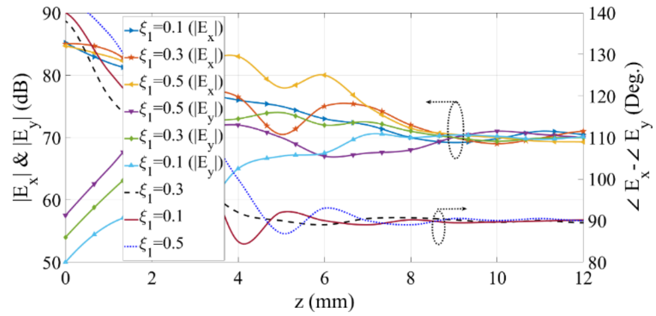

Figure 5.6: The amplitude and phase difference of the two orthogonal modes (TE_{10} and TE_{01}) in the dual-polarized antenna at 60-GHz.As a result, the condition for the two linearly-polarized modes with 90^o out of phase and equal amplitude is basically satisfied. The dimensions are given in Figure 5.4 (M. Farahani et al. [J1], @n.d. IEEE).

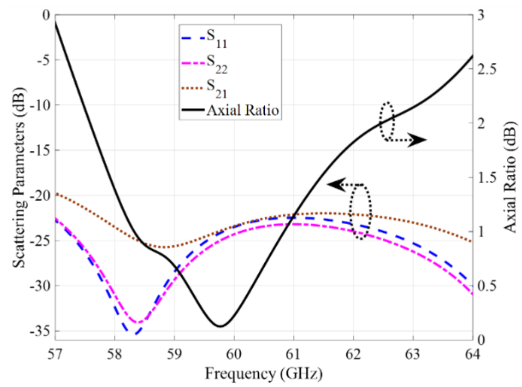

Figure 5.7: Simulated S-parameters and axial ratio of the progressive slot antenna (M. Farahani et al. [J1], @n.d. IEEE).

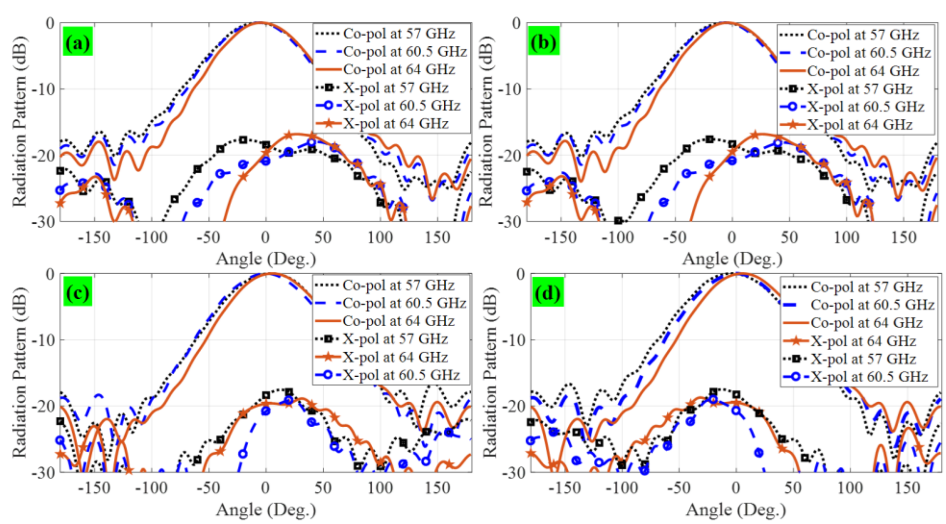

Figure 5.8: Simulated radiation patterns of the dual-polarized progressive slot antenna regarding different excited ports at 60-GHz.(a) xz-plane left-hand circularly-polarized. (b) xz-plane right-hand circularly-polarized. (c) yz-plane left-hand circularly-polarized. (d) yz-plane right-hand circularly-polarized (M. Farahani et al. [J1], @n.d. IEEE).

5.2.3 Design and Performance of Each Block of the Feeding Network

Each element of the feeding network is designed individually with desired return loss of higher than 20 dB to eliminate any possible mismatching among the different elements. Furthermore, to minimize the likely higher-order mode among the connected elements, a minimum connection length equals to half of a wavelength at 60-GHz is applied among the consecutive elements.

Design of the Phase Shifters:

One of the critical components in mmWave communication networks is phase shifter. The operation principle of various phase shifters introduced in literature can be categorized into three methods. The straight forward approach is using delay lines, which are called switched-line phase shifters [117]. Implementing phase shifters utilizing lumped elements to provide additional phase shift along with a matching network is a different method [118]. The reflection-type phase shifter is an example of this approach, which comprises a combination of a branch line coupler terminated to the varactor diodes at the terminals [118]. In the third method, changing the characteristics of the host guiding structure may induce an additional phase shift [119]. The structure of the proposed phase shifter is shown in Figure 5.9(a). The intended phase shifter is studied as a novel waveguide, called Hedgehog [23]. It comprised of an array of pins in both lower and upper walls of the host hollow waveguide. The dispersion diagram of the Hedgehog waveguide is shifted up associated with the host hollow waveguide, as represented in Figure 5.10. In other words, the propagation constant difference among the Hedgehog and hollow waveguides is a fixed value across the entire working frequency range from 57 to 64 GHz, that indicates the phase shift for the traveling waves in the Hedgehog waveguide compared to the host hollow waveguide is fixed value across the entire operating frequency range and can be defined as following:

$$\theta = (\beta_{CW} - \beta_{HW})L \qquad (5-9)$$

In here, θ is the phase shift, and L is the length of the Hedgehog waveguide, as demonstrated in Figure 5.9. β_{HW} and β_{CW} are the propagation constant of Hedgehog and hollow waveguides, respectively.

Furthermore, a transition from Hedgehog to hollow waveguides is essential for combining Hedgehog with hollow waveguides. One of the advantages of the introduced Hedgehog waveguide is its low-loss characteristics [23]. Therefore, supplementary attention should be considered for the transition structure, particularly, the degeneration of its low-loss characteristics by the additional losses by the transition parts. Besides, it is determined that the phase difference is constant across the entire working frequency range; nevertheless, a non-professional transition could degenerate the phase response. The effect of the transition parts on the total phase response and the method to making this impact zero have been studied in [23].

Figure 5.9(a) illustrates the designed transition and phase shifter. The physical length of L is chosen utilizing (5-9) to obtain a 45^o phase shift. The dimensions are $L = 5.4$, $L_1 = 1.8$, $L_2 = 2.4$, $a = 3.8$, $b = 1.6$, $A_r = 0.4$, $h_r = 0.13$, $g = 0.2$, all in millimeters. For a 180^o phase shift, the Hedgehog waveguide and transition dimensions are the same and L is chosen utilizing (5-9) to obtain 180^o phase shift. The S-parameters and phase shift of the intended Hedgehog phase shifters employing the proposed transition are exhibited in Figure 5.11.

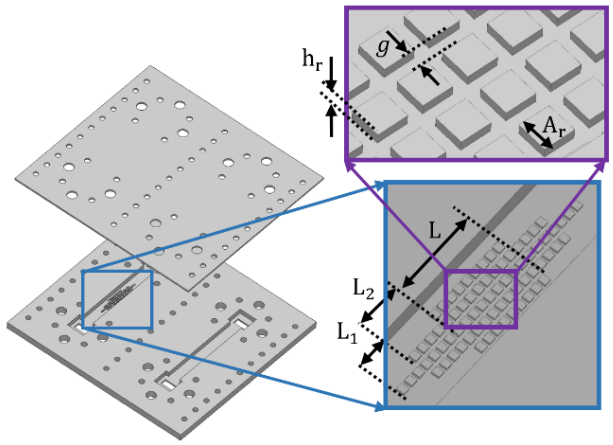

Figure 5.9: The Hedgehog waveguide phase shifter and designed transition.The dimensions are $L = 5.4$, $L_1 = 1.8$, $L_2 = 2.4$, $h_r = 0.13$, $A_r = 0.4$, $g = 0.2$, $a = 3.8$, $b = 1.6$, all in millimeters (M. Farahani et al. [23], @2019 IEEE).

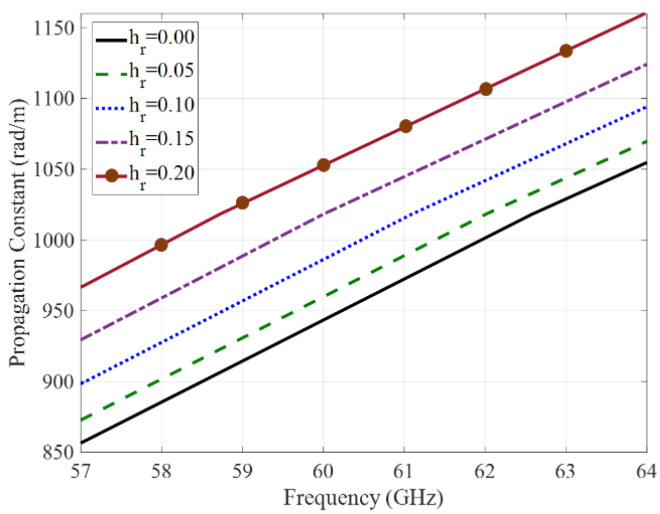

Figure 5.10: Dispersion diagram of the Hedgehog waveguide carried out using CST Microwave Studio eigenmode solver.The dimensions are $A_r = 0.4$, $g = 0.2$, $a = 3.8$, $b = 1.6$, all in millimeters (M. Farahani et al. [J1], @n.d. IEEE).

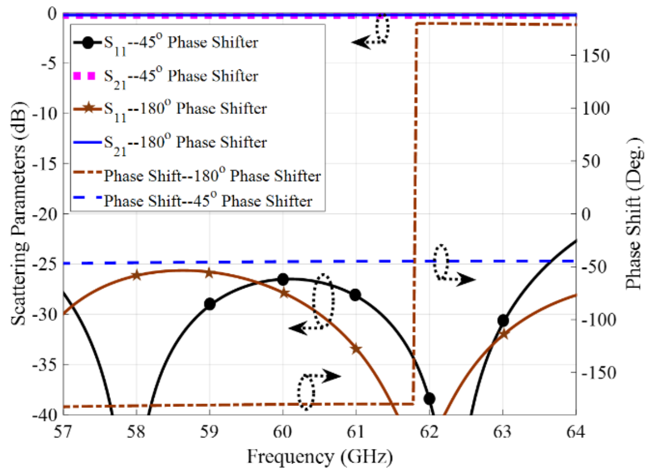

Figure 5.11: The phase response and scattering parameters of the proposed phase shifters (M. Farahani et al. [J1], @n.d. IEEE).

Design of the Coupler and Cross Coupler:

Various approaches for designing a 3-dB waveguide coupler have been introduced in literature [160]-[163]. The structure shown in Figure 5.12 is manipulated to design both coupler and cross coupler realized in the hollow waveguide technology. The structure consists of two hollow waveguides with a coupling aperture in the common wall and two distracting appendages. The coupler is operating in TE_{10} mode, and its performance can be foretold by the method presented in [163]. In addition to TE_{10} mode, the high order mode of TE_{20} exists in the coupling region. By exciting the port $P1$, the received signals at the ports $P2$ and $P3$ can be considered as $\cos((\beta_1 - \beta_1) \times \frac{L_{p1}}{2})$ and $\sin((\beta_1 - \beta_1) \times \frac{L_{p1}}{2})$, respectively. β_1 and β_2 are propagation constants concerning TE_{10} and TE_{20} modes, respectively. Thus, dimensions for coupler and cross coupler can be determined as follows:

$$\begin{cases} (\beta_1 - \beta_1) \times \dfrac{L_{p1}}{2} = \dfrac{\pi}{4} & (for\ coupler) \\ (\beta_1 - \beta_1) \times \dfrac{L_{p1}}{2} = \dfrac{\pi}{2} & (for\ cross\ coupler) \end{cases} \qquad (5-10)$$

Meanwhile, it is required to optimize the structures due to the presence of high order modes, and the optimized dimensions are presented in Table 5.1. Figure 5.13 displays the S-parameters and output phase difference of the intended coupler and cross coupler. As can be observed, the offered coupler has convenient isolation, flat 3-dB power division, and low output phase error. Also, the cross coupler has acceptable isolation.

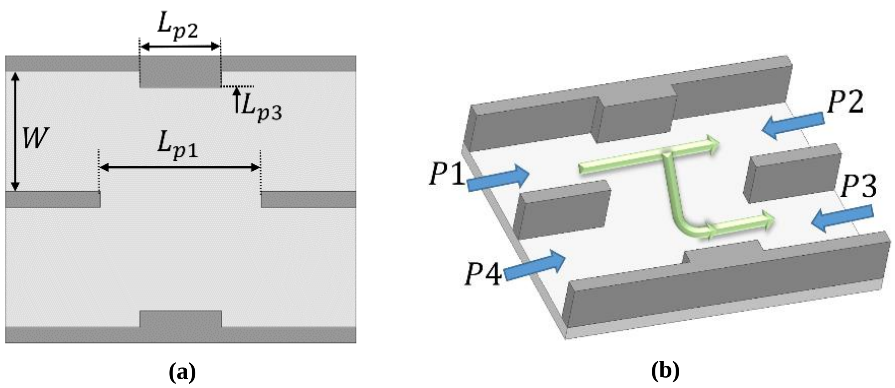

Figure 5.12: The proposed structure for designing the coupler and cross coupler consists of two hollow waveguides with a coupling aperture in the common wall and two distracting appendages. (a) Top view. (b) Side view. (M. Farahani et al. [J1], @n.d. IEEE).

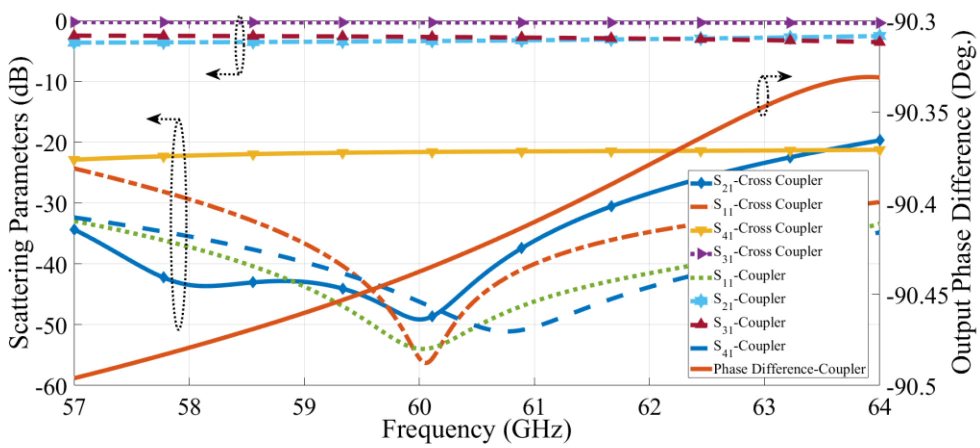

Figure 5.13: Scattering parameters and output phase difference of the coupler and cross coupler (M. Farahani et al. [J1], @n.d. IEEE).

Table 5.1: Coupler and cross coupler dimensions, all in millimeters (M. Farahani et al. [J1], @n.d. IEEE).

Dimensions	L_{p1}	L_{p2}	L_{p3}	W
Coupler	5.09	2.57	0.51	3.8
Cross coupler	9.3	4.5	0.9	3.8

Design of the Unbalanced Power Dividers:

The amplitude tapering technique [134] is employed to reduce sidelobes. The four unbalance power dividers have to feed the antenna elements. As can be understood from Figure 5.1, magnitudes of the antenna element's excitations are symmetrical with respect to the center and tapered to the sides if different arguments of $90 - q$, $90 - g$, g, and q ($0 < q < g < 45^o$) from the top to the bottom be chosen as the coupling factor for the four unbalanced power dividers. The $q = 31.72^o$ and $g = 36.86^o$ are chosen utilizing Particle Swarm Optimization (PSO) [141]. The SLL is then limited to 19 dB utilizing this approach for all beams in the E-plane. Four T-junctions are employed to design unbalanced power dividers to reduce the area of the feeding network. According to the signal flow diagram in Figure 5.1, two separate two-way unbalance power dividers indicated as UPD1 and UPD2 must be designed. The output ports of unbalance power dividers require to have in-phase outputs. Figure 5.14 presents the intended unbalance power dividers. The optimized parameters are illustrated in Table 5.2. For obtaining the $q = 31.72^o$ and $g = 36.86^o$, the right in-phase outputs, return loss, and power division ratio are achieved by optimizing the location of the posts in the T-junctions. Figure 5.15 illustrates S-parameters of the designed unbalanced power dividers.

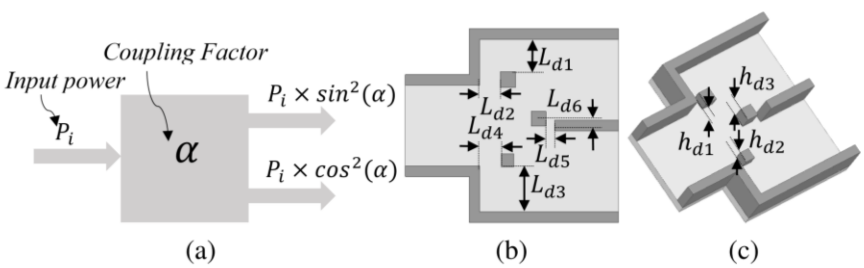

Figure 5.14: The unbalance power dividers.(a) Power division ratio. (b) UPD1. (c) UPD2 (M. Farahani et al. [J1], @n.d. IEEE).

Table 5.2: Dimensions of unbalance power dividers, all in millimeters.

	L_{d1}	L_{d2}	L_{d3}	L_{d4}	L_{d5}	L_{d6}	h_{d1}	h_{d2}	h_{d3}
UPD1	**1.52**	**0.95**	**1.67**	**1**	**0.4**	**0.25**	**0.6**	**0.54**	**0.81**
UPD2	**1.77**	**0**	**1.66**	**0.76**	**0.57**	**1.07**	**0.76**	**1.02**	**0.69**

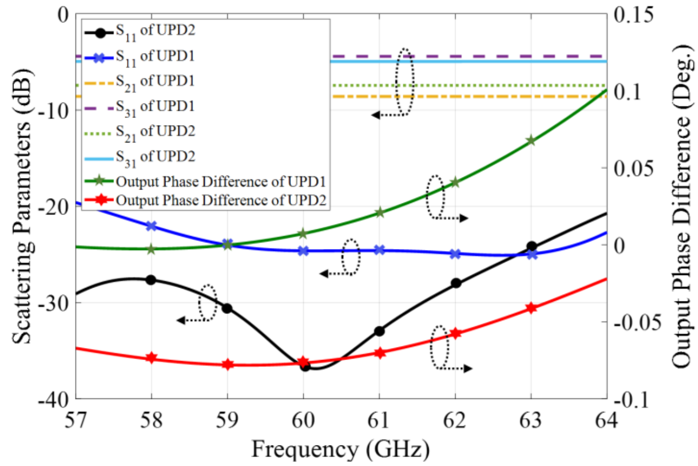

Figure 5.15: S-parameters and output phase difference of UPD1 and UPD2 unbalance power dividers (M. Farahani et al. [J1], @n.d. IEEE).

5.2.4 Experimental Results

In this project, the final configuration of the implemented dual LH/RH CP beamforming network is illustrated, and simulation results are compared with experimental ones. As demonstrated in Figure 5.16(a), the intended beamforming network includes three layers that are joined on each other. The layers are fabricated with Die forming method. Die forming is a well-known metal part fabrication technique. The prototype, usually a metal alloy layer, is permanently grown around a die via plastic clause by building and etching processes. Furthermore, simulations may be conducted to prevent breaks, damages, ridges, and spreading. The main shortcoming is that it is very challenging to separate the die and the pin plate if the pins are tall and slim.

The beamformer includes 8 input ports associated with 8 different output beams, which four of them are RHCP and four others are LHCP. The beamformer adjusts the signals to provide the required uniform progressive-phase signals and reducing sidelobes at the dual-polarized antennas' ports. The beamformer comprises several building blocks consists of phase shifters, couplers, unbalanced power dividers, and crossovers (Figure 5.16(b)). Meanwhile, it is worthy to state that these several building blocks are designed and simulated individually, with a desired input return loss more than 20 dB to cancel any possible mismatching among different components. Furthermore, the port distance among two consecutive elements is considered at least $\lambda_g/2$ to reduce higher-order mode among the elements, where λ_g is the guided wavelength of the dominant mode (TE_{10}). The beamforming network performance can be determined by analyzing the network block diagram in Figure 5.1. The non-uniform amplitude distribution and progressive phase variations at output ports are described in Section II. As it has been mentioned before, the non-uniform amplitude distribution leads to smaller sidelobes by providing a tapered excitation for the antenna elements.

The dual-polarized antennas are fed by the provided signals in the upper and lower ports of the antennas utilizing the upper and lower layer beamforming networks (Figure 5.16). A vertical rectangular waveguide (WR-15) to a horizontal hollow waveguide transition is introduced here for measurement purposes (Figure 5.17). It is intended for minimizing the reflections and insertion losses in the entire working frequency range of the beamformer. The physical parameters of the transition are indicated in Figure 5.17(a). Furthermore, the S-parameters of the transition are shown in Figure 5.17(c). The simulation results show that the return loss and insertion loss are better than -20 dB and 0.1 dB, respectively.

The input reflection coefficients of the entire beamformer carried out utilizing Ansys HFSS are compared with experimental ones in Figure 5.18(a) and (b). The input reflection coefficients are below -14 dB in the entire working frequency range from 57 to 64 GHz. The yz-plane far-field results, regarding four RHCP and four LHCP beams at 60.5-GHz, are presented in Figure 5.19 and Figure 5.20, respectively. The normalized xz-plane patterns are presented in Figure 5.21 and Figure 5.22 for all ports at 60.5-GHz. Note that those results are provided for various rotated xz-planes, where the radiation patterns are pointed toward, concerning different exciting ports. The simulated and measured sidelobes are smaller than -19 dB and -17 dB, respectively. This difference among simulated and measured results is acceptable because of the imperfect antenna test setup where the feeding WR-15 may influence the radiation pattern. The 3D filtering ability of a beamformer can be determined by a parameter called beam overlap level (BOL) [164]. The beam overlap level of the intended beamformer is more than 12 dB. The scan loss concerning the four RHCP beams are 0.2 dB, 1.9 dB, 1.9 dB, 0.2 dB, and 0.2 dB, 1.9 dB, 1.9 dB, 0.2 dB concerning the four LHCP beams. The half-power beamwidths are 9^o, 10^o, 10^o, 9^o, for the four RHCP beams, and 9^o, 10^o, 10^o, 9^o, for the four LHCP beams. The axial ratios in yz-plane are presented in Figure 5.19 and Figure 5.20 for the RHCP and LHCP beams at 60.5-GHz, respectively. The measured maximum RH/LH CP gains associated with different input ports are compared with simulated ones in Figure 5.23. Another important parameter that can assess the loss performance of the intended beamformer is the conductor losses [165], and it can be defined by the difference between the measured directivity and gain. The measured maximum conductor losses are estimated 0.4 dB, 0.45 dB at 60.5 GHz for right-hand and left-hand ports, respectively.

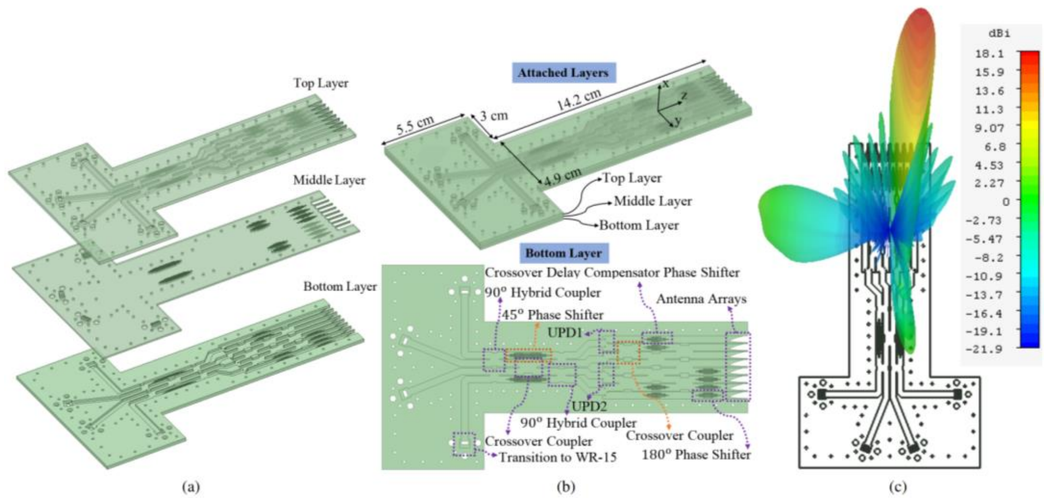

Figure 5.16: The proposed beamforming network.(a) Three separate layers of the beamformer. (b) The beamformer consists of three separate layers which are attached on each other. Attached layers are on the top, and bottom layer is shown on the lower side. (c) 3D radiation pattern at 60-GHz (M. Farahani et al. [J1], @n.d. IEEE).

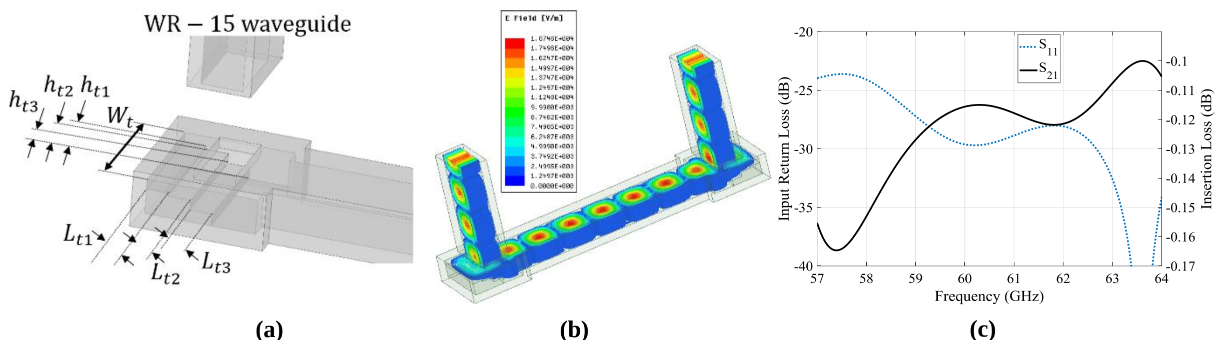

Figure 5.17: Vertical WR-15 transition to the horizontal hollow waveguide.(a) Transition parameters. (b) Magnitude of travelling electric fields. (c) Scattering parameters of the transition (M. Farahani et al. [J1], @n.d. IEEE).

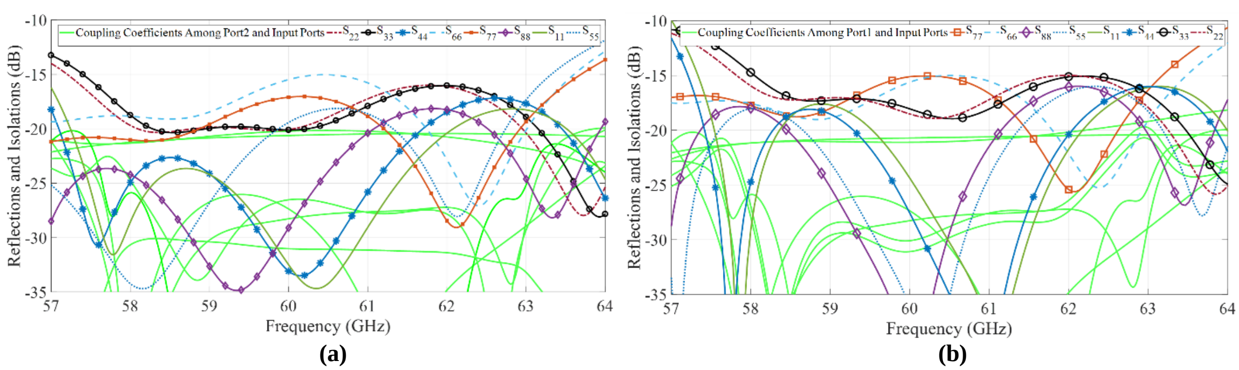

Figure 5.18: Input return losses and coupling coefficients for $Port$ 1 and 2.(a) Simulated. (b) Measured. For simplicity, only the measured coupling coefficients among $Port$ 1 and input ports and simulated coupling coefficients among $Port$ 2 and input ports are plotted. All other coupling coefficients among the input ports are lower than -20 dB. Note that due to the space limitation, we did not assign legend to different coupling coefficients (M. Farahani et al. [J1], @n.d. IEEE).

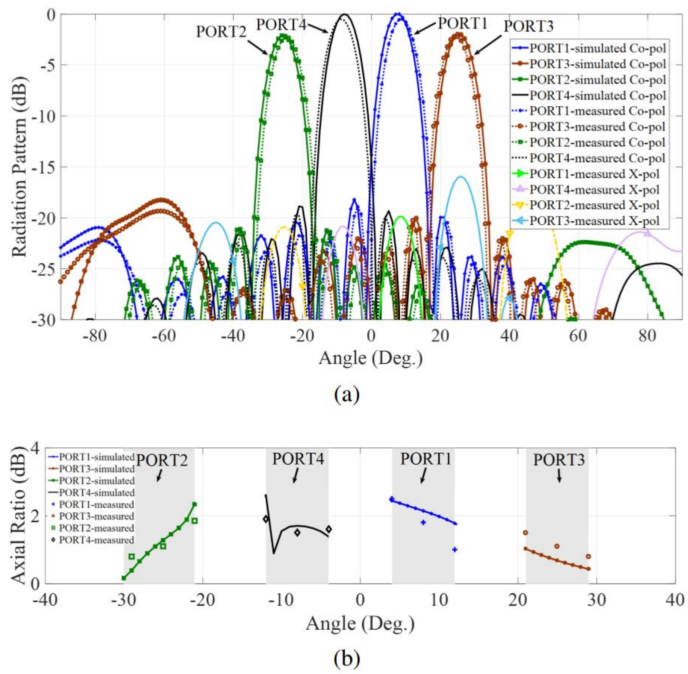

Figure 5.19: yz-plane far-field results concerning four right-hand circularly polarized patterns.(a) Normalized simulated and measured yz-plane radiation patterns concerning different input ports excitation at 60.5 GHz. (b) Simulated and measured axial ratio concerning different input ports excitation at 60.5 GHz (M. Farahani et al. [J1], @n.d. IEEE).

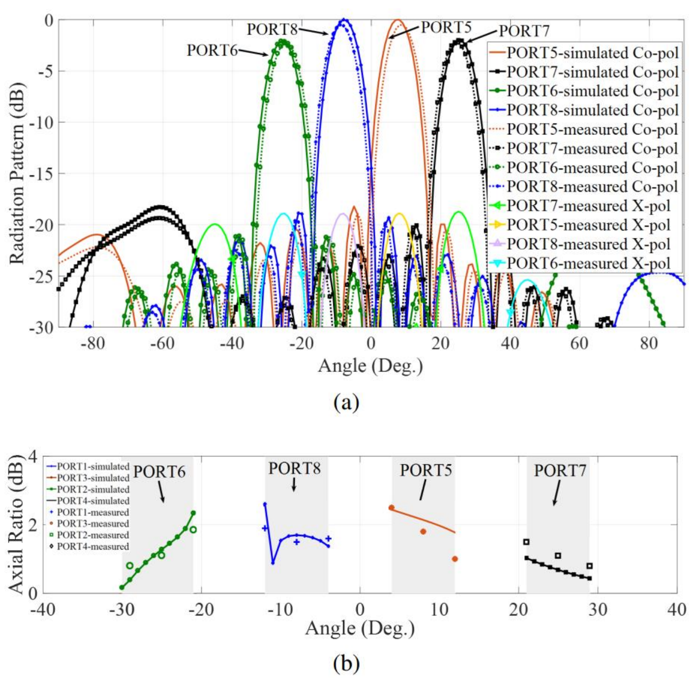

Figure 5.20: yz-plane far-field results concerning four left-hand circularly polarized patterns.(a) Normalized simulated and measured yz-plane radiation patterns concerning different input ports excitation at 60.5 GHz. (b) Simulated and measured axial ratio concerning different input ports excitation at 60.5 GHz (M. Farahani et al. [J1], @n.d. IEEE).

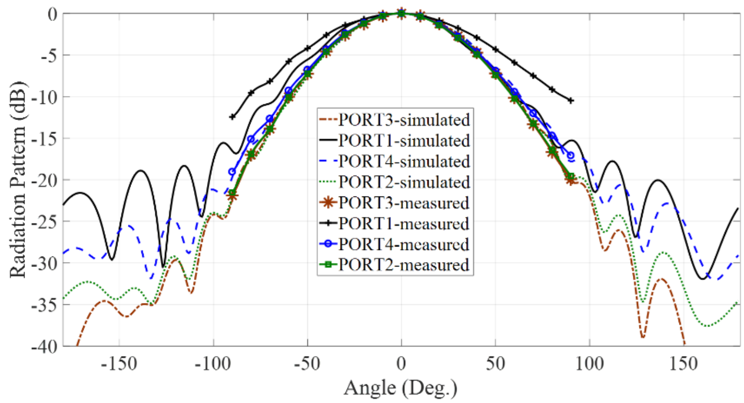

Figure 5.21: Normalized simulated and measured xz-plane radiation patterns concerning right-hand circularly polarized ports excitation at 60.5 GHz. They are calculated and measured in different rotated xz-planes containing the direction of maximum radiation for each beam (M. Farahani et al. [J1], @n.d. IEEE).

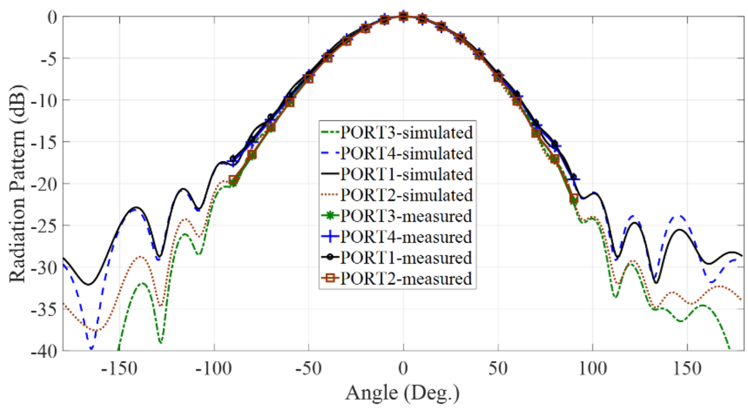

Figure 5.22: Normalized simulated and measured xz-plane radiation patterns concerning left-hand circularly polarized ports excitation at 60.5 GHz. They are calculated and measured in different rotated xz-planes containing the direction of maximum radiation for each beam (M. Farahani et al. [J1], @n.d. IEEE).

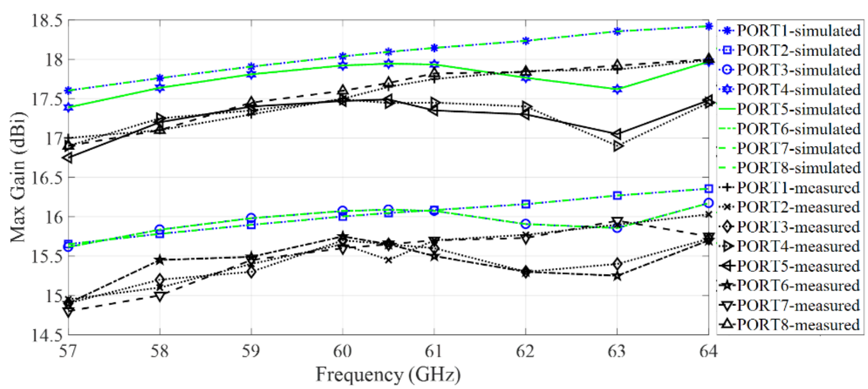

Figure 5.23: Measured and simulated maximum LH/lRH CP gains concerning different input ports (M. Farahani et al. [J1], @n.d. IEEE).

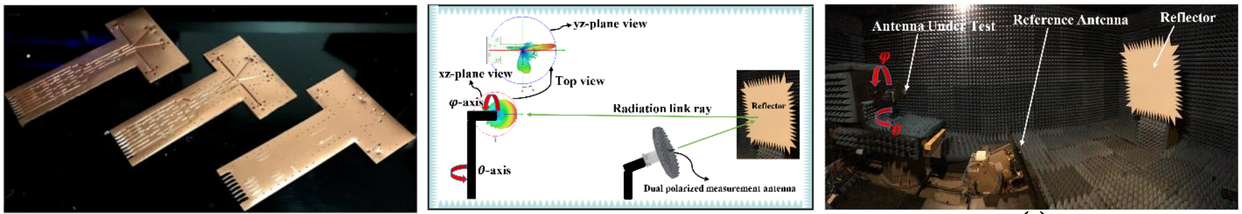

(a) (b) (c)

Figure 5.24: (a) Photo of the fabricated prototype. (b) Radiation pattern measurement setup. (c) Anechoic chamber test setup (M. Farahani et al. [J1], @n.d. IEEE).

5.3 Highly Efficient 30-GHz 2×2 Beamformer Based on Rectangular Air-Filled Coaxial Line

In this work, the principal concept of the Butler matrix (BM) has been derived from the structures presented in [166]-[168] where they have the same BM structure implemented in different guiding structures. In [166], the printed ridge gap (PRGW) is practiced. In [167], the SIW is employed, while the traditional microstrip transmission line is utilized in [168]. Alternatively, the same BM structure is utilized but with an alternative low-loss and wideband square air-filled coaxial transmission line as a guiding structure. In the traditional square coaxial line, the central conductor sustained by shorted microstrip stubs restrains the bandwidth, raises the losses, and complicates the fabrication [169]-[172]. To overcome this extreme disadvantages, a method of the quarter-wavelength stubs is introduced. These stubs are planned to suspend the central conductor of the coaxial line and facilitate the fabrication without the support of the dielectric suspender, leading to an increase of bandwidth and a decrease of losses. The proposed beamformer is excited through four conventional WR-28 ports, which by coax-to-hollow transitions are joined. Other grants of this research include improving the gain, decreasing the sideloe levels (SLLs), and obtaining an efficiency of more than 90%.

5.3.1 Topology of Beamformer Network

Here, the structure of the proposed beamformer network with 2D scanning ability is demonstrated and explained. As presented in Figure 5.25, this network is comprised of four low-loss broadband 3-dB hybrid couplers. There is no need for any phase shifter and crossover coupler (see Figure 5.25). Four input ports (P1 to P4) are related to four output ports (A1 to A4) through the presented structure. A 2×2 array antenna are excited through the recommended beamformer to achieve a 360^{o} lateral scan in 90^{o} steps. Considering that the coupling among the antennas is negligible, the normalized array factor of the array antenna with uniform amplitude excitations in the far-field region is represented by [173]

$$AF_n = \cos\left(\frac{k_o d_x \sin(\theta_o)\cos(\varphi_o) + \beta_x}{2}\right) \times \cos\left(\frac{k_o d_y \sin(\theta_o)\sin(\varphi_o) + \beta_y}{2}\right) \qquad (5-11)$$

where k_o is the free-space wavenumber corresponding to $2\pi/\lambda_o$, d_x and d_y are the antenna inter-element spacing in the x- and y- directions in the azimuth plane. In addition, β_x and β_y are the inter-element phase shifts in the x- and y- directions, respectively [173]-[174].

Furthermore, the SP4T switch allows the beam selection by connecting one of the BM input ports to the transceiver [168]. Figure 5.26 displays the radiation patterns of the introduced beamformer concerning different port excitation.

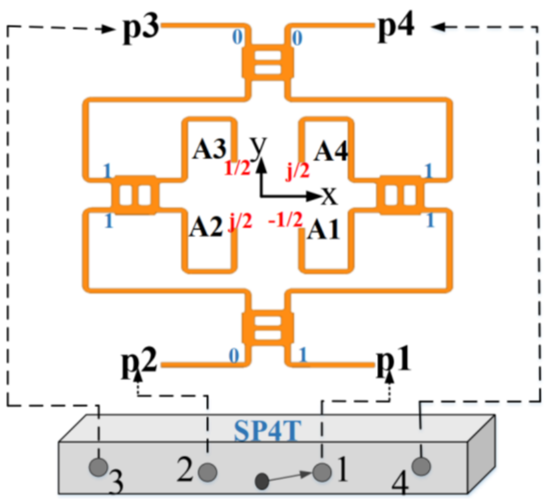

Figure 5.25: Block diagram of the 4×4 beamformer network (M. Akbari et al. [J2], @n.d. IEEE).

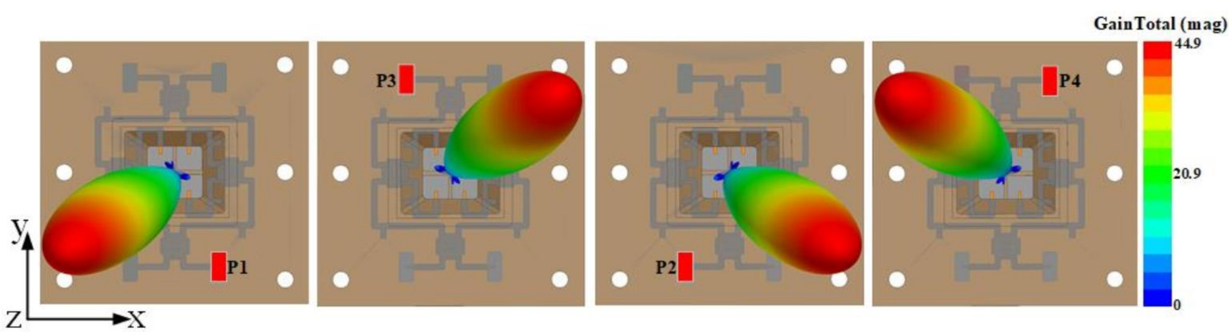

Figure 5.26: Simulated radiation patterns of the beamformer network at 30-GHz with respect to the exciting ports (M. Akbari et al. [J2], @n.d. IEEE).

5.3.2 Rectangular Coaxial Transmission Line

The proposed rectangular coaxial transmission line is represented in Figure 5.27. As can be seen, it includes the exterior and central conductors drawn in gray and orange colors, respectively. The proposed coaxial transmission line is planned in three separate layers to facilitate the fabrication using CNC machining. The characteristic impedance of the line is

$$Z_o = \sqrt{\frac{L_{line}}{C_{line}}} = \frac{1}{v_p C_{line}} \qquad (5-12)$$

where v_p is the phase velocity in the line corresponding to the speed of light in free-space [172]. Thus the characteristic impedance is evaluated using the value of the capacitance per unit length (C_{line}). In [175], some equations were obtained for two cases. The first case is when the width and thickness of the central conductor are greater than the gaps ($w > wa$) and ($h > ha$), the capacitance can be given as [172], [175]

$$C_{line} = 2\varepsilon\left(\frac{w}{ha} + \frac{h}{wa}\right) + \frac{4\varepsilon}{\pi}\left[\ln\left(\frac{wa^2 + ha^2}{4ha^2}\right) + 2\frac{ha}{wa}tan^{-1}(\frac{wa}{ha})\right] + \frac{4\varepsilon}{\pi}\left[\ln\left(\frac{wa^2 + ha^2}{4wa^2}\right) + 2\frac{wa}{ha}tan^{-1}(\frac{ha}{wa})\right] \qquad (5-13)$$

where all dimentions are illustrated in Figure 5.27. The permittivity of the dielectric ε is equal to ε_o (8.85×10-12 F/m). In the second case which the central conductor is extrimly thin ($ha > h$), the capacitance can be calculated as [172], [175]

$$C_{line} = \frac{2\varepsilon w}{ha} + \frac{4\varepsilon}{\pi ln2}\left[1 + \cot(\frac{\pi wa}{2ha + h})\right] \times \left[\frac{h + 2ha}{2ha}\ln\left(\frac{4ha + h}{h}\right) + \ln\left(\frac{h(4ha + h)}{4ha^2}\right)\right] \qquad (5-14)$$

To verify these expressions, various samples of the square coaxial transmission lines with various dimensions are simulated utilizing Ansys HFSS [176]. The characteristic impedance of them are presented in Table 5.3. The losses of the coaxial transmission line can be determined as the sum of dielectric and conductor losses. Considering that the air-filled rectangular coaxial is analyzed here, the dielectric loss can be disregarded; therefore the conductor loss α_c, according to [172], [175], and [177] can be represented as

$$\alpha_c = \alpha\left[1 + \frac{2}{\pi}tan^{-1}(1.4(\frac{\Delta}{\delta_s})^2)\right] \qquad (5-15)$$

where Δ and δ_s are the rms surface roughness and skin depth of the conductor ($\delta_s = \sqrt{2/\omega\sigma\mu}$) respectively. The term of α is given as

$$\alpha = \frac{\Delta z_o}{\sigma\mu v_p \delta^2 z_o} \qquad (5-16)$$

where σ and μ correspond to the conductivity and permeability, respectively. Moreover, v_p, z_o, Δz_o are the phase velocity in the line, characteristic impedance, and the variation in the impedance [172].

Table 5.3: Impedance line configurations for rectangular coaxial line (All dimensions are in mm) (M. Akbari et al. [J2], @n.d. IEEE).

h	**0.9**	**0.9**	**0.6**	**0.6**	**0.6**	**0.5**	**0.4**	**0.3**	**0.2**	**0.15**
ha	**0.1**	**0.3**	**0.45**	**0.45**	**0.85**	**0.8**	**0.8**	**0.85**	**0.85**	**0.85**
w	**0.9**	**0.9**	**1.25**	**0.6**	**0.8**	**0.5**	**0.4**	**0.3**	**0.2**	**0.15**
wa	**0.1**	**0.3**	**0.9**	**0.54**	**0.85**	**0.8**	**0.8**	**0.85**	**0.85**	**0.85**
Zo (Ohm)	**9.9**	**26.6**	**40.4**	**50.2**	**69.7**	**81.3**	**92**	**110**	**131**	**147.7**

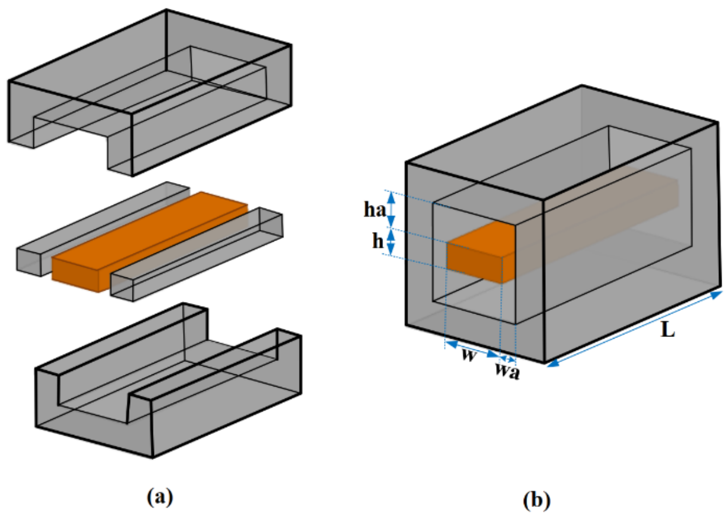

Figure 5.27: Rectangular coaxial Transmission line (a) separated layers, including top, middle, and bottom layers, for facilitating the fabrication process and (b) the whole structure after integrating three layers (M. Akbari et al. [J2], @n.d. IEEE).

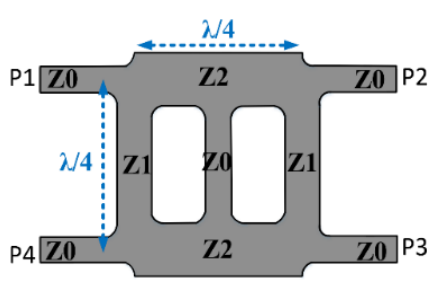

Figure 5.28: The topology of two-section hybrid coupler (M. Akbari et al. [J2], @n.d. IEEE).

5.3.3 Coupler Design

The proposed beamformer is comprised of four hybrid couplers as shown in Figure 5.25. It is a very well known technique that cascading two or several sections and properly selecting the impedances of the main and the coupled lines would lead to a wideband operation [34]. It is based on the fact that conventional one stage coupler has a narrow bandwidth due to the quarter wavelength lines. The intended coupler is depicted in Figure 5.28. Utilizing HFSS software, optimization is carried out to obtain the widest bandwidth. The dimensions of the proposed hybrid, associated with the parameters specified in Figure 5.27, are presented in Table 5.4. As displayed in Figure 5.29, the configuration of several layers of the intended coupler is drawn. It is apparent that the top and bottom layers, in grey color, are jointly the exterior conductor and the middle layer, in orange color, is considered as the central conductor. The simulated S-parameters of the intended coupler carried out utilizing HFSS are illustrated in Figure 5.30. Figure 5.31 is shown the amplitude and phase imbalance over the working frequency band. The bandwidth of approximately 28% from 26.5 GHz to 35 GHz is achieved using this technique.

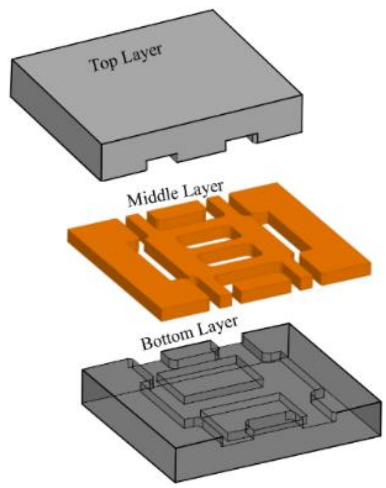

Figure 5.29: Sketch of three layers of the proposed coupler including the top and bottom layer as the outer conductor in grey color and middle layer as an inner conductor in orange color (M. Akbari et al. [J2], @n.d. IEEE).

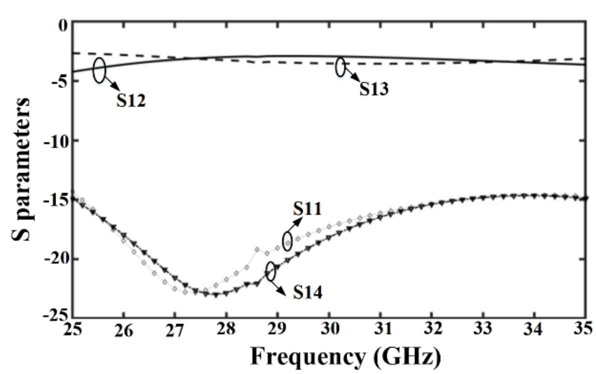

Figure 5.30: The frequency response of S-parameters belonged to the proposed hybrid coupler (M. Akbari et al. [J2], @n.d. IEEE).

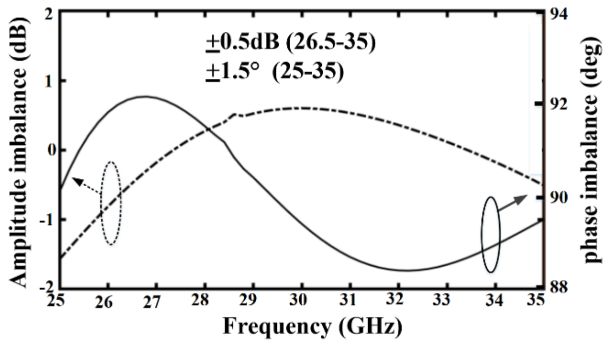

Figure 5.31: The amplitude and phase imbalance response of the proposed hybrid coupler (M. Akbari et al. [J2], @n.d. IEEE).

Table 5.4: Hybrid coupler dimentions (M. Akbari et al. [J2], @n.d. IEEE). (All dimensions are in mm)

h	ha	w	wa	Z
0.6	0.45	0.6	0.45	Z0
0.6	0.85	0.8	0.85	Z1
0.6	0.45	1.25	0.9	Z2

5.3.4 Antenna Design

An open-ended waveguide is utilized as a radiating element. It has a simple structure that has wide impedance bandwidth as well as a perfect radiation pattern. One of the significant challenges connected with this kind of antenna is its large aperture size which could cause a problem for designing arrays where inter-element spacing needs to be about a half wavelength (λ/2). As a result, designing open-ended waveguide array will be challenging because of the aperture size (7.112 mm) at 30-GHz which is bigger than the inter-element spacing of 5 mm (λ/2), leading to a deterioration of radiation pattern performance [178]-[179]. Several methods have been introduced in literature to reduce either the cutoff frequency or the aperture size. Nevertheless, most of them have risen the design complexity and fabrication cost. Here, the aperture size of the open-ended waveguide antenna is selected 5.8 mm × 6.5 mm to obtain a cut-off frequency of 25.8 GHz. The minimum inter-element spacing among the radiating elements considering the fabrication limitations is selected as 6.8 mm (0.68 λ at 30-GHz). Thus, the SLLs are somewhat sacrificed in the price of design simplicity and lower cost. Figure 5.32 shows a schematic of both a single antenna and a 2×2 antenna array. To attach the coaxial feed line to the waveguide antenna, a transition is necessary. Hence, an optimization utilizing Ansys HFSS is conducted to achieve a wideband transition. Figure 5.33 shows simulation results of the single antenna and the 2×2 antenna array.

The gain of the antenna is slightly enhanced with increasing frequency. Ideally, it is expected that the gain in a 2×2 antenna array with uniformly-spaced arrays experiences a 6 dB enhancement compared to the single antenna. Nevertheless, an average of 4.5 dB gain boost is observed. The deviation of 1.5 dB is caused by a misalignment among array factor and single radiating element patterns. As stated earlier, the SLLs are slightly sacrificed in lieu of design simplicity and fabrication cost. In the next section, we introduce two design alternatives to improve radiation performance while containing the side lobes.

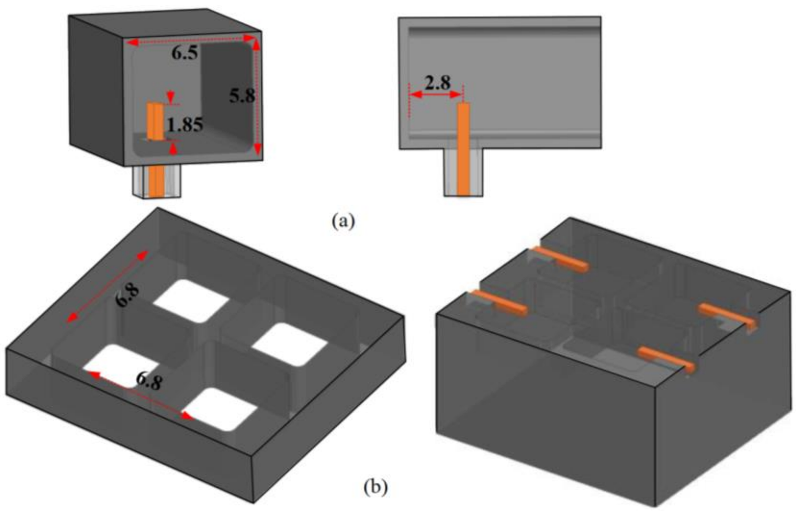

Figure 5.32: Illustration of the waveguide antenna; (a) single antenna and (b) 2×2 antenna array (M. Akbari et al. [J2], @n.d. IEEE).

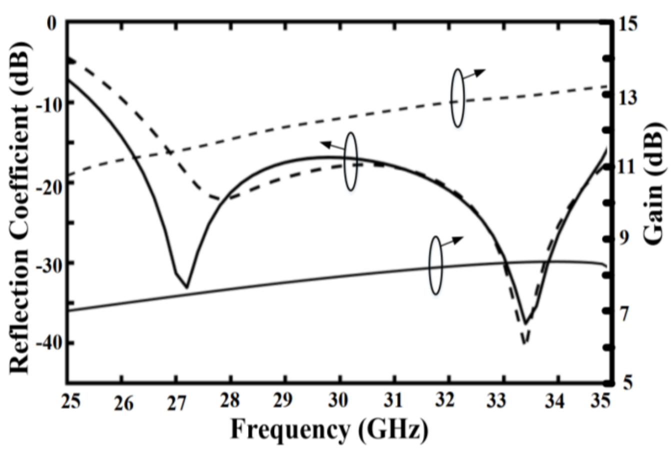

Figure 5.33: The numerical results of the reflection coefficient and the gain of the single antenna and 2×2 antenna array.Solid and dashed lines indicate gain of the single antenna and 2×2 antenna array, respectively (M. Akbari et al. [J2], @n.d. IEEE).

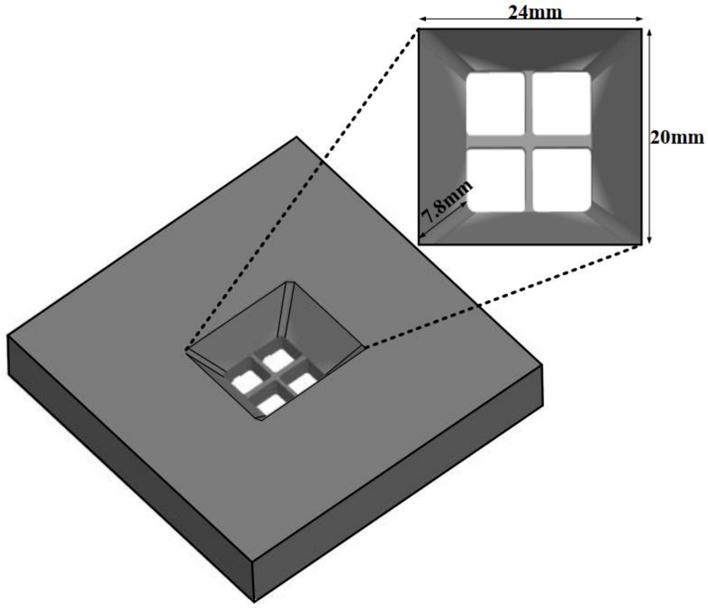

Figure 5.34: Schematic of the radiating part of the proposed beamformer in the form of horn antenna (M. Akbari et al. [J2], @n.d. IEEE).

5.3.5 Gain Enhancement and Sidelobe Supression

As discussed in the preceding section, due to the large aperture size the SLL was compromised, which resulted in a degeneration of the radiation performance of the uniform antenna arrays. To improve the antenna gain and contain the side lobes, two methods are introduced. Initially, with expanding the depth of the intended beamformer case, the aperture of the array is expanded and modified in the style of horn antenna (see Figure 5.34). This method improves the beamformer gain from 12.4 dB to 15.3 dB at the working frequency of 30-GHz. But, it still suffers from the surface waves induced in the antenna aperture that affects the radiation performance of the intended beamformer. Figure 5.35 shows the surface current induced on the antenna aperture. To resolve the surface wave problem, a rectangular-shaped stub is implimented with a thickness of $\lambda/4$ and loaded with PEC (short circuit). Therefore, the stub impedance on the antenna aperture acts as an open circuit, where it blocks the surface current toward outside of the rectangular-shaped stub on the top layer of the antenna (see Figure 5.35(b)). Figure 5.36 determines the radiation pattern of the intended beamformer. It should be noted that altering the design of the antenna aperture from a simple 2×2 waveguide antenna array to the configuration presented in Figure 5.34, the gain is increased from 12.4 dB to 15.3 dB (see Figure 5.36).

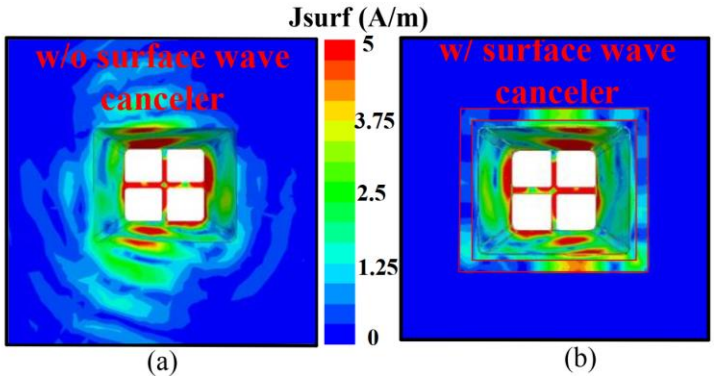

Figure 5.35: Simulation results of the surface current induced on the antenna aperture: (a) the structure without surface wave canceler, and (b) the proposed design (M. Akbari et al. [J2], @n.d. IEEE).

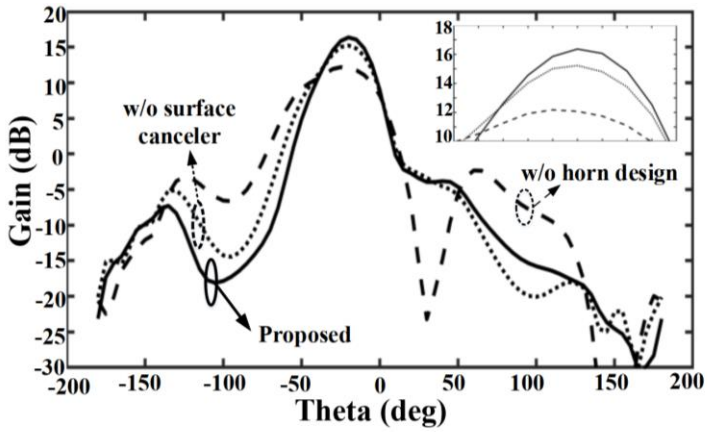

Figure 5.36: The radiation pattern of three different design in the radiating part of the proposed beamformer; including the design shown in Figure 5.32(b) without horn-shaped aperture, the design shown in Figure 5.34 without surface wave canceler, and the proposed design (Figure 5.35(b)) at the operating frequency of 30-GHz (M. Akbari et al. [J2], @n.d. IEEE).

5.3.6 Implimentation of the Proposed Beamformer

The implementation of the designed beamformer is displayed in Figure 5.37. As stated in the preceding sections, the square air-filled coaxial transmission line is selected as the guiding structure, where the upper and lower layers represent the exterior conductor, while the central layer is the interior conductor. Furthermore, the network is excited through four standard WR-28 waveguide ports (see Figure 5.37(d)). As an outcome, it is needed to use the presented transition from coaxial to waveguide shown in Figure 5.38(a). Moreover, the performance of the U-band line presented in Figure 5.38(b) is important and is investigated through parametric studies. As discussed earlier, the traditional approach for sustaining the interior conductor in the air-filled line is based on adopting the shorted stubs. Nevertheless, this approach defines the operation bandwidth, raises the losses, and twists the fabrication. To overcome this difficulty, we recommend practicing quarter-wavelength stubs, so that the stubs can suspend the interior conductor and expedite the fabrication method without employing the dielectric support. Figure 5.39 exhibits the S-parameters of the transition from coaxial to waveguide the beamformer, U-shaped curve and the quarter-wave stubs, introduced in Figure 5.38. The simulated gains for each port at 30-GHz are almost 16.5 dBi.

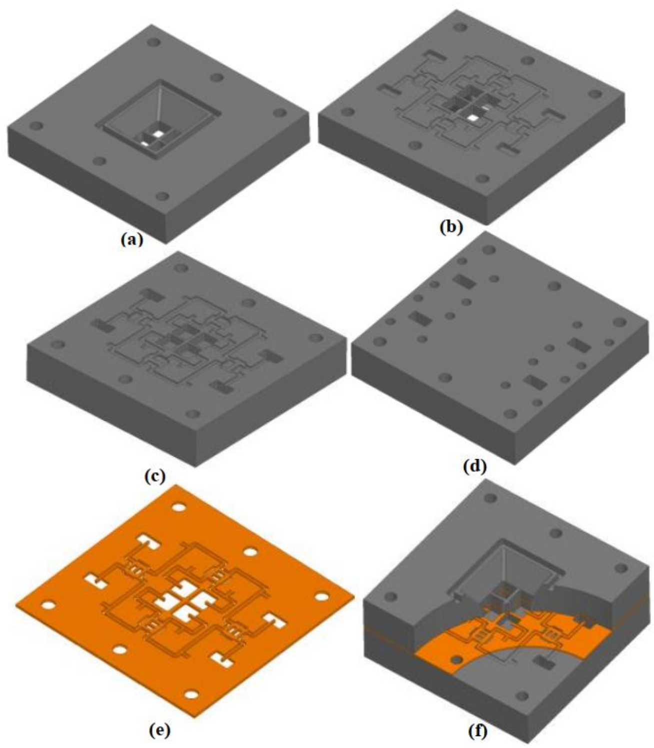

Figure 5.37: The proposed 4×4 beamformer design including three different layers; (a) front view of the top layer (the antenna aperture), (b) back view of the top layer, (c) front view of the bottom layer, (d) back view of the bottom layer, (e) the middle layer (inner conductor), and (f) the proposed three-layer design (M. Akbari et al. [J2], @n.d. IEEE).

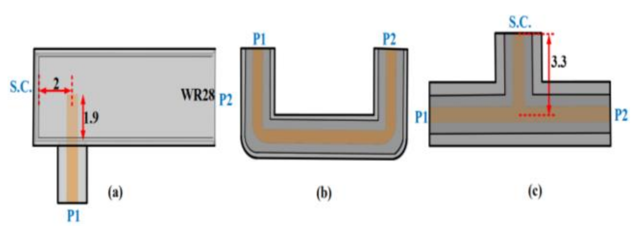

Figure 5.38: Schematics of three different designs; (a) transition for connecting waveguide WR-28 to the coaxial, (b) the U-shaped bend, and (c) the quarter wave short circuit transformer (M. Akbari et al. [J2], @n.d. IEEE).

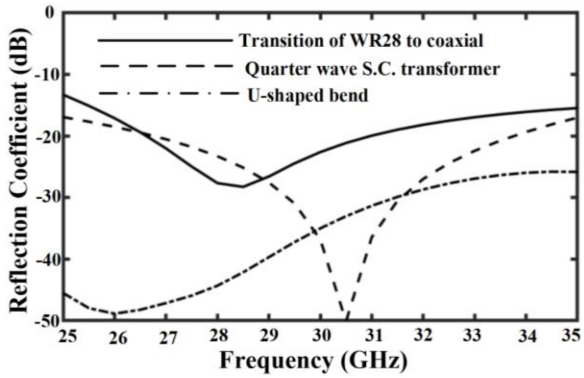

Figure 5.39: Frequency response of reflection coefficient for three different designs shown in Figure 5.38 (M. Akbari et al. [J2], @n.d. IEEE).

The two dimentional Butler matrix beamformer, implimented in air-filled coaxial transmision line, is fabricated as displayed in Figure 5.40. The intended beamformer is included of three separate layers: two upper and lower layers represent the outer conductor and the central layer represents the interior conductor. Different holes are considered at the sides for screws in order to adjust and assemble the prototype. The S-parameters of the intended prototype are measured utilizing a two-port vector network analyzer through WR-28 input ports while the two other ports were connected to matched loads, shown in Figure 5.41. It can be seen out that both the input reflection coefficients and mutual couplings are lower than -10 dB within the entire working frequency-band. Further, the simulated and experimental results quite well follow each other as presented in Figure 5.41.

An anechoic chamber test setup, shown in Figure 5.42, is used to measure maximum radiation gain and radiation patterns of the fabricated prototype. The far-field test setup is accomplished by relocating the antenna under test in the hemisphere (-120^o to $+120^o$) with steps of 5^o. The measurement and simulation results regarding the radiation patterns, when the intended beamformer is separately excited by one port while other ports are connected to matched loads, are shown in Figure 5.43. The maximum gains are approximately constant over the entire working frequency-bands, as it is represented in Figure 5.44. It can be noted that the measured maximum gain encounters a small variation of ± 0.5 dB over the working frequency-band, exhibiting definite agreement with the numerical results. The slight inconsistency in the measured results could be due to inaccuracies in the fabrication and adjustment in the calibration setup. The simulated radiation efficiency is exhibited in Figure 5.44, which is more than 90% over the entire working frequency-band. The performance of the intended beamformer network is compared in Table 5.5 with other related beamformers implemented in different guiding structures in the literature.

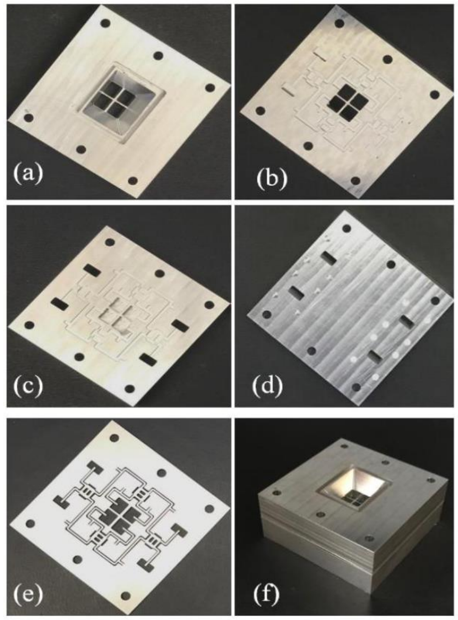

Figure 5.40: The photo of fabricated design including three different layers ; (a) front view of the top layer (the antenna aperture), (b) back view of the top layer, (c) front view of the bottom layer, (d) back view of the bottom layer, (e) the middle layer (inner conductor), and (f) the proposed three-layer design (M. Akbari et al. [J2], @n.d. IEEE).

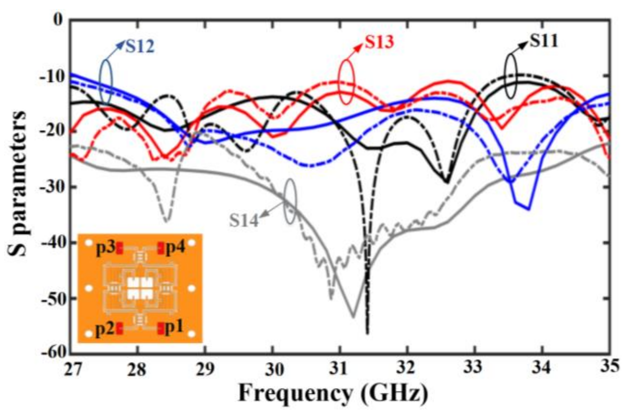

Figure 5.41: The measurement and simulation results of the scattering parameters.Solid and dashed lines represent the simulation and measurement results, respectively (M. Akbari et al. [J2], @n.d. IEEE).

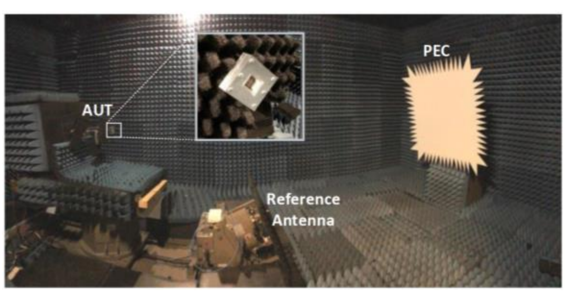

Figure 5.42: The measurement setup for the radiation pattern.AUT is the antenna under test (M. Akbari et al. [J2], @n.d. IEEE).

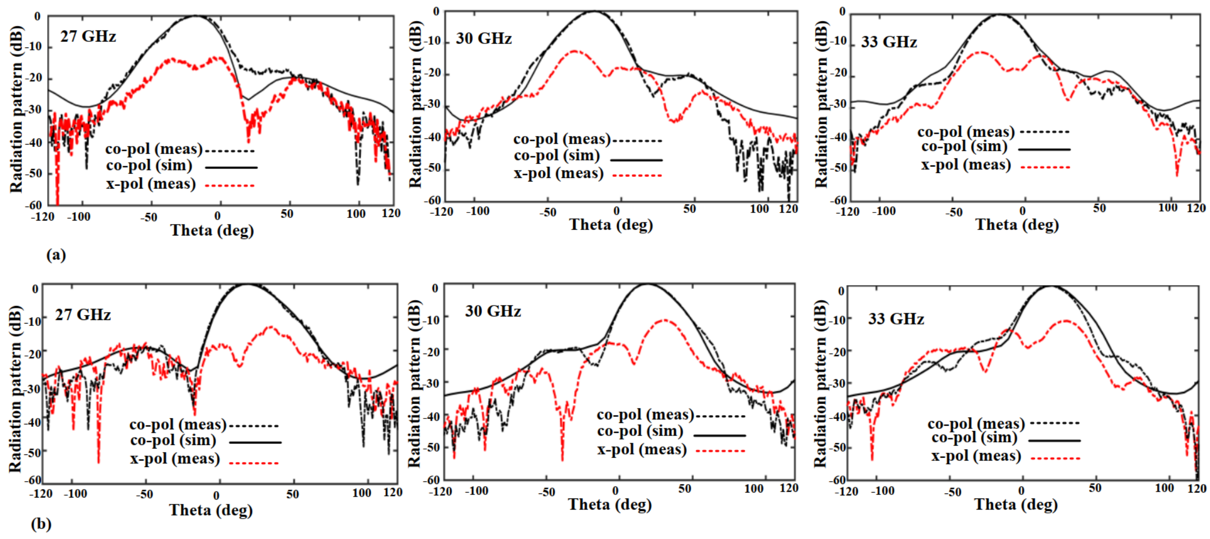

Figure 5.43: Measured and simulated results of the radiation patterns at frequencies of 27 GHz, 30 GHz, and 33 GHz when the proposed structure is excited by (a) port 1 (up) and (b) port 2 (down) (M. Akbari et al. [J2], @n.d. IEEE).

Table 5.5: Comparing the proposed beamformer with some othe reported beamformers in literature (M. Akbari et al. [J2], @n.d. IEEE).

Reference	Guiding Technology	BSN Structure	Antenna Type	Scanning Beam	Bandwidth (%)	Gain (dBi)	Size (λ^2)
[7]	Microstrip	Two Layers	4×4 (Patch)	4	19	12	11.5×6.7
[166]	Printed Ridge Gap Waveguide	Two Layers	2×2 (ME-dipole)	4	20	10.3	5.6×7.1
[167]	SIW	Two Layers	4×4 (Slot)	4	11	12.2	8.1×7.3
[174]	SIW	Four Layers	2×2 (Ring)	4	7.5	12	2.86×2.86
[180]	SIW	Six Layers	2×4 (Slot)	8	8.5	11.8	6.8×5.3
[181]	SIW	Four Layers	4×4 (Slot)	16	13.3	13.2	4.6×16.5
[182]	SIW	One Layers	4×4 (Slot)	4	13.3	12.5	8×7
[183]	Coplanar Waveguide (CPW)	Six Layers	4×4 (Cavity)	4	7	15.3	5.6×4
This work	Rectangular Coaxial	Three Layers	2×2 (Waveguide)	4	25.8	16.5	6×6

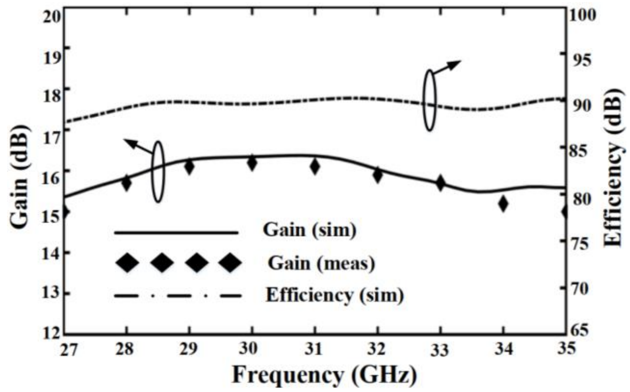

Figure 5.44: The measured and simulated results of the gain and efficiency (M. Akbari et al. [J2], @n.d. IEEE).

5.4 Conclusion

In this project, an 8-beams dual RH/LH CP array antenna employing an 8×8 beamforming network has been investigated and implemented. The eight generated beams by the beamforming network cover a field of view of $\pm 30^o$. The working frequency range of the system is 10.75% at 60.5-GHz that can support the entire unlicensed frequency range from 57 to 64 GHz. The proposed beamformer has been used to generate the uniform progressive-phase signals (i.e., $\pm 45^o$ and $\pm 135^o$) at the output ports and reduce sidelobes to lower than -19 dB. The antenna elements arrangement has been separated into two sub-arrays with radiating elements separation distance of $4 \times S$ leading to entering grating lopes in the visible zone, and a state-of-the-art technique has been presented to reduce grating lobe difficulty. The maximum gain variation across the working frequency range is smaller than 0.7 dB thanks to the employed low phase-error Hedgehog waveguide phase shifters. Performing hybrid coupler and cross coupler with low insertion loss characteristics (typically smaller than 0.1 dB) and wideband phase response is an simple and straight forward method; nevertheless, phase shifters implemented in hollow waveguide have a high amount of phase error. To overcome the high amount of propagation losses at the 60-GHz mmWave band, the low-loss components such as couplers and cross couplers in the beamforming network have been realized in hollow waveguide utilizing a diffusion bonding technique, and Hedgehog waveguide has been employed only for designing low-loss and low phase-error phase shifters. Adopting this approach, the radiation efficiency of above 90% is obtained for each port. The design theory has been validated through simulation and measurement.

Furthermore, an extremely qualified two-dimensional (2D) 2×2 beamformer at the 30-GHz band has been investigated and designed. Respecting the nature of the input ports, guiding structure, and antenna design, this arrangement is well-referred to as a waveguide-coaxial-waveguide beamformer network. The beamformer network can produce four switched beams. The measurement results determined that the network has a broadband performance (25.8%) with the radiation efficiency of more than 90% over the working frequency-band at 30-GHz. Furthermore, a flat gain (16.5±0.5 dB) and a sidelobe level (SLL) (lower than -20 dB) were obtained. These advantages candidate the intended beamformer a charming competitor for future 5G demands.

Chapter 6 Conclusion and Future Work

6.1 Conclusion

In this thesis, multiple approaches from the physical layer to the network layer have been proposed and investigated to overcome obstacles in developing the mmWave networks. However, each approach has its advantages and shortcomings, and these approaches should be combined in an intelligent way to achieve robust and efficient network performance.

In wireless systems, the throughput of the communication link is one of the most influential pointers to assess the performance. The throughput, however, deeply will be defined by the characteristic of the propagation channel, like propagation path loss, the separation of devices, the noise, etc. The Friis free-space path loss model indicates that the 60-GHz mmWave band has an approximately 28 dB loss more than the 5 GHz band. Moreover, extra loss of 7-15.5 dB/km power loss requires to be added in the received signal at 60-GHz mmWave due to the atmospheric absorption. Also, rainfall influences the performance of the mmWave systems. Approximately 8-18 dB/km losses should be considered as atmospheric attenuation for the rainfall rate of 50 mm per hour. Besides, the 60-GHz waves experience the limited capability of penetration. Moreover, although the physical size of antennas is so small, the design of the antenna feeding networks become complex and a challenging matter for designers due to the high amount of losses at mmWave frequency-band. To overcome blockage, multiple approaches from the physical layer to the network layer have been proposed.

As an initial work, MIMO systems have been investigated, and novel approaches proposed and developed in order to design proper MIMO antennas for mmWave applications. In this regard, two distinguished approaches have been proposed to reduce the mutual coupling due to the spatial fields. In the first approach, a valuable technique for reducing the mutual coupling among mmWave dielectric resonator antennas (DRAs) using a new metamaterial polarization-rotator (MPR) wall has been studied and performed. The mutual coupling has been decreased by installing MPR walls among DRAs, which were located in the H-plane. Utilizing this MPR walls, the TE modes of the antennas become orthogonal, which decreases the mutual coupling among the antennas. In the second approach, a novel method has been proposed to reduce the coupling due to spatial electromagnetic interaction among two circularly-polarised radiating elements utilizing an FSS superstrate layer.

In the next step, an extensive study of high gain antennas for the modern mmWave antenna applications has been performed. This confirms the contribution of gain enhancement methods in the future antenna mmWave applications. As a commencement, a wideband high gain antenna has been designed for mmWave applications using a superstrate layer placed above the antenna. Further, a beam-steering technique using phase gradient metasurface has been proposed and investigated. This work gave an in-depth vision of the millimeter-wave antenna system and its measurement techniques. However, we have faced difficulty in fabrication due to mechanical shortcomings in this work, and no acceptable measurement results were achieved.

To answer the demands of low-loss guiding structures at mmWave, the main objective of the thesis has been considered to be designing of low-loss high-efficiency guiding structure for mmWave applications. A novel waveguide structure has been proposed that has several advantages compared to the conventional transmission lines reported in the literature. The main advantage of the Hedgehog waveguide is that it can support propagation with lower loss. Moreover, the fact that the electromagnetic fields are captured to space within the waveguide, radiation losses are kept very low, resulting in good immunity from external electromagnetic disturbance compared to the microstrip technology. Another main advantage of the Hedgehog waveguide has been the compatibility with the hollow waveguides, which gives an extra degree of freedom to use the proposed waveguide for several mmWave designs. Moreover, the ridge gap waveguide and the transition method to microstrip has been investigated and developed, and a low-loss multi-aperture hybrid coupler with ridge gap technology has been designed and fabricated.

Ultimately, novel kinds of beamformer networks have been presented. As the first approach, the proposed beamformer network has been implemented by the proposed Hedgehog waveguide. The proposed high-efficiency beamformer network has 8-beams with the dual-polarization operation. Moreover, a 4×8 pattern control network has been utilized for increasing the number of the radiating element and suppressing sidelobes in the proposed LH/RH CP beamformer network. This dual-polarized beamformer network has been implemented in Hedgehog and hollow waveguide technology using a diffusion bonding technique. Diffusion bonding, also known as diffusion welding, is a solid-state joining process that is based on the atomic diffusion of elements at the joining interface. The progressive slot technique has used as a traveling-wave antenna for having a wideband axial-ratio at 60-GHz frequency-band from 57 GHz to 64 GHz. The sidelobes have been suppressed lower than -19 dB over the visible scanning range. The operating bandwidth of the system has been 10.75% at 60-GHz, and the radiating efficiency of the system has been above 90% for each port. Furthermore, an extremely qualified two-dimensional (2D) 2×2 beamformer at the 30-GHz band has been investigated and designed. The beamformer network can produce four switched beams. The measurement results determined that the network has a broadband performance (25.8%) with the radiation efficiency of more than 90% over the working frequency-band at 30-GHz. Furthermore, a flat gain (16.5±0.5 dB) and a sidelobe level (SLL) (lower than -20 dB) were obtained. These advantages candidate the intended beamformer a charming competitor for future 5G demands.

6.2 Future Work

The research work performed in this thesis as part of the doctoral course opens a new window in the mmWave components and their applications in antenna domain. However, it is observable that there are many other investigations to be explored in this area which give way for future research possibilities as explained in the following paragraphs.

Hedgehog waveguide, consisting of a bed of nails embedded in a host rectangular hollow waveguide, has been proposed and investigated as a promising state-of-the-art low-loss waveguide for mmWave frequency-bands. Hedgehog waveguide gets its name from its electromagnetic behavior. As hedgehogs root through hedges and other undergrowth in search of their favorite food, the proposed waveguide root through its embedded bed of nails. When we choose a host waveguide technology, it is worthwhile spending some time weighing up the pros and cons of the various types of waveguides on offer. The proposed Hedgehog waveguide is extremely low-loss and is compatible with the hollow waveguide technology, which gives the ability to develop different components such as low-loss flat phase response phase shifters. Through my Ph.D., the proposed Hedgehog waveguide is analytically investigated, and a transition to the hollow waveguide is designed. Moreover, the low-loss nature of the designed Hedgehog waveguide is compared with the ridge gap waveguide, Substrate Integrated Waveguide (SIW), hollow waveguide, and microstrip line. Finally, the proposed waveguide is designed, simulated and fabricated. The simulated and measured results show a good agreement, which validates the proposed concept.

The proposed novel Hedgehog waveguide structure that has several advantages compared to the conventional waveguides and transmission lines reported in the literature. The main advantage of the Hedgehog waveguide is that it can support propagation with lower loss. Moreover, the fact that the electromagnetic fields are captured to space within the waveguide, radiation losses are kept very low, resulting in good immunity from external electromagnetic disturbance compared to the microstrip technology. Another main advantage of the Hedgehog waveguide is the compatibility with the hollow waveguides, which gives an extra degree of freedom to use the proposed waveguide for several mmWave designs.

Through my PhD, different mmWave components has been presented and implemented in Hedgehog waveguide such as a low-loss phase shifter and a dual polarized beamformer network. As future work, Hedgehog waveguide can be used for designing high-efficiency mmWave components and networks.

Moreover, the presented technique for reducing mutual coupling using polarization rotator walls can be employed in antenna arrays in order to compensate the gain drop due to the beam-misalignment in the surrounding radiating elements.

Chapter 7 Résumé

7.1 Résumé

Les bandes d’ondes millimétriques ont récemment beaucoup attiré l’attention des chercheurs. Ils ont le potentiel pour répondre aux exigences des systèmes et applications de communication émergents. En outre, les systèmes à grande vitesse, grande largeur de bande et grande capacité font des communications à 60-GHz un choix approprié pour les communications sans fil à courte portée. Motivée par l'augmentation de la charge de trafic sur les réseaux cellulaires et l'augmentation correspondante du trafic sur le réseau, la communication de périphérique à périphérique (D2D) avec une onde millimétrique en 60-GHz (mmWave) est une solution possible pour gérer cette tâche future. La largeur de bande de fréquence disponible pour 60-GHz est beaucoup plus élevée par rapport à une communication conventionnelle telle que 5 GHz, qui génère certaines caractéristiques spécifiques pour la propagation de 60-GHz mmWave. En outre, mmWave à 60-GHz possède un spectre sans licence avec une bande passante disponible de 7 GHz pour transmettre le paquet de données, ce qui permet au débit maximum d'atteindre 2 Gbps de plus [184], ce qui signifie que les besoins en données peuvent être satisfaits par une augmentation du trafic.

Cependant, la communication à 60-GHz pose de sérieux obstacles au développement des réseaux mmWave à 60-GHz. Dans les communications sans fil, le débit de la liaison de communication est l’un des indicateurs les plus importants pour l’estimation des performances. Cependant, le débit dépend fortement des caractéristiques du canal de propagation, telles que l'affaiblissement du trajet, la distance entre les dispositifs, le bruit, etc. Grâce à la formule du modèle d'affaiblissement du trajet de l'espace libre Friis, l'affaiblissement du trajet pour 60-GHz a une valeur proche de 28 dB perte plus par rapport au 5 GHz mmWave. Parallèlement, une perte supplémentaire (perte de puissance de 7-15,5 dB / km) doit être prise en compte dans le signal reçu à des fréquences porteuses de 60-GHz en raison de l'absorption atmosphérique [65]. Outre ces facteurs, le taux de précipitations affecte également les performances du système. Atténuation atmosphérique supplémentaire d'environ 8 à 18 dB / km alors que le taux de précipitations est de 50 mm par heure [65]. Outre la forte atténuation, la radio en ondes millimétriques 60-GHz présente également une faible capacité de pénétration [66]. En outre, bien que la taille physique des antennes soit si petite, la conception des réseaux d’alimentation en antennes devient complexe et pose un problème pour les concepteurs en raison du nombre élevé de pertes dans la bande de fréquence à onde millimétrique de 60-GHz.

Pour surmonter le blocage, plusieurs approches de la couche physique à la couche réseau ont été proposées. Cependant, chaque approche a ses avantages et ses inconvénients, et ces approches doivent être combinées de manière intelligente pour obtenir des performances réseau robustes et efficaces.

7.2 Introduction et Motivation

Dans [1], Sanjib Sur et al. ont mené une étude sur les réseaux WLAN intérieurs à base de 802.11ad 60-GHz (Figure 7.1), concernant l'impact des diagrammes de rayonnement flexibles sur les performances de la couche liaison, pour différents environnements en blocage / mobilité. Contrairement à la perception conventionnelle selon laquelle les faisceaux de 60-GHz se comportent de manière pseudo-optique, il a été constaté que les diagrammes de rayonnement fortement directionnels subissent moins de pertes de pénétration au travers d'obstacles typiques (sauf le corps humain) dans un environnement de bureau, et qu'une couverture peut être réalisée au-delà d'une seule pièce (Figure 7.2). Un résultat secondaire est que le gain MIMO à 60-GHz devient corrélé à la distance entre l'émetteur et le récepteur (Figure 7.3), au lieu de l'espacement entre les éléments, comme supposé dans les modèles théoriques de communication [1].

En ce qui concerne les scénarios de mobilité des dispositifs, il a été observé que l'algorithme de recherche de motif du 802.11ad coûte plus de temps de canal que la transmission de données Gbps et dégrade donc le débit, même pour un diagramme de rayonnement de 22.5^0 ouverture du faisceau avec une zone de recherche relativement petite. Le 802.11ad suggère un mode quasi-omni tentant d'accélérer la procédure de découverte du client AP en élargissant les diagrammes de rayonnement. Pourtant, cela aide rarement, car le canal à 60-GHz lui-même présente un angle d'arrivée (AOA) dense modèle. Il a également été découvert, pour la première fois, que les liaisons 802.11ad ont tendance à être asymétriques en raison de l'interaction complexe entre les diagrammes de rayonnement et la dynamique de l'environnement. De plus, même des faisceaux absolument étroits (par exemple 3.4^o) peuvent fuir des signaux provoquant des interférences et dégrader la réutilisation spatiale en raison de la réflexion et des forts lobes latéraux de l'antenne.

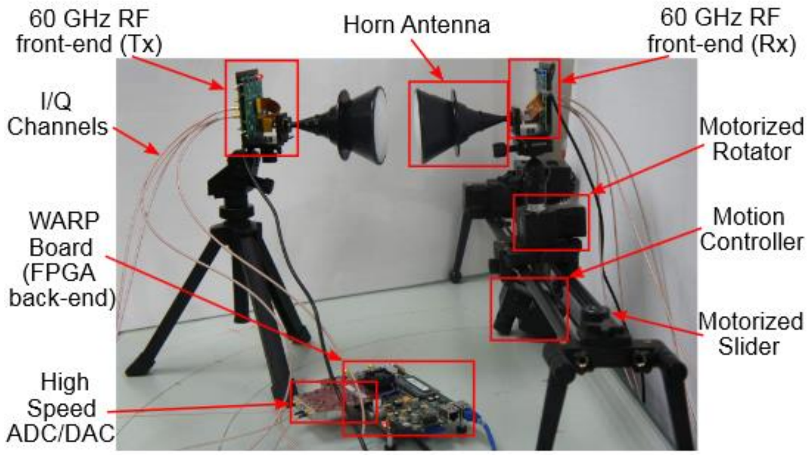

Figure 7.1: Plateforme radio logicielle de 60-GHz (S. Sur et al. [1], @2015 ACM).

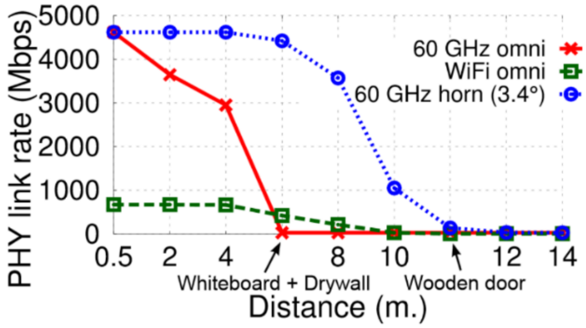

Figure 7.2: Débit et couverture en environnement intérieur.La puissance de transmission des liaisons à 60-GHz est calibrée pour correspondre au minimum de RSS requis pour un débit binaire maximal à 50 cm. Le WiFi est calibré pour avoir un gain supérieur de 28 dB à 60-GHz (S. Sur et al. [1], @2015 ACM).

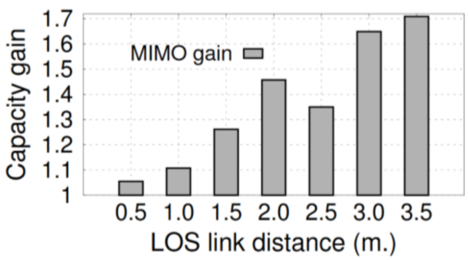

Figure 7.3: Gain de capacité 2×2 MIMO pour différentes distances de liaison (S. Sur et al. [1], @2015 ACM).

Les chercheurs ont proposé plusieurs techniques pour améliorer les caractéristiques des antennes en bande de fréquence à ondes millimétriques.

Les systèmes à ondes millimétriques offrent un débit de données élevé en raison d'une bande passante importante, mais souffrent d'un faible budget de liaison. Ceci est dû au blocage du signal de l'onde millimétrique par des obstacles d'une taille comparable à celle de la longueur d'onde du signal. Les différentes analyses visant à améliorer la force du signal sont rapportées. L'un d'eux suggère l'utilisation d'antennes directives qui garantissent la transmission du signal s'il existe une communication en ligne de visée entre l'émetteur et le récepteur.

L'autre variante possible est la mise en forme de faisceau à entrées multiples (MIMO) qui utilise les statistiques de canal pour orienter le faisceau, améliorant ainsi le gain de multiplexage et le gain de formation de faisceau. Plusieurs auteurs ont étudié la réduction du couplage mutuel entre les éléments rayonnants dans les systèmes MIMO, ce qui, dans la plupart des cas, entraîne une dégradation des caractéristiques de rayonnement attendues et affecte à la fois le diagramme de rayonnement de l'élément intégré et l'impédance d'entrée de l'élément [2]-[7]. Le couplage mutuel a un impact sur les performances du système MIMO en modifiant l'impédance d'entrée des éléments rayonnants, en augmentant le niveau des lobes latéraux et en dégradant la forme du diagramme de rayonnement [2]. Dans [2], il est indiqué que pour optimiser la capacité de canal des systèmes MIMO et améliorer le rapport signal sur bruit, l'espacement entre les éléments devrait être minimal. Cependant, l'espacement entre les éléments est généralement considéré comme une demi-longueur d'onde en raison de limitations de mise en œuvre. Un tel espacement engendre un fort couplage mutuel entre les éléments rayonnants. Le haut degré d'isolation et le faible coefficient de corrélation d'enveloppe (CEC) sont importants dans les systèmes MIMO [3]. Le code ECC est lié au couplage mutuel et il est proportionnel au couplage mutuel entre deux canaux [3]. Le couplage mutuel est principalement dû à trois composantes, les ondes de surface, le couplage entre les lignes d'alimentation et le couplage dû aux champs spatiaux. Pour réduire le couplage mutuel dû aux ondes de surface, une bande interdite peut être obtenue au moyen de structures à bande interdite électromagnétique (EBG) afin de bloquer la propagation des ondes de surface vers l'antenne suivante [2]. Pour réduire le couplage mutuel dû aux lignes d'alimentation, il existe certaines techniques dans la littérature telles que l'utilisation d'un réseau d'alimentation symétrique [8]. Il existe également d'autres techniques pour réduire le couplage mutuel, notamment les capes elliptiques confocales à métasurface [4], les fentes d'éléments parasites [5] et les résonateurs à cavité [6]. En raison de la limitation de l'espace de fabrication dans la bande de fréquence à ondes millimétriques, ces méthodes ne sont pas pratiques. L'espacement entre les éléments dans les réseaux d'antennes MIMO à ondes millimétriques est inférieur à quelques millimètres. Dans [7], un mur de surface sélectif en fréquence a été utilisé pour réduire le couplage mutuel. Une autre approche pour la réduction de couplage mutuel utilisant une paroi de bande coplanaire entre deux antennes est décrite dans [9]. Un mur de blindage de métasurface dans [10] et une surface sélective en fréquence dans [11] ont été conçus dans notre groupe de recherche pour la réduction du couplage mutuel. Cependant, ces techniques dégradent le diagramme de rayonnement de l'antenne. Cela est dû au fait que le mur de surface sélectif en fréquence ou le mur de bande coplanaire ne correspond pas. En conséquence, le diagramme de rayonnement est incliné en raison des ondes réfléchies par le mur encastré entre les antennes. La prochaine génération de réseaux de données sans fil ou de communications mobiles 5G devrait fonctionner sur des réseaux fonctionnant dans la bande des 60-GHz (57-64 GHz) pour la prochaine génération de réseaux de données sans fil urbains denses (5G) et le WiFi [12]. Un système MIMO massif est un bon candidat qui offre d'excellents gains en termes de capacité et de performances de liaison pour la 5G. Un tel système MIMO massif est mis en œuvre en utilisant un très grand nombre d'antennes au niveau de la station de base et généralement un petit système d'antenne MIMO dans des appareils portatifs [13]. Dans un tel système MIMO (système d'antenne MIMO massif de station de base et système d'antenne MIMO de petits appareils portables), la corrélation de canaux dégradera considérablement les performances du système MIMO global, par exemple sa capacité. En conséquence, les antennes des appareils portatifs doivent être conçues de manière à avoir la corrélation la plus faible, ce qui ne peut être obtenu uniquement par un réseau d'antennes MIMO à faible couplage mutuel. En plus d'avoir un faible couplage mutuel, le diagramme de rayonnement ne doit pas être dégradé pour obtenir la corrélation spatiale la plus faible.

Une autre analyse visant à améliorer la force du signal est la formation de faisceau. Les systèmes d'antennes intelligentes à commutation de faisceaux peuvent être meilleur marché qu'un réseau équivalent phasé, en particulier lorsque peu de signaux de faisceau sont nécessaires. Récemment, des systèmes d'antennes intelligentes à commutation de faisceaux, tels que la matrice de Butler, ont été étudiés pour améliorer les performances des réseaux 60GHz mmWave. La popularité de la matrice de Butler en tant que formateur de faisceau dans une antenne intelligente à faisceaux multiples commutée est due à de nombreux avantages. Premièrement, il peut être facilement implémenté en utilisant des hybrides et des déphaseurs. Deuxièmement, les faisceaux générés sont orthogonaux du type Woodward-Lawson et ont une largeur de faisceau étroite et une directivité élevée. Troisièmement, il a la longueur de chemin minimale et le nombre de composants par rapport aux autres réseaux de formation de faisceau à excitation uniforme. Cependant, en raison de la petite dimension et de la perte de propagation importante aux fréquences millimétriques, la conception de réseaux de formation de faisceaux dans la plage de fréquences millimétriques a été une tâche ardue pour les concepteurs. Au cours de la dernière décennie, plusieurs efforts ont été déployés pour inventer une nouvelle ligne de transmission à haut rendement et à faibles pertes pour les gammes de fréquences hyperfréquences à haute fréquence et à ondes millimétriques. Par exemple, la technologie des guides d'ondes intégrés au substrat (SIW) a été développée au cours de la dernière décennie en tant que ligne de transmission à faibles pertes [14]-[16]. Cependant, la conception des composants hyperfréquences, tels que les coupleurs avec la technologie SIW, altère les performances de la ligne de transmission SIW à faibles pertes, en raison de la perturbation de la caractéristique de la ligne de transmission SIW hôte [17]-[19]. Pour surmonter ces problèmes, une autre approche alternative, appelée technologie de guide d’onde à crête-gap, a été proposée [20]. Le guide d'ondes Ridge-gag est une ligne de transmission à très faibles pertes aux fréquences millimétriques [20]-[22]. Dans cette technologie, les champs électriques et magnétiques sont capturés entre deux surfaces métalliques et deux parois latérales ouvertes. Par conséquent, les champs électriques et magnétiques voyagent dans l'entrefer. Dans la ligne de transmission à fente faussée, les pertes sont inférieures à celles de la ligne de transmission SIW en raison du fait que les ondes électriques et magnétiques voyagent dans les airs et le diélectrique hôte dans les lignes de transmission à fente fente et SIW, respectivement. De plus, la mise en œuvre de pli, de fente ou de toute perturbation dans la ligne de transmission SIW détériore sa nature caractéristique à faible perte, en raison de la perturbation de la caractéristique de la ligne de transmission hôte SIW. Cependant, la ligne de transmission faîtière est moins sensible aux perturbations telles que le pliage ou la fente. Par exemple, à la fois dans SIW et entre crêtes, l'effet de charge d'une courbure dans la ligne de transport sera compensé, mais la différence vient du fait que SIW est remplie d'un diélectrique, qui présente des pertes électriques et magnétiques. En SIW et en crête-gap, l’effet de chargement du pli est compensé en tronquant le coin, mais la vague se reflétera plusieurs fois au coin. Ces ondes réfléchies dans SIW et Ridge-Gap voyagent respectivement dans l'air et dans le diélectrique hôte, ce qui rend le SIW encore plus nuisible aux perturbations de la ligne de transmission.

7.3 Antennes mmWave MIMO Efficaces

Les performances d'un système MIMO dépendent principalement de la présence de plusieurs canaux indépendants. Dans les systèmes MIMO, plusieurs canaux dépendants vont dégrader les performances d'un système MIMO, par exemple sa capacité. La corrélation de canaux est un paramètre permettant de mesurer la similarité ou la vraisemblance entre les canaux dans les systèmes MIMO. Dans le pire des cas, si les canaux sont complètement corrélés, le système MIMO agira comme un système de communication à une seule antenne. En général, la capacité du canal est inversement proportionnelle à la corrélation du canal. Dans les systèmes MIMO, la corrélation de canaux est généralement due à la corrélation spatiale et au couplage mutuel d'antenne [51]-[52]. La corrélation spatiale définie par la direction du signal à trajets multiples. Les signaux à trajets multiples seront transmis par l'émetteur dans une direction angulaire spatiale, nommée angle de départ (AOD), plutôt que dans une direction spécifique. Pour le récepteur, il existe la même définition pour les signaux à trajets multiples reçus, appelée angles d'arrivée (AOA). La corrélation spatiale est inversement proportionnelle à l'AOD et à l'AOA. Le scénario idéal est donc que l'AOA au récepteur se situe à 360^o sur le plan (plan en H) perpendiculaire aux antennes dipôles et que le diagramme de rayonnement des antennes dipôles soit omnidirectionnel (voir Figure 7.4). Cependant, cela est impossible dans des circonstances réelles. Par exemple, les concepteurs ont l'intention d'utiliser des antennes rayonnant un demi-espace pour des raisons pratiques telles que l'augmentation du gain ou la limitation du rayonnement vers le corps dans les appareils portatifs. De plus, les deux antennes dipôles s'affectent et ne présentent pas de diagramme de rayonnement omnidirectionnel. Le meilleur scénario pratique consiste donc à disposer de deux antennes rayonnantes demi-espace avec une distance minimale entre les éléments et la même caractéristique de rayonnement, autant que possible. Dans ce travail, notre priorité était de concevoir une antenne MIMO à faible coefficient de corrélation. Pour atteindre cet objectif, les deux éléments rayonnants de l'antenne MIMO proposée devraient avoir la même caractéristique rayonnante, sinon, même s'ils ont un faible couplage mutuel, la corrélation est élevée. La corrélation entre les canaux dans un système MIMO est liée au couplage mutuel et elle est proportionnelle au couplage mutuel entre deux canaux si la corrélation spatiale est faible [3].

7.3.1 Paroi de polarisation-rotateur des métamatériaux et antenne MIMO

La réduction du couplage mutuel entre les éléments rayonnants dans les systèmes MIMO, qui, dans la plupart des cas, entraîne une dégradation des caractéristiques de rayonnement attendues et affecte à la fois le diagramme de rayonnement de l'élément intégré et l'impédance d'entrée de l'élément, a été étudiée par plusieurs auteurs [2]-[3], [7]-[11], [49]-[50]. Un degré élevé d'isolation et un faible coefficient de corrélation d'enveloppe (ECC) sont des paramètres importants dans les systèmes MIMO [3]. Le code ECC est lié au couplage mutuel et il est proportionnel au couplage mutuel entre deux canaux [3]. Le couplage mutuel est principalement dû à trois composantes: les ondes de surface, le couplage entre les lignes d'alimentation et le couplage dû aux champs spatiaux. Pour réduire le couplage mutuel dû aux ondes de surface, une bande interdite peut être obtenue au moyen de structures à bande interdite électromagnétique (EBG) afin de bloquer la propagation des ondes de surface vers l'antenne adjacente [2]. Pour réduire le couplage mutuel dû aux lignes d'alimentation, il existe certaines techniques dans la littérature telles que l'utilisation d'un réseau d'alimentation symétrique [8]. Dans [7], un mur de surface sélectif en fréquence a été utilisé pour réduire le couplage mutuel dû aux champs spatiaux. Une autre approche pour la réduction de couplage mutuel utilisant une paroi de bande coplanaire entre deux antennes a été rapportée dans [9]. Une paroi de blindage de métasurface dans [10] et une surface sélective en fréquence dans [11] ont été conçues pour la réduction du couplage mutuel. Cependant, ces techniques dégradent le diagramme de rayonnement de l'antenne. Cela est dû au fait qu'un mur de surface sélectif en fréquence ou un mur en bande coplanaire ne correspond pas. En conséquence, le diagramme de rayonnement est incliné en raison des ondes réfléchies par le mur encastré entre les antennes.

Ici, une technique efficace pour réduire le couplage mutuel entre les antennes à résonateur diélectrique à ondes millimétriques (DRA) utilisant une nouvelle paroi pour le métamatériel de polarisation-rotateur (MPR) est présentée et présentée. Le couplage mutuel est réduit en incorporant une paroi MPR entre deux antennes à résonateur diélectrique, qui sont placées dans le plan H. En utilisant ce mur MPR, les modes TE des antennes deviennent orthogonaux, ce qui réduit le couplage mutuel entre les deux éléments rayonnants. Le couplage mutuel est réduit de plus de 16 dB en moyenne lorsque les murs MPR sont placés entre les antennes. Le mur MPR proposé n'a pratiquement aucun effet sur les caractéristiques de l'antenne en termes d'impédance d'entrée et de diagramme de rayonnement. Le MPR est inspiré de la technique décrite dans [55] qui consiste en deux paires de SRR torsadés, et le résonateur à anneau divisé (SRR) en diagonale est identique. Dans ce travail, le mur MPR comprend une structure périodique de cellules unitaires de métamatériaux, comme illustré à la Figure 7.5. Le couplage copolaire et croisé opposé simulé entre les modes, à la fois en réflexion et en transmission, est représenté en termes de paramètres S à la Figure 7.6.

Intégration de murs MPR et de réseaux d'antennes à résonateur diélectrique:

Le réseau d'antennes à résonateur diélectrique (DRA) est conçu sur la base de la référence [2]. L'antenne DRA est constituée d'un résonateur diélectrique cylindrique ayant une permittivité relative de 10.2 (RT6010). Le mode fondamental $HEM_{11\delta}$ est excité en excitant l'antenne DRA avec une fente au centre du résonateur diélectrique. La configuration du réseau d'antennes 1×2 DRA est disposée dans le plan H avec une distance de centre à centre de 2.5 mm correspondant à $\lambda_o/2$ à 60-GHz. Pour réduire le couplage mutuel entre les éléments rayonnants DRA, le mur MPR est placé entre les deux antennes. Le système d'antenne MIMO avec le mur MPR proposé est fabriqué et mesuré. La photographie du prototype fabriqué est présentée à la Figure 7.11. Les coefficients de couplage et de réflexion mutuels mesurés du système d'antenne proposé sont illustrés aux Figure 7.8 et Figure 7.9. Les diagrammes de rayonnement des réseaux d'antennes DRA MIMO avec et sans paroi de métasurface entre les deux éléments rayonnants sont illustrés à la Figure 7.10.

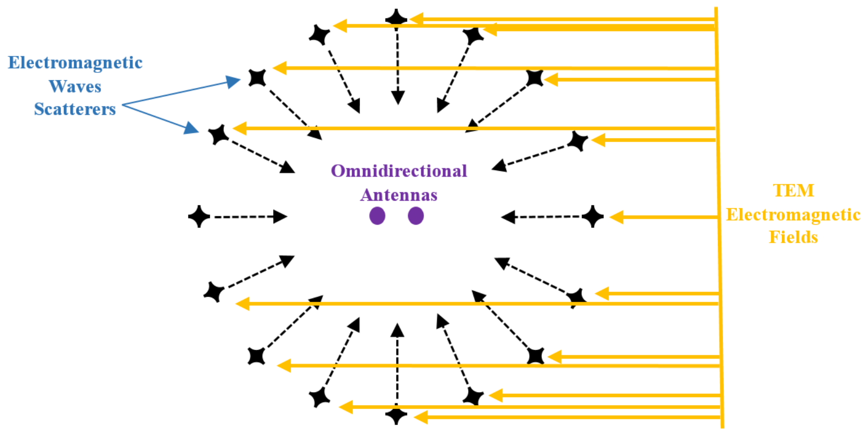

Figure 7.4: Le scénario idéal en termes de corrélation la plus faible entre les deux canaux dans un système MIMO.L'AOA du récepteur est 360^o sur le plan (plan H) perpendiculaire à une antenne dipôle et les diagrammes de rayonnement des antennes dipôles sont omnidirectionnels.

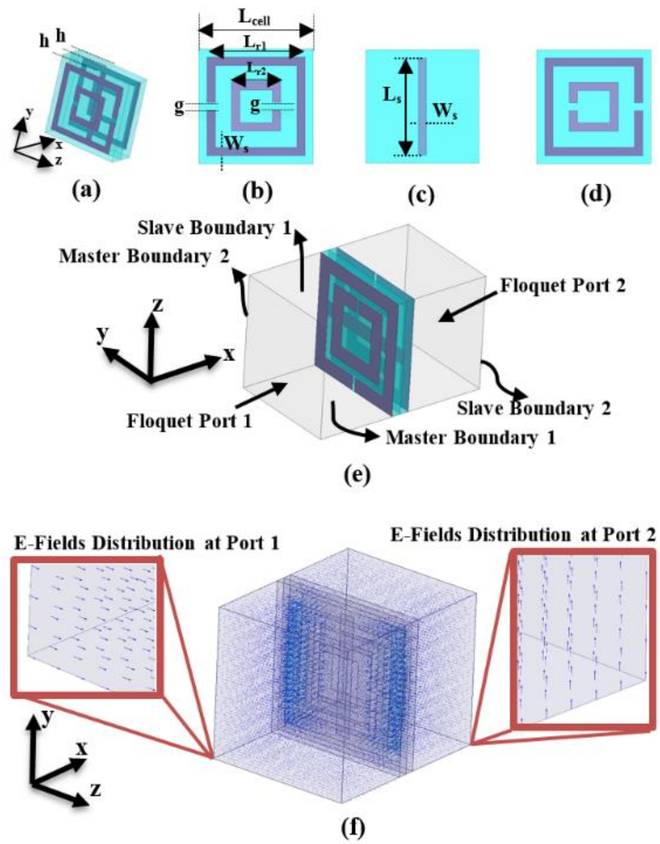

Figure 7.5: (a) Vue en perspective de la cellule élémentaire, (b) Semblable au SRR métallique sur la surface supérieure, (c) Bande métallique au milieu, (d) Semblable au SRR métallique sur la surface inférieure, (e) Conditions aux limites spécifiques et excitation définie du port de Floquet pour extraire les paramètres de diffusion, (f) distribution des champs E à 60-GHz.Les dimensions sont $L_{cell} = 2$, $L_{r1} = 1.6$, $L_{r2} = 1$, $g = 0.05$, $W_s = 0.2$, $h = 0.127$ et le tout en millimetres (M. Farahani et al. [47], @2017 IEEE).

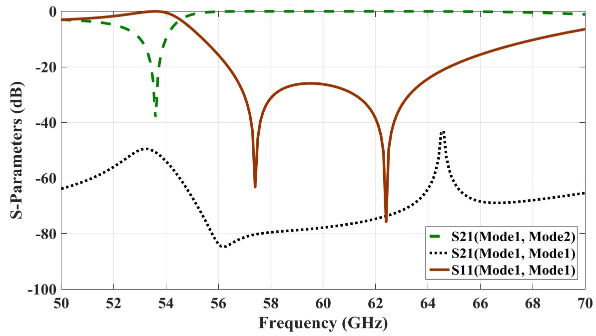

Figure 7.6: Coefficients de transmission/réflexion de la cellule unitaire MPR propose (M. Farahani et al. [47], @2017 IEEE).

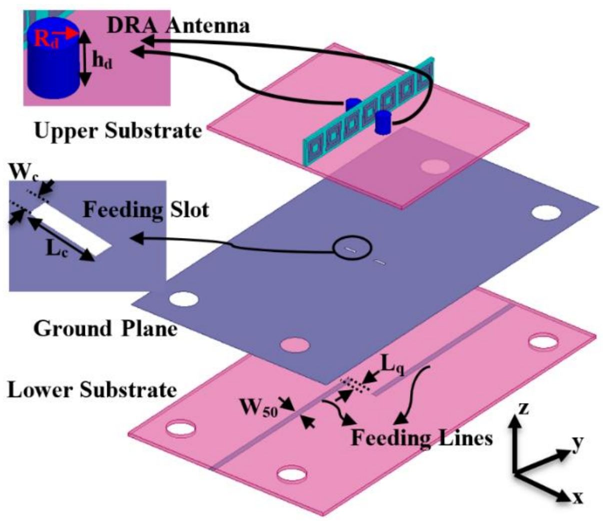

Figure 7.7: Disposition de l'antenne 1×2 DRA MIMO avec le mur MPR.Les dimensions sont $R_d = 0.53$, $h_d = 1.27$, $W_c = 0.18$, $L_c = 0.87$, $W_{50} = 0.41$, $L_q = 0.3$ et le tout en millimètres (M. Farahani et al. [47], @2017 IEEE).

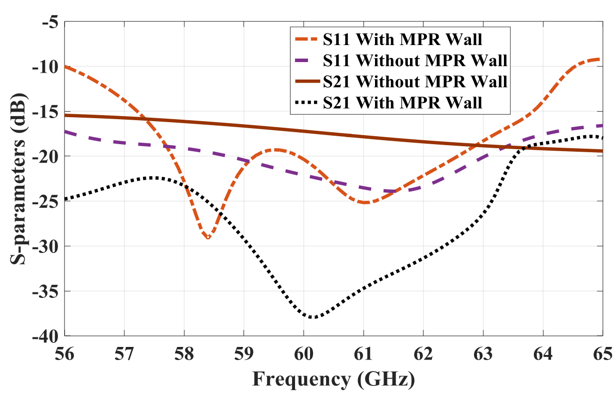

Figure 7.8: Résultats de la simulation des paramètres S d'antennes MIMO 1×2 DRA avec et sans paroi MPR entre les deux éléments rayonnants (M. Farahani et al. [47], @2017 IEEE).

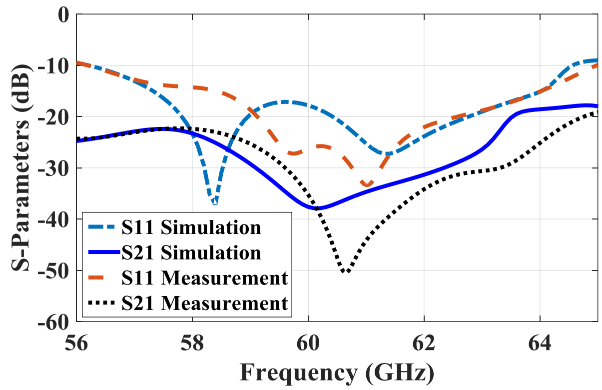

Figure 7.9: Résultats simulés et mesurés d’un système d’antenne MIMO 1×2 DRA avec paroi MPR entre deux éléments rayonnants (M. Farahani et al. [47], @2017 IEEE).

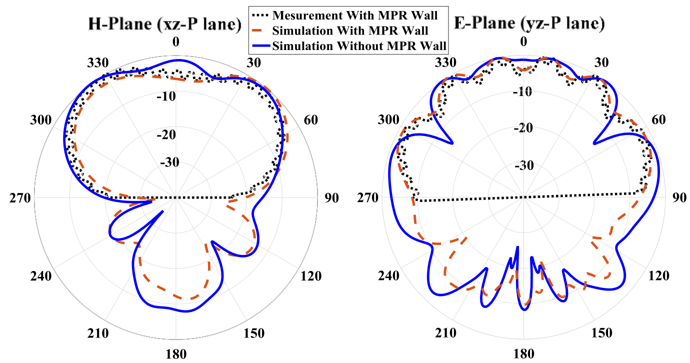

Figure 7.10: Diagramme de rayonnement simulé et mesuré du système d'antenne MRAI 1×2 DRA avec et sans paroi MPR entre deux éléments rayonnants (M. Farahani et al. [47], @2017 IEEE).

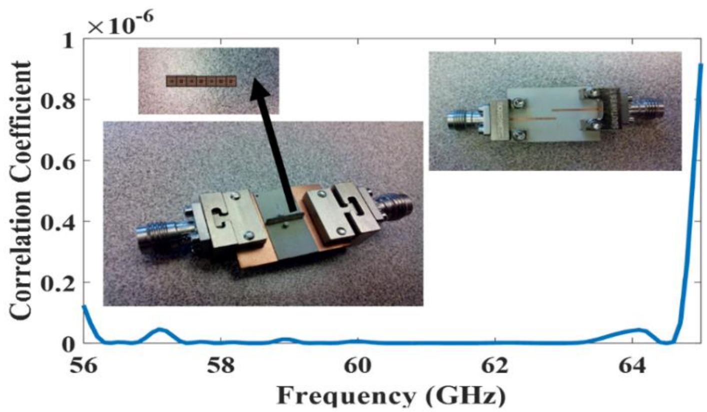

Figure 7.11: Résultat mesuré pour le coefficient de corrélation entre les deux antennes DRA MIMO avec paroi MPR entre les deux éléments rayonnants et la photo du prototype fabriqué proposé (M. Farahani et al. [47], @2017 IEEE).

7.3.2 Surface ondulée millimétrique-onde pour la réduction de couplage mutuel

Dans cette section, une surface ondulée est proposée pour réduire le couplage mutuel. La surface ondulée proposée présente une bande interdite dans la direction de propagation vers l'antenne adjacente. La structure proposée ne dégrade pas le diagramme de rayonnement dans les bandes d'ondes millimétriques, mais à une fréquence inférieure, elle a un impact significatif sur le diagramme de rayonnement.

1×2 Antenne dipole:

Le diagramme schématique du réseau d'antennes dipôles 1×2 utilisé est présenté à la Figure 7.12. Chaque antenne est alimentée par une ligne microruban. Le plan de masse s'est terminé au milieu de la ligne L_2 pour fonctionner comme un balun et entraîne les ports dipôles avec un décalage de phase de 180 degrés. L'antenne dipôle n'est pas mise à la terre et rayonne dans les deux demi-espaces. La distance de l'antenne est égale à la moitié de la longueur d'onde de l'espace libre. Rogers RT6002 est utilisé comme substrat hôte avec une permittivité relative de $\varepsilon_r = 2.94$ et les dimensions de l'antenne sont indiquées à la Figure 7.12.

Surface corrugée et réduction du couplage mutuel:

La surface ondulée conventionnelle et la surface ondulée proposée sont illustrées à la Figure 7.13. La surface ondulée conventionnelle fonctionne comme une surface douce le long de la direction X [57], et l'impédance de surface peut être obtenue comme suit:

$$Z_X = \frac{E_X}{H_Y} = j\left(\frac{W}{P}\right)\eta \tan k_g d \qquad (7-1)$$

L'impédance de surface est infinie lorsque $d = \lambda_g/4$, ce qui correspond à une surface constituée d'une mince bande parallèle de PEC et de PMC orientée dans la direction Y (Figure 7.13c). La largeur de bande utilisable est comprise entre $0 < k_g d < \pi$, bien que des ondes de surface puissent exister lorsque $d \neq \lambda_g/4$. En pratique, une bande passante relative utilisable va jusqu'à 3%, bien que la meilleure performance douce d'E-Plane soit lorsque $k_g d = \pi/2$.

L'impédance de surface de la surface ondulée proposée (Figure 7.13b) peut être obtenue comme suit:

$$Z_X = \frac{E_X}{H_Y} = j\left(\frac{W}{P}\right)\eta \cot k_g d \qquad (7-2)$$

L'impédance de surface est infinie lorsque $d = \lambda_g/2$, ce qui correspond à une surface constituée d'une mince bande parallèle de PEC et de PMC orientée dans la direction Y (Figure 7.13c). Comme il a été dit, cette surface ondulée est une bande très étroite; dans la pratique, la largeur de bande relative utilisable va jusqu'à 3%. Pour améliorer la bande passante de la surface ondulée proposée, une surface ondulée à double bande

(Figure 7.13d) a été conçue pour couvrir la bande de fréquences de 57-64 GHz (6% de bande passante relative).

La surface ondulée proposée est placée entre les éléments d'antenne et est illustrée à la Figure 7.14. Cette structure ne peut être utilisée que dans les bandes de fréquence millimétriques. Aux bandes de fréquences hyperfréquences, jusqu'à 20 GHz, $d = \lambda_g/2$ est grand et l'incrustation de cette structure entre les antennes a donc un impact significatif sur le diagramme de rayonnement et va charger l'impédance d'entrée de chaque élément d'antenne en bloquant l'antenne rayonnement, et n'est donc pas utile dans ces bandes de fréquences. Le réseau d'antennes proposé avec la surface ondulée et sans la surface ondulée est simulé en utilisant HFSS. Les paramètres de diffusion de l'antenne proposée sont présentés à la Figure 7.15.

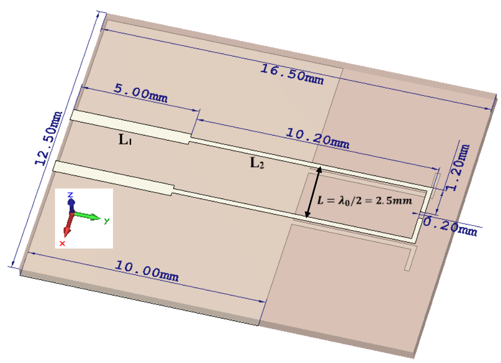

Figure 7.12: Diagramme schématique du réseau d'antennes dipôles 1×2 (M. Farahani et al. [48], @2016 IEEE).

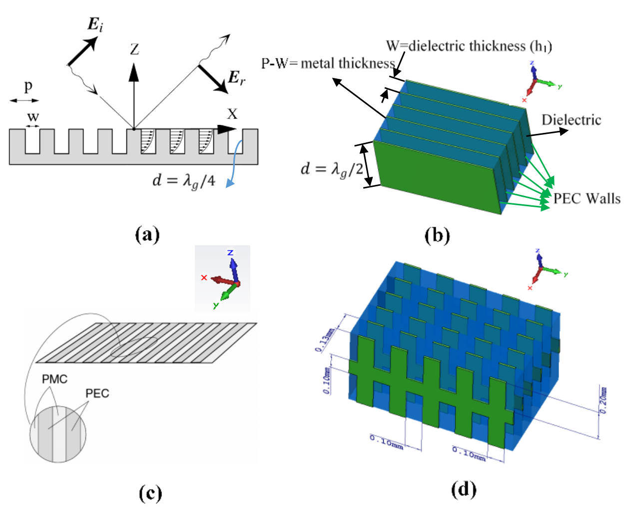

Figure 7.13: Surfaces ondulées.(a) Surface ondulée conventionnelle. (b) Surface ondulée proposée. (c) Modèle équivalent de surface ondulée. d) Surface ondulée à double bande proposée (M. Farahani et al. [48], @2016 IEEE).

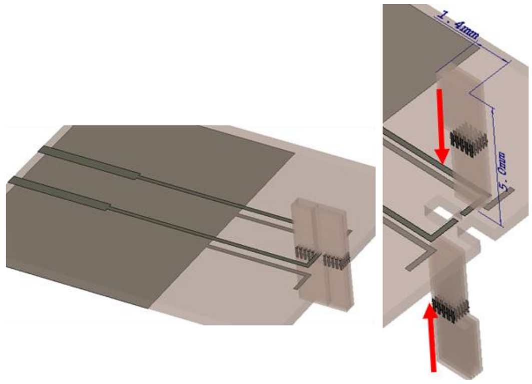

Figure 7.14: Réseau d'antennes dipôles 1×2 proposé avec surface ondulée (M. Farahani et al. [48], @2016 IEEE).

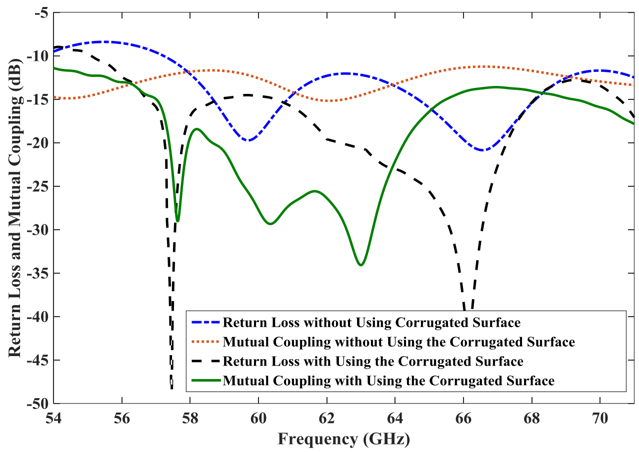

Figure 7.15: Perte de retour et couplage mutuel du réseau d'antennes 1×2, avec et sans la surface ondulée (M. Farahani et al. [48], @2016 IEEE).

7.3.3 Antenne MIMO à ondes millimétriques et superstrat FSS

1×2 MIMO Antennas:

Une nouvelle approche pour supprimer le couplage mutuel des champs électromagnétiques spatiaux entre deux antennes à polarisation circulaire (CP) utilisant une technique de surface sélective en fréquence (FSS) aux environs de 30 GHz est présentée. La couche FSS du type à transmission avec capacité CP est placée au sommet de deux antennes à entrées multiples et sorties multiples (MIMO). L'étude montre que la couche FSS peut supprimer en moyenne 10 dB couplage mutuel entre deux antennes CP-MIMO adjacentes. La technique proposée ne dégrade pas les performances d'impédance et de rayonnement de l'antenne par rapport à l'antenne sans couche FSS.

La géométrie des antennes CP-MIMO avec superstrat FSS est illustrée à la Figure 7.16. La conception de base consiste en trois substrats, le plus bas est Rogers 3006 avec une permittivité relative de 6,15 et les supérieurs sont de Rogers 5880 avec une permittivité relative de 2,2. La couche supérieure du substrat central comporte deux pièces métalliques circulaires. Dans le même temps, la distance entre les centres de correction est ‘d’ et égale à $\lambda_g/2$ (5 mm). Les deux patchs sont alimentés par des fentes dans le plan de masse commun sur la face supérieure de la couche inférieure. La superstrat FSS est séparé des antennes CP-MIMO par un espacement d’espace «h = 3,6 mm». La Figure 7.17a présente la vue 3D de la cellule unitaire du FSS ainsi que les dimensions correspondantes. Les résultats mesurés et simulés de l'antenne avec la superstrat du FSS sont illustrés à la Figure 7.18.

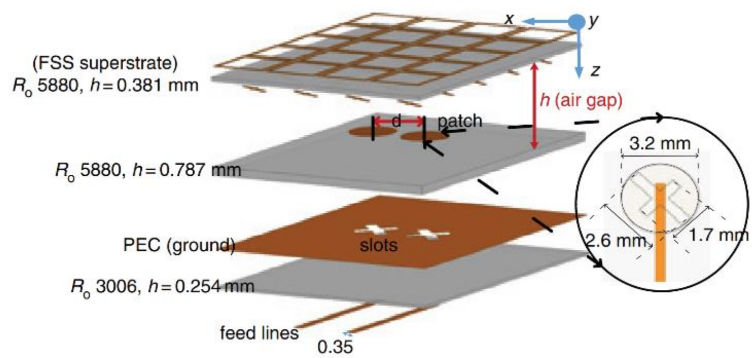

Figure 7.16: Schéma des antennes CP-MIMO avec superstrat du FSS (d = 0.5λ, h = 0.36λ à 30 GHz) (M. Akbari et al. [49], @2017 IET).

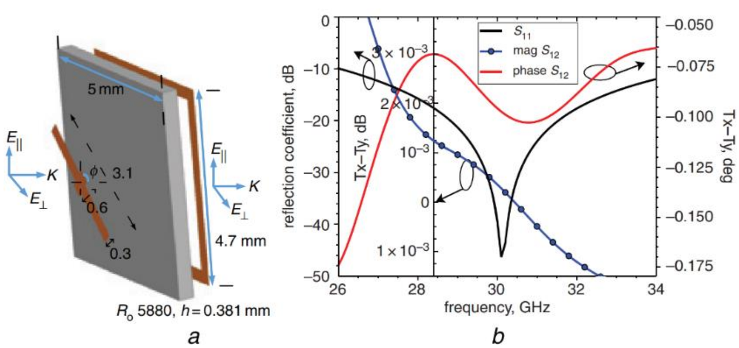

Figure 7.17: Résultats de structure et de paramètre S du modèle cellulaire unitaire du FSS. (a) Vue 3D de la cellule unitaire proposée du FSS. (b) Courbes du coefficient de réflexion ainsi que des différences de magnitude et de phase entre deux composantes du champ orthogonal (M. Akbari et al. [49], @2017 IET).

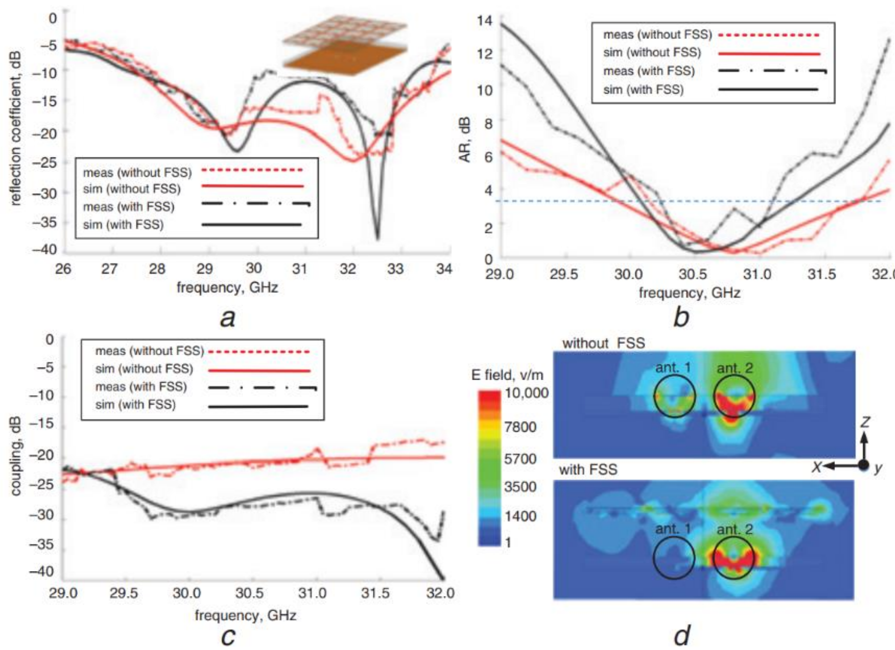

Figure 7.18: Résultats mesurés et simulés.(a) coefficient de réflexion. (b) Rapport axial. (c) couplage. (d) distributions de champ E à 30.5 GHz (M. Akbari et al. [49], @2017 IET).

2×2 Antennes MIMO:

Une approche efficace pour atténuer le couplage en champ proche entre des antennes à quatre ports à polarisation circulaire (CP) dans un système à plusieurs entrées et plusieurs sorties (MIMO) à 30 GHz est suggérée et étudiée. Ceci est obtenu en incorporant une superstrate de surface sélective en fréquence (FSS) de type à transmission à deux couches à base de bandes métalliques planes à dipôles croisés. Ce travail présente une comparaison entre le couplage mutuel lorsque les plaques rayonnent dans l'espace libre et en présence des couches du FSS. Les résultats simulés, lorsque les couches FSS sont appliquées, montrent une amélioration moyenne de 6-12 dB de l'isolement entre quatre antennes CP-MIMO adjacentes. De plus, une étude précise est effectuée sur les réflexions insignifiantes produites par les couches du FSS afin de les rediriger et d'éviter toute interférence. L'antenne CP-MIMO 2×2 proposée ainsi que la superstrate sont mises en œuvre et testées pour valider les résultats de la simulation. Les résultats expérimentaux des coefficients de couplage et de réflexion et du rapport axial montrent un accord acceptable avec ceux simulés correspondants.

La topologie de la couche FSS de type de transmission est illustrée à la Figure 7.19. Afin d'observer le comportement du FSS dipolaire croisé avec des éléments infinis, le modèle de cellule unitaire d'Ansys

HFSS, qui est une méthode par éléments finis (FEM) basée sur un simulateur de pleine onde, est appliqué. Dans ce modèle, deux ports Floquet à exciter ainsi que des frontières maître/esclave sont utilisés.

Afin de contribuer à la large bande de fréquences et au diagramme des côtés larges, une antenne micro-bande couplée à une seule ouverture (ACMA) est présentée. Comme illustré à la Figure 7.20, l'ACMA avec la capacité de polarisation circulaire consiste en deux diélectriques différents en tant que substrats: un substrat Rogers 3006 ($\varepsilon_r = 6.15$, $H_1 = 0.254$ mm) en bas, tandis que le haut est un substrat Rogers 5880 ($\varepsilon_r = 2.2$, $H_2 = 0.787$ mm). Au centre de l'ACMA, une plaque conductrice servant de plan de masse avec une fente transversale gravée au centre est utilisée pour fournir le couplage requis. En outre, une ligne d'alimentation microruban de 50 ohms et un patch en forme de cercle sont imprimés sur les couches inférieure et supérieure de l'ACMA, respectivement. L'antenne est conçue pour fonctionner à la fréquence centrale 30 GHz. Les résultats simulés du coefficient de réflexion et du rapport axial sont illustrés à la Figure 7.21, qui montre que l'ACMA couvre les impédances et les largeurs de bande CP comprises entre 28 GHz et 34 GHz (19,3%) et entre 29.2 GHz et 31 GHz (6%), respectivement.

Un système à plusieurs entrées et plusieurs sorties (MIMO) est considéré comme une technique permettant de multiplier la capacité d'une liaison radio utilisant plusieurs antennes d'émission et de réception pour exploiter la propagation par trajets multiples [62]. En utilisant ce concept, l'approche proposée dans ce travail vise à déterminer l'influence du couplage entre les éléments du MIMO-ACMA. Pour atteindre cet objectif, quatre éléments de l'ACMA sont formés en réseau deux à deux afin d'éclairer les couches du FSS. Le diagramme schématique du MIMO-ACMA est présenté à la Figure 7.22 et Figure 7.23, où les coefficients de couplage dans différentes directions et distances entre les ACMA sont définis avec les paramètres ‘‘C_d’’, ‘‘C_v’’, ‘‘C_h’’ et ‘‘di’’, respectivement.

La photographie de la structure mise en œuvre ainsi que la configuration de mesure sont observées aux Figure 7.24 et Figure 7.25. Il est à noter que les résultats simulés pour les coefficients de couplage S_{21}, S_{31} et S_{41} sont calculés directement à l'aide de HFSS. Les Figure 7.26 et Figure 7.27 présentent les paramètres S et le rapport axial simulés et expérimentaux de la conception proposée pour les deux cas de couplages air et FSS. Les mesures montrent un accord acceptable avec les simulations.

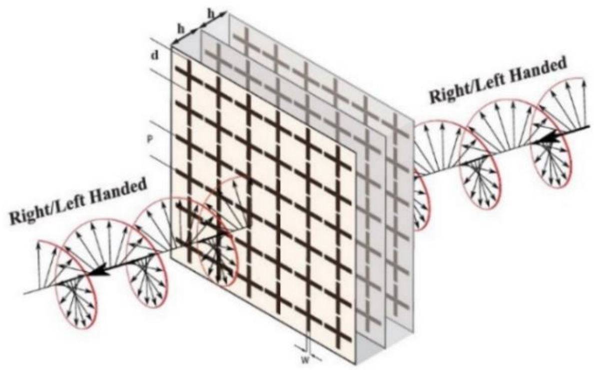

Figure 7.19: Modèle schématique du superstrat FSS de type transmission éclairant par une onde CP (les dimensions sont $h = 0.787$, $d = 2.7$, $P = 3$, and $W = 0.3$, le tout en millimètres) (M. Akbari et al. [50], @2017 IEEE).

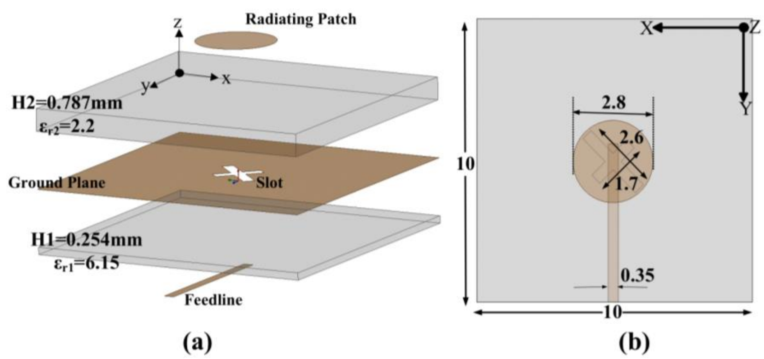

Figure 7.20: Géométrie de la vue latérale unique CP-ACMA (a) et (b) de la vue de dessus (M. Akbari et al. [50], @2017 IEEE).

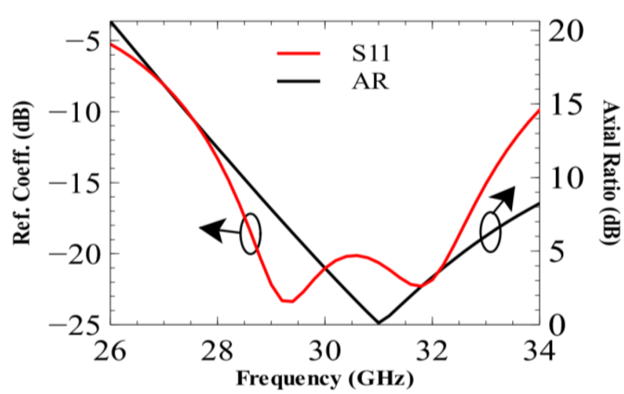

Figure 7.21: Coefficient de réflexion et rapport axial d'un patch CP à élément unique (M. Akbari et al. [50], @2017 IEEE).

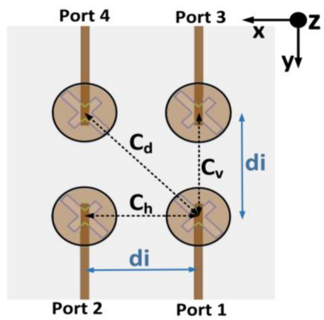

Figure 7.22: Diagramme schématique des MIMO-ACMA avec des coefficients de couplage (C_d, C_h, and C_v) et de l'espacement entre les éléments ACMA (di) (M. Akbari et al. [50], @2017 IEEE).

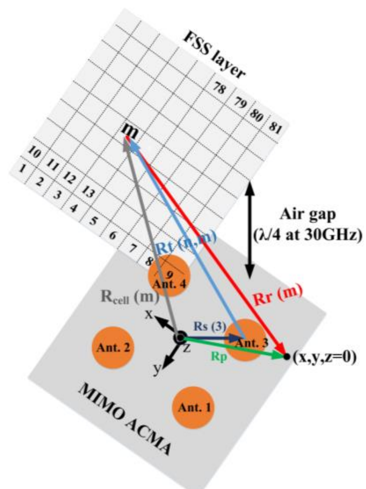

Figure 7.23: L'esquisse d'un réseau rectangulaire uniforme de 81 éléments FSS avec un espacement de 3 mm le long des axes x et y au-dessus de 2×2 MIMO-ACMA avec un entrefer de 2.5 mm le long de l'axe z (M. Akbari et al. [50], @2017 IEEE).

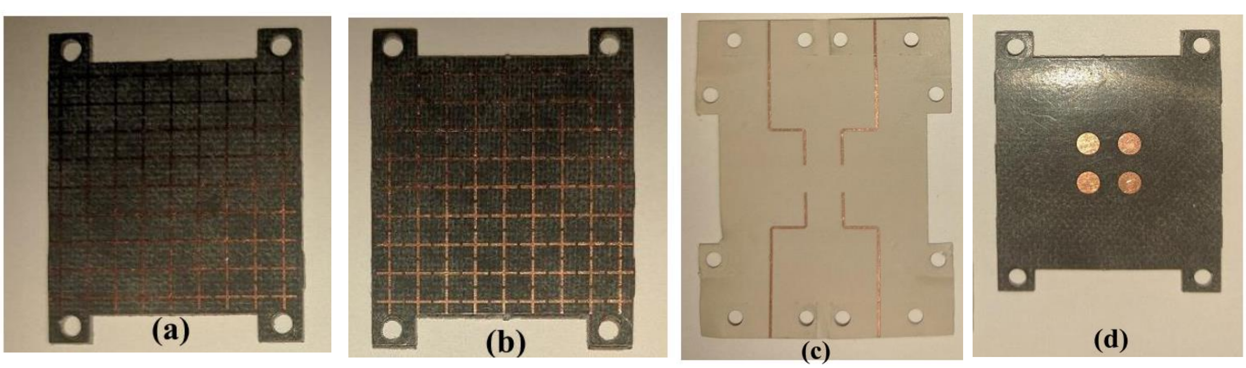

Figure 7.24: Photos des MIMO-ACMA 2×2 fabriqués: (a) et (b) des couches du FSS, (c) des lignes d'alimentation et (d) des correctifs (M. Akbari et al. [50], @2017 IEEE).

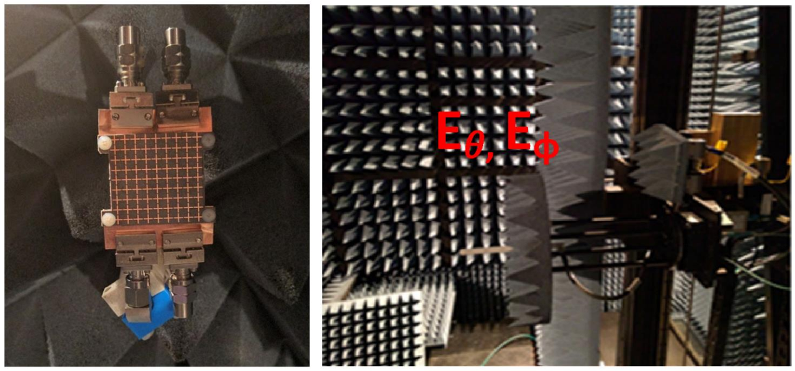

Figure 7.25: Photographie des antennes 2×2 CP-MIMO fabriquées à l'essai en tant qu'émetteur et du guide d'onde à extrémité ouverte (NSI RF WR28) en tant que récepteur dans la chambre anéchoïque en champ lointain (M. Akbari et al. [50], @2017 IEEE).

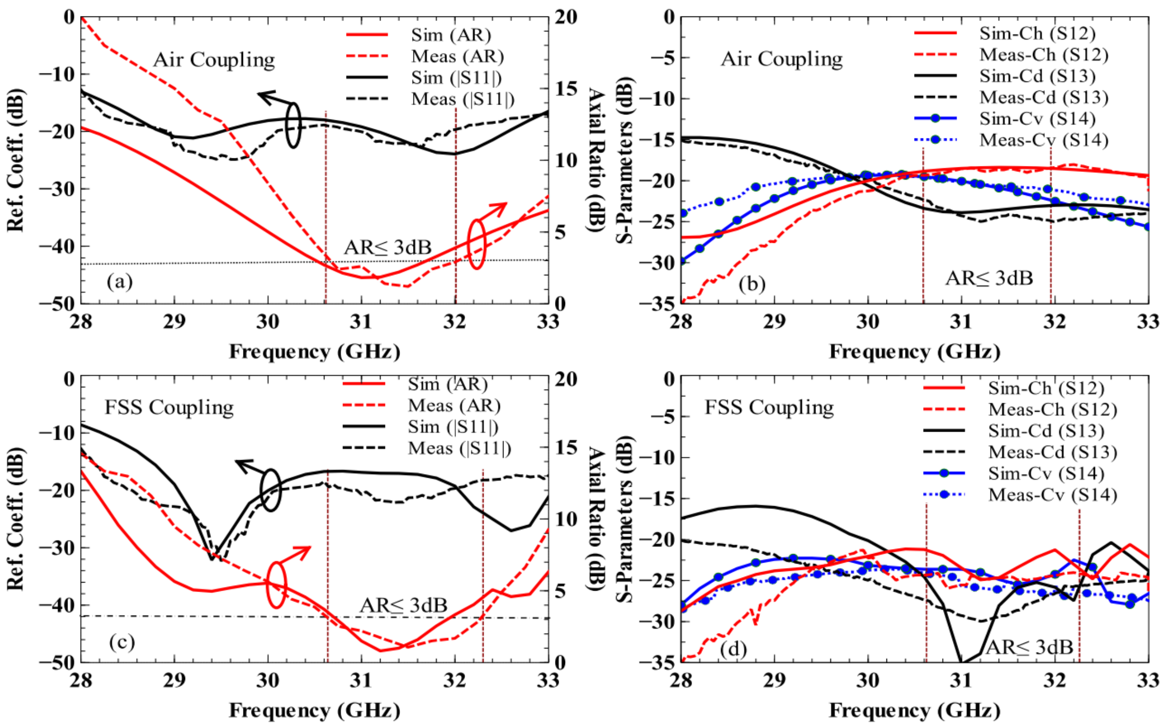

Figure 7.26: Résultats mesurés et simulés du rapport axial, du coefficient de réflexion pour différents cas de couplages air (a) et (c) FSS, ainsi que des résultats de couplage mesurés et simulés pour différents cas de couplages air (b) et (d) FSS (M. Akbari et al. [50], @2017 IEEE).

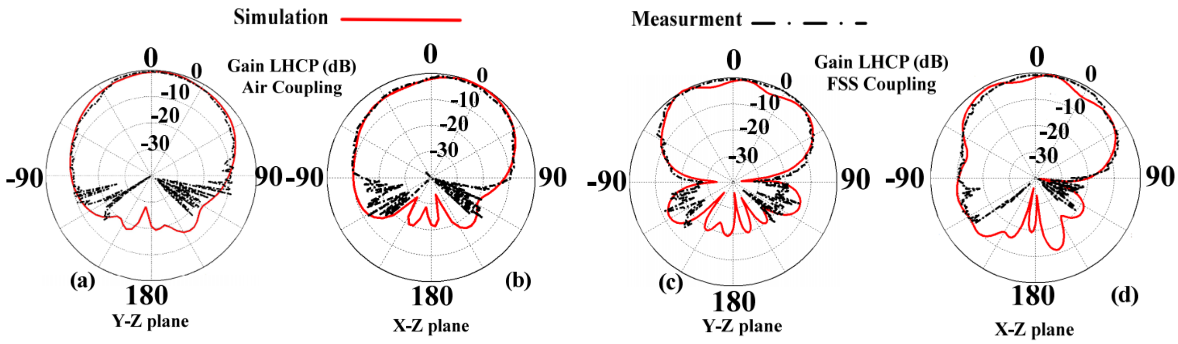

Figure 7.27: Gain LHCP mesuré et simulé pour les deux cas de couplage air (a), (b) et de couplage S (c), (d) dans les plans yz et xz à la fréquence 31 GHz (M. Akbari et al. [50], @2017 IEEE).

7.4 Antennes à gain élevé mmWave

La bande de fréquences mmWave à 60-GHz pose de sérieux obstacles au développement des réseaux à 60WHz mmWave. Dans les communications sans fil, le débit de la liaison de communication est l’un des indicateurs les plus importants pour l’estimation des performances. Cependant, le débit dépend fortement des caractéristiques du canal de propagation, telles que l'affaiblissement du trajet, la distance entre les dispositifs, le bruit, etc. Grâce à la formule du modèle d'affaiblissement du trajet de l'espace libre Friis, l'affaiblissement du trajet pour 60-GHz a une valeur proche de 28 dB perte plus par rapport à la bande des 5 GHz. Parallèlement, une perte supplémentaire (perte de puissance de 7-15,5 dB / km) doit être prise en compte dans le signal reçu à des fréquences porteuses de 60-GHz en raison de l'absorption atmosphérique [65]. Outre ces facteurs, le taux de précipitations affecte également les performances du système. Atténuation atmosphérique supplémentaire d'environ 8 à 18 dB / km alors que le taux de précipitations est de 50 mm par heure [65]. Outre la forte atténuation, la radio en ondes millimétriques 60-GHz présente également une faible capacité de pénétration [66]. En outre, bien que la taille physique des antennes soit si petite, la conception des réseaux d’alimentation en antennes devient complexe et pose un problème pour les concepteurs en raison du nombre élevé de pertes dans la bande de fréquence à onde millimétrique de 60-GHz.

Pour surmonter le blocage, plusieurs approches de la couche physique à la couche réseau ont été proposées. Cependant, chaque approche a ses avantages et ses inconvénients, et ces approches doivent être combinées de manière intelligente pour obtenir des performances réseau robustes et efficaces.

Contrairement à la perception conventionnelle selon laquelle les faisceaux de 60-GHz se comportent de manière pseudo-optique, les faisceaux fortement directionnels subissent moins de pertes de pénétration au travers d'obstacles typiques (sauf le corps humain) dans un environnement de bureau, et une couverture peut être atteinte au-delà d'une pièce unique [1].

Dans ce chapitre, différentes techniques sont étudiées pour augmenter le gain des antennes. Le développement d'un système fonctionnant dans la bande des 60-GHz pose un défi considérable en raison de la forte perte de propagation dans cette bande de fréquences, ce qui a nécessité la conception de récepteurs à haute sensibilité pour remédier à cet inconvénient. En ce qui concerne les antennes, il est nécessaire de développer des antennes directives à gain élevé.

7.4.1 Amélioration du gain avec la superposition FSS

Les systèmes 5G recherchent des antennes à gain élevé et à large bande fonctionnant dans la bande mmWave. Une méthode pour améliorer les caractéristiques de rayonnement (largeur de bande à gain de 3 dB) des antennes consiste à appliquer une approche de cavité de Fabry Perot (FPC) dans laquelle une surface de superstrate ou une surface partiellement réfléchissante (PRS) du FSS est incorporée à une amélioration des caractéristiques de rayonnement (gain de 3 dB largeur de bande) des antennes est en train d'appliquer une cavité Fabry Perot (une demi-longueur d'onde d'un plan de masse métallique crée une cavité remplie d'air. En éclairant le FPC avec une antenne source, il est possible d'améliorer considérablement les caractéristiques de rayonnement de l'antenne [67]-[70]. Ces antennes ont été conçues en utilisant différents types de superstrats PRS constitués de plaques ou fentes métalliques périodiques [71]-[73], de superstrats à dalles élec- triques monocouche [74] ou multicouches diélectriques [75]-[76]. Une des principales contraintes de telles cavités est leur bande passante gain / puissance de 3 dB, comme nous le verrons dans ce chapitre. Dans un premier temps, visant à obtenir la taille minimale de la superstrate PRS, nous présentons un modèle simple du rayons de diffraction et de transmission. La limitation de la largeur de bande de gain à 3 dB est l'un des inconvénients majeurs de l'antenne FPC. Par conséquent, pour élargir la largeur de bande de gain à 3 dB, une enquête est présentée dans la section suivante de ce chapitre, qui repose sur une méthode de la théorie de l'image et du support efficace.

Conception de la couche Superstrate:

Une FSS de 7×7 cellules est imprimée sur la face arrière de la superstrat (la troisième couche). Le superstrat est séparé du DRA par un intervalle d'air (H). De manière générale, des paramètres tels que les caractéristiques du DR (constante diélectrique, forme et dimension), la longueur et la largeur de l'ouverture de couplage, la hauteur de la superstrat par rapport au radiateur, les dimensions et la période des éléments du FSS sont des paramètres essentiels pour la commande différente fréquences de résonance pour les applications large bande. Les dimensions de la cellule du FSS et l'illustration de réflexions multiples et d'ondes qui fuient sont indiquées à la Figure 7.28. La Figure 7.29 montre les coefficients de réflexion et de transmission de la phase et de l'amplitude de la cellule élémentaire du FSS.

Pour améliorer le gain d'antenne, cette thèse propose une superstrat FSS au sommet d'une ouverture de base couplée à un DRA avec un entrefer de séparation. De plus, en utilisant un ou plusieurs superstrates FSS, diverses fréquences de résonance peuvent être obtenues, bien qu'il y ait une limitation due à la taille requise de l'antenne compacte. Il convient de noter qu'une superstrat du FSS réduira considérablement la largeur de bande de l'impédance. Les diagrammes de rayonnement 3D des variations du champ E du DRA et du RHCP couplées à l'ouverture à différentes phases sont illustrés aux Figure 7.30 et Figure 7.31, respectivement.

Les résultats mesurés et simulés du gain total, du rapport axial et du coefficient de réflexion sont illustrés à la Figure 7.32. Il est évident que la simulation et les résultats de mesure ont un accord acceptable. L'antenne fabriquée peut couvrir une largeur de bande d'impédance de 29 à 31.5 GHz (8.26%) avec un rapport de largeur axiale de 29.7 à 30.6 GHz (2.97%) et un gain total de 15.5 dB à la fréquence centrale de 30 GHz. La Figure 7.33 illustre le diagramme de rayonnement de la DRA proposée à la fréquence de fonctionnement (30 GHz) sur les plans x-z et y-z. On observe que le niveau des lobes latéraux (SLL) est proche de -13 dB sur les deux plans. De plus, les simulations et les mesures ont un accord acceptable.

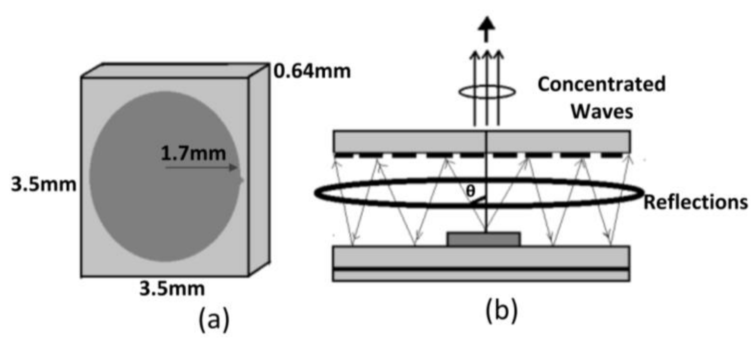

Figure 7.28: (a) Les dimensions de la cellule élémentaire du FSS et (b) l'illustration de réflexions multiples et d'ondes qui fuient (M. Akbari et al. [59], @2016 IEEE).

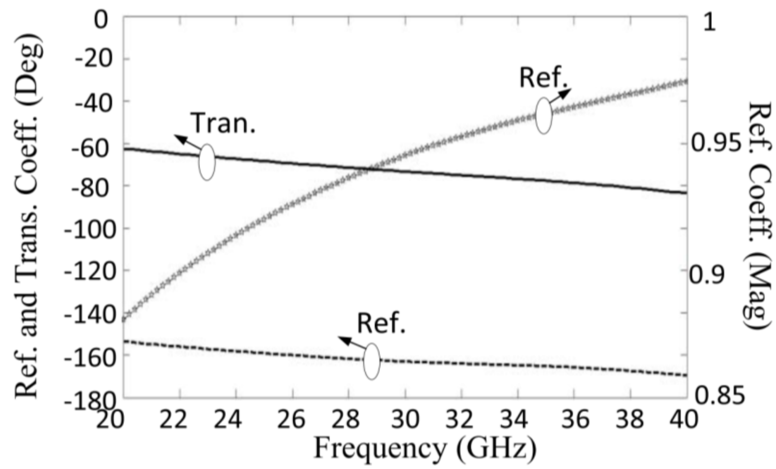

Figure 7.29: La phase et la magnitude des coefficients de réflexion et de transmission de la cellule unité du FSS (M. Akbari et al. [59], @2016 IEEE).

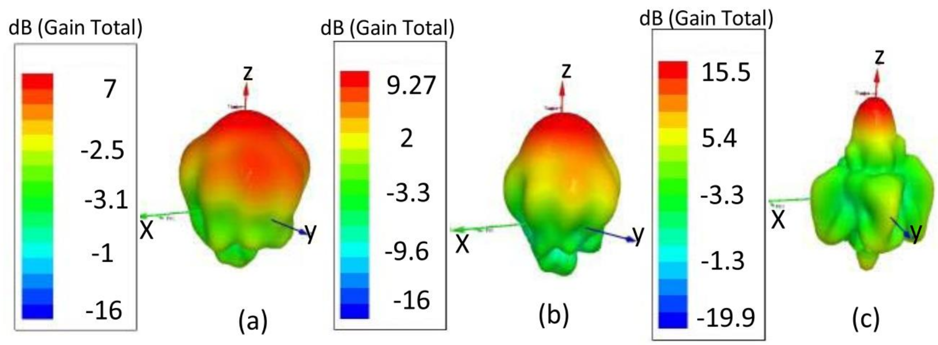

Figure 7.30: Diagrammes de rayonnement 3D du DRA couplé à l'ouverture à 30 GHz dans trois cas: (a) le DRA de base, (b) le DRA avec le seul superstrat et (c) le DRA avec le superstrat du FSS (M. Akbari et al. [59], @2016 IEEE).

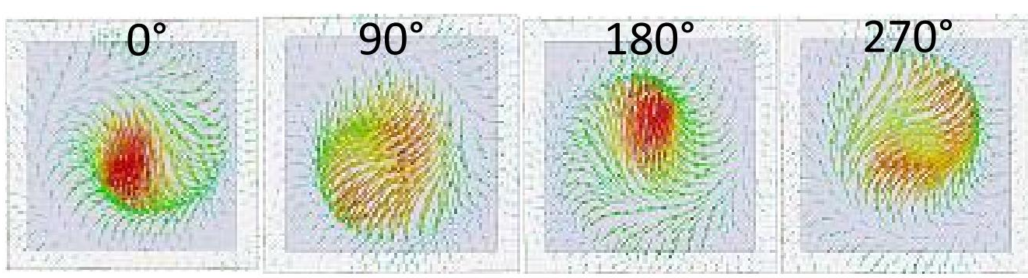

Figure 7.31: Variations du champ électromagnétique RHCP à différentes phases (a) 0^o, (b) 90^o, (c) 180^o, and (d) 270^o à la fréquence centrale 30 GHz (M. Akbari et al. [59], @2016 IEEE).

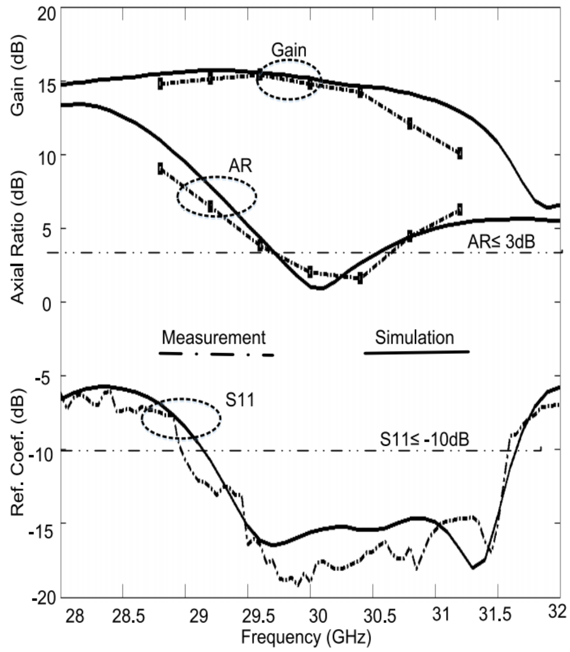

Figure 7.32: Courbes mesurées et simulées du gain total, du rapport axial et du coefficient de réflexion de l'antenne proposée (M. Akbari et al. [59], @2016 IEEE).

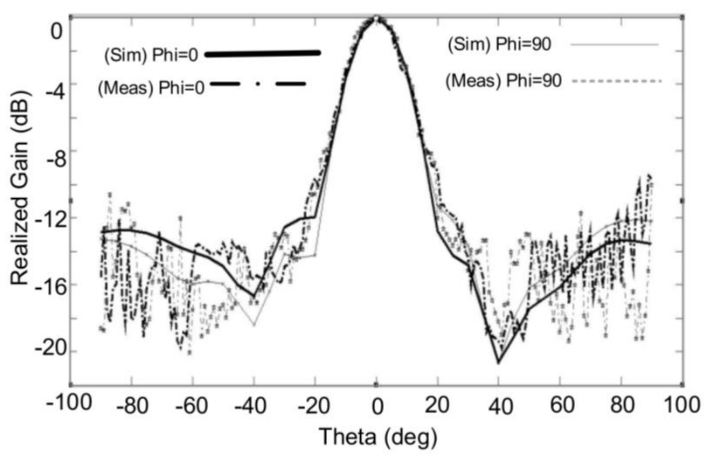

Figure 7.33: Le gain normalisé de l'antenne proposée à 30 GHz sur les deux plans phi=0 et phi=90 (M. Akbari et al. [59], @2016 IEEE).

7.4.2 Amélioration du gain à l'aide de la métasurface à gradient de phase (PGM)

Dans cette section, une antenne orientable à gain élevé utilisant une surface PGM est présentée. La surface proposée pour les platinoïdes est fixée au sommet d'une antenne de type patch annulée bordée alimentée par un guide d'ondes à fente. En faisant pivoter mécaniquement la surface du MGP autour de son centre, le diagramme de rayonnement peut être pivoté en continu.

Surface PGM et antenne patch Ridge Gap:

Pour orienter le faisceau principal de l'antenne patch à l'antenne proposée, la surface PGM conçue est placée sur un côté de l'antenne, comme indiqué à la Figure 7.34. La surface PGM proposée est intégrée au substrat hôte en demi-cercle du RO3003 avec une permittivité relative de 3, un rayon de 7.3 mm et une épaisseur de 0.13 mm. La Figure 7.34 montre la géométrie de la surface des platinoïdes. La surface de MGP comprend une structure périodique de cellules unitaires de patchs carrés placées sur un conducteur électrique parfait. Les ondes de surface se propagent selon l'axe radial avec un facteur de propagation $e^{(-\alpha_{PGM}-j\beta_{PGM})r}$. Pour analyser la propagation des ondes de surface le long de l'axe radial, il convient de prendre en compte la condition limite entre la surface du PGM et l'air, puis de résoudre les équations de Maxwell. En conséquence, la surface des platinoïdes renforce les ondes de surface et crée un autre centre de phase pour l'antenne avec une phase et une amplitude différentes, par rapport à l'autre section en demi-cercle du patch. Ce phénomène peut dévier le diagramme de rayonnement de l'antenne par rapport à l'axe large (axe z). Pendant ce temps, en faisant pivoter la surface du MGP autour de son axe, le diagramme de rayonnement balayera continuellement l'espace. De plus, en raison du fait que, grâce à cette technique, l'ouverture de rayonnement de l'antenne est augmentée, le gain de l'antenne a été augmenté à environ 15.2 dBi par rapport à l'antenne sans surface PGM, qui est d'environ 7 dBi.

L'antenne patch gap est intégrée au substrat hôte du RO3003 d'une épaisseur de 0.5 mm alimentée par le guide d'ondes inférieur. La fente au centre du patch excitera le mode fondamental. Dans le guide d'onde à l'intervalle de crête, les champs électriques et magnétiques sont capturés entre deux parois en PEC sur les côtés supérieur et inférieur et deux côtés ouverts. Une bande interdite suivant les directions x et y est obtenue en incorporant une structure semblable à un lit de crête de champignon le long des deux côtés ouverts, et seul le mode Q-TEM se propage à cette bande interdite.

L'antenne orientable par faisceau proposée a été simulée dans le système HFSS Ansys avec et sans surface PGM. Les résultats de la simulation montrent que le gain est augmenté d'environ 8 dBi par rapport à l'antenne sans surface PGM. Un gain de crête de 15.2 dBi avec un HPBW de 20^o est obtenu pour l'antenne avec la surface PGM. L'antenne proposée couvre la bande de fréquences de 57 à 64 GHz. Les paramètres de diffusion et le diagramme de rayonnement de l'antenne orientable par faisceau pour trois angles de rotation différents de la surface du MGP sont illustrés aux Figure 7.35 et Figure 7.36, respectivement.

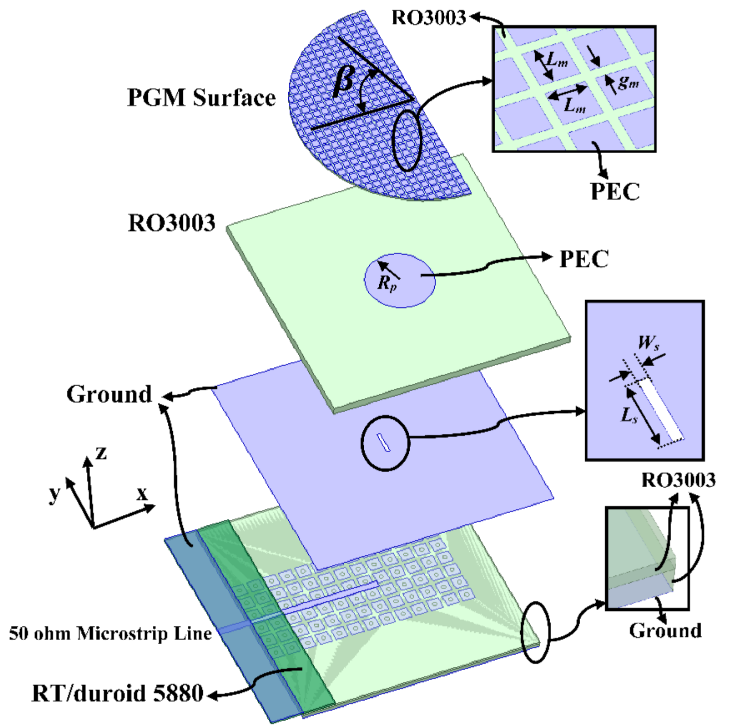

Figure 7.34: Schéma de montage de l'antenne à orientation de faisceau proposée.Les dimensions sont $R_p = 2$, $L_s = 1.35$, $W_s = 0.2$, $L_m = 0.4$, $g_m = 0.1$ et le tout en millimetres (M. Farahani et al. [64], @2018 IEEE).

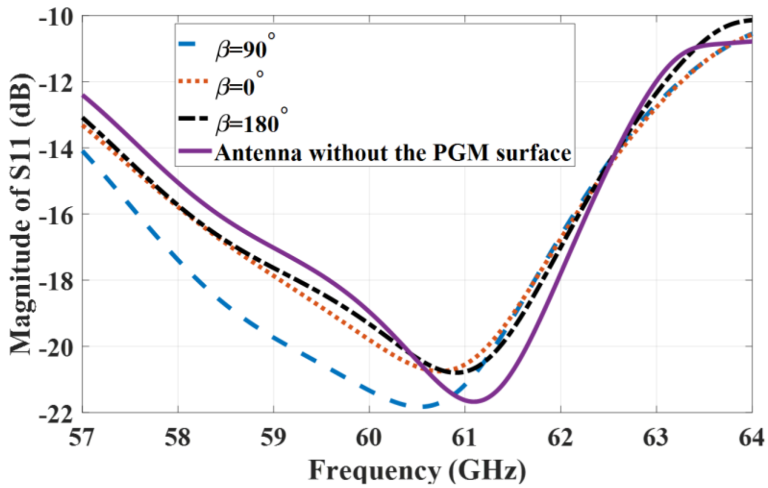

Figure 7.35: Paramètres de diffusion de l'antenne orientable par faisceau pour trois angles de rotation différents de la surface des platinoïdes (M. Farahani et al. [64], @2018 IEEE).

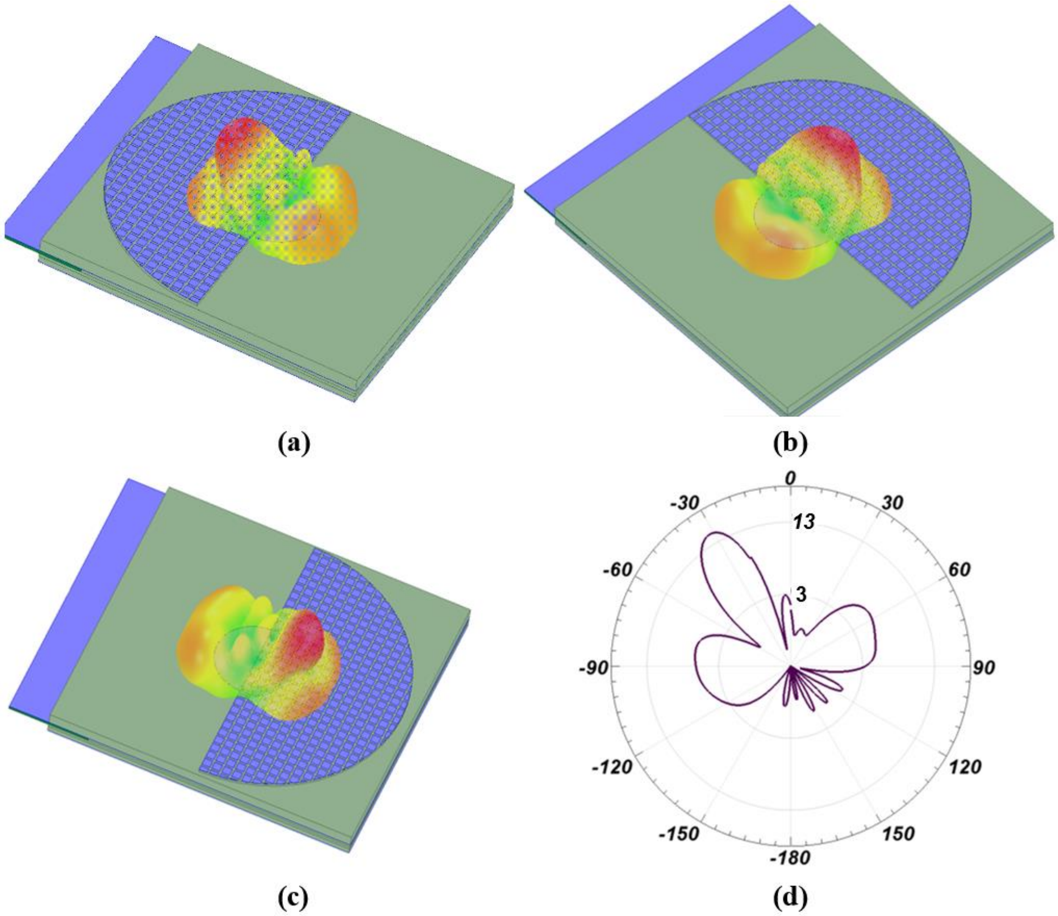

Figure 7.36: Diagramme de rayonnement de l'antenne orientable par faisceau pour trois angles de rotation différents de la surface du MGP. (a) $\beta = 0^o$. (b) $\beta = 90^o$ (c) $\beta = 180^o$. (d) diagramme de rayonnement du plan xz à $\beta = 0^o$ (M. Farahani et al. [64], @2018 IEEE).

7.5 Structures de guidage d'ondes à faibles pertes chez mmWave

Avoir la capacité de transmettre des signaux à travers des structures guidées est considéré comme le premier pas vers le développement de systèmes de communication. Des bandes de fréquences DC aux terahertz, chercheurs et ingénieurs ont mis au point différents types de lignes de transmission et de guides d'ondes, qui ont leurs avantages et leurs inconvénients [25]-[43]. Toute structure de guidage électromagnétique composée au moins de deux conducteurs séparés électriquement ne peut propager que le mode fondamental TEM, qui transmet des signaux à des fréquences arbitrairement basses et est appelée ligne de transmission. Les guides d'ondes sont des structures de guidage électromagnétiques qui ne propagent pas le mode TEM et se composent d'un seul conducteur. De plus, il existe une autre structure de guidage qui ne consiste pas du tout en un conducteur, appelée dalle diélectrique [44]. La capacité de prendre en charge les modes d'ordre supérieur dans les guides d'ondes leur permet de fonctionner dans des modes avec des performances de perte moins importantes que les lignes de transmission en modifiant la topologie de guide d'ondes hôte. Ce concept découle du fait que le mode de fonctionnement du guide d'ondes affecte les caractéristiques d'affaiblissement de propagation. Pour une meilleure compréhension, considérons un guide d’ondes à plaques parallèles simple. Le mode TEM transverse a un champ E distribué uniforme; cependant, alors qu'il est excité avec le mode TE, le champ E est nul sur les parois métalliques. Dans [90], il est montré que les pertes augmentent en réduisant l'espacement des plaques et en augmentant la fréquence pour le mode TEM, alors qu'elles sont réduites en augmentant l'espacement des plaques et la fréquence en mode TE. De plus, les guides d'ondes sont utilisés dans les hautes fréquences en raison de leurs pertes plus faibles, de leurs fuites moins importantes et de leur capacité à gérer une puissance supérieure à celle des lignes de transmission [41].

La FCC (Federal Communications Commission) a attribué une bande inimitable de 7 GHz de spectre sans licence allant de 57 GHz à 64 GHz [91]. Cette bande de fréquences permet de réaliser des liaisons RF de plusieurs gigabits par rapport au spectre disponible inférieur à 0,5 GHz compris entre 2 et 6 GHz pour les applications WiFi ou sans licence. Cependant, le développement de systèmes sans fil dans la bande des 60-GHz, en raison de la forte perte de propagation en espace libre, impose de concevoir des récepteurs à haute sensibilité pour remédier à cet inconvénient. Dans cet effort, la conception d’une ligne de transmission à haut rendement et à faibles pertes joue un rôle important dans la réalisation de cet objectif.

Les guides d'ondes intégrés au substrat (SIW) sont des guides d'ondes à faibles pertes qui ont été développés pour les fréquences micro-ondes et à ondes millimétriques au cours des 20 dernières années [40], [92]-[93]. En 2009, Per-Simon Kildal et al. ont proposé les idées d'une nouvelle structure guidée capable de propager des ondes quasi-TEM le long du trajet souhaité dans l'entrefer situé entre deux surfaces métalliques [94]-[95]. De plus, une ligne de transmission microruban réalisée en MHMIC, contrairement à celle réalisée sur un substrat conventionnel, peut également être utilisée dans la bande des 60-GHz [37]. Les différentes caractéristiques de ces structures de guidage sont comparées dans le Table 7.1. Les guides d’onde SIW sont plans et ont un faible coût de fabrication. Cependant, les champs électromagnétiques se déplacent à l'intérieur d'un substrat diélectrique hôte, ce qui peut augmenter les pertes dues à la tangente aux pertes diélectriques, en particulier dans la bande des 60-GHz. De plus, le diamètre des vias métalliques et la périodicité de ceux-ci deviennent plus petits afin de réduire les fuites [96], ce qui augmenterait la complexité et les coûts de fabrication. En outre, la capacité de gestion de la puissance est inférieure à celle des guides d'ondes creux, car leurs champs électromagnétiques se trouvent dans un substrat diélectrique, qui présente une rupture de tension plus faible que l'air dans un guide d'ondes creux. Contrairement aux guides d'ondes SIW, les pertes sont moins importantes du fait que les ondes se propagent dans l'air dans le guide d'ondes à crête gap [97]. En plus de meilleures performances de perte par rapport à SIW, le problème de contact métallique imparfait est éliminé par rapport aux guides d'ondes creux en raison du fait qu'il existe un intervalle d'air entre les plaques inférieure et supérieure dans la structure de guide d'ondes à fente, ce qui facilite la fabrication. [98]. Bien que le guide d'ondes à fente soit un bon candidat en tant que guide d'ondes à faibles pertes dans les bandes de fréquences mmWave, la fabrication d'un clou métallique très haut et mince augmente la complexité et le coût de fabrication des circuits conçus. Récemment, des tentatives ont été faites pour réduire le coût et la difficulté de ce processus de fabrication. Dans [99], des broches demi-hauteur sont présentées pour surmonter la difficulté et le coût des guides d'ondes à fente. Dans [42], M. Ebrahimpouri et al. Ont présenté une nouvelle méthode rentable pour faciliter la fabrication de la surface de la broche. Grâce à cette méthode, la facilité de fabrication est considérablement améliorée grâce au fait que la structure EBG utilisée consiste uniquement en des trous au lieu des broches. La périodicité de la cellule unitaire EBG est augmentée d'environ 2,5 fois les broches dans les guides d'ondes à fente.

La section 7.5.1 de ce chapitre explique la ligne de transmission à fentes et la méthode de transition au microruban. Un coupleur hybride multi-ouverture 3dB 90^o à faibles pertes est également conçu et fabriqué. Le coupleur a une très faible erreur de phase de sortie. Ceci est réalisé en considérant le fait que la théorie de Bethe sur la petite ouverture de couplage [100], ne peut pas montrer une expression exacte pour une grande ouverture carrée dans un coupleur à plusieurs ouvertures. Dans le cas d'une grande ouverture carrée, les coefficients de couplage et d'isolation dépendent de la fréquence et la phase varie sur la grande ouverture de couplage, ce qui peut être utilisé pour compenser la nature progressive du coupleur en phase.

Dans la section 7.5.2 de ce chapitre, nous proposons une nouvelle structure de guide d’ondes présentant plusieurs avantages par rapport aux lignes de transmission classiques décrites dans la littérature. Le principal avantage du guide d’ondes Hedgehog est qu’il peut supporter la propagation avec une perte moindre. De plus, du fait que les champs électromagnétiques sont capturés dans le guide d’onde, les pertes de rayonnement sont maintenues très faibles, ce qui confère une bonne immunité contre les perturbations électromagnétiques externes par rapport à la technologie du microruban. Un autre avantage principal du guide d’ondes Hedgehog est la compatibilité avec les guides d’ondes creux, ce qui offre un degré de liberté supplémentaire pour utiliser le guide d’ondes proposé pour plusieurs conceptions à ondes millimétriques.

7.5.1 Ligne de transmission Ridge Gap et coupleur hybride conçu à 3 dB

En raison de la petite dimension et de la forte perte de propagation aux fréquences millimétriques, la conception de réseaux de formation de faisceau dans la plage de fréquences millimétriques a été une tâche ardue pour les concepteurs. Au cours de la dernière décennie, plusieurs efforts ont été déployés pour inventer une nouvelle ligne de transmission à haut rendement et à faibles pertes pour les gammes de fréquences hyperfréquences à haute fréquence et ondes millimétriques. Par exemple, la technologie SIW a été développée au cours de la dernière décennie en tant que ligne de transmission à faible perte [14]-[16]. Cependant, la conception des composants hyperfréquences, tels que les coupleurs avec la technologie SIW, altère les performances du guide d'ondes SIW à faibles pertes, en raison de la perturbation de la caractéristique de guide d'onde SIW hôte [17]-[19].

Pour surmonter ces problèmes, une autre approche alternative, appelée technologie de guide d'onde à crête-gap, a été proposée [20]. Le guide d'ondes Ridge-gag est une ligne de transmission à très faibles pertes aux fréquences millimétriques [20]-[21], [33]. Dans cette technologie, les champs électriques et magnétiques sont capturés entre deux surfaces métalliques et deux parois latérales ouvertes. En incorporant une structure semblable à un lit de clous le long des deux côtés ouverts, une bande interdite est obtenue dans les directions x et y, comme illustré à la Figure 7.38. Dans la ligne de transmission à fentes fausses, les pertes sont inférieures à celles du guide d'onde SIW en raison du fait que les ondes électriques et magnétiques se propagent dans l'air et sur le diélectrique hôte dans les fentes dorsales et le guide d'onde SIW, respectivement.

Plusieurs techniques ont été introduites dans la littérature pour concevoir un coupleur hybride à faibles pertes, tel que les coupleurs de branche SIW [18] and [101], et un coupleur SIW à deux couches [102]. Ces techniques entraînent des pertes élevées dans la plage de fréquence des ondes millimétriques. Un autre problème avec ces techniques est une grande quantité d'erreur de phase de sortie qui provient de leur nature de phase progressive.

Dans cette section, la ligne de transmission RGW hôte et la méthode de transition vers microruban sont expliquées. Ensuite, la théorie du coupleur hybride à six étages compensé en phase proposé est étudiée et développée. Enfin, le coupleur proposé est conçu et discuté et les résultats expérimentaux sont mesurés et comparés à ceux simulés.

Théorie physique du guide d'ondes proposé pour Ridge Ridge Gap:

Le guide d'ondes à fente proposé est présenté à la Figure 7.37. Les champs électriques et magnétiques sont capturés entre deux surfaces métalliques et deux parois latérales ouvertes. En intégrant une structure semblable à un lit de clous le long des deux côtés ouverts, on obtient une bande interdite dans les directions x et y. Le diagramme de dispersion de la cellule unitaire de crête-gap et le diagramme de dispersion de la ligne de transmission de crête-gap de la Figure 7.37 sont réalisés avec CST et sont représentés à la Figure 7.38. Comme le montre la Figure 7.38, il existe une bande interdite située entre 45 et 68 GHz. Seul le mode Q-TEM peut se propager à cette bande interdite. Le guide d'onde crête-gap fonctionne sur le concept de plaques PEC sur PMC pour détruire les modes TEM globaux dans un guide d'ondes à plaques parallèles

(PEC-over-PEC) et présente la propriété unique de la propagation simultanée de plusieurs sources quasi locales dégénérées indépendantes Q-TEM ondes. Dans le sens longitudinal, il fonctionne comme une plaque PMC dans le sens transversal aux bandes. Ainsi, les plaques de surface PEC-sur-dures peuvent être considérées comme des plaques PEC-sur-PMC dans la direction transversale et comme des plaques PEC-sur-PEC dans la direction longitudinale. En conséquence, tout type de propagation est supprimé sauf la propagation de type TEM le long des bandes, c'est-à-dire qu'il n'existera que des ondes quasi-TEM se propageant le long des bandes.

Table 7.1: les différentes structures de guidage avec le guide d'ondes Hedgehog (M. Farahani et al. [23], @2019 IEEE).

Characteristic	**Ref.**	**Preferred Mode**	**Other Modes**	**Dispersion**	**BW**	**Loss**	**Component Integration**	**Fabrication Ease**	**Photo**
Microstrip	[37]	Quasi-TEM	TM, TE	Low	High	High	Easy	Real Easy	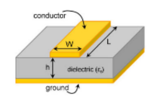
Substrate-Integrated Waveguide (SIW)	[40]	TE_{10}	TM, TE	Medium	Low	Medium	Hard	Easy	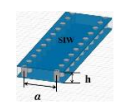
Hollow Waveguide	[41]	TE_{10}	TM, TE	Medium	Low	Low	Hard	Medium	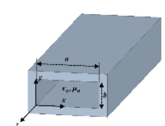
Ridge gap Waveguide	[34]	Quasi-TEM	NO	Medium	Low	Low	Hard	Easy	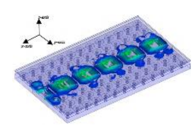
Gap Waveguide	[42]	TE_{10}	TM, TE	Medium	Low	Low	Hard	Real Easy	
Proposed Hedgehog Waveguide	This work	TE_{10}	NO	Medium	Low	Low	Hard	Medium	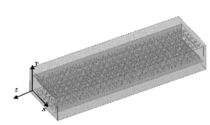

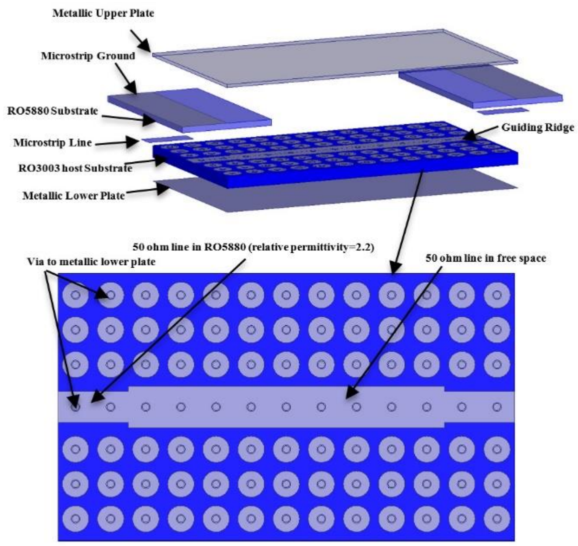

Figure 7.37: La transition du guide d'onde faîtière vers le guide d'onde à microruban (M. Farahani et al. [34], @2017 IEEE).

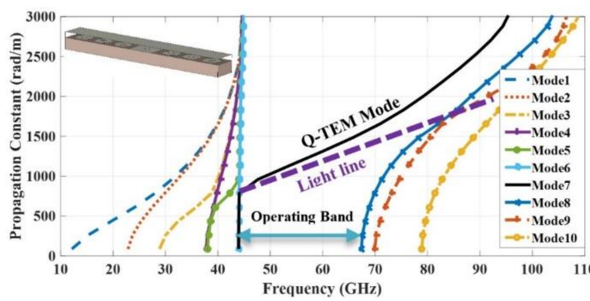

Figure 7.38: Diagramme de dispersion du guide d'ondes proposé à la Figure 7.37 (M. Farahani et al. [34], @2017 IEEE).

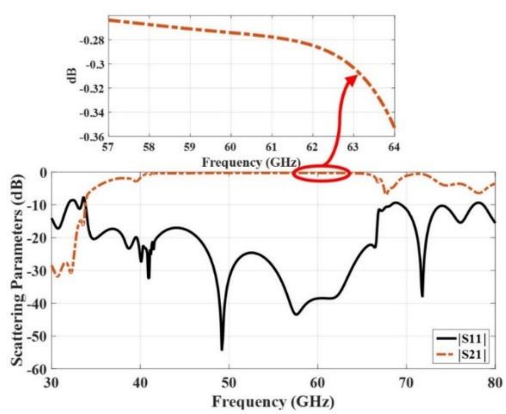

Figure 7.39: Paramètres de diffusion simulés de la transition proposée du guide d'ondes microruban au guide d'onde crête-gap Figure 7.37 (M. Farahani et al. [34], @2017 IEEE).

Théorie du coupleur hybride à six étages à compensation de phase:

La technique de la fente de couplage en série est utilisée pour concevoir un coupleur à 3 dB, comme illustré à la Figure 7.40. Il existe plusieurs techniques pour augmenter la largeur de bande de fonctionnement des coupleurs, telles que l'utilisation de plusieurs slots de couplage en série [103]. La théorie conventionnelle dans la littérature pour la conception de coupleurs directionnels à trous multiples [103] suppose que la puissance d'entrée du guide d'ondes d'alimentation est constante sur tous les trous en raison de sa faible quantité de couplage au niveau des trous. Toutefois, cela n'est pas correct dans le cas d'un couplage très serré au-dessus de -10 dB, car la plus grande partie de la puissance d'entrée fuyait vers le guide d'ondes couplé en raison de la grande quantité de couplage au niveau des trous. En considérant la structure des ouvertures de couplage à six fentes de la Figure 7.40, nous pouvons définir les composantes de puissance couplées en avant et en arrière dans le guide d'ondes supérieur, comme illustré à la Figure 7.40.

Les valeurs calculées de θ_1 and θ_2 à l'aide de Appendix B sont tracées à l'aide de Matlab et sont représentées à la Figure 7.41 en fonction de la fréquence. L'erreur de phase de sortie à grande ouverture de couplage (θ_2) est égale à zéro pour la fréquence inférieure à f_{co}. Pour la fréquence supérieure à f_{co}, la pente est négative et peut compenser la pente positive de θ_1. Par conséquent, une différence de phase de sortie très plate peut être obtenue pour des fréquences supérieures à f_{co} si θ_1 et θ_2 ont la même amplitude de pente avec un signe différent, comme le scénario idéal illustré à la Figure 7.41. Cependant, θ_2 in Appendix B n'est pas une ligne droite comme l'idéal θ_2, qui est représenté à la Figure 7.41 pour les fréquences supérieures à f_{co}. Le réel θ_2 est tracé en utilisant HFSS pour une ouverture typique afin de montrer le comportement réel de θ_2 (Figure 7.42). f_{co} définit la limite entre une petite zone d'ouverture et une grande zone d'ouverture. Dans une zone de petite ouverture, il n'y a pas de variation de phase au dessus de l'ouverture. En d'autres termes, dans les petites ouvertures, les coefficients de couplage et d'isolation (C_n et b_n) sont des quantités indépendantes de la fréquence [100]. f_{co} est affecté par la longueur d'ouverture (L_s) et la largeur d'ouverture (W_s). Cependant, en considérant que la longueur d'ouverture (L_s) est cinq fois plus grande que la largeur d'ouverture (W_s), f_{co} est principalement affectée par la longueur d'ouverture (L_s). La procédure de conception du coupleur est expliquée ci-après. Le coupleur est simulé en utilisant HFSS. La Figure 7.42 montre la différence de phase simulée pour différentes valeurs de W_s, L_s, θ_1 et θ_2. Nous avons considéré que la distance entre les ouvertures (S) était de 1.875 mm et que l'épaisseur de la paroi de couplage (h_m) était de 0.127 mm. Comme on peut le voir sur la Figure 7.42, la fréquence de résonance d'ouverture (f_{co}) est principalement affectée par la longueur d'ouverture (L_s). Changer la longueur d'ouverture (L_s) affectera également la pente du θ_2. On peut également constater que la pente de θ_2 est proportionnelle à la largeur d'ouverture (W_s), mais elle n'a pas d'impact significatif sur la fréquence de résonance de l'ouverture (f_{co}). La pente de θ_2 augmente en augmentant W_s. Nous nous attendions à ce comportement en raison du fait qu'en réduisant W_s, la force de couplage de l'ouverture sera réduite et il agira comme une petite ouverture de couplage avec une indépendance de fréquence.

Conception du coupleur hybride proposé:

La théorie susmentionnée est utilisée pour calculer la valeur initiale de la taille de l'ouverture de couplage du coupleur à six étages proposé. Le schéma final du coupleur basé sur la technologie de crête-gap est présenté à la Figure 7.43. Dans la section précédente, il est montré que dans les grandes ouvertures de couplage aux fréquences supérieures à f_{co}, θ_2 a une pente négative, ce qui peut compenser la pente positive de θ_1. Comme il a été montré précédemment, la fréquence de résonance d'ouverture (f_{co}) est principalement affectée par la longueur d'ouverture (L_s), et il est également montré que la pente de θ_2 est proportionnelle à la largeur d'ouverture (W_s), mais elle n'a pas impact significatif sur la fréquence de résonance d'ouverture (f_{co}) (Figure 7.41).

Experimental Results:

La Figure 7.44 montre une photo du coupleur fabriqué. Pour mesurer le coupleur fabriqué, nous devons prendre en compte la réponse du connecteur et la longueur des lignes de transmission à microruban d'alimentation dans la procédure d'étalonnage. Les paramètres de diffusion mesurés sont illustrés à la Figure 7.45. Sur cette figure, les pertes dues aux lignes d'alimentation microstrip et aux connecteurs sont prises en compte lors de l'étalonnage de l'équipement de mesure. La réponse en phase de sortie du coupleur proposé est illustrée à la Figure 7.46. La perte d'insertion est inférieure à 3.5 dB dans la bande de fréquence de fonctionnement (de 57 à 64 GHz). Le deuxième avantage de cette conception est l'erreur de phase de sortie, inférieure à 1 degré dans la bande de fréquence de fonctionnement.

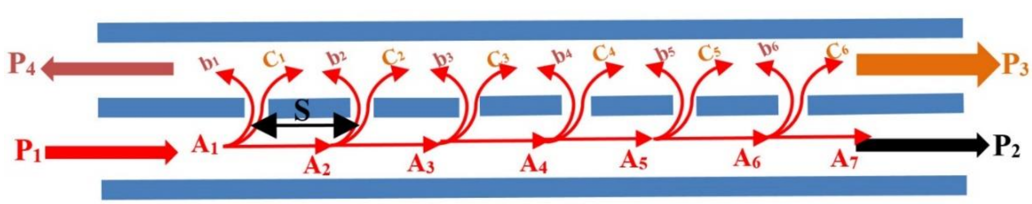

Figure 7.40: Géométrie du coupleur à six étages proposé (M. Farahani et al. [34], @2017 IEEE).

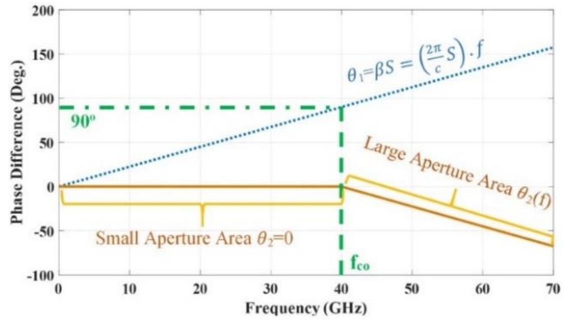

Figure 7.41: La grande différence de phase de sortie d'ouverture de couplage.Il est divisé en deux termes, la différence de phase de sortie linéaire (θ_1) et l'erreur de phase de sortie de grande ouverture de couplage (θ_2). θ_2 n'est pas une ligne droite comme l'idéal θ_2 qui est tracé sur cette figure (M. Farahani et al. [34], @2017 IEEE).

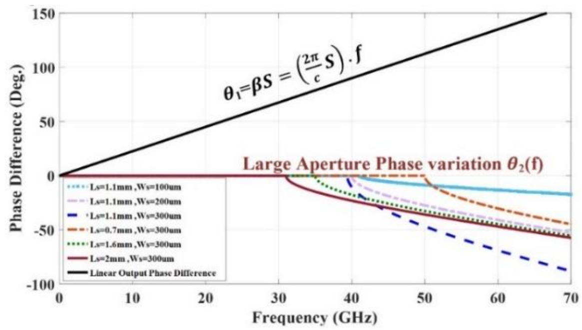

Figure 7.42: Différence de phase simulée en utilisant HFSS pour différentes valeurs de W_s et L_s. Nous avons considéré que la distance entre les ouvertures (S) était de 1.875 mm et que l'épaisseur de la paroi de couplage (h_m) était de 0.127 mm (M. Farahani et al. [34], @2017 IEEE).

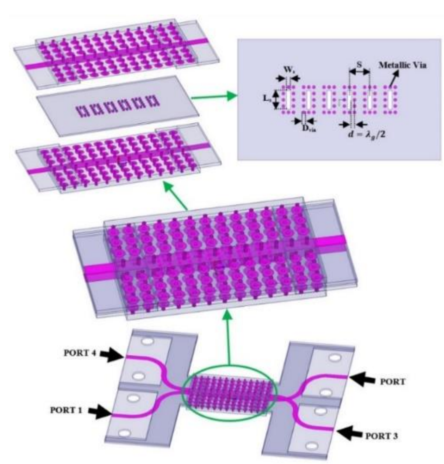

Figure 7.43: Géométrie du coupleur hybride à deux couches 3 dB proposé.($W_s = 0.35\ mm$, $L_s = 1.2\ mm$, $D_{via} = 0.3\ mm$, $D = 0.52\ mm$) (M. Farahani et al. [34], @2017 IEEE).

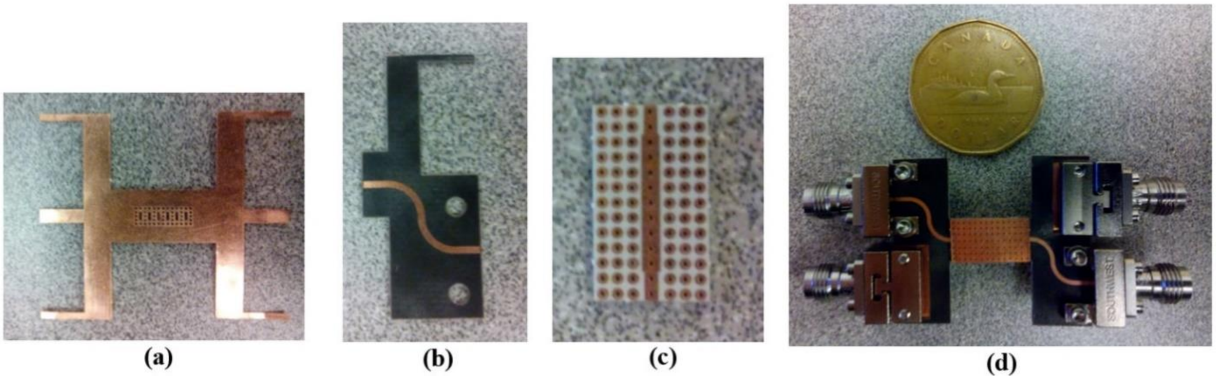

Figure 7.44: Photo du coupleur faîtage-écart proposé.(a) Mur de couplage. (b) Ligne d'alimentation microruban. (c) Hôte crête-gap. (d) Coupleur crête-écart proposé (M. Farahani et al. [34], @2017 IEEE).

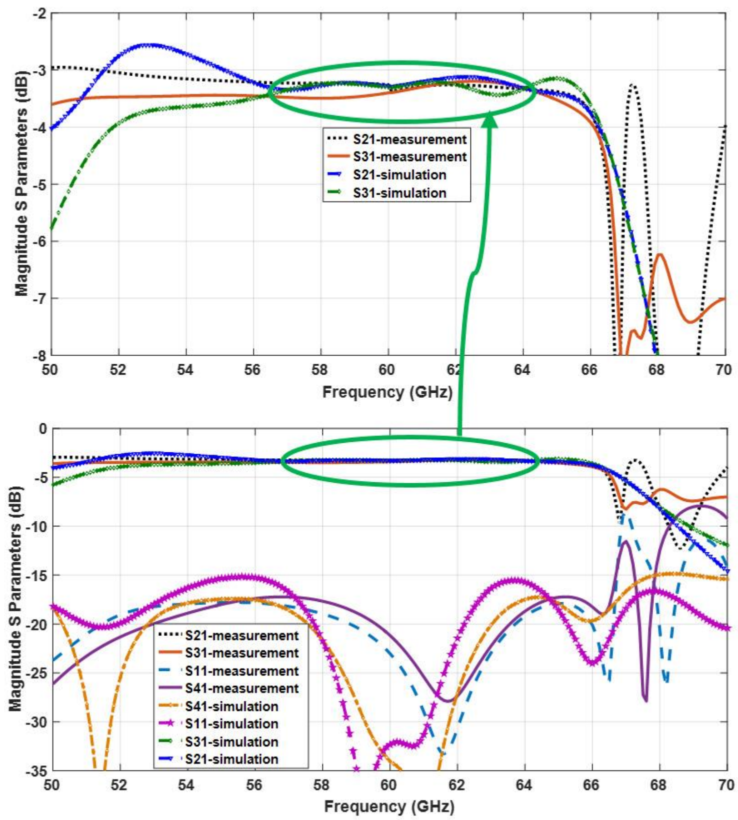

Figure 7.45: Résultats mesurés et simulés du coupleur hybride 3 dB proposé (M. Farahani et al. [34], @2017 IEEE).

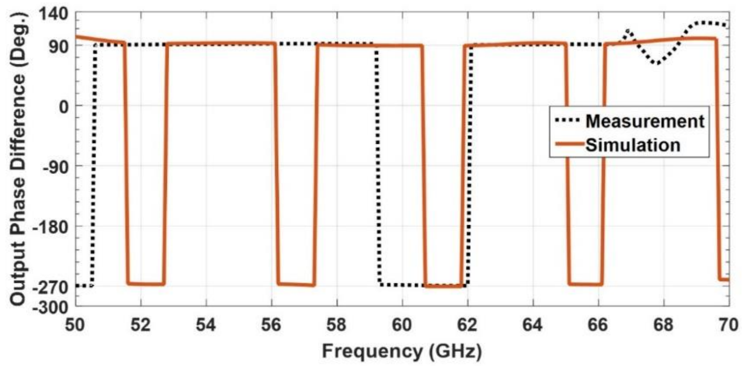

Figure 7.46: Réponse en phase de sortie du relais coupleur hybride proposé (M. Farahani et al. [34], @2017 IEEE).

7.5.2 Guide D'onde Hedgehog Et Son Application Dans La Conception D'un Déphaseur

Un nouveau guide d'ondes Hedgehog, composé d'un lit de clous encastrés dans un guide d'ondes creux rectangulaire, est proposé et étudié comme guide d'ondes à faible perte de pointe prometteur pour les bandes de fréquences à ondes millimétriques. Le guide d'onde Hedgehog proposé tire son nom de son comportement électromagnétique. Alors que les hérissons s'enracinent dans les haies et autres sous-bois à la recherche de leur nourriture préférée, le guide d'ondes proposé s'enracine dans son lit de clous incrusté. Lorsque nous choisissons une technologie de guide d'ondes hôte, il vaut la peine de prendre le temps de peser le pour et le contre des différents types de guides d'ondes proposés. Le guide d'ondes Hedgehog proposé présente une perte extrêmement faible et est compatible avec la technologie des guides d'ondes creux, ce qui permet de développer différents composants tels que des déphaseurs à réponse en phase plate à faibles pertes. Dans ce travail, le guide d'ondes Hedgehog proposé est étudié de manière analytique et une transition vers le guide d'ondes creux est conçue. De plus, la nature du guide d'ondes Hedgehog conçu pour les faibles pertes est comparée au guide d'onde à l'espace de crête, au guide d'onde intégré au substrat (SIW), au guide d'onde creux et à la ligne à microruban. Enfin, le guide d'onde proposé est conçu, simulé et fabriqué. Les résultats simulés et mesurés montrent un bon accord, ce qui valide le concept proposé.

Les guides d'ondes intégrés au substrat (SIW) sont des guides d'ondes à faibles pertes qui ont été développés pour les fréquences micro-ondes et à ondes millimétriques au cours des 20 dernières années [40], [92]-[93]. En 2009, Per-Simon Kildal et al. ont proposé les idées d'une nouvelle structure guidée capable de propager des ondes quasi-TEM le long du trajet souhaité dans l'entrefer situé entre deux surfaces métalliques [94]–[95]. De plus, une ligne de transmission microruban réalisée en MHMIC, contrairement à celle réalisée sur un substrat conventionnel, peut également être utilisée dans la bande des 60-GHz [37]. Les différentes caractéristiques de ces structures de guidage sont comparées dans le Table 7.1. Les guides d'onde SIW sont plans et ont un faible coût de fabrication. Cependant, les champs électromagnétiques se déplacent à l'intérieur d'un substrat diélectrique hôte, ce qui peut augmenter les pertes dues à la tangente aux pertes diélectriques, en particulier dans la bande des 60-GHz. De plus, le diamètre des vias métalliques et la périodicité de ceux-ci deviennent plus petits afin de réduire les fuites [96], ce qui augmenterait la complexité et les coûts de fabrication. En outre, la capacité de gestion de la puissance est inférieure à celle des guides d'ondes creux, car leurs champs électromagnétiques se trouvent dans un substrat diélectrique, qui présente une rupture de tension inférieure à celle de l'air dans un guide d'ondes creux. Contrairement aux guides d'ondes SIW, les pertes sont moins importantes du fait que les ondes se propagent dans l'air dans le guide d'ondes à crête gap [97]. En plus de meilleures performances de perte par rapport à SIW, le problème de contact métallique imparfait est éliminé par rapport aux guides d'ondes creux en raison du fait qu'il existe un intervalle d'air entre les plaques inférieure et supérieure dans la structure de guide d'ondes à fente, ce qui facilite la fabrication [98]. Bien que le guide d'ondes à fente soit un bon candidat en tant que guide d'ondes à faibles pertes dans les bandes de fréquences mmWave, la fabrication d'un clou métallique très haut et mince augmente la complexité et le coût de fabrication des circuits conçus. Récemment, des tentatives ont été faites pour réduire le coût et la difficulté de ce processus de fabrication. Dans [99], des broches demi-hauteur sont présentées pour surmonter la difficulté et le coût des guides d'ondes à fente. Dans [42], M. Ebrahimpouri et al. Ont présenté une nouvelle méthode rentable pour faciliter la fabrication de la surface de la broche. Grâce à cette méthode, la facilité de fabrication est considérablement améliorée grâce au fait que la structure EBG utilisée consiste uniquement en des trous au lieu des broches. La périodicité de la cellule unitaire EBG est augmentée d'environ 2,5 fois les broches dans les guides d'ondes à fente.

Dans ce travail, nous proposons une nouvelle structure de guide d’onde qui présente plusieurs avantages par rapport aux lignes de transmission conventionnelles décrites dans la littérature. Le principal avantage du guide d’ondes Hedgehog est qu’il peut supporter la propagation avec une perte moindre. De plus, du fait que les champs électromagnétiques sont capturés dans le guide d’onde, les pertes de rayonnement sont maintenues très faibles, ce qui confère une bonne immunité contre les perturbations électromagnétiques externes par rapport à la technologie du microruban. Un autre avantage principal du guide d’ondes Hedgehog est la compatibilité avec les guides d’ondes creux, ce qui offre un degré de liberté supplémentaire pour utiliser le guide d’ondes proposé pour plusieurs conceptions à ondes millimétriques.

Théorie physique du guide d'ondes proposé pour hérisson:

Le guide d'ondes Hedgehog proposé consiste en un guide d'ondes creux muni d'un lit de clous dans les parois supérieure et inférieure, comme illustré à la Figure 7.47(a). L'affaiblissement de propagation dans le guide d'ondes proposé est nettement inférieur à celui des guides d'ondes creux et autres guides d'ondes ou lignes de transmission conventionnels à la fréquence considérée, ce qui est étudié et étudié à la section 4.3.4.

L'affaiblissement de propagation à l'intérieur du guide d'ondes proposé provient principalement des pertes ohmiques sur les surfaces métalliques. Pour réduire les pertes métalliques dans les guides d'ondes, il convient de minimiser la densité d'énergie près des parois métalliques internes du guide d'ondes [105]. Par exemple, le mode de fonctionnement du guide d'ondes affecte les caractéristiques d'affaiblissement de propagation. Pour une meilleure compréhension, considérons un guide d’ondes à plaques parallèles simple. Le mode TEM transverse a un champ E distribué uniforme; cependant, alors qu'il est excité avec le mode TE, le champ E est nul sur les parois métalliques. Dans [90], il est montré que les pertes augmentent en réduisant l'espacement des plaques et en augmentant la fréquence pour le mode TEM, alors qu'elles sont réduites en augmentant l'espacement des plaques et la fréquence en mode TE. Outre la nature à faible perte du guide d’ondes proposé, il est compatible avec la technologie des guides d’ondes creux; et plus important encore, il possède une réponse en phase unique, ce qui le rend idéal pour la conception de déphaseurs large bande à faible perte dans les bandes de fréquence à ondes millimétriques. Également, un déphaseur de 45^o est conçu à l'aide de cette technologie.

Diagramme de dispersion du guide d'ondes proposé pour hérisson:

Le guide d'onde Hedgehog proposé est présenté à la Figure 7.47(a). Le guide d'ondes est considéré comme une combinaison cascadée périodique du guide d'ondes rectangulaire conventionnel et du guide d'ondes ondulé longitudinalement, comme illustré à la Figure 7.47(b). La Figure 7.48 représente les caractéristiques de dispersion du mode TE_{10} dans le guide d'ondes Hedgehog proposé.

Analyse des pertes de propagation dans le guide d'ondes proposé pour le hérisson:

A. Concept principal

Malgré la paroi conductrice parfaite où le champ électrique tangentiel est nul à la surface, l’existence de champs électriques tangentiels à la surface provoque une perte ohmique à la surface d’un guide d’onde métallique uniforme avec des valeurs de conductivité finies [113]. Pour réduire les pertes métalliques dans les guides d'ondes, il convient de minimiser la densité d'énergie à proximité des parois métalliques internes.

La capacité de prendre en charge les modes d’ordre supérieur dans les guides d’ondes leur donne la possibilité de fonctionner dans des modes avec des performances de perte plus faibles en modifiant la topologie de guide d’onde hôte, contrairement aux lignes de transmission qui ne peuvent propager que le mode fondamental TEM. Ce concept provient du fait que le mode de fonctionnement du guide d'ondes affecte les caractéristiques d'affaiblissement de propagation. Pour une meilleure compréhension, considérons un guide d'ondes à plaques parallèles simple. Le mode TEM transverse a un champ E distribué uniforme; cependant, alors qu'il est excité avec le mode TE, le champ E est nul sur les parois métalliques. Dans [90], il est montré que les pertes augmentent en réduisant l'espacement des plaques et en augmentant la fréquence pour le mode TEM, alors qu'elles sont réduites en augmentant l'espacement des plaques et la fréquence en mode TE.

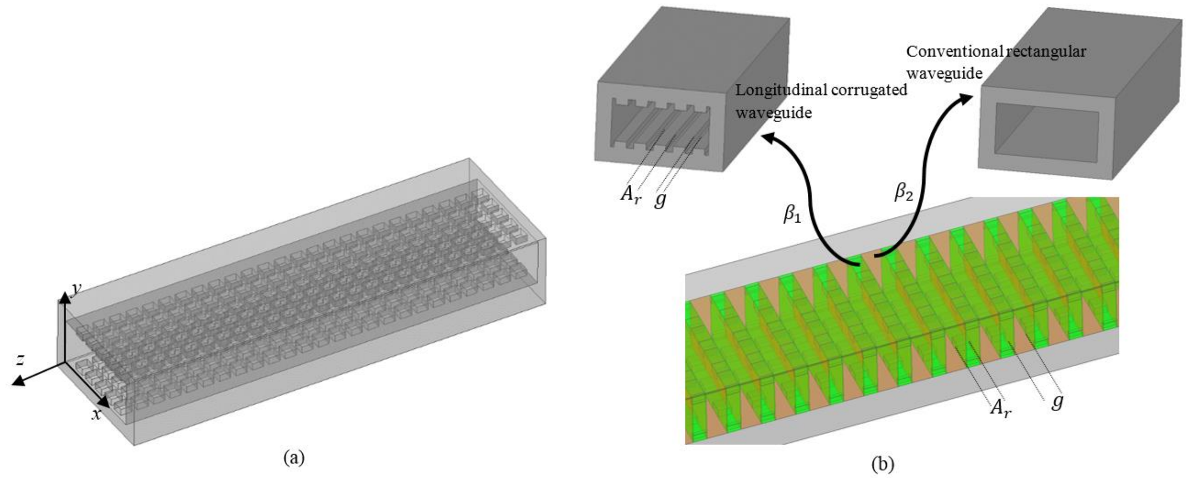

Figure 7.47: Le guide d'onde Hedgehog proposé.(a) Le guide d'onde Hedgehog consiste en un guide d'onde creux muni d'un lit de clous dans les parois supérieure et inférieure. (b) Considérant le guide d'ondes Hedgehog comme des combinaisons périodiques du guide d'ondes ondulé longitudinal en cascade et du guide d'ondes creux classique (M. Farahani et al. [23], @2019 IEEE).

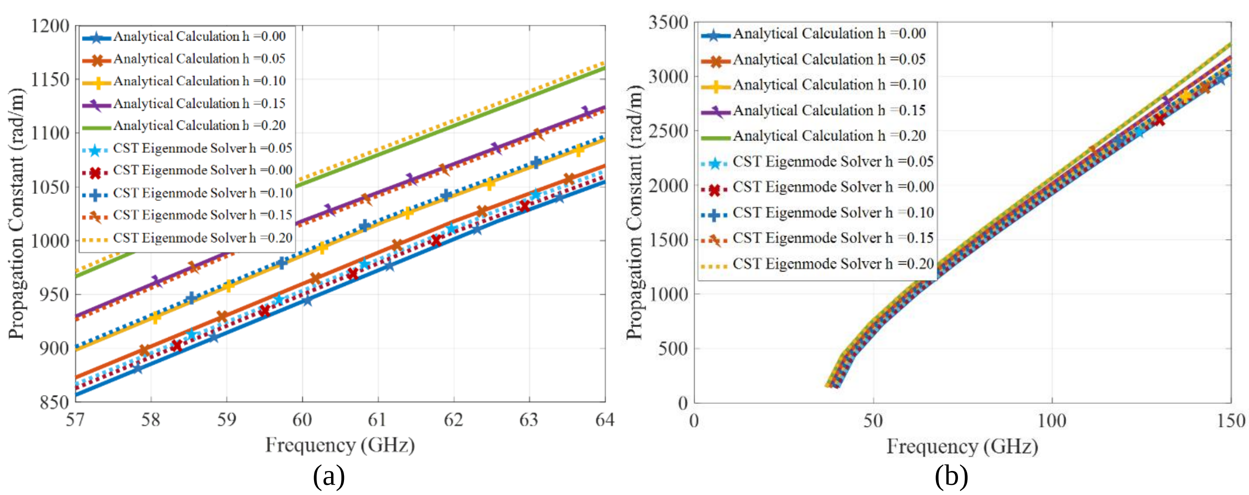

Figure 7.48: Diagramme de dispersion du guide d'ondes Hedgehog calculé par calcul analytique comparé aux résultats obtenus avec le solveur en mode propre de CST Microwave Studio. (a) de 57 à 64 GHz. (b) de 0 à 150 GHz. Les dimensions sont $A_r = 0.4$, $g = 0.2$, $a = 3.8$, $b = 1.6$, le tout en millimetres (M. Farahani et al. [23], @2019 IEEE).

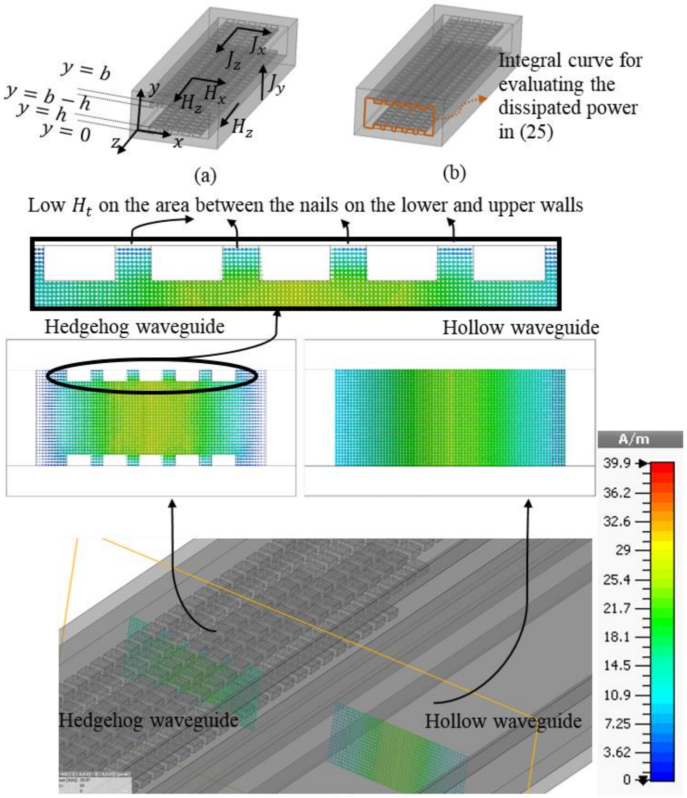

Figure 7.49: Indique que la densité d'énergie près des parois métalliques internes du guide d'ondes est réduite.(a) Champs existants à l'intérieur du guide d'ondes et courants sur les parois internes du guide d'ondes. (b) La puissance dissipée peut être évaluée en intégrant H_t autour de la courbe indiquée sur le plan $z = 0$. (c) Vecteurs de champ magnétique dans le plan $z = 0$. Le $|H_t|$ la densité sur le métal est réduite dans la zone située entre les broches du guide d'onde Hedgehog propose (M. Farahani et al. [23], @2019 IEEE).

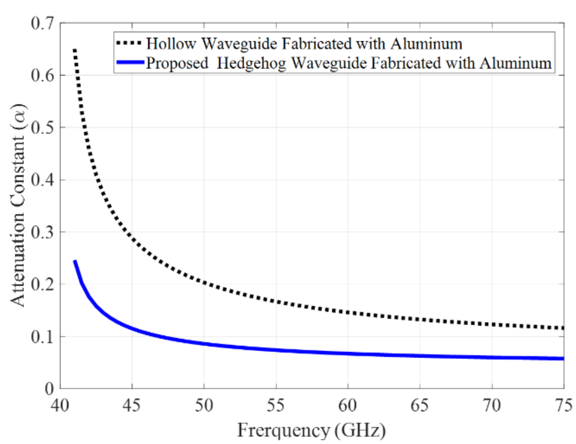

Figure 7.50: Comparaison des constantes d'atténuation du guide d'ondes Hedgehog et du guide d'ondes creux en aluminium.Les dimensions sont $h = 0.13$, $A_r = 0.4$, $g = 0.2$, $a = 3.8$, $b = 1.6$, le tout en millimetres (M. Farahani et al. [23], @2019 IEEE).

B. Résultats expérimentaux

Extraire les résultats expérimentaux est un peu compliqué et la configuration de test suivante doit être poursuivie afin de pouvoir extraire uniquement la perte de propagation du guide d'onde Hedgehog proposé et d'éliminer les pertes dues aux transitions. Comme indiqué dans [21], soustraire S_{21}^{Case2} de S_{21}^{Case1}, en se référant aux guides d'ondes de longueurs différentes indiquées à la Figure 7.51, éliminerait complètement les pertes dues aux guides d'ondes creux de guide d'ondes à hérisson et vertical à horizontal transitions de guides d'ondes creux. Pour calculer l'affaiblissement de propagation expérimental par mètre du guide d'onde Hedgehog, l'équation (7-3) peut être utilisée [21]. Les pertes de propagation expérimentales en dB par mètre sont illustrées à la Figure 7.52 à des fins de comparaison entre les deux guides d'ondes.

$$Hedgehog\ Waveguide\ Loss = \frac{S_{21}^{\text{Case2}} - S_{21}^{\text{Case1}}}{L_{g2} - L_{g1}} \qquad (7-3)$$

$$Hollow\ Waveguide\ Loss = \frac{S_{21}^{\text{Case4}} - S_{21}^{\text{Case3}}}{L_{g2} - L_{g1}} \qquad (7-4)$$

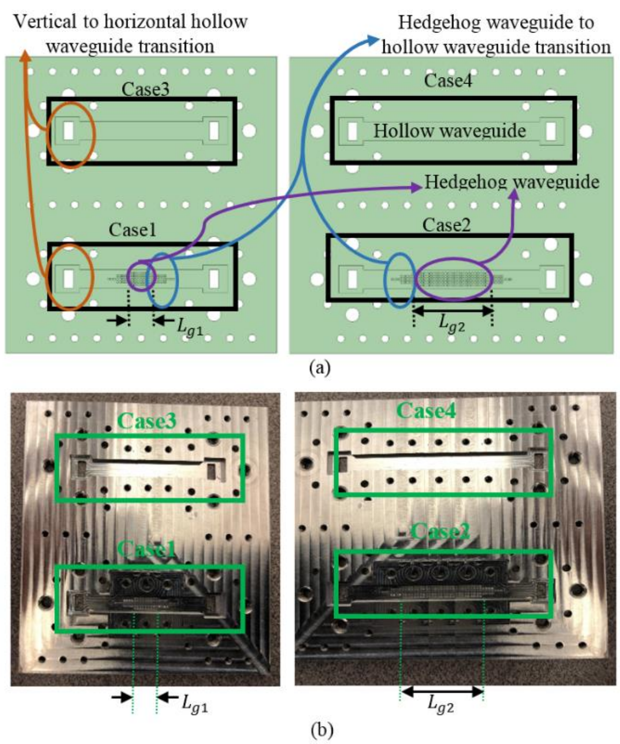

Figure 7.51: Deux guides d'ondes Hedgehog de longueurs différentes pour mesurer les pertes de propagation par mètre à l'aide de l'équation (4-48). Les parties supérieures des guides d'ondes ne sont pas représentées pour des raisons de simplicité. (a) Vue de dessus du bas du corps des guides d'ondes. (b) Photo de prototypes fabriqués (M. Farahani et al. [23], @2019 IEEE).

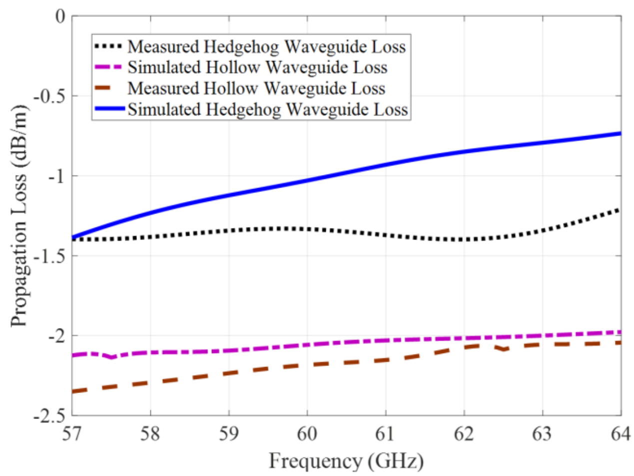

Figure 7.52: Comparaison des résultats des pertes de propagation expérimentales de Hedgehog et des guides d'ondes creux en dB par metre (M. Farahani et al. [23], @2019 IEEE).

Shifter de phase de guide d'ondes de hérisson:

A. Concept principal

Les déphaseurs sont des composants clés pour le développement de réseaux de communication RF et millimétriques. Différentes techniques ont été proposées pour concevoir des déphaseurs dans la littérature qui peuvent être classées en trois groupes. Le premier groupe est constitué de lignes à retard, appelées déphaseurs à ligne commutée [117]. Un autre groupe est constitué de ceux dont le déphasage est causé par des éléments localisés associés à une ligne de transmission distribuée. Le déphaseur de type à réflexion, composé d'un coupleur hybride chargé de deux condensateurs variables, est un exemple de ce type [118]. Le troisième groupe comprend ceux qui présentent des déphasages différents en modifiant les caractéristiques de la ligne de transmission hôte [119]. Dans ce travail, nous utilisons le guide d'ondes Hedgehog proposé pour modifier le diagramme de dispersion du guide d'ondes creux afin d'obtenir un déphaseur large bande à faible erreur de phase. La Figure 7.53 montre le diagramme de dispersion du guide d'ondes Hedgehog. On peut voir sur cette figure que la constante de propagation dans le guide d'onde est augmentée en augmentant la hauteur des broches carrées. En d'autres termes, la différence de constante de propagation entre le guide d'ondes conventionnel et le guide d'ondes Hedgehog est constante sur la bande de fréquence de fonctionnement (de 57 à 64 GHz), ce qui correspond à la variation de phase de la onde progressive dans le guide d'ondes Hedgehog par rapport au guide d'ondes creux classique est constante sur la bande de fréquence de fonctionnement et est calculée comme suit

$$\theta = \beta_{diff3} \times L \qquad (7-5)$$

où θ est la phase décalée par rapport au guide d'ondes creux classique et L est la longueur du guide d'ondes Hedgehog. β_{diff3} est la différence de constante de propagation entre le guide d'ondes Hedgehog et le guide d'ondes creux, comme illustré à la Figure 7.53(e).

La Figure 7.54 montre le déphaseur et la transition conçue. Les paramètres de réponse de phase et de diffusion du déphaseur proposé utilisant la transition proposée sont illustrés aux Figure 7.55 et Figure 7.56, respectivement. Les longueurs de L, L_1, L_2 sont sélectionnées en utilisant (7-5) pour obtenir un déphasage de 45^o. Les dimensions sont $L = 5.4$, $L_1 = 1.8$, $L_2 = 2.4$, $h = 0.13$, $A_r = 0.4$, $g = 0.2$, $a = 3.8$, $b = 1.6$, le tout en millimètres.

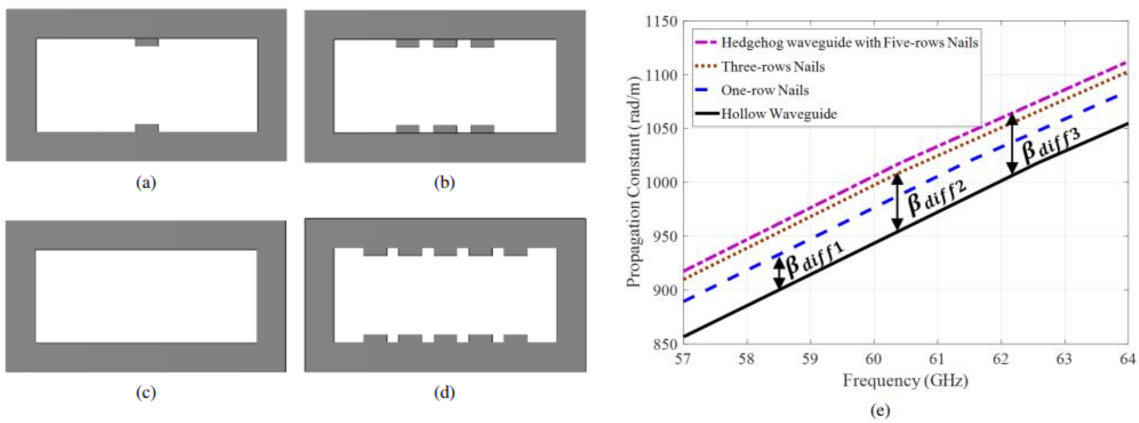

Figure 7.53: Diagramme de dispersion extraite de guides d'ondes avec (a) une rangée de clous. (b) Trois rangées de clous (c) Guide d'ondes Hollow (d) Guide d'ondes proposé pour Hedgehog avec cinq parties crues de clous.Vue croisée des guides d'ondes en (a) à (d) (M. Farahani et al. [23], @2019 IEEE).

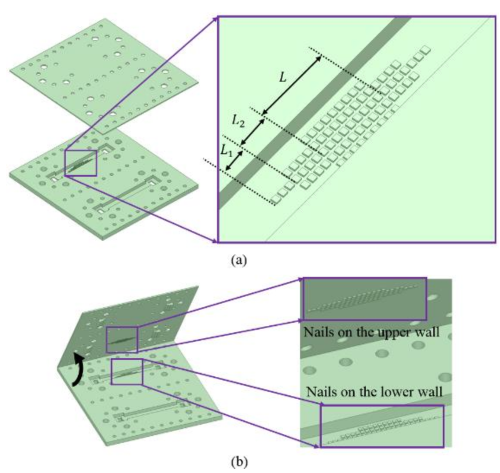

Figure 7.54: Le déphaseur de guide d'onde Hedgehog proposé et la transition conçue (M. Farahani et al. [23], @2019 IEEE).

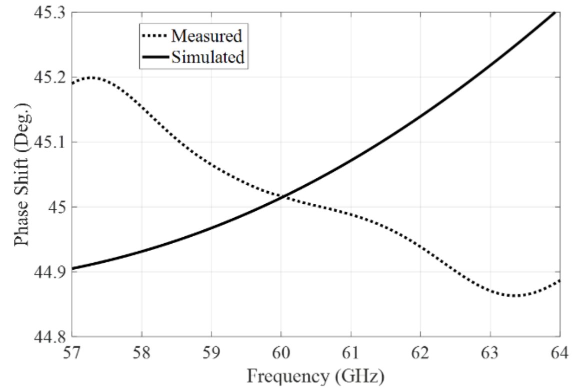

Figure 7.55: Réponse de phase du déphaseur propose (M. Farahani et al. [23], @2019 IEEE).

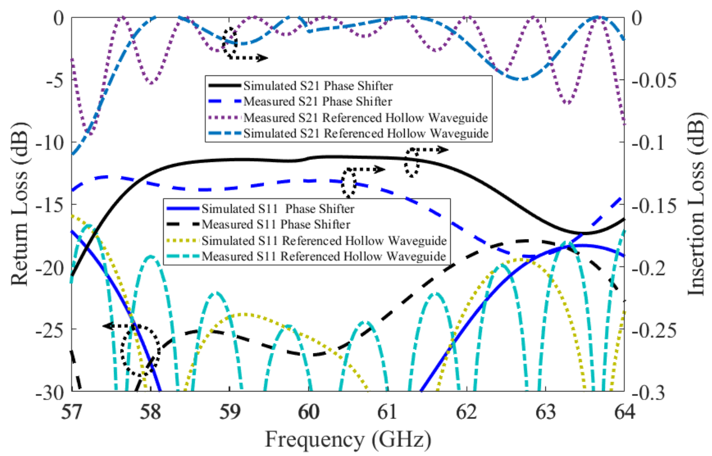

Figure 7.56: Paramètres de diffusion mesurés et simulés du déphaseur propose (M. Farahani et al. [23], @2019 IEEE).

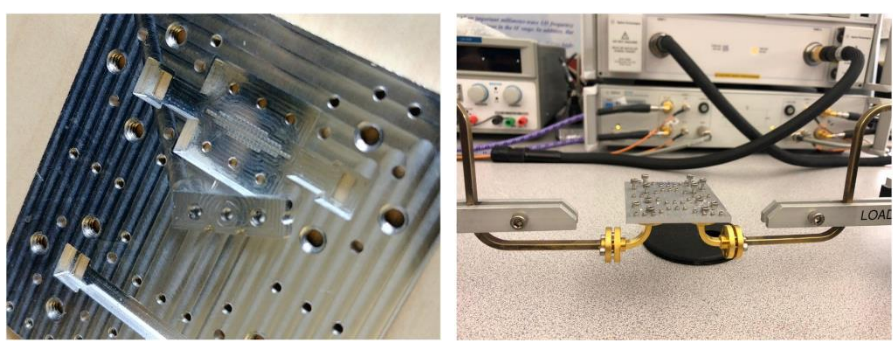

(a) (b)

Figure 7.57: La photo du prototype fabriqué et de la configuration de test.(a) Prototype fabriqué. (b) Configuration de test (M. Farahani et al. [23], @2019 IEEE).

Résultats expérimentaux:

La photo du prototype fabriqué et la configuration de test sont illustrées à la Figure 7.57. L'analyseur de réseau de la série PNA et le contrôleur de tête millimétrique N5260A avec connexion de guide d'ondes WR-15 standard sont utilisés pour mesurer le dispositif. Pour compenser l'effet de la transition verticale à horizontale et des pertes du guide d'ondes creux, un guide d'ondes creux classique est intégré sur la même plaquette à côté du déphaseur. La Figure 7.56 montre les paramètres de diffusion mesurés et simulés du déphaseur proposé. L'affaiblissement de retour mesuré est inférieur à -20 dB dans toute la bande de fréquences (de 57 à 64 GHz). Les résultats numériques et expérimentaux s'accordent assez bien. La perte d'insertion est inférieure à 0.2 dB dans toute la bande de fréquence. La Figure 7.55 montre la réponse de phase mesurée et simulée, comparée au guide d'ondes creux classique intégré à côté du déphaseur. Un déphasage exact de 45^o avec une erreur de phase inférieure à 0.4^o est obtenu dans la bande de fréquence de fonctionnement.

7.6 Réseaux de transformateurs de faisceaux à la fine pointe de la technologie mmWave

La bande de fréquence millimétrique 60-GHz a suscité un grand intérêt, car elle peut fournir des ressources spectrales beaucoup plus disponibles pour répondre aux besoins croissants de la 5G, la prochaine génération de communications mobiles, pour une meilleure qualité d'expérience [24]. Cependant, les signaux en ondes millimétriques subissent une perte de propagation importante, une réluctance pénétrante, un impact de pluie et une absorption atmosphérique. Pour compenser cette lacune, une stratégie consiste à concevoir un système de pointe utilisant un grand nombre de dispositions d'antenne au niveau des terminaux dans les réseaux de communication à ondes millimétriques, pouvant offrir des diagrammes de direction élevés pour compenser la propagation sévère. perte. De plus, les mouvements de l'utilisateur réduisent l'alignement du faisceau et exigent une formation continue, ce qui renforce sensiblement la responsabilité du formateur [24]. Ceci existe particulièrement pour la rotation des utilisateurs. Les expériences confirment qu'un léger déréglage de 18^o dégrade le bilan de la liaison d'environ 17 dB dans un système avec une largeur de faisceau du diagramme de rayonnement de 7^o. D'après les sensibilités de codage IEEE 802.11ad [24]. le débit le plus élevé diminuerait jusqu'à 6 Gbps lors de cette dégradation ou couperait complètement la connexion.

Afin de résoudre ce problème, la matrice de Butler peut être un candidat compétent en tant que réseau de formation de faisceaux à faible coût lorsque nous recherchons une alternative possible [124]. La combinaison de ce réseau passif de formation de faisceau avec un réseau linéaire d'éléments rayonnants serait utilisée dans les futures technologies 5G. Dans la bande de fréquence de 60-GHz, les réseaux de formation de faisceau du CP sont intéressés car ils permettent d'éliminer un éventuel décalage de polarisation entre l'émetteur et le récepteur et permettent de réduire les effets de trajets multiples par rapport aux systèmes polarisés linéairement [130], tout en améliorant leur productivité. pour atténuer les évanouissements et les trajets multiples indésirables [130]-[132]. Par ailleurs, avec une matrice Butler 4×4 conventionnelle, vous pouvez atteindre un gain d'environ 9 dBi, ce qui n'est pas suffisant dans la bande des 60-GHz.

7.6.1 Réseau Beamformer polarisé à double polarisation gauche/droite

Dans ce travail, un nouveau réseau de formation de faisceaux CP LH/RH à haute efficacité et à double polarisation est conçu dans la bande de fréquences de 60-GHz. Le guide d'ondes Hedgehog est utilisé comme une structure de guidage à très faible perte pour concevoir les déphaseurs requis [23]. La constante d'atténuation à l'intérieur du guide d'ondes Hedgehog est considérablement inférieure aux structures de guidage conventionnelles équivalentes, par exemple, les guides d'ondes SIW, à crête gap, creuses et à gap dans la bande des 60-GHz [23]. Le formeur de faisceau proposé fournit les signaux de phase progressive uniformes afin d'alimenter un réseau d'antennes avec les huit diagrammes de rayonnement distingués associés à chacun des huit ports d'entrée. Pour augmenter le gain et supprimer les lobes secondaires, un réseau d'alimentation 8×8 est utilisé. En utilisant le réseau d'alimentation proposé, les lobes secondaires sont supprimés à une valeur inférieure à -19 dB. En augmentant le nombre d'éléments rayonnants à 8, la directivité du formeur de faisceau proposé augmente d'environ 3 dB. L'antenne à fente progressive est utilisée pour fournir un rapport axial à large bande. La bande passante de 10.75% et l'efficacité de rayonnement de 90% pour chaque port sont obtenues en utilisant le réseau de formation de faisceau proposé.

Architecture de réseau Beamforming proposée:

Pour augmenter le gain de rayonnement du réseau de formation de faisceaux à matrice de Butler, le nombre des éléments rayonnants est augmenté à l'aide du réseau introduit illustré à la Figure 7.58. Selon cette figure, le réseau de formation de faisceau se compose de deux réseaux de matrice de Butler 4×4 et de deux réseaux de contrôle de configuration.

Le réseau de contrôle de configuration vise à préparer les signaux requis pour les premier et second sous-réseaux décrits à la Figure 7.58. Comme illustré sur cette figure, le nombre d'éléments rayonnants devient deux fois supérieur, ce qui résulte en une amélioration de gain de 3 dB. Les caractéristiques de rayonnement de la matrice proposée à la Figure 7.58 dépendent de la répartition en phase et en amplitude des signaux d'alimentation de chaque élément de la matrice, des propriétés de motif, de la disposition géométrique et de l'espacement entre les éléments des éléments de la matrice [134]. Une structure directive dans une direction spécifique, tout en maintenant le niveau des lobes latéraux (SLL) faible, est un grand désir, dans les réseaux d'antennes, de contourner les interférences avec d'autres canaux et d'augmenter l'efficacité du rayonnement de l'antenne [127], [135]-[138]. Dans la plupart des cas, cela s'effectue en gérant la phase et la magnitude des signaux d'alimentation. Dans une matrice de Butler alimentant un petit réseau linéaire, la SLL peut être minimisée en développant les éléments rayonnants et en prenant en compte la «condition de réseau» [139]-[140] sans détériorer les caractéristiques de rayonnement globales du réseau. En utilisant cette théorie, le nombre d'éléments rayonnants est doublé dans une matrice de Butler 4 × 4 en mettant en oeuvre le réseau de contrôle de configuration (Figure 7.58) entre la matrice de Butler et les éléments rayonnants.

La SLL d'un réseau linéaire à espacement égal est d'environ -13.5 dB [134]. Cependant, le couplage spatial entre les antennes et les réflexions au niveau des ports d'antenne détériorent la SLL jusqu'à moins de 10 dB [134]. De plus, en augmentant l'espacement entre les éléments de plus d'une longueur d'onde, les lobes du réseau apparaîtront dans la zone visible. Dans notre cas, en raison de la géométrie de l'antenne à double polarisation conçue, l'espacement entre les éléments est d'environ $0.85\lambda_o$. Pour réduire la SLL et éliminer l'effet des réseaux de lobes, le nombre d'éléments rayonnants est doublé [139]-[141]. Cela rendra donc le réseau de formation de faisceau plus compliqué comparé à un réseau matriciel 4×4 Butler classique. Pour avoir des degrés de liberté plus élevés, la technique de réduction d'amplitude [134] est utilisée pour supprimer davantage les lobes secondaires. Les quatre diviseurs de puissance non équilibrés ont pour rôle d'alimenter les éléments rayonnants de manière déséquilibrée. Comme on peut le voir à la Figure 7.58, la magnitude des signaux des éléments rayonnants est symétrique par rapport au centre et est effilée vers les bords si différents arguments de $90-q$, $90-g$, g et q $(0 < q < g < 45^o)$ du haut vers le bas, sélectionnez les facteurs de couplage pour les quatre diviseurs de puissance non équilibrés. Les $q = 31.72^o$ et $g = 36.86^o$ sont sélectionnés à l'aide de l'optimisation de l'essaimage de particules (PSO) [141]. En conséquence, la SLL est réduite à 19 dB avec cette technique pour tous les faisceaux du plan E. Le diagramme de rayonnement simulé avec et sans réduction de SLL est représenté à la Figure 7.59.

Le schéma fonctionnel du réseau de contrôle de modèle proposé est illustré à la Figure 7.58. Selon cette figure, le réseau de contrôle de configuration est constitué de trois étages de sections croisées et de déphaseurs. Le réseau de contrôle de configuration prépare les signaux requis pour les premier et deuxième sous-réseaux illustrés à la Figure 7.58. Pour obtenir le tableau déphasé uniformément, le deuxième sous-tableau doit être 180^o en retard par rapport au premier sous-tableau, comme illustré à la Figure 7.60. Cette condition est appliquée dans le schéma de principe du réseau de contrôle de modèle en mettant en œuvre les déphaseurs 180^o, comme illustré à la Figure 7.58. La Figure 7.60 montre le diagramme de phase des signaux dans le réseau de formation de faisceau. En excitant les $port$ 1 et 2, la phase progressive de $\pm 45^o$ et $\pm 135^o$ sera générée respectivement aux ports de sortie de la matrice de Butler, comme indiqué à gauche dans la

Figure 7.60. Le réseau de contrôle de modèle divise les signaux de sortie de la matrice de Butler entre les deux sous-réseaux.

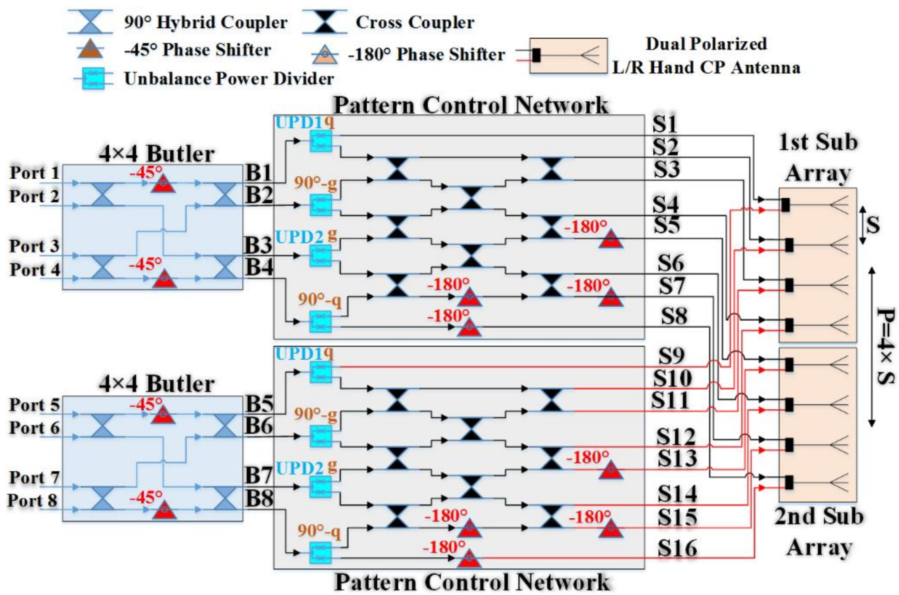

Figure 7.58: Architecture de réseau de formation de faisceaux à polarisation circulaire à polarisation double gauche/droite proposée (M. Farahani et al. [J1], @n.d. IEEE).

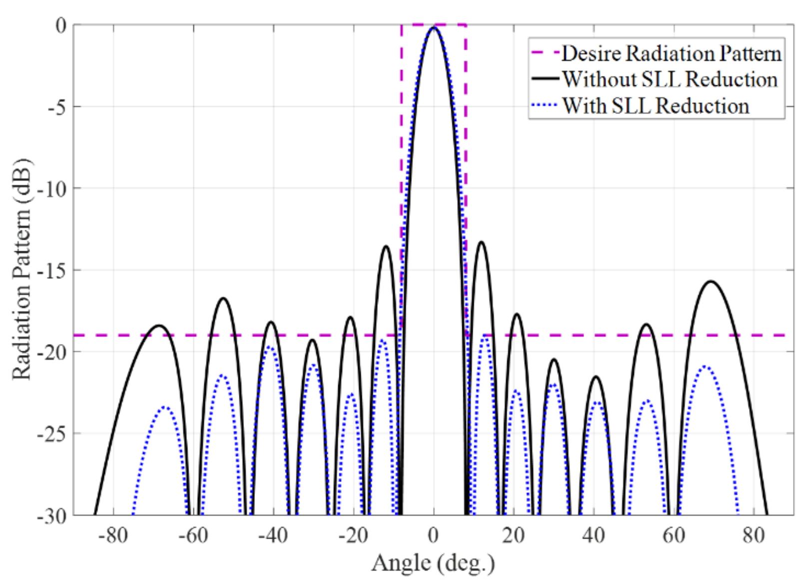

Figure 7.59: Le diagramme de rayonnement simulé avec et sans réduction de SLL (M. Farahani et al. [J1], @n.d. IEEE).

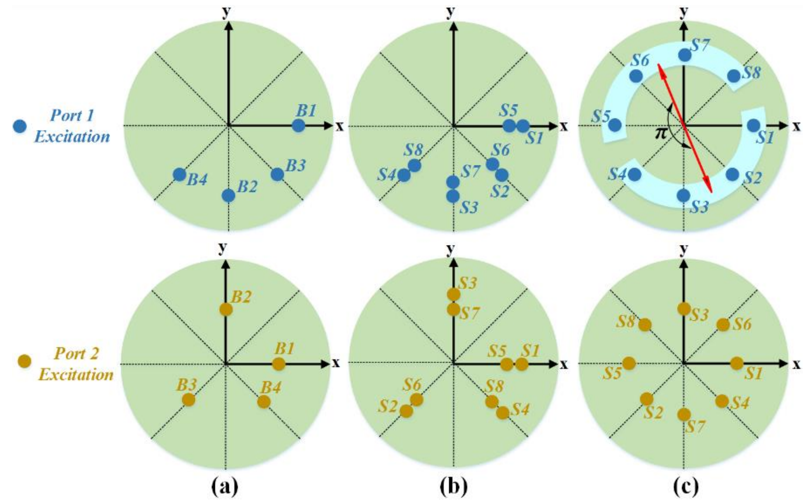

Figure 7.60: Diagramme de phaseur du formeur de faisceau proposé à la Figure 7.58 (M. Farahani et al. [J1], @n.d. IEEE).

Antenne à fente progressive à ondes progressives:

Dans ce travail, nous proposons une nouvelle antenne à polarisation circulaire gauche/droite à double polarisation mise en œuvre dans un guide d'ondes creux. La Figure 7.61 montre la vue 3D de l'antenne CP proposée à double polarisation LH/RH. L'antenne est constituée de deux guides d'ondes fixés l'un sur l'autre et d'une fente triangulaire sur le mur commun afin de créer le mode d'axe x requis. De plus, il y a deux fentes sur les murs inférieur et supérieur, comme indiqué dans [154].

La théorie principale pour analyser le fonctionnement du CP dans le guide d'ondes creux à deux couches proposé est basée sur des analyses en mode impair et en mode pair. Les guides d'ondes rectangulaires d'alimentation des $port$ 1 et 2 fonctionnent en mode TE_{10}. En excitant le $port$ 1, le champ d'alimentation TE_{10} sera transformé en autres modes pouvant être analysés par des champs de modes impair et pair, comme illustré à la Figure 7.62. Les champs électriques ont la même direction dans les guides d'ondes inférieur et supérieur en considérant le champ à mode pair et la direction inverse dans les guides d'ondes inférieur et supérieur en considérant le champ à mode impair (voir Figure 7.62). Ceux-ci mènent au mode TE_{10} inchangé sur le port $P1$ sans avoir le couplage mutuel entre les ports 1 et 2. Un autre mode le long de l'axe des x (TE_{01}) sera excité progressivement en passant le long de la fente du triangle (BB'), comme illustré à la Figure 7.62. Par ailleurs, il est bien connu que l'onde électromagnétique à polarisation circulaire est composée de deux modes à polarisation linéaire avec 90^{o} déphasés et de même amplitude [159]. Les différentes longueurs d'onde guidées de deux modes TE_{10} et TE_{01} permettent d'obtenir le déphasage requis de 90 ^ o. Enfin, grâce à la fente progressive des côtés supérieur et inférieur, la condition pour une amplitude égale est fondamentalement remplie. La largeur de la fente augmente progressivement en se déplaçant vers l'ouverture de l'antenne sur les côtés supérieur et inférieur, ce qui stimule l'augmentation de l'amplitude TE_{01} (voir la Figure 7.62). De ce fait, la condition pour les deux modes linéairement polarisés avec 90^o déphasé et de même amplitude est parfaitement remplie.

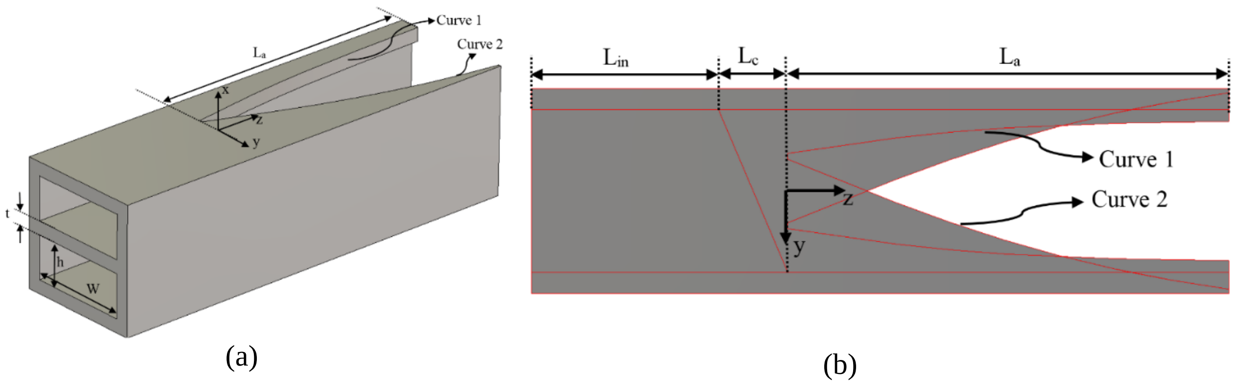

Figure 7.61: Vue 3D de l'antenne CP double droite/gauche proposée.(a) vue de côté. (b) vue de dessus. Les dimensions sont: $L_a = 10.31$, $L_c = 1.62$, $L_{in} = 6$, $h = 1.6$, $W = 3.8$, $t = 1$, $M_0 = 0.74$, $M_1 = 3$, $M_2 = 0.87$, $M_3 = 1.65$, le tout en millimètres $\xi_1 = 0.22\ (mm^{-1})$, $\xi_2 = 0.4\ (mm^{-1})$ (M. Farahani et al. [J1], @n.d. IEEE).

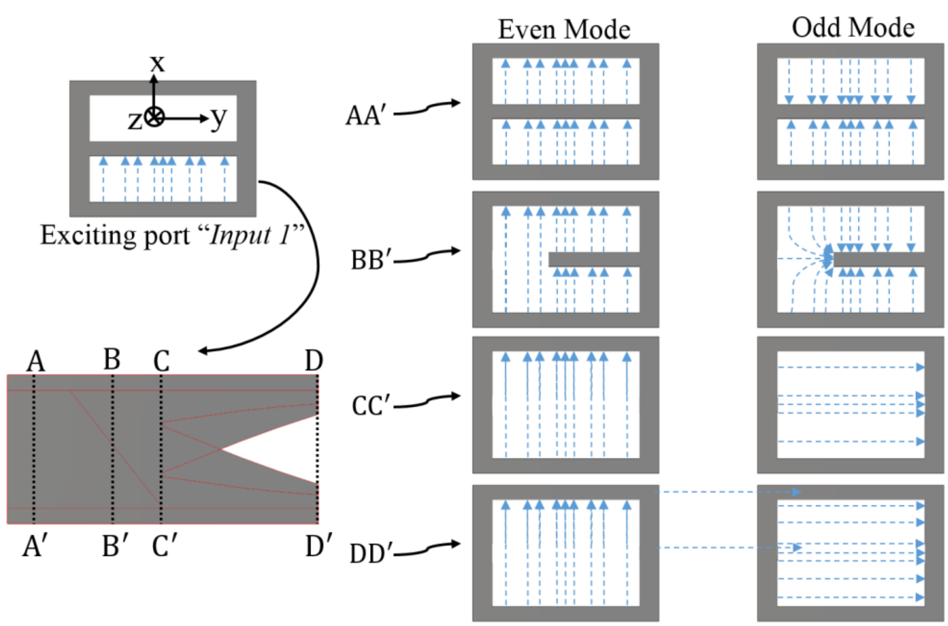

Figure 7.62: La théorie principale pour l'excitation de l'onde CP dans le guide d'ondes creux à deux couches proposé peut être étudiée sur la base d'analyses en mode impair et en mode pair.Les guides d'ondes rectangulaires d'alimentation des $port$ 1 et 2 fonctionnent en mode TE_{10}. Les champs électriques à différents plans sont illustrés (M. Farahani et al. [J1], @n.d. IEEE).

De plus, en excitant le $port$ 2 alternativement, la théorie de l'excitation de l'onde CP est identique, alors que les vecteurs de champ ne sont inversés qu'en mode impair. De plus, les vecteurs de champ tournent dans le sens opposé sur l'ouverture d'antenne excitée par le $port$ 2, à l'opposé de celle excitée par le $port$ 1. Par conséquent, une double opération de polarisation circulaire gauche/droite peut être obtenue pour l'antenne présentée en excitant chacun des différents ports d'entrée.

L'antenne conçue est simulée à l'aide du logiciel Ansys HFSS. Les paramètres de diffusion simulés et le rapport axial de l'antenne sont présentés à la Figure 7.63. Comme on peut le constater, les coefficients de réflexion sont inférieurs à -25 dB. De plus, l'isolation entre les ports est inférieure à -20 dB dans la bande de fréquence d'observation. Les diagrammes de rayonnement, concernant différents ports excités, à 60-GHz sont présentés à la Figure 7.64.

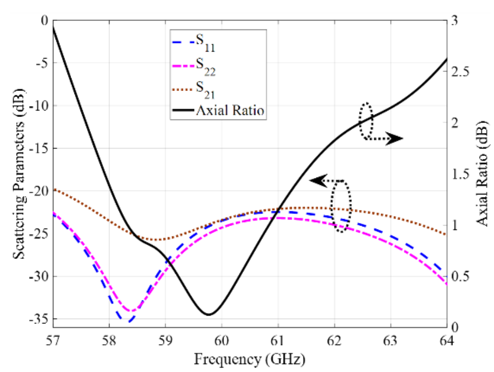

Figure 7.63: Paramètres de diffusion et rapport axial simulés de l'antenne à fente progressive à double polarisation(M. Farahani et al. [J1], @n.d. IEEE).

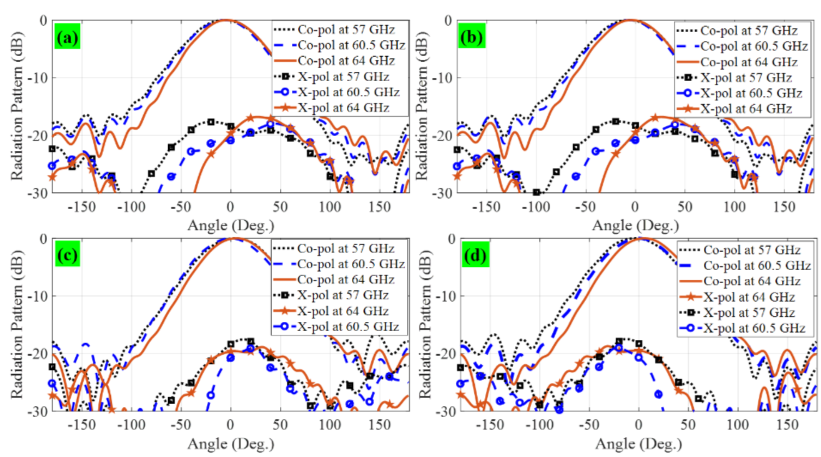

Figure 7.64: Diagrammes de rayonnement simulés de l'antenne à fente progressive à double polarisation concernant différents ports excités à 60-GHz.(a) Polarisation circulaire gauche dans le plan xz. (b) polarisation circulaire droite dans le plan xz. (c) plan yz polarisé circulairement à gauche. (d) plan yz à polarisation circulaire droite(M. Farahani et al. [J1], @n.d. IEEE).

Conception et performance de chaque bloc du réseau d'alimentation:

Chaque composant du réseau d'alimentation est conçu séparément avec des paramètres de diffusion entrée/sortie souhaités inférieurs à 20 dB afin de réduire toute éventuelle discordance probable entre les différents composants. De plus, afin de réduire le possible mode d'ordre supérieur parmi les composants connectés, une longueur de connexion minimale de la moitié d'une longueur d'onde à 60-GHz est considérée parmi les composants consécutifs.

Résultats expérimentaux:

Dans cette section, la configuration complète du réseau de formation de faisceau à polarisation circulaire double polarisation gauche/droite réalisé est présentée et les résultats de la simulation comparés à ceux de l'expérimental. Comme l'illustre la Figure 7.65, le réseau de formation de faisceau proposé est constitué de trois couches distinctes qui sont attachées l'une à l'autre. Les couches sont fabriquées avec la technique de matriçage. Le formage à la matrice est un procédé de fabrication de composants métalliques populaire. Le prototype, généralement une couche de métal, est formé en permanence autour d'une matrice par l'intermédiaire d'une clause en plastique par des procédés de construction et de gravure. De plus, des simulations peuvent être effectuées pour prévenir les ruptures, les dommages, les crêtes et la propagation. L'inconvénient principal est qu'il est très difficile de séparer la matrice et la plaque à ongles si les ongles sont longs et fins.

L'appareil de formation de faisceau se compose de 8 ports d'entrée associés à 8 diagrammes de rayonnement de sortie différents, dont quatre sont polarisés circulairement à droite et quatre autres sont polarisés circulairement à gauche. Le beamformer ajuste les signaux pour préparer les signaux de phase progressive uniformes demandés et pour supprimer les lobes secondaires au niveau des ports des antennes à double polarisation. Le beamformer comprend différents blocs de construction composés de coupleurs, de déphaseurs, de répartiteurs et de diviseurs de puissance non équilibrés (Figure 7.65). Dans le même temps, il est utile de mentionner que ces différents blocs de construction sont conçus et simulés séparément, avec une perte de retour d'entrée souhaitée inférieure à 20 dB afin d'éliminer toute disparité probable entre les différents composants. De plus, la distance entre deux composants consécutifs doit être considérée comme étant au moins égale à $\lambda_g/2$ afin d'éliminer le mode d'ordre supérieur parmi les composants, où λ_g est la longueur d'onde guidée du mode dominant (TE_{10}).

Les pertes de retour d'entrée de l'ensemble de la structure effectuées à l'aide de HFSS sont comparées aux résultats de mesure pour les ports d'entrée de la Figure 7.66(a) et (b). Les pertes en retour d'entrée sont inférieures à -14 dB dans la largeur de bande de fonctionnement du trou, de 57 à 64 GHz. Les résultats de champ lointain dans le plan yz, relatifs aux quatre diagrammes de polarisation circulaire à droite à 60.5 GHz, sont présentés à la Figure 7.67. Les gains mesurés concernant l'excitation de quatre ports d'entrée droite/gauche sont comparés à ceux simulés à la Figure 7.68. Cette différence entre les résultats simulés et les résultats mesurés est attendue en raison de la configuration imparfaite du test d’antenne, dans laquelle le WR-15 en train d’alimenter peut affecter le diagramme de rayonnement. La Figure 7.69 montre la photo du prototype fabriqué et de la configuration de mesure du diagramme de rayonnement.

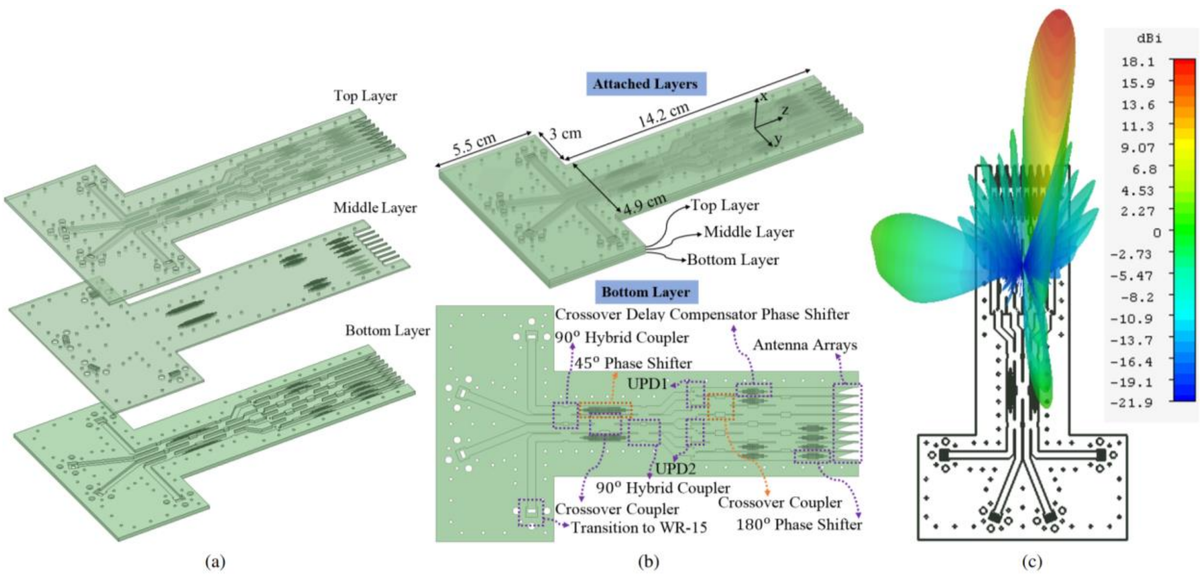

Figure 7.65: Le réseau de formation de faisceau proposé se compose de trois couches distinctes qui sont attachées les unes aux autres.(a) Couches attachées. (b) Séparez les couches(M. Farahani et al. [J1], @n.d. IEEE).

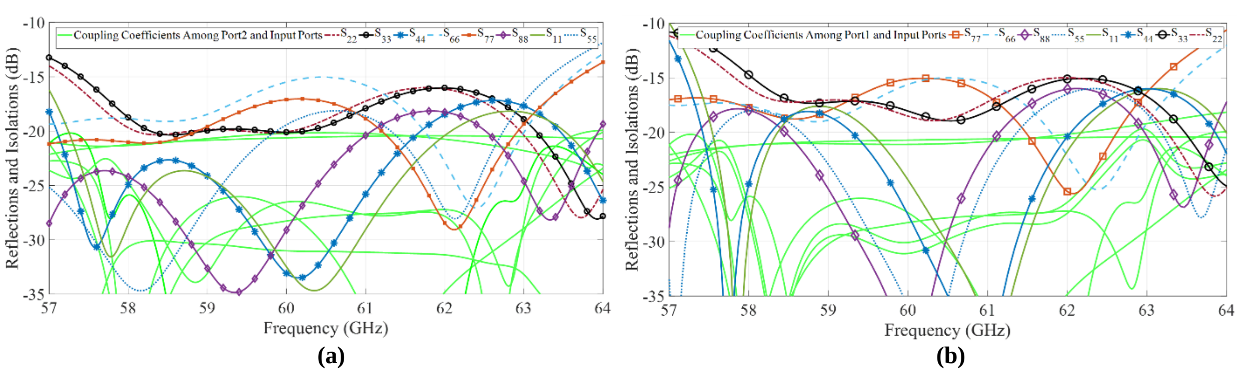

Figure 7.66: Pertes de retour d'entrée pour tous les ports.(a) simulé. b) Mesures (M. Farahani et al. [J1], @n.d. IEEE).

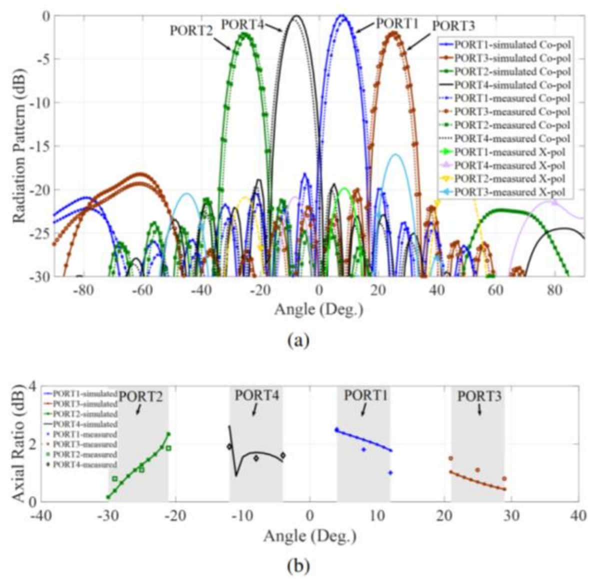

Figure 7.67: Résultats du champ lointain dans le plan yz concernant quatre motifs polarisés circulairement à droite.(a) Diagrammes de rayonnement normalisés, simulés et mesurés dans le plan yz, concernant l'excitation de différents ports d'entrée à 60.5 GHz. (b) Rapport axial simulé et mesuré concernant l'excitation de différents ports d'entrée à 60.5 GHz (M. Farahani et al. [J1], @n.d. IEEE).

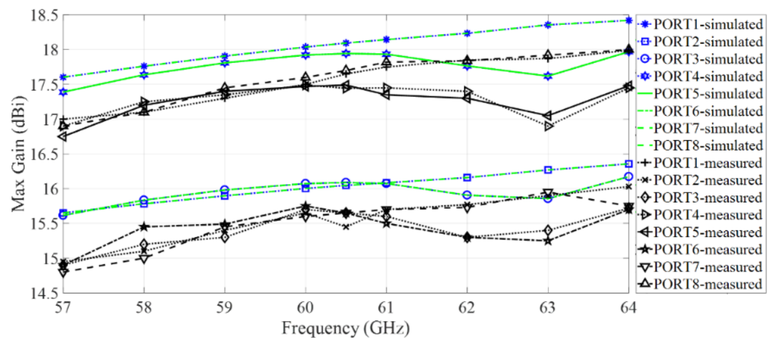

Figure 7.68: Gains maximaux CP mesurés et simulés à droite/à gauche concernant différents ports d'entrée (M. Farahani et al. [J1], @n.d. IEEE).

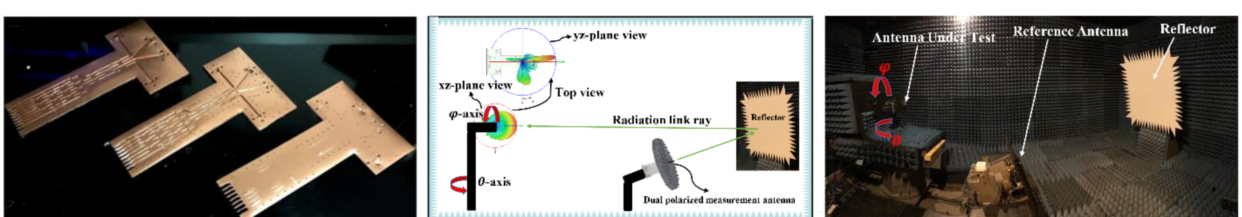

(a) (b) (c)

Figure 7.69: (a) Photo du prototype fabriqué. (b) Configuration de la mesure du diagramme de rayonnement (M. Farahani et al. [J1], @n.d. IEEE).

7.6.2 Formateur de faisceau 2×2 30-GHz très efficace basé sur une ligne coaxiale rectangulaire remplie d'air

Dans ce travail, le concept principal de la matrice de Butler (BM) a été dérivé de la structure de BM présentée dans [166]-[168] où ils ont la même structure de BM mise en œuvre dans différentes structures directrices. Dans [166], le faîte de crête imprimé (PRGW) est pratiqué. Dans [167], le SIW est utilisé, alors que la ligne de transmission traditionnelle à microruban est utilisée dans [168]. En variante, la même structure BM est utilisée, mais avec la ligne de transmission coaxiale remplie d'air carrée à faible perte et à large bande carrée comme structure de guidage. Dans la ligne coaxiale carrée traditionnelle, le conducteur central supporté par des tronçons de microruban raccourcis limite la bande passante, augmente les pertes et complique la fabrication [169]-[172]. Pour surmonter ces inconvénients extrêmes, une méthode des tronçons de quart d'onde est introduite. Ces talons sont prévus pour suspendre le conducteur central de la ligne coaxiale et faciliter la fabrication sans le support de la suspente diélectrique, entraînant une augmentation de la largeur de bande et une diminution des pertes. Le formeur de faisceau proposé est excité par quatre ports WR-28 conventionnels, qui sont reliés par des transitions coaxial-creux. Parmi les autres subventions de cette recherche, citons l'amélioration du gain, la diminution du niveau de la lisière latérale et l'obtention d'une efficacité supérieure à 90%.

Topologie du réseau Beamformer:

Ici, la structure du réseau de fibrage proposé avec capacité de balayage 2D est démontrée et expliquée. Comme présenté à la Figure 7.70, ce réseau est composé de quatre coupleurs hybrides à 3 dB à large bande et à faible perte. Il n'est pas nécessaire d'utiliser un coupleur déphaseur ou croisé (voir Figure 7.70). Quatre ports d'entrée (P1 à P4) sont associés à quatre ports de sortie (A1 à A4) via la structure présentée. Une antenne réseau à réseau 2×2 est excitée par le formeur de faisceau recommandé pour obtenir un balayage latéral 360^o par tranches de 90^o.

De plus, le commutateur SP4T permet la sélection du faisceau en connectant l'un des ports d'entrée BM à l'émetteur-récepteur [168]. La Figure 7.71 présente les diagrammes de rayonnement du formateur de faisceau introduit concernant l'excitation de différents ports.

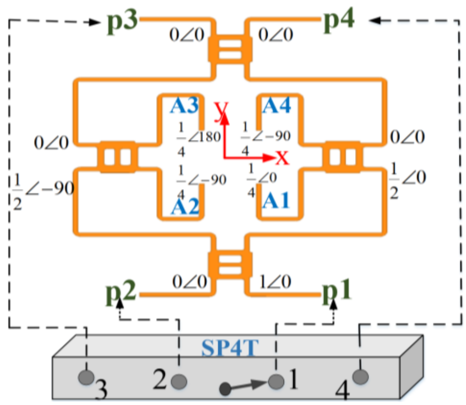

Figure 7.70: Le schéma de principe du réseau 4×4 beamformer (M. Akbari et al. [J2], @n.d. IEEE).

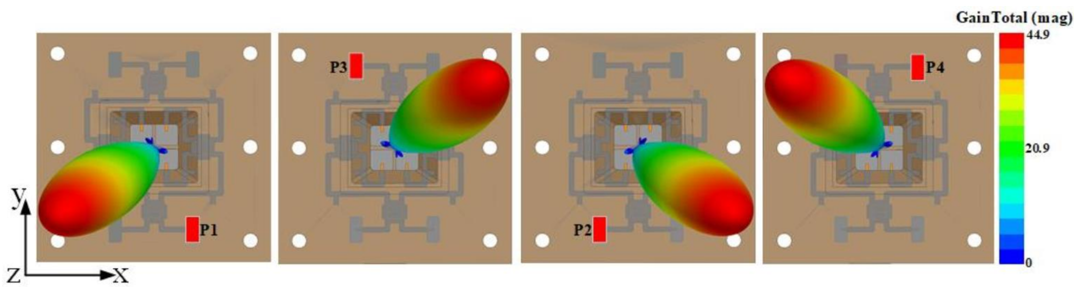

Figure 7.71: Diagrammes de rayonnement simulés du réseau de formation de faisceaux proposé à 30 GHz par rapport aux ports passionnants (M. Akbari et al. [J2], @n.d. IEEE).

Mise en œuvre du transformateur de faisceau proposé:

La mise en œuvre du beamformer conçu est illustrée à la Figure 7.72. Comme indiqué dans les sections précédentes, la ligne de transmission carrée remplie d'air carrée est choisie comme structure de guidage, les couches supérieure et inférieure représentant le conducteur extérieur, tandis que la couche centrale est le conducteur intérieur. En outre, le réseau est excité par quatre ports de guide d'ondes WR-28 standard (voir Figure 7.72(d)).

Le transformateur de faisceau à matrice de Butler à deux dimensions, implémenté dans une ligne de transmission coaxiale remplie d'air, est fabriqué comme indiqué à la Figure 7.73. Le formeur de faisceau prévu est constitué de trois couches distinctes: deux couches supérieure et inférieure représentent le conducteur extérieur et la couche centrale représente le conducteur intérieur. Différents trous sont considérés sur les côtés pour les vis afin d'ajuster et d'assembler le prototype. Les paramètres S du prototype souhaité sont mesurés à l'aide d'un analyseur de réseau vectoriel à deux ports via des ports d'entrée WR-28, les deux autres ports étant connectés à des charges adaptées. On peut constater que les coefficients de réflexion en entrée et les couplages mutuels sont inférieurs à -10 dB dans toute la bande de fréquence de travail. De plus, les résultats simulés et expérimentaux se suivent assez bien, comme le montre la Figure 7.74.

Une configuration de test de chambre anéchoïque, illustrée à la Figure 7.75, est utilisée pour mesurer le gain de rayonnement maximal et les diagrammes de rayonnement du prototype fabriqué. Les résultats de mesure et de simulation concernant les diagrammes de rayonnement, lorsque le formateur de faisceau prévu est excité séparément par un port tandis que les autres ports sont connectés à des charges adaptées. Les gains maximaux sont approximativement constants sur l'ensemble des bandes de fréquences de travail, comme il est représenté aux Figure 7.77 et Figure 7.76. On peut noter que le gain maximal mesuré rencontre une faible variation de ± 0,5 dB sur la bande de fréquences de travail, ce qui témoigne d'un accord certain avec les résultats numériques.

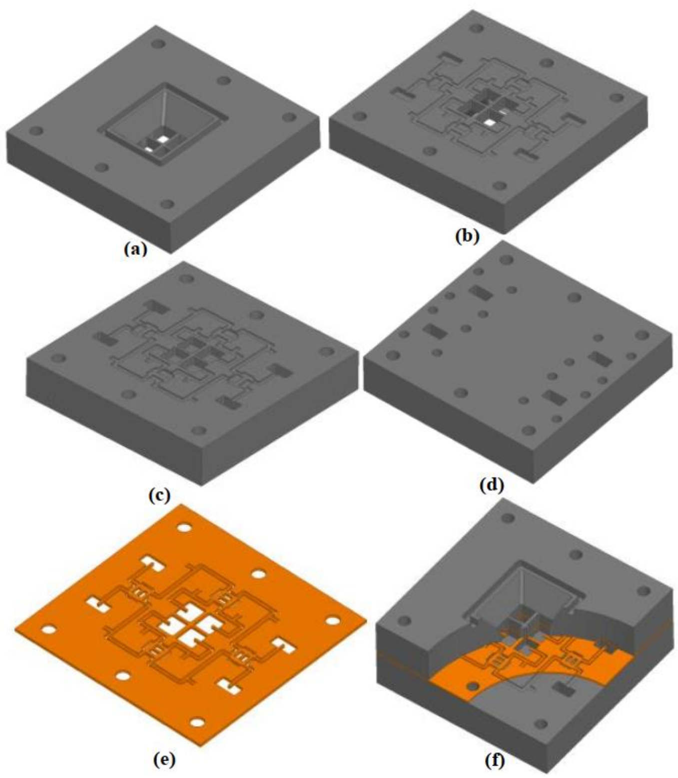

Figure 7.72: La conception proposée de 4 × 4 faisceaux de lumière comprenant trois couches différentes; (a) vue de face de la couche supérieure (ouverture de l'antenne), (b) vue de l'arrière de la couche supérieure, (c) vue de face de la couche inférieure, (d) vue de l'arrière de la couche inférieure, (e) au centre couche (conducteur interne), et (f) la conception à trois couches proposée (M. Akbari et al. [J2], @n.d. IEEE).

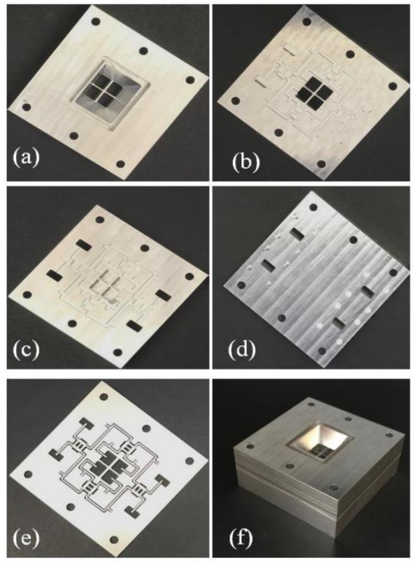

Figure 7.73: La photo du dessin fabriqué; (a) vue de face de la couche supérieure (ouverture de l'antenne), (b) vue de l'arrière de la couche supérieure, (c) vue de face de la couche inférieure, (d) vue de l'arrière de la couche inférieure, (e) au centre couche (conducteur interne), et (f) la conception à trois couches proposée (M. Akbari et al. [J2], @n.d. IEEE).

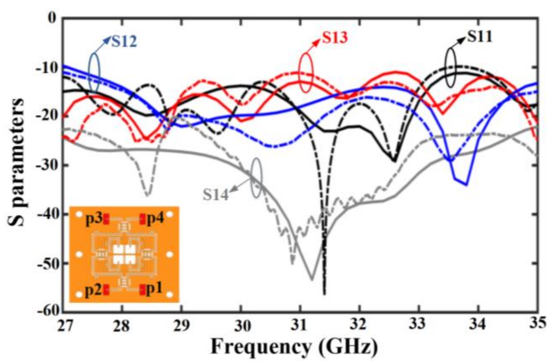

Figure 7.74: Les résultats de mesure et de simulation des paramètres de diffusion.Les lignes continues et en pointillés représentent les résultats de la simulation et de la mesure, respectivement (M. Akbari et al. [J2], @n.d. IEEE).

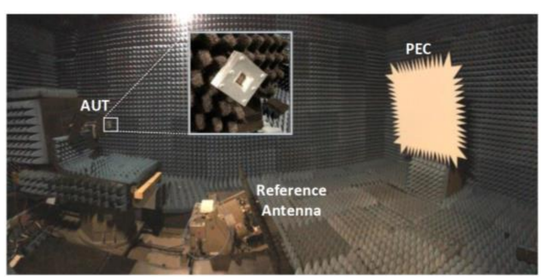

Figure 7.75: La configuration de mesure pour le diagramme de rayonnement.AUT est l'antenne à l'essai (M. Akbari et al. [J2], @n.d. IEEE).

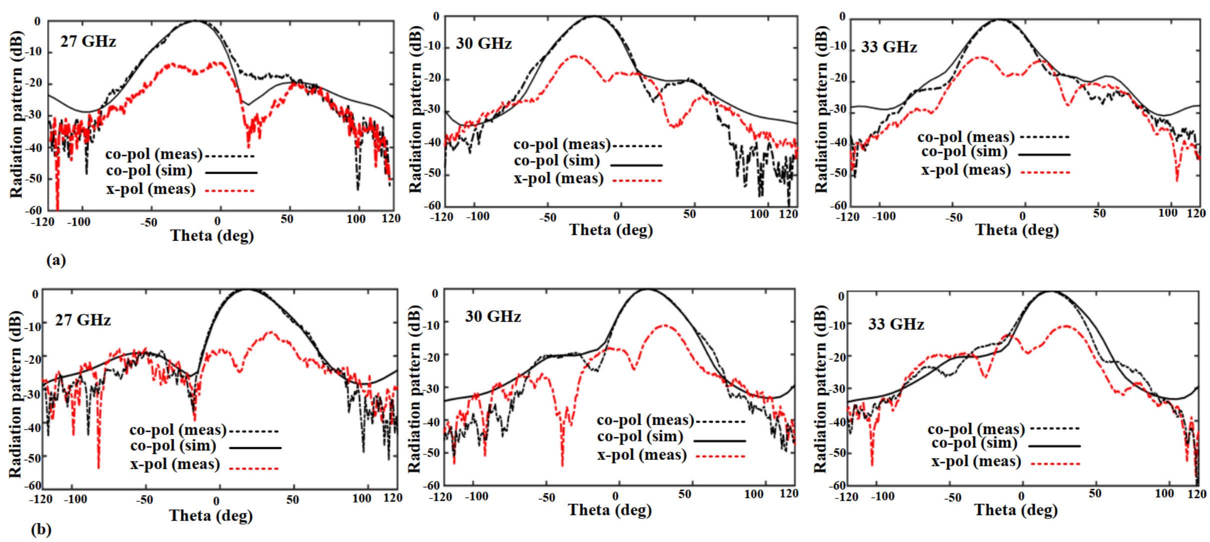

Figure 7.76: Résultats mesurés et simulés du diagramme de rayonnement à des fréquences de 27 GHz, 30 GHz et 33 GHz lorsque la structure proposée est excitée par (a) les ports 1 (haut) et (b) le port 2 (bas) (M. Akbari et al. [J2], @n.d. IEEE).

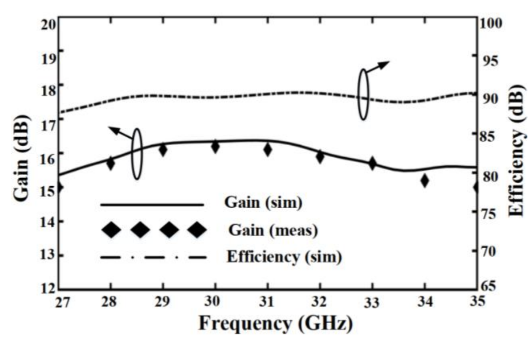

Figure 7.77: Les résultats mesurés et simulés du gain et de l'efficacité (M. Akbari et al. [J2], @n.d. IEEE).

7.7 Conclusion et travaux futurs de la thèse

Conclusion:

Dans cette thèse, plusieurs approches de la couche physique à la couche réseau ont été proposées et étudiées pour surmonter les obstacles au développement des réseaux mmWave. Cependant, chaque approche a ses avantages et ses inconvénients, et ces approches doivent être combinées de manière intelligente pour obtenir des performances réseau robustes et efficaces.

Dans les communications sans fil, le débit de la liaison de communication est l’un des indicateurs les plus importants pour l’estimation des performances. Cependant, le débit dépend fortement des caractéristiques du canal de propagation, telles que l'affaiblissement du trajet, la distance entre les dispositifs, le bruit, etc.

Grâce à la formule du modèle d'affaiblissement du trajet de l'espace libre Friis, l'affaiblissement du trajet pour 60-GHz est de près de 28 dB perte plus par rapport au 5 GHz mmWave. Parallèlement, une perte supplémentaire (perte de puissance de 7-15,5 dB/km) doit être prise en compte dans le signal reçu à des fréquences porteuses de 60-GHz en raison de l'absorption atmosphérique [65]. Outre ces facteurs, le taux de précipitations affecte également les performances du système. Atténuation atmosphérique supplémentaire d'environ 8 à 18 dB/km alors que le taux de précipitations est de 50 mm par heure [65]. Outre la forte atténuation, la radio en ondes millimétriques 60-GHz présente également une faible capacité de pénétration [66]. En outre, bien que la taille physique des antennes soit si petite, la conception des réseaux d'alimentation en antennes devient complexe et pose un problème pour les concepteurs en raison du nombre élevé de pertes dans la bande de fréquence à onde millimétrique de 60-GHz. Pour surmonter le blocage, plusieurs approches de la couche physique à la couche réseau ont été proposées.

Le premier objectif du travail consiste à concevoir et à développer ces approches pour des applications dans les bandes de fréquences à ondes millimétriques. Dans un premier temps, les systèmes MIMO ont été étudiés et de nouvelles approches ont été proposées et développées afin de concevoir des antennes MIMO appropriées pour les applications mmWave. Un nouveau procédé a été proposé afin de rendre les éléments rayonnants adjacents dans une antenne réseau MIMO orthogonaux en termes de réception de signaux les uns des autres. En ce qui concerne différents mur de rotateur de polarisation présenté et développé.

Dans l'étape suivante, une étude approfondie des antennes à gain élevé pour les applications d'antenne modernes mmWave a été réalisée. Ceci confirme la contribution des méthodes d'amélioration du gain dans les futures applications mmWave d'antenne. Pour commencer, une antenne large bande à gain élevé a été conçue pour les applications mmWave utilisant une couche superstrate placée au-dessus de l'antenne. En outre, une technique d'orientation du faisceau utilisant une métasurface à gradient de phase (PGM) a été proposée et étudiée. Ce travail a permis une vision en profondeur du système d'antenne à ondes millimétriques et de leurs techniques de mesure. Cependant, nous avons rencontré des difficultés de fabrication en raison de défauts mécaniques dans ce travail, et aucun résultat de mesure acceptable n'a été obtenu.

L'objectif principal du travail est de concevoir une nouvelle structure de guidage à haute efficacité et à faibles pertes pour les applications mmWave. Une nouvelle structure de guide d'onde a été proposée qui présente plusieurs avantages par rapport aux lignes de transmission conventionnelles décrites dans la littérature. Le principal avantage du guide d'ondes Hedgehog est qu'il peut supporter la propagation avec une perte moindre. De plus, du fait que les champs électromagnétiques sont capturés dans le guide d'onde, les pertes de rayonnement sont maintenues très faibles, ce qui confère une bonne immunité contre les perturbations électromagnétiques externes par rapport à la technologie du microruban. Un autre avantage principal du guide d'ondes Hedgehog est la compatibilité avec les guides d'ondes creux, ce qui offre un degré de liberté supplémentaire pour utiliser le guide d'ondes proposé pour plusieurs conceptions à ondes millimétriques. De plus, la ligne de transmission à fentes et la méthode de transition au microruban sont étudiées et développées, et un coupleur hybride à multiples ouvertures et à faibles pertes à 3 dB 90^{o} avec la technologie à fentes est créé et fabriqué.

Enfin, un nouveau type de réseau de formation de faisceaux a été présenté. Le réseau de formation de faisceaux proposé est mis en oeuvre par le nouveau guide d'onde proposé par Hedgehog. Le réseau de formation de faisceaux à haute efficacité proposé comporte 8 faisceaux fonctionnant en double polarisation. De plus, un réseau de contrôle de configuration 4×8 est utilisé pour augmenter le nombre d'éléments rayonnants et supprimer les lobes latéraux dans le réseau de formation de faisceaux à polarisation double polarisée gauche/droite proposé (LH/RH CP). Ce réseau de formation de faisceaux à double polarisation est mis en œuvre dans la technologie Hedgehog et la technologie de guide d'onde creux en utilisant une technique de collage par diffusion. Le soudage par diffusion, également appelé soudage par diffusion, est un processus d'assemblage à l'état solide qui repose sur la diffusion atomique d'éléments situés à l'interface de l'assemblage. La technique de la fente progressive est utilisée comme antenne à ondes progressives pour avoir un rapport axial à large bande dans la bande de fréquence de 60-GHz, de 57 GHz à 64 GHz. Les lobes secondaires sont supprimés à une valeur inférieure à -19 dB sur la plage de balayage visible. La bande passante de fonctionnement du système est de 10.75% à 60-GHz et l'efficacité de rayonnement du système est supérieure à 90% pour chaque port.

Travaux Futures:

Le travail de recherche effectué dans le cadre de cette thèse ouvre une nouvelle fenêtre sur les composants mmWave et leurs applications dans le domaine des antennes. Cependant, il est observable qu'il existe de nombreuses autres enquêtes à explorer dans ce domaine qui ouvrent la voie à de futures possibilités de recherche, comme expliqué dans les paragraphes suivants.

Le guide d'ondes Hedgehog, constitué d'un lit de clous encastrés dans un guide d'ondes creux rectangulaire, a été proposé et étudié comme guide d'ondes à faibles pertes de pointe prometteur pour les bandes de fréquences à ondes millimétriques. Le guide d'onde Hedgehog tire son nom de son comportement électromagnétique. Alors que les hérissons s'enracinent dans les haies et autres sous-bois à la recherche de leur nourriture préférée, le guide d'ondes proposé s'enracine dans son lit de clous incrusté. Lorsque nous choisissons une technologie de guide d'ondes hôte, il vaut la peine de prendre le temps de peser le pour et le contre des différents types de guides d'ondes proposés. Le guide d'ondes Hedgehog proposé présente une perte extrêmement faible et est compatible avec la technologie des guides d'ondes creux, ce qui permet de développer différents composants tels que des déphaseurs à réponse en phase plate à faibles pertes. Dans le cadre de ma thèse, le guide d'ondes Hedgehog proposé est analysé de manière analytique et une transition vers le guide d'ondes creux est conçue. De plus, la nature du guide d'ondes Hedgehog conçu pour les faibles pertes est comparée au guide d'onde à l'espace de crête, au guide d'onde intégré au substrat (SIW), au guide d'onde creux et à la ligne à microruban. Enfin, le guide d'onde proposé est conçu, simulé et fabriqué. Les résultats simulés et mesurés montrent un bon accord, ce qui valide le concept proposé.

La nouvelle structure de guide d'ondes Hedgehog proposée présente plusieurs avantages par rapport aux lignes de transmission conventionnelles décrites dans la littérature. Le principal avantage du guide d'ondes Hedgehog est qu'il peut supporter la propagation avec une perte moindre. De plus, du fait que les champs électromagnétiques sont capturés dans le guide d'onde, les pertes de rayonnement sont maintenues très faibles, ce qui confère une bonne immunité contre les perturbations électromagnétiques externes par rapport à la technologie du microruban. Un autre avantage principal du guide d'ondes Hedgehog est la compatibilité avec les guides d'ondes creux, ce qui offre un degré de liberté supplémentaire pour utiliser le guide d'ondes proposé pour plusieurs conceptions à ondes millimétriques.

Dans le cadre de ma thèse, différents composants mmWave ont été présentés et mis en œuvre dans le guide d'onde Hedgehog, notamment un déphaseur à faible perte et un réseau de formation de faisceaux à double polarisation. En tant que travail futur, le guide d'onde Hedgehog peut être utilisé pour concevoir des composants et des réseaux à haute efficacité mmWave.

De plus, la technique présentée pour réduire le couplage mutuel en utilisant des parois de rotateur de polarisation peut être utilisée dans des réseaux d'antennes afin de compenser la chute de gain due au désalignement du faisceau dans les éléments rayonnants environnants.

References

[1] S. Sur, V. Venkateswaran, X. Zhang, P. Ramanathan, “60 GHz Indoor Networking through Flexible Beams: A Link-Level Profiling,” SIGMETRICS’15, June 15–19, 2015, Portland, OR, USA.

[2] M. J. Al-Hasan, T.A. Denidni, A.R. Sebak, “Millimeter-Wave Compact EBG Structure for Mutual Coupling Reduction Applications,” IEEE Trans. Antennas Propag., vol.63, no.2, pp.823-828, Feb. 2015.

[3] J. R. Costa, E. B. Lima, C. R. Medeiros, and C. A. Fernandes, “Evaluation of a new wideband slot array for MIMO performance enhancement in indoor WLANs,” IEEE Trans. Antennas Propag., vol. 59, no. 4, pp. 1200–1206, Apr. 2011.

[4] H. M. Bernety, A. B. Yakovlev, “Reduction of Mutual Coupling Between Neighboring Strip Dipole Antennas Using Confocal Elliptical Metasurface Cloaks,” IEEE Trans. Antennas Propag., vol.63, no.4, pp.1554-1563, April 2015.

[5] L. Minz and R. Garg, “Reduction of mutual coupling between closely spaced PIFAs,” Electron. Lett., vol. 46, no. 6, pp. 392–394, 2010.

[6] G. R. Alvey, H. K. Pan and J. T. Bernhard, “Investigation into Techniques for Packaging Cosite Microstrip Patch Antennas into Handheld Devices,” in Antenna Technology Small Antennas and Novel Metamaterials, IEEE International Workshop on, pp.45-48, 2006.

[7] M. Ghaderi and N. C. Karmakar, “Frequency Selective Surface for reducing mutual coupling in antenna arrays,” Microwave Conference Proceedings (APMC), 2011 Asia-Pacific, Melbourne, VIC, 2011, pp. 1877-1880.

[8] C. Oikonomopoulos-Zachos, “Double layer compact four-port antenna using a symmetrical feeding technique for future MIMO antenna systems at 5.6GHz,” 2010 IEEE Antennas and Propagation Society International Symposium, Toronto, ON, 2010, pp. 1-4.

[9] H. Qi, L. Liu, X. Yin, H. Zhao and W. J. Kulesza, “Mutual Coupling Suppression Between Two Closely Spaced Microstrip Antennas With an Asymmetrical Coplanar Strip Wall,” IEEE Antennas Wireless Propag. Lett., vol. 15, no., pp. 191-194, 2016.

[10] A. Dadgarpour, B. Zarghooni, B. S. Virdee, T. A. Denidni, A. A. Kishk, “Mutual Coupling Reduction in Dielectric Resonator Antennas Using Metasurface Shield for 60 GHz MIMO Systems,” IEEE Antennas Wireless Propag. Lett., vol.PP, no.99, pp.1-1, 2016.

[11] R. Karimian, A. Kesavan, M. Nedil, T. A. Denidni, “Low Mutual Coupling 60-GHz MIMO Antenna System with Frequency Selective Surface Wall,” IEEE Antennas Wireless Propag. Lett., vol.PP, no.99, pp.1-1, 2016.

[12] S. Kumari M., S. A. Rao and N. Kumar, “Characterization of mmWave link for outdoor communications in 5G networks,” Advances in Computing, Communications and Informatics (ICACCI), 2015 International Conference on, Kochi, 2015, pp. 44-49.

[13] X. Liu and X. Wang, “Efficient Antenna Selection and User Scheduling in 5G Massive MIMO-NOMA System,” 2016 IEEE 83rd Vehicular Technology Conference (VTC Spring), Nanjing, 2016, pp. 1-5.

[14] X. Zou, F. Z. Geng, Y. Li and Y. Leng, “Phase Inverters Based on Substrate Integrated Waveguide,” IEEE Microw. Wireless Compon. Lett., vol. 27, no. 3, pp. 227-229, March 2017.

[15] S. Wang, D. Zhang, Y. Zhang, L. Qing and D. Zhou, “Novel Dual-Mode Bandpass Filters Based on SIW Resonators under Different Boundaries,” IEEE Microw. Wireless Compon. Lett., vol. 27, no. 1, pp. 28-30, Jan. 2017.

[16] J. K. E. Moldovan, R. G. Bosisio and Ke Wu, “W-band multiport substrate-integrated waveguide circuits,” IEEE Trans. Microw. Theory Tech., vol. 54, no. 2, pp. 625-632, Feb. 2006.

[17] G. Li, K. Song, F. Zhang and Y. Zhu, “Novel Four-Way Multilayer SIW Power Divider With Slot Coupling Structure,” IEEE Microw. Wireless Compon. Lett., vol. 25, no. 12, pp. 799-801, Dec. 2015.

[18] T. Djerafi, K. Wu and S. O. Tatu, “3 dB 90o Hybrid Quasi-Optical Coupler With Air Field Slab in SIW Technology,” IEEE Microw. Wireless Compon. Lett., vol. 24, no. 4, pp. 221-223, April 2014.

[19] A. A. M. Ali, H. B. El-Shaarawy and H. Aubert, “Compact wideband double-layer half-mode substrate integrated waveguide 90°deg coupler,” Electronics Letters, vol. 47, no. 10, pp. 598-599, May 12 2011.

[20] A. Polemi, S. Maci and P. S. Kildal, “Dispersion Characteristics of a Metamaterial-Based Parallel-Plate Ridge Gap Waveguide Realized by Bed of Nails,” IEEE Trans. Antennas Propag., vol. 59, no. 3, pp. 904-913, March 2011.

[21] H. Raza, J. Yang, P. S. Kildal and E. Alfonso Alós, “Microstrip-Ridge Gap Waveguide–Study of Losses, Bends, and Transition to WR-15,” IEEE Trans. Microw. Theory Tech., vol. 62, no. 9, pp. 1943-1952, Sept. 2014.

[22] A.U. Zaman, T. Vukusic, M. Alexanderson, P. S. Kildal, “Design of a Simple Transition From Microstrip to Ridge Gap Waveguide Suited for MMIC and Antenna Integration,” IEEE Antennas Wireless Propag. Lett., vol. 12, no. , pp. 1558-1561, 2013.

[23] M. Farahani, M. Nedil, and T. A. Denidni, “A novel hedgehog waveguide and its application in designing a phase shifter compatible with hollow waveguide technology,” IEEE Trans. Microw. Theory Techn., pp. 1–11, 2019.

[24] IEEE 802.11 Working Group, “IEEE 802.11ad, Amendment 3: Enhancements for Very High Throughput in the 60 GHz Band,” 2012.

[25] H. C. Zhang, Q. Zhang, J. F. Liu, W. Tang, Y. Fan, and T. J. Cui, "Smaller-loss planar SPP transmission line than conventional microstrip in microwave frequencies," Scientific Reports, vol. 6, pp. 1–10, Mar. 2016.

[26] L. Ye, Y. Xiao, Y. Liu, L. Zhang, G. Cai, and Q. H. Liu, "Strongly Confined Spoof Surface Plasmon Polaritons Waveguiding Enabled by Planar Staggered Plasmonic Waveguides," Scientific Reports, vol. 6, pp. 1–8, Dec. 2016.

[27] S. J. Berry, T. Campbell, A. P. Hibbins, and J. R. Sambles, "Surface wave resonances supported on a square array of square metallic pillars," Appl. Phys. Lett., pp. 1–8, Mar. 2012.

[28] G. Gallot, S. P. Jamison, R. W. McGowan, and D. Grischkowsky, "Terahertz waveguides," J. Opt. Soc. Am. B, vol. 17, no. 5, pp. 851–863, May 2000.

[29] Y. L. et al., "Adiabatic and Ultracompact Waveguide Tapers Based on Digital Metamaterials," IEEE J. Sel. Topics Quantum Electron., vol. 25, no. 3, pp. 1–6, May 2019.

[30] S. R, R. K. Gupta, N. DasGupta, and B. K. Das, "Ultra-Broadband Add-Drop Filter/Switch Circuit Using Subwavelength Grating Waveguides," IEEE J. Sel. Topics Quantum Electron., vol. 25, no. 3, pp. 1–11, May 2019.

[31] S. Zhou, G. Pan, C. Pan, and C. Davis, "On Modeling and Measurement of GCPW for Automotive Radar Applications," in Proceedings, EPEPS- 2018, San Jose, CA, Oct. 2018, pp. 221–223.

[32] A. Tamayo-Domnguez, J. Fernandez-Gonzalez, and M. Sierra-Prez, "Groove Gap Waveguide in 3-D Printed Technology for Low Loss, Weight, and Cost Distribution Networks," IEEE Trans. Microw. Theory Techn., vol. 65, no. 11, pp. 4138–4147, Nov. 2017.

[33] A. U. Zaman, T. Vukusic, M. Alexanderson, and P. Kildal, "Design of a Simple Transition From Microstrip to Ridge Gap Waveguide Suited for MMIC and Antenna Integration," IEEE Antennas Wireless Propag. Lett., vol. 12, pp. 1558–1561, 2013.

[34] M. Farahani, M. Akbari, M. Nedil, T. A. Denidni and A. R. Sebak, "A Novel Low-Loss Millimeter-Wave 3-dB 90° Ridge-Gap Coupler Using Large Aperture Progressive Phase Compensation," in IEEE Access, vol. 5, pp. 9610-9618, 2017.

[35] N. Esparza, P. Alcon, L. F. Herran, and F. Las-Heras, "Substrate Integrated Waveguides Structures Using Frequency Selective Surfaces Operating in Stop-Band (SBFSS-SIW)," IEEE Microw. Wireless Compon. Lett., vol. 26, no. 2, pp. 113–115, Feb. 2016.

[36] J. L. Cano, A. Mediavilla, and A. R. Perez, "Full-Band Air-Filled Waveguide-to-Substrate Integrated Waveguide (SIW) Direct Transition," IEEE Microw. Wireless Compon. Lett., vol. 25, no. 2, pp. 79–81, Feb. 2015.

[37] D. Hammou, T. Djerafi, M. Nedil, and S. O. Tatu, "Considerations for On-Wafer Millimeter-Wave Measurements on Thin Ceramic Substrate," IEEE Trans. Instrum. Meas., vol. 65, no. 2, pp. 441–447, Feb. 2016.

[38] X. Li and et al., “Microstrip angular log-periodic slow wave structure on quartz substrate with coaxial input/output coupler,” The J. of Eng., vol. 2018, no. 14, pp. 692–697, 2018.

[39] M. M. Nazarov and et al., “Eight-Capillary Cladding THz Waveguide With Low Propagation Losses and Dispersion,” IEEE Trans. THz Sci. Technol., vol. 8, no. 2, pp. 183–191, Mar. 2018.

[40] Y. Zhang, S. Shi, R. D. Martin, and D. W. Prather, “Broadband SIW-to- Waveguide Transition in Multilayer LCP Substrates at W-Band,” IEEE Microw. Wireless Compon. Lett., vol. 27, no. 3, pp. 224–226, Mar. 2017.

[41] E. F. Kuester, Theory of Waveguides and Transmission Lines. CRC Press 1 edition, 2018.

[42] M. Ebrahimpouri, E. Rajo-Iglesias, Z. Sipus, and O. Quevedo-Teruel, “Cost-Effective Gap Waveguide Technology Based on Glide-Symmetric Holey EBG Structures,” IEEE Trans. Microw. Theory Techn., vol. 66, no. 2, pp. 927–934, Feb. 2018.

[43] Z. G. Wang, Y. Q. Zhou, L. M. Yang, and C. Gong, “Waveguide-based terahertz metamaterial functional components,” J. Phys. D, Appl. Phys., vol. 50, no. 37, Aug. 2017.

[44] A. Torabi and A. A. Shishegar, “Combination of characteristic Green’s function technique and rational function fitting method for computation of modal reflectivity at the optical waveguide end-facet,” Int. Conf. Phot., Opt. and Laser Tech., Mar. 2015.

[45] M. Farahani, M. Akbari, M. Nedil and T. A. Denidni, "Mutual coupling reduction in dielectric resonator MIMO antenna arrays using metasurface orthogonalize wall," 2017 11th European Conference on Antennas and Propagation (EUCAP), Paris, 2017, pp. 985-987.

[46] M. Farahani, et al., "Mutual coupling reduction in millimeter-wave MIMO dielectric resonator antenna using metamaterial polarization rotator wall," IEEE Intern. Symp. on Antennas and Propag. & USNC/URSI National Radio Science Meeting, San Diego, CA, 2017.

[47] M. Farahani et al., "Mutual Coupling Reduction in Millimeter-Wave MIMO Antenna Array Using a Metamaterial Polarization-Rotator Wall," IEEE Antennas and Wireless Propag. Lett., vol. 16, pp. 2324-2327, 2017.

[48] M. Farahani, J. Zaid, J. Pourahmadazar, T. A. Denidni and M. Nedil, "Millimeter-wave couraggated surface for mutual coupling reduction between dipole antennas," Inter. Symp. on Antenna Tech. and Applied Electromag. (ANTEM), Montreal, QC, 2016, pp. 1-2.

[49] M. Akbari, M. M. Ali, M. Farahani, A. R. Sebak and T. Denidni, “Spatially mutual coupling reduction between CP-MIMO antennas using FSS superstrate,” Electronics Letters, vol. 53, no. 8, pp. 516-518, 4 13 2017.

[50] M. Akbari, H. Abo Ghalyon, M. Farahani, A. R. Sebak and T. A. Denidni, “Spatially Decoupling of CP Antennas Based on FSS for 30-GHz MIMO Systems,” IEEE Access, vol. 5, no. , pp. 6527-6537, 2017.

[51] J. Zhou, J. Chen, L. Qiu and H. Kikuchi, “Effects of antenna correlation and mutual coupling on the performance of MIMO system in a three-dimensional multipath channel,” Millimeter Waves (GSMM), 2012 5th Global Symposium on, Harbin, 2012, pp. 139-142.

[52] W. Fan, X. Carreño Bautista de Lisbona, F. Sun, J. Ø. Nielsen, M. B. Knudsen and G. F. Pedersen, "Emulating Spatial Characteristics of MIMO Channels for OTA Testing," in IEEE Transactions on Antennas and Prop., vol. 61, no. 8, pp. 4306-4314, Aug. 2013.

[53] R. Lech, M. Mazur and J. Mazur, "Analysis and Design of a Polarizer Rotator System," IEEE Trans. on Antennas and Propag., vol. 56, no. 3, pp. 844-847, March 2008.

[54] Z. Sipus, D. Bojanjac, M. Bosiljevac, “Constitutive Parameters of Metamaterial Structures Used for Invisible Cloak Realization” European Office of Aerospace Research and Development Unit 4515 Box 14, APO AE 09421.

[55] C. Huang, X. Ma, M. Pu, G. Yi, Y. Wang, X. Luo, “Dual-band 90° polarization rotator using twisted split ring resonators array” Optics Communications 291 (2013) 345–348.

[56] Q. Lai, C. Fumeaux, G. Almpanis, H. Benedickter, and R. Vahldieck, “Simulation and experimental investigation of the radiation efficiency of a dielectric resonator antenna,” presented at the Proc. IEEE Int Symp/ Antennas Propag., Jul. 5–11, 2008.

[57] P. S. Kildal, Foundations of Antenna Engineering: A Unified Approach for Line-of-Sight and Multipath, Kildal Antenn AB, 2015 (www.kildal.se).

[58] M. M. Bait-Suwailam, M. S. Boybay and O. M. Ramahi, "Electromagnetic Coupling Reduction in High-Profile Monopole Antennas Using Single-Negative Magnetic Metamaterials for MIMO Applications," *IEEE Trans. Antennas and Propag.*, vol. 58, no. 9, pp. 2894-2902, Sep. 2010.

[59] M. Akbari, S. Gupta, M. Farahani, A. R. Sebak and T. A. Denidni, "Gain Enhancement of Circularly Polarized Dielectric Resonator Antenna Based on FSS Superstrate for MMW Applications," IEEE Trans. Antennas Propag., vol. 64, no. 12, pp. 5542-5546, Dec. 2016.

[60] Akbari, M., Gupta, S., Farahani, M., et al.: ‘Analytic study on CP enhancement of millimeter wave DR and patch subarray antennas’, Int. J. RF Microw. Comput.-Aided Eng., 2017, 27, (1), pp. 1–11.

[61] D. Singh, A. Kumar, S. Meena, and V. Agarwala, ‘‘Analysis of frequencyselective surfaces for radar absorbing materials,’’Prog. Electromagn.Res. B, vol. 38, pp. 297–314, Feb. 2012.

[62] H. Lipfert, "MIMO OFDM (space time coding-spatial multiplexing increasing performance and spectral efficiency in wireless systems)," Insti-tut Fur Rundfunktechnik, Munich, Germany, Tech. Rep., Aug. 2007.

[63] E. Saenz, I. Ederra, R. Gonzalo, S. Pivnenko, O. Breinbjerg, andP. D. Maagt, "Coupling reduction between dipole antenna elements byusing a planar meta-surface," IEEE Trans. Antennas Propag., vol. 57, no. 2,pp. 383–394, Feb. 2009.

[64] M. Farahani, J. Pourahmadazar, T. Denidni and M. Nedil, "Millimeter-Wave High-Gain Ridge Gap Beam Steerable Antenna for 5G wireless Networks," Intern. Symp. on Antenna Tech. and Applied Electromag. (ANTEM), Waterloo, ON, 2018, pp. 1-2.

[65] F. Giannetti, M. Luise and R. Reggiannini, “Mobile and personal communications in 60 GHz band: A survey, Wireless Personal Communications”, vol. 10, pp. 207-243, 1999.

[66] Daniels, R.C., Heath, R.W., “60 GHz Wireless Communications: Emerging Requirements and Design Recommendations,” Vehicular Technology Magazine, IEEE, volume: 2, issue: 3, pp 41-50, 2008.

[67] A. Ip and D. R. Jackson, “Radiation from cylindrical leaky waves,” IEEE Trans. Antennas Propag., vol. 38, no. 4, pp. 482-488, 1990.

[68] Y. J. Lee, J. Yeo, and R. Mittra, “Design of a high-directivity electromagnetic bandgap (EBG) resonator antenna using a frequency-selective surface (FSS) superstrate,” Microw. Opt. Technol. Lett., vol. 43, pp. 462–467, 2004.

[69] A. P. Feresidis and J. C. Vardaxoglou, “High gain planar antenna using optimised partially reflective surfaces,” Proc. Inst. Elect. Eng. Microw. Antennas Propag., vol. 148, pp. 345–350, 2001.

[70] Z. G. Liu, “Fabry-Perot Resonator Antenna,” Journal of infrared millimetre and terahertz waves, vol. 31, pp. 391-403, 2010.

[71] T. X. Zhao, D. R. Jackson, J. T. Williams, and A. A. Oliner, “General formulas for 2-D leaky wave antennas,” IEEE Trans. Antennas Propag., vol. 53, , no. 11, pp. 3525-3533, 2005.

[72] T. Zhao, D. R. Jackson, J. T. Williams, H. Y. D. Yang, and A. A. Oliner, “2-D periodic leaky wave antennas-part I: metal patch design,” IEEE Trans. Antennas Propag., vol. 53, no. 11, pp. 3505- 3514, 2005.

[73] T. Zhao, D. R. Jackson, and J. T. Williams, “2-D periodic leaky-wave antennas-part II: slot design,” IEEE Trans. Antennas Propag., vol. 53, no.11 , pp. 3515-3524, 2005.

[74] D. R. Jackson and N. G. Alexopoulos, “Gain enhancement methods for printed circuit antennas,” IEEE Trans. Antennas Propag., vol. 33, pp. 976-987, 1985.

[75] D. R. Jackson, A. A. Oliner, and A. Ip, “Leaky-wave propagation and radiation for a narrow beam multiple-layer structure,” IEEE Trans. Antennas Propag., vol. 41, no. 3, pp. 344-348, 1993.

[76] R. Gardelli, M. Albani, and F. Capolino, “Array thinning by using antennas in a Fabry-Perot cavity for gain enhancement,” IEEE Trans. Antennas Propag., vol. 54, no. 7, pp. 1979-1990, 2006.

[77] R. K. Mongia and A. Ittipiboon, “Theoretical and experimental investigations on rectangular dielectric resonator antennas,” IEEE Trans. Antennas Propagat., vol. 45, no. 9, pp. 1348-1356, 1997.

[78] K.M. luk and k.w. Leung, “Dielectric resonator antennas,” Research Studies Press Ltd. Baldock, Hertfordshire, England, 2003.

[79] D. M. Pozar, Microwave Engineering, Fourth Edition, Wiley, 2012.

[80] A. Foroozesh and L. Shafai, "Investigation Into the Effects of the Patch-Type FSS Superstrate on the High-Gain Cavity Resonance Antenna Design," IEEE Trans. Antennas and Propag., vol. 58, no. 2, pp. 258-270, Feb. 2010.

[81] G. Lovat, P. Burghignoli, F. Capolino, and D. R. Jackson, “Highly-directive planar leaky-wave antennas: a comparison between metamaterial-based and conventional designs,” in Proc. Europ. Microw. Assoc., pp. 12-21, 2006.

[82] B. Han, X. Yang and H. Xue, "A millimeter-wave fabry-perot antenna with high-gain and circular polarization operation," Proceedings of 2014 3rd Asia-Pacific Conference on Antennas and Propagation, Harbin,pp. 40-43, 2014.

[83] A. A. Oliner, “Leaky-wave antennas,” in Antenna Engineering Handbook, R. C.Johnson, Ed., ed New York: McGraw Hill, 1993.

[84] D. Jie, J. Wang, H. Zhang and G. Wang, "Channel Capacity of 60 GHz Wireless Communication Systems over Indoor Line-of-Sight and Non-Line-of-Sight Channels," Int. Conf. on Wireless Com. Net. and Mobile Comp. Sept 2010, pp. 1–4.

[85] A. Dadgarpour et al., "Passive Beam Switching and Dual-Beam Radiation Slot Antenna Loaded With ENZ Medium and Excited Through Ridge Gap Waveguide at Millimeter-Waves," IEEE Trans. Antennas and Propag, vol. 65, no. 1, pp. 92-102, Jan. 2017.

[86] M. Mantash, A. Kesavan and T. A. Denidni, "Beam-Tilting Endfire Antenna Using a Single-Layer FSS for 5G Communication Networks," in IEEE Antennas and Wireless Propagation Letters, vol. 17, no. 1, pp. 29-33, Jan. 2018.

[87] I. Kim and Y. Rahmat-Samii, "Electromagnetic band gap-dipole sub-array antennas creating an enhanced tilted beams for future base station," in IET Microwaves, Antennas & Propagation, vol. 9, no. 4, pp. 319-327, 19 3 2015.

[88] A. Dadgarpour, B. Zarghooni, B. S. Virdee and T. A. Denidni, "Enhancement of Tilted Beam in Elevation Plane for Planar End-Fire Antennas Using Artificial Dielectric Medium," IEEE Trans. Antennas Propag., vol. 63, no. 10, pp. 4540-4545, Oct. 2015.

[89] M. Farahani, T. A. Denidni and M. Nedil, “Design of a Low Output-Phase Error Ridge-Gap Coupler for Antenna Arrays Applications,” IEEE Inter. Symposium on Antennas and Propag. & USNC/URSI National Radio Science Meeting, Boston, MA, 2018. pp. 1099-1100.

[90] R. Mendis and D. M. Mittleman, “An investigation of the lowest-order transverse-electric (TE1) mode of the parallel-plate waveguide for THz pulse propagation,” J. Opt. Soc. Am. B, vol. 26, no. 9, pp. A6–A13, Sep. 2009.

[91] Radio-Spectrum-Allocation. Federal communications commission (fcc). [Online]. Available: https://www.fcc.gov/.

[92] Z. Zhang and K. Wu, “A Broadband Substrate Integrated Waveguide (SIW) Planar Balun,” IEEE Microw. Wireless Compon. Lett., vol. 17, no. 12, pp. 843–845, Dec. 2007.

[93] E. D. Caballero, H. Esteban, A. Belenguer, and V. Boria, “Efficient Analysis of Substrate Integrated Waveguide Devices Using Hybrid Mode Matching Between Cylindrical and Guided Modes,” IEEE Trans. Microw. Theory Techn., vol. 60, pp. 232–243, Feb. 2012.

[94] P. Kildal, “Three metamaterial-based gap waveguides between parallel metal plates for mm/submm waves,” in Eur. Conf. Antennas and Propag., Mar. 2009, pp. 28–32.

[95] P. Kildal, A. U. Zaman, E. Rajo-Iglesias, E. Alfonso, and A. Valero-Nogueira, “Design and experimental verification of ridge gap waveguide in bed of nails for parallel-plate mode suppression,” IET Microw., Antennas Propag., vol.5, pp. 262–270, Feb. 2011.

[96] D. Deslandes and K. Wu, “Design Consideration and Performance Analysis of Substrate Integrated Waveguide Components,” in Eur. Microw. Conf., Sep. 2002, pp. 1–4.

[97] A. A. Brazlez et al., “Design and Validation of Microstrip Gap Waveguides and Their Transitions to Rectangular Waveguide, for Millimeter-Wave Applications,” IEEE Trans. Microw. Theory Techn., vol. 63, no. 12, pp. 4035–4050, Dec. 2015.

[98] A. U. Zaman, M. Alexanderson, T. Vukusic, and P. Kildal, “Gap Waveguide PMC Packaging for Improved Isolation of Circuit Components in High-Frequency Microwave Modules,” IEEE Trans. Compon., Packag. and Manuf. Technol., vol. 4, no. 1, pp. 16–25, Jan. 2014.

[99] F. Fan, J. Yang, and P. Kildal, “Half-height pins - a new pin form in gap waveguide for easy manufacturing,” in Eur. Conf. Antennas and Propag. (EuCAP), Apr. 2016, pp. 1–4.

[100] R. Levy, ‘‘Improved single and multiaperature waveguide coupling theory, including explanation of mutual interactions,’’ IEEE Trans. Microw. Theory Techn., vol. 28, no. 4, pp. 331–338, Apr. 1980.

[101] B. Liu, W. Hong, Y. Zhang, J. x. Chen and K. Wu, “Half-mode substrate integrated waveguide (HMSIW) double-slot coupler,” Electronics Letters, vol. 43, no. 2, pp. 113-114, January 18 2007.

[102] A. Ali, H. Aubert, N. Fonseca and F. Coccetti, “Wideband two-layer SIW coupler: design and experiment,” Electronics Letters, vol. 45, no. 13, pp. 687-689, June 18 2009.

[103] H. Schmiedel, “Series-configuration of multi-line directional-coupler sections with improved coupling,” Microwave Symposium Digest, 2004 IEEE MTT-S International, 2004, pp. 339-342 Vol.1.

[104] S. B. Cohn, “Microwave Coupling by Large Apertures,” in Proceedings of the IRE, vol. 40, no. 6, pp. 696-699, June 1952.

[105] O. Mitrofanov, R. James, F. A. Fernandez, T. K. Mavrogordatos, and J. A. Harrington, “Reducing Transmission Losses in Hollow THz Waveguides,” IEEE Trans. THz Sci. Technol., vol. 1, no. 1, pp. 124–132, Sep. 2011.

[106] G. L. Matthaei and et al., Microwave Filters, Impedance-Matching Networks, and Coupling Structures. McGraw-Hill, 1985.

[107] Y. H. Cho and H. J. Eom, “Analysis of a ridge waveguide using overlapping T-blocks,” IEEE Trans. Microw. Theory Techn., vol. 50, no. 10, pp. 2368–2373, Oct. 2002.

[108] A. Wexler, “Solution of Waveguide Discontinuities by Modal Analysis,” IEEE Trans. Microw. Theory Techn., vol. 15, no. 9, pp. 508–517, Sep. 1967.

[109] H. Patzelt and F. Arndt, “Double-Plane Steps in Rectangular Waveguides and Their Application for Transformers, Irises, and Filters,” IEEE Trans. Microw. Theory Techn., vol. 30, no. 5, pp. 771–776, May. 1982.

[110] R. E. Collin, Field Theory of Guided Wave. New York: McGraw-Hill, 1960.

[111] L. D. Landau, L. P. Pitaevskii, and E. Lifshitz, Electrodynamics of Continuous Media. Pergamon, Oxford, 1984.

[112] S. Marini, M. Mattes, B. Gimeno, and V. E. Boria, “Improved Computation of Propagation Losses in Waveguide Structures Using Perturbation of Boundary Conditions,” IEEE Microw. Wireless Compon. Lett., vol. 21, no. 11, pp. 577–579, Nov. 2011.

[113] S. Marini, M. Mattes, B. Gimeno, P. Soto, and V. E. Boria, “Advanced analysis of propagation losses in rectangular waveguide structures using perturbation of boundary conditions,” in IEEE MTT-S Int. Microw. Work. Ser. on mmW Integ. Tech., Sep. 2011.

[114] A. D. MacDonald, D. U. Gaskell, and H. N. Gitterman, “Microwave Breakdown in Air, Oxygen, and Nitrogen,” Phys. Rev., vol. 130, pp. 1841–1850, Jun. 1963.

[115] I. Medina and P. A. Calva, Emerging Waveguide Technology. Open access peer-reviewed chapter, intechopen., 2018.

[116] H. E. King, “Rectangular Waveguide Theoretical CW Average Power Rating,” IRE IEEE Trans. Microw. Theory Techn., vol. 9, no. 4, pp. 349–357, Jul. 1961.

[117] J. Lee and S. Kim, “60 GHz switched-line-type phase shifter using body floating switches in 0.13 m CMOS technology,” Electronics Letters, vol. 48, no. 7, pp. 376–378, March 2012.

[118] C. Lin, S. Chang, C. Chang, and Y. Shu, “Design of a Reflection-Type Phase Shifter With Wide Relative Phase Shift and Constant Insertion Loss,” IEEE Trans. Microw. Theory Techn., vol. 55, no. 9, pp. 1862–1868, Sep. 2007.

[119] A. Benleulmi, N. Y. Sama, P. Ferrari, and F. Domingue, “Substrate Integrated Waveguide Phase Shifter for Hydrogen Sensing,” IEEE Microw. Wireless Compon. Lett., vol. 26, no. 9, pp. 744–746, Sep. 2016.

[120] K. Han, H. Cui, X. Sun, and J. Zhang, “The design of a 60 GHz low loss hybrid phase shifter with 360 degree phase shift,” in Int. Symp. on Commun. and Inf. Technol. (ISCIT), Sep. 2014, pp. 551–554.

[121] R. D. Paolis, F. Coccetti, S. Payan, M. Maglione, and G. Guegan, “Characterization of ferroelectric BST MIM capacitors up to 65 GHz for a compact phase shifter at 60 GHz,” in Eur. Microw. Conf., Oct. 2014, pp. 492–495.

[122] H.-T. Kim and et al., “V-band 2-b and 4-b low-loss and low-voltage distributed MEMS digital phase shifter using metal-air-metal capacitors,” IEEE Trans. Microw. Theory Techn., vol. 50, no. 12, pp. 2918–2923, Dec. 2002.

[123] M. Jost and et al., “Miniaturized Liquid Crystal Slow Wave Phase Shifter Based on Nanowire Filled Membranes,” IEEE Microw. Wireless Compon. Lett., vol. 28, no. 8, pp. 681–683, Aug. 2018.

[124] Q. Yang, Y. Ban, K. Kang, C. Sim, and G. Wu, “SIW Multibeam Array for 5G Mobile Devices,” IEEE Access, vol. 4, pp. 2788–2796, 2016.

[125] S. Karamzadeh, V. Rafii, M. Kartal, and B. S. Virdee, “Compact and Broadband 4×4 SIW Butler Matrix With Phase and Magnitude Error Reduction,” IEEE Microw. Wireless Compon. Lett., vol. 25, no. 12, pp. 772–774, Dec 2015.

[126] Y. Li and K. Luk, “A Multibeam End-Fire Magnetoelectric Dipole Antenna Array for Millimeter-Wave Applications,” IEEE Trans. Antennas Propag., vol. 64, no. 7, pp. 2894–2904, July 2016.

[127] Q. Yang, Y. Ban, J. Lian, Z. Yu, and B. Wu, “SIW Butler Matrix with Modified Hybrid Coupler for Slot Antenna Array,” IEEE Access, vol. 4, pp. 9561–9569, 2016.

[128] D. Kim, J. Hirokawa, and M. Ando, “Design of Waveguide Short-Slot Two-Plane Couplers for One-Body 2-D Beam-Switching Butler Matrix Application,” IEEE Trans. Microw. Theory Techn., vol. 64, no. 3, pp. 776–784, March 2016.

[129] M. Jost, R. Reese, H. Maune, and R. Jakoby, “In-plane hollow waveguide crossover based on dielectric insets for millimeter-wave applications,” in 2017 IEEE MTT-S International Microwave Symposium (IMS), June 2017, pp. 188–191.

[130] X. Cheng, Y. Yao, T. Tomura, J. Hirokawa, T. Yu, J. Yu, and X. Chen, “A Compact Multi-Beam End-Fire Circularly Polarized Septum Antenna Array for Millimeter-Wave Applications,” IEEE Access, vol. 6, pp. 62 784–62 792, 2018.

[131] S. Gao, Q. Luo, and F. Zhu, Circularly polarized antennas. John Wiley & Sons, 2014.

[132] B. Kim, B. Pan, S. Nikolaou, Y. Kim, J. Papapolymerou, and M. M. Tentzeris, “A novel single-feed circular microstrip antenna with reconfigurable polarization capability,” IEEE Trans. Antennas Propag., vol. 56, no. 3, pp. 630–638, March 2008.

[133] H. Ren, B. Arigong, M. Zhou, J. Ding, and H. Zhang, “A Novel Design of 4×4Butler Matrix With Relatively Flexible Phase Differences,” IEEE Antennas Wireless Propag. Lett., vol. 15, pp. 1277–1280, 2016.

[134] C. A. Balanis, Modern Antenna Handbook. John Wiley & Sons, 2008.

[135] L. Zhong, Y. Ban, J. Lian, Q. Yang, J. Guo, and Z. Yu, “Miniaturized SIW Multibeam Antenna Array Fed by Dual-Layer 8 8 Butler Matrix,” IEEE Antennas Wireless Propag. Lett., vol. 16, pp. 3018–3021, 2017.

[136] J. Lian, Y. Ban, C. Xiao, and Z. Yu, “Compact Substrate-Integrated 4×8 Butler Matrix With Sidelobe Suppression for Millimeter-Wave Multibeam Application,” IEEE Antennas Wireless Propag. Lett., vol. 17, no. 5, pp. 928–932, May 2018.

[137] J. Lian, Y. Ban, Q. Yang, B. Fu, Z. Yu, and L. Sun, “Planar MillimeterWave 2-D Beam-Scanning Multibeam Array Antenna Fed by Compact SIW Beam-Forming Network,” IEEE Trans. Antennas Propag., vol. 66, no. 3, pp. 1299–1310, March 2018.

[138] K. Tekkouk, J. Hirokawa, R. Sauleau, M. Ettorre, M. Sano, and M. Ando, “Dual-Layer Ridged Waveguide Slot Array Fed by a Butler Matrix With Sidelobe Control in the 60-GHz Band,” IEEE Trans. Antennas Propag., vol. 63, no. 9, pp. 3857–3867, Sep. 2015.

[139] J. Shelton, “Reduced sidelobes for Butler-matrix-fed linear arrays,” IEEE Trans. Antennas Propag., vol. 17, no. 5, pp. 645–647, Sep. 1969.

[140] J. P. Shelton, “Multibeam planar arrays,” Proceedings of the IEEE, vol. 56, no. 11, pp. 1818–1821, Nov 1968.

[141] V. S. Gangwar, A. K. Singh, and S. P. Singh, “An Effective Approach for the Synthesis of Unequally Spaced Antenna Array by Estimating Optimum Elements Density on the Aperture,” IEEE Antennas Wireless Propag. Lett., vol. 16, pp. 2278–2282, 2017.

[142] Y. Jiang, K. Li, J. Gao, and H. Harada, “Antenna space diversity and polarization mismatch in wideband 60GHz-Millimeter-wave wireless system,” IEEE 20th Int. Symposium on Personal, Indoor and Mobile Radio Communications, Sep. 2009, pp. 1781–1785.

[143] Hao Xu, V. Kukshya and T. S. Rappaport, "Spatial and temporal characteristics of 60-GHz indoor channels," in IEEE Journal on Selected Areas in Communications, vol. 20, no. 3, pp. 620-630, April 2002.

[144] T. Manabe, Y. Miura, and T. Ihara, “Effects of antenna directivity and polarization on indoor multipath propagation characteristics at 60 GHz,” IEEE Journal on Selected Areas in Communications, vol. 14, no. 3, pp. 441–448, April 1996.

[145] T. Manabe, et al., “Polarization dependence of multipath propagation and highspeed transmission characteristics of indoor millimeter-wave channel at 60 GHz,” IEEE Trans. Vehicular Tech., vol. 44, no. 2, pp. 268–274, May 1995.

[146] P. J. Gibson, “The Vivaldi Aerial,” in 1979 9th European Microwave Conference, Sep. 1979, pp. 101–105.

[147] B. Stockbroeckx and A. Vander Vorst, “Electromagnetic modes in conical transmission lines with application to the linearly tapered slot antenna,” IEEE Trans. Antennas Propag., vol. 48, no. 3, pp. 447–455, March 2000.

[148] B. Stockbroeckx and A. Vander Vorst, "Copolar and cross-polar radiation of Vivaldi antenna on dielectric substrate," in IEEE Transactions on Antennas and Propagation, vol. 48, no. 1, pp. 19-25, Jan. 2000.

[149] S. Sugawara, Y. Maita, K. Adachi, K. Mori, and K. Mizuno, “A mmwave tapered slot antenna with improved radiation pattern,” in 1997 IEEE MTT-S International Microwave Symposium Digest, vol. 2, June 1997, pp. 959–962 vol.2.

[150] A. M. De Oliveira, M. B. Perotoni, S. T. Kofuji, and J. F. Justo, “A Palm Tree Antipodal Vivaldi Antenna With Exponential Slot Edge for Improved Radiation Pattern,” IEEE Antennas Wireless Propag. Lett., vol. 14, pp. 1334–1337, 2015.

[151] L. Chen, Z. Lei, R. Yang, J. Fan, and X. Shi, “A Broadband Artificial Material for Gain Enhancement of Antipodal Tapered Slot Antenna,” IEEE Trans. Antennas Propag., vol. 63, no. 1, pp. 395–400, Jan 2015.

[152] G. K. Pandey, H. Verma, and M. K. Meshram, “Compact antipodal Vivaldi antenna for UWB applications,” Electronics Letters, vol. 51, no. 4, pp. 308–310, 2015.

[153] X. Cheng, Y. Yao, T. Yu, Z. Chen, J. Yu, and X. Chen, “Analysis and Design of a Low-Cost Circularly Polarized Horn Antenna,” IEEE Trans. Antennas Propag., vol. 66, no. 12, pp. 7363–7367, Dec 2018.

[154] X. Cheng, Y. Yao, Z. Chen, J. Yu, and X. Chen, “Compact Wideband Circularly Polarized Antipodal Curvedly Tapered Slot Antenna,” IEEE Antennas Wireless Propag. Lett., vol. 17, no. 4, pp. 666–669, April 2018.

[155] X. Cheng, Y. Yao, J. Hirokawa, T. Tomura, T. Yu, J. Yu, and X. Chen, “Analysis and Design of a Wideband Endfire Circularly Polarized Septum Antenna,” IEEE Trans. Antennas Propag., vol. 66, no. 11, pp. 5783–5793, Nov 2018.

[156] X. Cheng, Y. Yao, J. Yu, and X. Chen, “Circularly Polarized SubstrateIntegrated Waveguide Tapered Slot Antenna for Millimeter-Wave Applications,” IEEE Antennas Wireless Propag. Lett., vol. 16, pp. 2358–2361, 2017.

[157] Y. Yao, X. Cheng, J. Yu, and X. Chen, “Analysis and Design of a Novel Circularly Polarized Antipodal Linearly Tapered Slot Antenna,” IEEE Trans. Antennas Propag., vol. 64, no. 10, pp. 4178–4187, Oct 2016.

[158] Y. Yao, X. Cheng, C. Wang, J. Yu, and X. Chen, “Wideband Circularly Polarized Antipodal Curvedly Tapered Slot Antenna Array for 5G Applications,” IEEE Journal on Selected Areas in Communications, vol. 35, no. 7, pp. 1539–1549, July 2017.

[159] M. Farahani, M. Akbari, M. Nedil, A. R. Sebak, and T. A. Denidni, “Miniaturised circularly-polarised antenna with high-constitutive parameter substrate,” Electronics Letters, vol. 53, no. 20, pp. 1343–1344, 2017.

[160] Y. Zhang, Q. Wang, and H. Xin, “A Compact 3 dB E-Plane Waveguide Directional Coupler With Full Bandwidth,” IEEE Microw. Wireless Compon. Lett., vol. 24, no. 4, pp. 227–229, April 2014.

[161] L. T. Hildebrand, “Results for a simple compact narrow-wall directional coupler,” IEEE Microwave and Guided Wave Letters, vol. 10, no. 6, pp. 231–232, June 2000.

[162] X. Deng, Z. Wang, K. Xu, and B. Yan, “Compact full Ka-band waveguide directional coupler based on large aperture array,” Electronics Letters, vol. 52, no. 11, pp. 936–937, 2016.

[163] S. Yamamoto, et al., “Length reduction of a shortslot directional coupler in a single-layer dielectric substrate waveguide by removing dielectric near the side walls of the coupler,” IEEE Antennas and Propag. Society Symp., vol. 3, Monterey, CA,June 2004.

[164] F. F. Manzillo, et all, “An ltcc beam-switching antenna with high beam overlap for 60-ghz mobile access points,” IEEE Inter. Symp. on Antennas and Propag. USNC/URSI National Radio Science Meeting, July 2017, pp. 1441–1442.

[165] D. Liu, B. Gaucher, U. Pfeiffer, and J. Grzyb, Advanced MillimeterWave Technologies: Antennas, Packaging and Circuits. John Wiley & Sons, 2009.

[166] M. M. M. Ali and A. Sebak, “2-D Scanning Magnetoelectric Dipole Antenna Array Fed by RGW Butler Matrix,” IEEE Trans. Antennas Propag., vol. 66, no. 11, pp. 6313-6321, Nov. 2018.

[167] T. Djerafi and K. Wu, “A Low-Cost Wideband 77-GHz Planar Butler Matrix in SIW Technology,” IEEE Trans. Antennas Propag., vol. 60, no. 10, pp. 4949-4954, Oct. 2012.

[168] P. Baniya and K. L. Melde, “Switched-Beam Endfire Planar Array With Integrated 2-D Butler Matrix for 60 GHz Chip-to-Chip Space-Surface Wave Communications, ” IEEE Antennas and Wireless Propag. Lett., vol. 18, no. 2, pp. 236-240, Feb. 2019.

[169] D. S. Filipovic, M. V. Lukic, Y. Lee and D. L. Fontaine, “Monolithic Rectangular Coaxial Lines and Resonators With Embedded Dielectric Support,” IEEE Microwave and Wireless Compon. Lett., vol. 18, no. 11, pp. 740-742, Nov. 2008.

[170] E. Brown, A. Cohn, C. Bang, M. Lockard, B. Byrne, N. Vandlli, D. McPherson, and G. Zhang, “Characteristics of microfabricated rectangular coax in Ka band,” Microw. Opt. Technol. Lett., vol. 40, no. 5, pp. 365–368, Mar. 2004.

[171] J.-B. Yoon, B.-I. Kim, Y.-S. Choi, and E. Yoon, “3-D construction of monolithic passive components for RF and microwave ICs using thick-metal surface micromachining technology,” IEEE Trans. Microw. Theory Tech., vol. 51, no. 1, pp. 279–288, Jan. 2003.

[172] J. R. Reid, E. D. Marsh, and R. T. Webster, “Micromachined rectangular coaxial transmission lines,” IEEE Trans. Microw. Theory Tech., vol. 54, no. 8, pp. 3433–3442, Aug. 2006.

[173] P. Baniya, A. Bisognin, K. L. Melde and C. Luxey, "Chip-to-Chip Switched Beam 60 GHz Circular Patch Planar Antenna Array and Pattern Considerations," IEEE Trans. Antennas Propag., vol. 66, no. 4, pp. 1776-1787, Apr. 2018.

[174] A. B. Guntupalli, T. Djerafi, and K. Wu, “Two-dimensional scanning antenna array driven by integrated waveguide phase shifter,” IEEE Trans. Antennas Propag., vol. 62, no. 3, pp. 1117–1124, Mar. 2014.

[175] T. -. Chen, "Determination of the Capacitance, Inductance, and Characteristic Impedance of Rectangular Lines," in IRE Trans. on Microwave Theory and Techniques, vol. 8, no. 5, pp. 510-519, September 1960.

[176] “ANSYS HFSS,” ANSYS, Inc., 2018, [Online]. Available: www.ansys.com/products/electronics/ansys-hfss.

[177] T. Edwards, Foundations for Microstrip Circuit Design, 2nd ed. New York: Wiley, 1992.

[178] A. Lalbakhsh, M. Afzal, K. P. Esselle, and S. Smith “Wideband NearField Correction of a Fabry-Perot Resonator Antenna,” IEEE Trans. Antennas Propag., vol. 67, no. 3, pp. 1975–1980, March. 2019.

[179] A. Lalbakhsh, et al. “Single dielectric Wideband Partially Reflecting Surface with Variable Reflection Components for Realization of a Compact High-gain Resonant Cavity Antenna,” IEEE Trans. Antennas Propag., vol. 67,no. 3, pp. 1916–1921, March. 2019.

[180] W. Yang, Y. Yang, W. Che, C. Fan and Q. Xue, “94-GHz Compact 2-D Multibeam LTCC Antenna Based on Multifolded SIW Beam-Forming Network,” IEEE Trans. Antennas Propag., vol. 65, no. 8, pp. 4328-4333, Aug. 2017.

[181] J.-W. Lian, Y.-L. Ban, Q.-L. Yang, B. Fu, Z.-F. Yu, and L.-K. Sun, “Planar millimeter-wave 2-D beam-scanning multibeam array antenna fed by compact SIW beam-forming network,” IEEE Trans. Antennas Propag., vol. 66, no. 3, pp. 1299–1310, Mar. 2018.

[182] Y. J. Cheng, W. Hong, and K. Wu, “Millimeter-wave multibeam antenna based on eight-port hybrid,” IEEE Microw. Wireless Compon. Lett., vol. 19, no. 4, pp. 212–214, Apr. 2009.

[183] Y. J. Cheng, X. Y. Bao, and Y. X. Guo, “60-GHz LTCC miniaturized substrate integrated multibeam array antenna with multiple polarizations,” IEEE Trans. Antennas Propag., vol. 61, no. 12, pp. 5958–5967, Dec. 2013.

[184] Athanasiou, G., Weeraddana, P.C.;; Fischione, C. ; Orten, P., “Communication Infrastructures in Industrial Automation: The Case of 60 GHz Millimeter Wave Communications”, Emerging Tech. & Factory Auto. (ETFA), IEEE 18th Conf. on, pp. 1-6, 2013.

[185] J. Wallace and M. Jensen, “Mutual coupling in MIMO wireless systems a rigorous network theory analysis,” IEEE Trans. Wireless Commun., vol. 3, no. 4, pp. 1317–1325, Jul. 2004.

[186] P. Kildal and M. N. M. Kehn, “The ridge gap waveguide as a wideband rectangular hard waveguide,” in Eur. Conf. Antennas and Propag., Apr. 2010, pp. 1–4.

[187] S. Zarbakhsh, M. Akbari, M. Farahani, A. Ghayekhloo, T. A. Denidni and A. Sebak, "Optically Transparent Sub-Array Antenna Based on Solar panel for CubeSat Application," IEEE Trans. Antennas Propag., 2019. doi: 10.1109/TAP.2019.2938740.

[188] J. Zaid, M. Farahani and T. A. Denidni, “Magneto-dielectric substrate-based microstrip antenna for RFID applications,” IET Microwaves, Antennas & Propagation, vol. 11, no. 10, pp. 1389-1392, 16 8 2017.

[189] Jamal Zaid, M. Farahani, Tayeb A. Denidni, “A compact circularly-polarized GPS antenna using LTCC technology,” Microwave and Optical Technology Letters, Vol. 58, No. 12, December 2016.

[190] R. Karimian, H. Oraizi, S. Fakhte and M. Farahani, “Novel F-Shaped Quad-Band Printed Slot Antenna for WLAN and WiMAX MIMO Systems,” IEEE Antennas and Wireless Propagation Letters, vol. 12, pp. 405-408, 2013.

[191] J. Pourahmadazar, M. Farahani and T. A. Denidni, “Printed Gap Waveguide Rotman Lens for Millimetre-wave Applications,” International Symposium on Antenna Technology and Applied Electromagnetics (ANTEM), Waterloo, ON, 2018, pp. 1-2.

[192] M. Akbari, et al., “A sequential-phase feed antenna subarray based on ridge gap waveguide,” IEEE Intern. Symp. on Antennas and Propag. & USNC/URSI National Radio Science Meeting, San Diego, CA, 2017, pp. 2125-2126.

[193] J. Zaid, et al., “Miniaturized microstrip patch antenna using Electromagnetic Band Gap (EBG) structures for multiport passive UHF RFID-tag applications,” IEEE Intern. Symp. on Antennas and Propag. USNC/URSI National Radio Science Meeting, San Diego, 2017.

[194] M. Akbari, M. Farahani, A. R. Sebak and T. A. Denidni, “A 30GHz high-gain circularly-polarized pattemsteerable antenna based on parasitic patches,” European Conference on Antennas and Propagation (EUCAP), Paris, 2017, pp. 3044-3046.

[195] M. Farahani, J. Zaid, T. A. Denidni and M. Nedil, “Miniaturized two dimensional circular polarized magnetodielectric substrate antenna,” IEEE International Symposium on Antennas and Propagation (APSURSI), Fajardo, 2016, pp. 1103-1104.

[196] J. Zaid, M. Farahani and T. A. Denidni, “A CP-GPS antenna using low temperature cofired ceramic technology,” IEEE International Symposium on Antennas and Propagation (APSURSI), Fajardo, 2016, pp. 121-122.

[197] J. Zaid, M. Farahani and T. A. Denidni, “Miniatunrized microstrip patch antenna using electromagnetic bandgap (EBG) for GPS applications,” 17th International Symposium on Antenna Technology and Applied Electromagnetics (ANTEM), Montreal, QC, 2016, pp. 1-2.

[198] J. Pourahmadazar, et al., “Planar microwave lens based beam-forming phased antenna array system using non-coplanar SIW fed bowtie antenna,” International Symposium on Antenna Technology and Applied Electromagnetics (ANTEM), Montreal, QC, 2016, pp. 1-4.

[199] M. Akbari, et al., "Bandwidth enhancement of 4×4 subarrays circularly polarized rectangular dielectric resonator antenna by sequential feeding network," 2016 10th European Conference on Antennas and Propagation (EuCAP), Davos, 2016, pp. 1-4.

[200] M. Akbari, et al., "A New Antenna with Dual Band-Notched Function by Shorting Pin and S-Shaped Coupling Element," 015 IEEE International Conference on Ubiquitous Wireless Broadband (ICUWB), Montreal, QC, 2015, pp. 1-5.

[201] M. Akbari, et al., "UWB Antenna with 3.5-/5.5-GHz Dual Band-Notched Characteristics Using Two Radiating Stubs," 2015 IEEE International Conference on Ubiquitous Wireless Broadband (ICUWB), Montreal, QC, 2015, pp. 1-4.

[202] M. Akbari, et al., "A linear to circular polarizer based on frequency selective surface operating 30GHz applications," 2016 17th International Symposium on Antenna Technology and Applied Electromagnetics (ANTEM), Montreal, QC, 2016, pp. 1-2.

[203] M. Akbari, M. Farahani, A. Sebak and T. A. Denidni, "Ka-Band Linear to Circular Polarization Converter Based on Multilayer Slab With Broadband Performance," in IEEE Access, vol. 5, pp. 17927-17937, 2017.

[204] D. Pozar, Microwave Engineering. Reading, MA: Addison-Wesley, 1990.

Appendix A

Calculate the Coupling:

P_3 can be extracted by substituting A_n and C_n in (4-2), with assuming that C_n are equal to b_n which are equal for the six apertures ($C_\mathrm{n} = b_\mathrm{n} = C$).

$$P_3 = A_1 C e^{-j\beta 5S} + A_2 C e^{-j\beta 4S} + A_3 C e^{-j\beta 3S} + A_4 C e^{-j\beta 2S} + A_5 C e^{-j\beta S} + A_1 C \qquad (4-14)$$

By substituting $A_\mathrm{n}$from (4) into (14), we have

$$P_3 = P_1 C e^{-j\beta 5S}\left[1 + (1-2C) + (1-2C)^2 + (1-2C)^3 + (1-2C)^4 + (1-2C)^5\right] \qquad (4-15)$$

The finite geometric series has the following simple formula

$$1 + x + x^2 + x^3 + x^4 + \cdots + x^n = \frac{1 - x^{n+1}}{1 - x} \qquad (4-16)$$

$$\xrightarrow{Simplifying\ (15)\ using\ (16)} P_3 = P_1 e^{-j\beta 5S}\left[\frac{1-(1-2C)^6}{2}\right] \qquad (4-17)$$

By substituting C from (4-5) into (4-17), we have

$$Coupling = 10\log\left|\frac{P3}{P1}\right|$$

$$= 10\log\left|\frac{1-\left(1 - 1.016 \times {W_s}^3 \times \frac{\tan\left(\frac{\pi f}{2 f_{co}}\right)}{\frac{\pi f}{2 f_{co}}} e^{\left(-\frac{2\pi h_m f_{co} Q}{C_0}\sqrt{1-\left(\frac{f}{f_{co}}\right)^2}\right)}\right)^6}{2}\right| \qquad (18)$$

Appendix B

Calculate the Output Phase Difference:

The phase difference between the two output ports (θ) is given by (9). P_2 can be written as

$$\xrightarrow{from\ (4-1)\ and\ (4-4)} P_2 = P_1(1-2C)^6 e^{-j\beta 6S} \qquad (4-19)$$

$$\xrightarrow[by\ (4-17) and\ (4-19)]{substituting\ P_3\ and\ P_2\ in\ (9)} \theta = \beta S + \angle\left[\frac{1-(1-2C)^6}{2(1-2C)^6}\right] \qquad (4-20)$$

By substituting C from (5) in (4-20), the following equation can be achieved for the output phase difference.

$$\theta = \beta S + \angle\left[\frac{1-\left(1-2\times 0.508\times {W_s}^3\times\frac{\tan\left(\frac{\pi f}{2f_{co}}\right)}{\frac{\pi f}{2f_{co}}}e^{\left(-\frac{2\pi h_m f_{co} Q}{C_0}\sqrt{1-\left(\frac{f}{f_{co}}\right)^2}\right)}\right)^6}{2\left(1-2\times 0.508\times {W_s}^3\times\frac{\tan\left(\frac{\pi f}{2f_{co}}\right)}{\frac{\pi f}{2f_{co}}}e^{\left(-\frac{2\pi h_m f_{co} Q}{C_0}\sqrt{1-\left(\frac{f}{f_{co}}\right)^2}\right)}\right)^6}\right] \qquad (4-21)$$